

The Role of Aerosols in the Troposphere: Radiative Forcing, Model Response, and Uncertainty Analysis

by

Wenwei Pan

S.B. in Atmospheric Physics, Beijing University (1988)

S.M. in Meteorology, Massachusetts Institute of Technology (1993)

Submitted to the Department of Earth, Atmospheric and Planetary Sciences
in partial fulfillment of the requirements for the degree of

Doctor of Philosophy in Meteorology

at the

MASSACHUSETTS INSTITUTE OF TECHNOLOGY

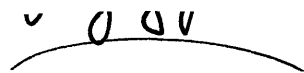
June 1996

© Massachusetts Institute of Technology 1996. All rights reserved.

Author....

.....
Department of Earth, Atmospheric and Planetary Sciences
May 3, 1996

Certified by ..



.....
Gregory J. McRae
Bayer Professor
Thesis Supervisor

Certified by ..



.....
Ronald G. Prinn
TEPCO Professor
Thesis Supervisor

Accepted by ..



.....
Thomas H. Jordan
Department Head

MASSACHUSETTS INSTITUTE OF TECHNOLOGY
WITHDRAWN
FROM
MAY 15 1996
MIT LIBRARIES
LIBRARIES

The Role of Aerosols in the Troposphere: Radiative Forcing, Model Response, and Uncertainty Analysis

by
Wenwei Pan

Submitted to the Department of Earth, Atmospheric and Planetary Sciences
on May 3, 1996, in partial fulfillment of the
requirements for the degree of
Doctor of Philosophy in Meteorology

Abstract

This thesis addresses the role of aerosols in the troposphere from three perspectives: (1) the radiative forcing by aerosols; (2) responses of meteorological and chemical fields to the aerosol radiative forcing; (3) uncertainty analysis of the radiative forcing by anthropogenic sulfate aerosols.

The sensitivity of the direct radiative forcing by anthropogenic sulfate aerosols to their optical properties, concentrations and the ambient humidity has been investigated in an explicit radiative transfer model with available aerosol and meteorological data. Results indicate that aerosol concentrations and optical properties contribute about equally to the factor-of-three difference in the estimates of this forcing in the literature. The use of constant humidity scaling factors for aerosol optical properties is a good approximation, provided that these factors in the visible wavelength are kept the same as the observed ones. Neglecting the humidity effect on aerosol single-scattering albedo and asymmetry factor will only lead to a 10% overestimate of the result.

The global distribution of radiative flux changes at the top of the atmosphere and the surface due to climatological aerosols in d'Almeida et al. [36] is calculated with the radiative transfer scheme by Fu and Liou [51]. At the top of the atmosphere aerosols decrease the net downward short-wave radiation in most parts of the globe. Increases occur mainly in the Saharian desert region, its downwind equatorial east Atlantic, and part of Australia. At the surface the decrease of the net downward short-wave radiation is more than a factor of 2 larger than that at the top of the atmosphere. Decreases of the net outgoing long-wave radiation are about an order of magnitude smaller than changes of the short-wave radiation. Changes in short- and long-wave radiation are characterized by large spatial variations and gradients. The annual global mean radiative forcing owing to aerosols increases by about a factor of 2 when the humidity effect on aerosol optical properties is included. Replacing the boundary layer heights as prescribed in the aerosol data set by the actual values decreases the result by a similar factor.

The mechanism and magnitude of meteorological and chemical responses to aerosol radiative forcings are studied in three different models: a one-dimensional radiative-convective equilibrium model, a mesoscale meteorological model, and a photochemical air quality model. The simulations in the one-dimensional radiative-convective model show that the prescribed time-invariant short-wave heating in the lower troposphere causes an increase of the long-wave heating in the upper troposphere and a decrease of the convective heating throughout the troposphere. As a result, the model atmosphere at the new equilibrium is cooler and drier. Analysis of the surface energy balance in the model shows that the equilibrium temperature change depends not only on the external forcing but also on the internal feedbacks. A negative feedback between the surface temperature and the sensible and latent

heat fluxes and a positive feedback between the surface temperature and atmospheric water vapor are evident. The negative feedback coefficient increases by a factor of 4 to 5 when the equilibrium is reached. In the meantime, the positive feedback coefficient also increases to its equilibrium value, which is comparable to the magnitude of the negative feedback. As a result, the initial sensitivity of surface temperature change to aerosol radiative forcing is about a factor of 4 to 5 smaller than the equilibrium sensitivity. The transient surface temperature change approaches the equilibrium one with a characteristic time scale, which depends on both feedback factors and surface properties.

The mesoscale model is set up in the Southern California Air Quality Study (SCAQS) region and model predictions without aerosols are validated against the SCAQS measurements. Four aerosol types with low- and high-level concentrations from the climatological aerosol data set in d'Almeida et al. [36] are introduced into the mesoscale model. The single-column simulations show that in response to large decreases in the incoming solar radiation due to aerosols surface temperature changes are less sensitive than those in the one-dimensional radiative-convective model. This attributes to the difference between initial and equilibrium sensitivity of surface temperature change to aerosol radiative forcing. The three-dimensional mesoscale simulations indicate that the domain averaged relative changes are -30 to 10% for boundary layer height, -30 to 40% from wind speed, and -20 to 0% for net downward SW radiation. Temperature changes vary from -1.5 to 0.5°C, and wind direction changes vary within 50 degrees.

Simulations in the photochemical air quality model with either uniformly perturbed or aerosol-induced meteorological fields show that the chemical fields are more sensitive to changes in temperature, wind, and boundary layer height. The domain-averaged relative changes of ground level concentrations of chemical species range up to 10% due to the prescribed low-level aerosol loading. Shifting aerosol loading from the low-level to high-level appears to almost double the concentration response of species during the day. Changes at specific sites can be much larger than the domain-averaged changes. The spatial pattern in the response of chemical fields bears little or no resemblance to that in any single meteorological perturbation.

The uncertainty of the direct and indirect radiative forcing by anthropogenic sulfate aerosols has been addressed with a new uncertainty analysis technique. The probability density function of the direct radiative forcing under the influence of 9 uncertain parameters is calculated for four different models. The mean value of the result varies from 0.3 to 1.3 W/m² with a 95% confidence range of 0.1 to 4.2 W/m². Variance analysis identifies the sulfate yield and lifetime as the two primary uncertain parameters. The probability density function of the indirect radiative forcing has been evaluated in 5 different models with respect to 20 uncertain parameters. The mean value of the indirect forcing varies from 1.2 to 1.7 W/m² with a 95% confidence range of 0.1 to 5.2 W/m². Variance analysis ranks aerosol size distribution as the leading contributor to the model uncertainty.

Thesis Supervisor: Gregory J. McRae
Title: Bayer Professor

Thesis Supervisor: Ronald G. Prinn
Title: TEPCO Professor

Acknowledgments

First of all, I would like to offer sincere gratitude to my advisors, Dr. Gregory J. McRae and Dr. Ronald G. Prinn, for their help and support through the course of this thesis work. I would also like to thank my committee members, Dr. Michael J. P. Cullen(UKMO), Dr. Kerry A. Emanuel, and Dr. Mario J. Molina for their valuable inputs and time commitment.

I also would like to extend my sincere thanks to my fellow graduate students and post-doctoral researchers: Gary G. Adamkiewicz, Dr. Josep C. Angril, Alejandro Cano-Ruiz, Morten A. Engel, Jonathan W. Fox, Jose L. Jimenez, Gene C. Lin, Betty Pun, Cheng Wang, Mort D. Webster, and Zhongxiang Wu for their friendship and assistance. To some of the former members in Dr. McRae's group, I would especially like to thank Dr. Peter S. Wyckoff for his outstanding help on computer related problems, Dr. Menner A. Tatang for his help and interaction on my uncertainty analysis, Dr. Jonathan P. Knight for sharing with me his politically oriented views, and Dr. Timothy J. Resch for his help on aerosol dynamics.

The completion of this thesis also benefits from assistance of a number of individuals outside MIT. Several people deserve special mention: Dr. Brian W. Golding of UKMO for his help and advice on using the UKMO nonhydrostatic mesoscale model, Dr. Nilton O. Renno of the University of Arizona for his help on his radiative-convective model, Drs. W. Ridgway and M.-D. Chou of NASA/GSFC and Dr. Q. Fu of Dalhousie University for providing the radiation codes, and Dr. H. Rodhe of Stockholm University for providing the global column burden data of sulfate aerosols.

Financial support of this research was provided by NASA Grants NAGW 474 (1993-1995) and NAG1 1805 (1996), NSF Grants ATM 92-16340 and ATM 95-23616 (1995-1996), the MIT PEEER Lee and Geraldine Martin Foundation Fund (1993-1994), and the U.S. Environmental Protection Agency (1993-1996).

Finally I am especially grateful to my wife, Yang Zhong, and our parents in China, for their wonderful love, care and encouragement.

Contents

1	Introduction	21
1.1	Thesis Statement	21
1.2	Background and Motivation	21
1.3	Objective	23
1.4	Thesis Outline	23
2	Role of Aerosols in the Troposphere	25
2.1	Governing Equations	25
2.2	Observational Evidence	26
2.3	Modeling Study	27
2.3.1	Direct Effect	27
2.3.2	Indirect Effect	27
2.4	Current Understanding	28
2.5	Research Targets	29
2.5.1	The Direct Radiative Forcing by Aerosols	29
2.5.2	Mechanism of Model Responses to Aerosol Radiative Forcing	29
2.5.3	Coupling Between Aerosol and Meteorological Processes	30
2.5.4	Aerosol Effects on Modeling of Gas-phase Chemistry	31
2.5.5	Uncertainty Analysis of Radiative Forcing by Anthropogenic Aerosols	31
2.6	Research Strategies	31
3	Aerosol Models and Optical Properties	33
3.1	Multi-component Aerosol Dynamics	33
3.1.1	Coagulation	33
3.1.2	Growth	34
3.1.3	Sources	34
3.1.4	Sinks	35
3.2	Dynamical Aerosol Models	35
3.3	Static Aerosol Models	36
3.4	Aerosol Optical Properties	37
4	Radiative Forcing by Aerosols	43
4.1	Radiative Transfer in the Presence of Aerosols	43
4.2	Radiative Forcing by Anthropogenic Aerosols	46
4.3	Radiative Forcing by Climatological Aerosols	49
4.4	Conclusions	69
5	Model Responses to Aerosol Radiative Forcing: 1. Radiative-convective	

Equilibrium	82
5.1 Introduction	82
5.2 Model Description and Sensitivity	83
5.3 Model Responses to Aerosol Radiative Forcing	84
5.4 Mechanism of Model Responses	85
5.5 Conclusions	92
6 Model Responses to Aerosol Radiative Forcing: 2. Mesoscale Meteorology	93
6.1 Model Description	93
6.2 Model Sensitivity and Validation	95
6.3 Single Column Simulations	110
6.4 Three-dimensional Simulations	122
6.5 Conclusions	133
7 Model Responses to Aerosol Radiative Forcing: 3. Photochemical Air Quality	134
7.1 Model Description	134
7.2 Model Sensitivity to Meteorological Fields	135
7.3 Model Responses to Aerosol-induced Meteorological Changes	137
7.4 Conclusions	145
8 Uncertainty Analysis in Large Implicit Models	149
8.1 Sources of Uncertainty in Atmospheric Modeling	149
8.2 Parametric Uncertainty Analysis	151
8.2.1 Monte Carlo Method	151
8.2.2 Deterministic Equivalent Modeling Method with Collocation	152
8.2.3 Verification: Comparison to Analytic Solution	154
8.3 Random Field Representation	156
8.4 The Cascading Scheme	166
8.5 Conclusions	168
9 Applications of Uncertainty Analysis: 1. Direct Radiative Forcing by Anthropogenic Sulfate Aerosols	169
9.1 Introduction	169
9.2 Model Structures	172
9.3 Uncertainty Analysis	173
9.4 Conclusions	179
10 Applications of Uncertainty Analysis: 2. Indirect Radiative Forcing by Anthropogenic Sulfate Aerosols	183
10.1 Introduction	183
10.2 Model Structures	183
10.3 Uncertainty Analysis	187
10.4 Conclusions	187
11 Conclusions	194
11.1 Summary	194
11.2 Implications and Future Work	196

A Subroutine for Calculating Aerosol Optical Properties	197
B A Climatological Aerosol Data Set	207
C Shell Scripts of Generating Initial Data for Mesoscale Model	218
D IMAQS Shell Scripts	226

List of Figures

3-1	Four mechanisms for coagulation [112]. Nomenclature: r, s = particle radii, k = Boltzmann's constant, T = temperature, η_a = dynamic viscosity of air, $\alpha = 1.257 + 0.4 \exp(-1.10r/\lambda_a)$ (from Cunningham slip-flow correction), λ_a = mean free path of air, Γ = shear rate, $\varepsilon = O(10) \text{ cm}^2/\text{s}^3$ rate of energy dissipation per unit mass for turbulent eddies, ν_a = kinematic viscosity of air, and $V_{S,r}$ = Stokes terminal velocity for particle of radius r	41
3-2	Different mechanisms that may act as the rate limiting step for droplet growth and the corresponding expressions for the mass growth rate [120]. Symbols are defined in Nomenclature.	42
4-1	Clear sky radiative flux and heating rates for 5 atmospheric types.	45
4-2	The relationship between the A_a/R_a and surface albedo for zero forcing of the atmosphere-surface system.	47
4-3	Comparison of global-mean DRF by anthropogenic sulfate aerosols estimated by various studies, along with the increased radiative forcing caused by the increases in carbon dioxide (CO_2) and total greenhouse gases (G) from preindustrial time to 1990. C91, C92, KB, BT, and P are defined in the text, and error bars indicate the ranges of the forcing for 95% confidence where they apply. Only the magnitudes of the forcings are shown here.	47
4-4	Monthly averaged surface albedo.	51
4-5	Monthly averaged cloud fraction.	52
4-6	Monthly averaged boundary layer relative humidity.	53
4-7	Monthly averaged column burden of anthropogenic sulfate aerosols.	54
4-8	Monthly averaged direct radiative forcing by anthropogenic sulfate aerosols: top-January; bottom-July.	55
4-9	Monthly averaged aerosol number density at surface.	56
4-10	Monthly averaged aerosol extinction coefficient at surface for $0.5 \mu m$ and a hypothetical relative humidity of 0 %.	57
4-11	Monthly averaged aerosol scattering coefficient at surface for $0.5 \mu m$ and a hypothetical relative humidity of 0 %.	58
4-12	Monthly averaged aerosol single scattering albedo at surface for $0.5 \mu m$ and a hypothetical relative humidity of 0 %.	59
4-13	Monthly averaged aerosol asymmetry factor at surface for $0.5 \mu m$ and a hypothetical relative humidity of 0 %.	60
4-14	Monthly averaged aerosol optical depth at surface for $0.5 \mu m$ and a hypothetical relative humidity of 0 %.	61
4-15	Monthly averaged aerosol extinction coefficient at surface for $0.5 \mu m$ and a boundary layer relative humidity from Figure 4-6.	63

4-16	Monthly averaged aerosol scattering coefficient at surface for 0.5 μm and a boundary layer relative humidity from Figure 4-6.	64
4-17	Monthly averaged aerosol single scattering albedo at surface for 0.5 μm and a boundary layer relative humidity from Figure 4-6.	65
4-18	Monthly averaged aerosol asymmetry factor at surface for 0.5 μm and a boundary layer relative humidity from Figure 4-6.	66
4-19	Monthly averaged aerosol optical depth at surface at surface for 0.5 μm and a boundary layer relative humidity from Figure 4-6.	67
4-20	Change of radiative flux and heating rates for 7 aerosol types.	68
4-21	Radiative flux change at the top of the atmosphere in January using a hypothetical relative humidity and a fixed boundary layer height: top-short-wave; bottom-long-wave.	70
4-22	Radiative flux change at the top of the atmosphere in January using a fixed boundary layer height and a relative humidity from Figure 4-6: top-short-wave; bottom-long-wave.	71
4-23	Radiative flux change at the top of the atmosphere in January using a varying boundary layer height and a relative humidity from Figure 4-6: top-short-wave; bottom-long-wave.	72
4-24	Radiative flux change at the surface in January using a hypothetical relative humidity and a fixed boundary layer height: top-short-wave; bottom-long-wave.	73
4-25	Radiative flux change at the surface in January using a fixed boundary layer height and a relative humidity from Figure 4-6: top-short-wave; bottom-long-wave.	74
4-26	Radiative flux change at the surface in January using a varying boundary layer height and a relative humidity from Figure 4-6: top-short-wave; bottom-long-wave.	75
4-27	Radiative flux change at the top of the atmosphere in July using a hypothetical relative humidity and a fixed boundary layer height: top-short-wave; bottom-long-wave.	76
4-28	Radiative flux change at the top of the atmosphere in July using a fixed boundary layer height and a relative humidity from Figure 4-6: top-short-wave; bottom-long-wave.	77
4-29	Radiative flux change at the top of the atmosphere in July using a varying boundary layer height and a relative humidity from Figure 4-6: top-short-wave; bottom-long-wave.	78
4-30	Radiative flux change at the surface in July using a hypothetical relative humidity and a fixed boundary layer height: top-short-wave; bottom-long-wave.	79
4-31	Radiative flux change at the surface in July using a fixed boundary layer height and a relative humidity from Figure 4-6: top-short-wave; bottom-long-wave.	80
4-32	Radiative flux change at the surface in July using a varying boundary layer height and a relative humidity from Figure 4-6: top-short-wave; bottom-long-wave.	81
5-1	Vertical profiles of equilibrium variables without aerosols (A) and with aerosols (B): a. Temperature; b. Absolute humidity.	85

5-2	Vertical profiles of equilibrium heating rate without aerosols (A) and with aerosols (B): a: short-wave (SW) heating rate; b. long-wave (LW) heating rate; c. heating rate due to diffusion; d. heating rate due to convection; e. moistening rate due to diffusion; f. moistening rate due to convection. . . .	86
5-3	Time series of $\Delta T_s/\Delta R_{ext}(dn)$, f_- , and f_+ for different aerosols with fixed absolute humidity.	89
5-4	Time series of $\Delta T_s/\Delta R_{ext}(dn)$, f_- , and f_+ for different water vapor treatments with low-level averaged-continental aerosols.	90
5-5	A schematic diagram showing how surface temperature change depends on both aerosol radiative forcing and internal processes in the model: a. short-wave; b. long-wave. Symbols are defined in the text.	91
6-1	Topography height of the SCAQS region on the UTM projection plane. . .	96
6-2	The analyzed meteorological fields from ECMWF on the SCAQS UTM projection plane at 06 GMT of August 27, 1987.	99
6-3	Observed surface temperature and wind for 13 PST of August 27, 1987. Dashed contours show the topography.	101
6-4	Observed surface temperature and wind for 23 PST of August 27, 1987. Dashed contours show the topography.	102
6-5	Mean and RMS errors of simulated surface temperature using different surface parameters for August 27, 1987. Nomenclature: $0.1r_s$ —reducing r_s by a factor of 10; $2\alpha/2z_0/2\beta$ —doubling α , z_0 and β	103
6-6	Mean and RMS errors of simulated surface wind speed using different surface parameters for August 27, 1987. Nomenclature: $0.1r_s$ —reducing r_s by a factor of 10; $2\alpha/2z_0/2\beta$ —doubling α , z_0 and β	104
6-7	Mean and RMS errors of simulated surface wind direction using different surface parameters for August 27, 1987. Nomenclature: $0.1r_s$ —reducing r_s by a factor of 10; $2\alpha/2z_0/2\beta$ —doubling α , z_0 and β	105
6-8	Mean and RMS errors of simulated surface temperature using different initial conditions for August 27, 1987. Nomenclature: ECMWF—ECMWF analysis; LAX/ECMWF—ECMWF vertical profiles at Los Angeles International Airport; EMUA/SCAQS—SCAQS soundings at El Monte-9528 Telstar for boundary layer and LAX/ECMWF for upper layers; -2Z/-32Z/-1Z-2, 32, or 1 hour earlier than the time origin.	106
6-9	Mean and RMS errors of simulated surface wind speed using different initial conditions for August 27, 1987. Nomenclature: ECMWF—ECMWF analysis; LAX/ECMWF—ECMWF vertical profiles at Los Angeles International Airport; EMUA/SCAQS—SCAQS soundings at El Monte-9528 Telstar for boundary layer and LAX/ECMWF for upper layers; -2Z/-32Z/-1Z-2, 32, or 1 hour earlier than the time origin.	107
6-10	Mean and RMS errors of simulated surface wind direction using different initial conditions for August 27, 1987. Nomenclature: ECMWF—ECMWF analysis; LAX/ECMWF—ECMWF vertical profiles at Los Angeles International Airport; EMUA/SCAQS—SCAQS soundings at El Monte-9528 Telstar for boundary layer and LAX/ECMWF for upper layers; -2Z/-32Z/-1Z-2, 32, or 1 hour earlier than the time origin.	108

6-11	Comparison of vertical profiles of temperature, relative humidity, and horizontal velocity from ECMWF analysis and SCAQS observation at two stations, Los Angeles International Airport (LAX) and El Monte-9528 Telstar (EMDU), which are close to each other.	109
6-12	Simulated screen level temperature and first level absolute humidity for 12 PST of August 27, 1987.	111
6-13	Simulated boundary layer height and first level wind for 12 PST of August 27, 1987.	112
6-14	Simulated surface net downward solar radiation flux for 12 PST of August 27, 1987.	113
6-15	Comparisons of short-wave and long-wave surface radiative flux and mid-day atmospheric heating rate using QFU scheme for CCONT aerosol type.	114
6-16	Comparisons of short-wave surface radiative flux and atmospheric heating rate using different radiation schemes for CCONT aerosol type.	116
6-17	Diurnal variations of model variable in single column simulations without aerosols at 12 PST of August 27, 1987.	118
6-18	Vertical profiles of model variables in single column simulations without aerosols at 12 PST of August 27, 1987.	119
6-19	Change of diurnal variations due to aerosol radiative forcing in single column simulations of 12 PST of August 27, 1987.	120
6-20	Change of vertical profiles due to aerosol radiative forcing in single column simulations of 12 PST of August 27, 1987.	121
6-21	Relative change of net surface shortwave flux due to aerosols at 12 PST of August 27, 1987: top-low number density; bottom-high number density.	123
6-22	Relative change of surface temperature due to aerosols at 12 PST of August 27, 1987: top-low number density; bottom-high number density.	124
6-23	Relative change of water vapor mixing ratio at 10 m due to aerosols at 12 PST of August 27, 1987: top-low number density; bottom-high number density.	125
6-24	Relative change of mixing layer height due to aerosols at 12 PST of August 27, 1987: top-low number density; bottom-high number density.	126
6-25	Relative change of horizontal wind speed at 10 m due to aerosols at 12 PST of August 27, 1987: top-low number density; bottom-high number density.	127
6-26	Relative change of horizontal wind direction at 10 m due to aerosols at 12 PST of August 27, 1987: top-low number density; bottom-high number density.	128
6-27	Diurnal variation of temperature, absolute humidity and solar radiation at surface, 10 m wind, and boundary layer height on August 27, 1987 at the center of the modeling domain.	129
6-28	Aerosol-induced changes of diurnal variation of temperature, absolute humidity and solar radiation at surface, 10 m wind, and boundary layer height on August 27, 1987 at the center of the modeling domain.	130
6-29	Vertical profiles of temperature, absolute humidity, turbulent kinetic energy, vertical diffusivity, and wind at 12 PST of August 27, 1987 at the center of the modeling domain.	131
6-30	Aerosol-induced changes of vertical profiles of temperature, absolute humidity, turbulent kinetic energy, vertical diffusivity, and wind at 12 PST of August 27, 1987 at the center of the modeling domain.	132

7-1	Simulated ground level concentrations of NO, NO ₂ , SO ₂ , SO ₃ , HO ₂ , O ₃ , NIT, and CO at 12 PST of August 27, 1987 using analyzed meteorological fields.	138
7-2	Simulated ground level concentrations of NO, NO ₂ , SO ₂ , SO ₃ , HO ₂ , O ₃ , NIT, and CO at 23 PST of August 27, 1987 using analyzed meteorological fields.	139
7-3	Relative change of ground level concentrations of NO, NO ₂ , SO ₂ , SO ₃ , HO ₂ , O ₃ , NIT, and CO corresponding to 50% change in surface temperature at 12 PST of August 27, 1987.	140
7-4	Relative change of ground level concentrations of NO, NO ₂ , SO ₂ , SO ₃ , HO ₂ , O ₃ , NIT, and CO corresponding to 50% change in surface absolute humidity at 12 PST of August 27, 1987.	141
7-5	Relative change of ground level concentrations of NO, NO ₂ , SO ₂ , SO ₃ , HO ₂ , O ₃ , NIT, and CO corresponding to 50% change in surface solar radiation at 12 PST of August 27, 1987.	142
7-6	Relative change of ground level concentrations of NO, NO ₂ , SO ₂ , SO ₃ , HO ₂ , O ₃ , NIT, and CO corresponding to 50% change in boundary layer height at 12 PST of August 27, 1987.	143
7-7	Relative change of ground level concentrations of NO, NO ₂ , SO ₂ , SO ₃ , HO ₂ , O ₃ , NIT, and CO corresponding to 50% change in wind field at 12 PST of August 27, 1987.	144
7-8	Relative change of spatial distribution of simulated ground level concentrations of NO, NO ₂ , SO ₂ , SO ₃ , HO ₂ , O ₃ , NIT, and CO at 12 PST of August 27, 1987 with low level aerosol loading.	146
7-9	Relative change of spatial distribution of simulated ground level concentrations of NO, NO ₂ , SO ₂ , SO ₃ , HO ₂ , O ₃ , NIT, and CO at 12 PST of August 27, 1987 with high level aerosol loading.	147
7-10	Relative change of ground-level O ₃ concentration at two selected sites on August 27, 1987.	148
8-1	A schematic diagram for comparing measurements and model prediction in the presence of uncertainty.	150
8-2	A schematic diagram for improving model comparison through reducing parametric uncertainty (ΔP) and structural uncertainty (ΔS).	151
8-3	Comparison of the PDFs from MCM with different sampling points, with the analytical PDF.	157
8-4	L_2 -norm error (%) between the PDFs from MCM and analytical PDF.	158
8-5	Comparison of the PDFs from DEMM with different approximation orders.	158
8-6	L_2 -norm error (%) between the PDFs from DEMM and the analytical PDF with different approximation orders.	159
8-7	The relative error estimated using Equation (9) for different approximation orders in DEMM.	159
8-8	Annual mean of total cloud fraction and its first five associated eigenfunctions.	162
8-9	Annual mean of sea level pressure and its first five associated eigenfunctions.	163
8-10	Eigenvalue spectrum for annual mean sea level pressure and total cloud fraction for the number of M values needed to explain 95% of the variance.	164
8-11	Eigenvalue spectrum for sea level pressure and total cloud fraction for the number of M values needed to explain 95% of the variance.	164
8-12	Probability density functions for the first five random variables of total cloud fraction.	165

8-13	Probability density functions for the first five random variables of sea level pressure.	165
8-14	Illustration of cascading schemes: three cascading levels for Charlson et al.'s model [24].	167
9-1	The PDF of mixed layer relative humidity used in this paper. It is assumed to be a beta distribution with mean of 0.75 and standard deviation of 0.13.	174
9-2	The PDFs of global-mean DRF by anthropogenic sulfate aerosols using 10000 sampling points MCM for D2, D3, and D4. The PDF for D1 is analytically obtained.	175
9-3	Comparison of PDFs from 10000 sampling points MCM, second order DEMM and 1000 samplings points MCM for D1.	176
9-4	Comparison of PDFs from a 10000 sampling point MCM, a second order DEMM and a 1000 sampling point MCM for D2.	177
9-5	Comparison of PDFs from a 10000 sampling point MCM, a second order DEMM and a 1000 sampling point MCM for D3.	178
9-6	Comparison of PDFs from a 10000 sampling point MCM, a second order DEMM and a 1000 sampling point MCM for D4.	178
9-7	Comparison of PDFs from DEMM for D1, D2, D3, and D4.	179
9-8	The mean and 95% confidence range of global-mean direct radiative forcing by anthropogenic sulfate aerosols estimated by MCM and DEMM for D1, D2, D3, and D4.	180
9-9	Normalized variance contribution by each uncertain parameter to direct radiative forcing by sulfate aerosols.	181
9-10	Direct radiative forcing by anthropogenic sulfate aerosols with respect to geometric man radius and standard deviation of the size distribution.	182
10-1	Comparison of global-mean IRF by anthropogenic sulfate aerosols estimated by various studies, along with the radiative forcing change by carbon dioxide (CO_2) and total greenhouse gases (G) from preindustrial time to 1990. C92, KC, BR, JRS, and CP are defined in the text, and error bars indicate the ranges of the forcing for 95% confidence where they apply. Only the magnitudes of the forcings are shown here.	184
10-2	Probability density function of the indirect radiative forcing by anthropogenic sulfate aerosols: I1.	188
10-3	Probability density function of the indirect radiative forcing by anthropogenic sulfate aerosols: I2.	189
10-4	Probability density function of the indirect radiative forcing by anthropogenic sulfate aerosols: I3.	189
10-5	Probability density function of the indirect radiative forcing by anthropogenic sulfate aerosols: I4.	190
10-6	Probability density function of the indirect radiative forcing by anthropogenic sulfate aerosols: I5.	190
10-7	Probability density functions of the indirect radiative forcing by anthropogenic sulfate aerosols for five model structures.	191
10-8	Mean and 95% confidence range of the indirect radiative forcing by anthropogenic sulfate aerosols for five model structures.	191

10-9	Normalized variance contribution to the indirect radiative forcing by uncertain parameters.	192
10-10	Indirect radiative forcing as function of geometric mean and standard deviation of size distribution for I1.	193
B-1	Size distributions of the components and of the modes of the multimodal components normalized to number density of 1 cm^{-3}	209
B-2	Real and imaginary parts of the wavelength-dependent refractive index of several aerosol components.	210
B-3	Size distributions of 10 aerosol types.	212
B-4	Wavelength dependence of optical properties of aerosol components.	214
B-5	Wavelength dependence of optical properties of aerosol types.	215
B-6	Wavelength dependence of optical properties of clean continental aerosols at different relative humidities.	216

List of Tables

1.1	Global sources, production mechanisms, components, and source strengths of atmospheric aerosols	22
2.1	A survey of research on direct tropospheric aerosol effect on surface temperature change.	28
4.1	Sensitivity of the annual global mean DRF by anthropogenic sulfate aerosols to AOPs, humidity scaling functions, and column burden.	50
4.2	The annual global mean of radiative flux changes by climatological aerosols for different cases.	69
5.1	Key parameters used in the 1-D RCM. ϵ_i are the precipitation efficiencies in Emanuel's cumulus convection scheme.	84
5.2	Net radiative flux change at model tropopause, and temperature change at surface at equilibrium as well as the resulting model sensitivity for various radiative forcing perturbation scenarios in the 1-d RCM, where a number density of $5 / \text{cm}^3$ for the mineral aerosols aloft is assumed for minerals above CM and MP.	87
5.3	Surface temperature and energy budget for clear sky and clean continental aerosol experiments.	88
6.1	Land use categories and their corresponding surface roughness $z_0(\text{m})$, albedo α , resistance to evaporation $r_s(m^{-1})$, soil thermal contact coefficient $\beta(Jm^{-2}Ks^{-1/2})$, and aerosol type.	97
6.2	Variability range of aerosol optical properties of different dry aerosol types at two selected wavelength.	98
6.3	Radiative forcing and corresponding changes in the surface sensible/latent/ground heat fluxes and temperature at 12 PST of August 27, 1987. f_- is the positive feedback coefficient as defined in the previous chapter.	117
6.4	The mean and standard deviation of changes in meteorological fields due to aerosol radiative forcing on August 27, 1987. Temperature and radiation are at the surface; wind and humidity are at the first level (10m).	133
7.1	The mean and standard deviation of relative changes(%) of chemical fields due to uniform perturbation or aerosol-induced changes in meteorological fields on August 27, 1987.	137
8.1	Number of sampling points required to achieve some error bounds with different methods.	152

8.2	Central values, uncertainty factors for log-normally distributed parameters used in the Monte Carlo and the DEMM simulations.	155
8.3	Normalized variance contribution by each uncertain parameter estimated by DEMM and the sensitivity and standard deviation for Charlson et al.'s model [24].	157
9.1	A summary of treatment of model structures in different studies for computing the direct radiative forcing by anthropogenic sulfate aerosols, where LR stands for Langner and Rodhe [83], and other symbols are defined in the text.	170
9.2	A summary of specification of model parameters in different studies for computing the direct radiative forcing by anthropogenic sulfate aerosols, where symbols are defined in the text. All parameters are column value, except those indicated by (x, y) are two-dimensional. "/" indicates an item either not available or not applicable.	171
9.3	Central values, uncertainty factors for log-normally distributed parameters used in the Monte Carlo and the probabilistic collocation simulations. . . .	173
9.4	Comparison of mean (μ), standard deviation (σ), and 95% confidence range ($R_{95\%}$) for D1.	174
9.5	Comparison of mean (μ), standard deviation (σ), and 95% confidence range ($R_{95\%}$) for D2.	175
9.6	Comparison of mean (μ), standard deviation (σ), and 95% confidence range ($R_{95\%}$) for D3.	175
9.7	Comparison of mean (μ), standard deviation (σ), and 95% confidence range ($R_{95\%}$) for D4.	176
9.8	Normalized variance contribution by each uncertain parameter estimated by DEMM for D2, D3, and D4.	180
10.1	Uncertain parameters used in the estimate of indirect radiative forcing by anthropogenic sulfate aerosols.	188
B.1	Parameters characterizing the size distributions for different aerosol components for an assumed relative humidity of 0%.	208
B.2	Aerosol components, their number density fraction, and geographical locations for different aerosol types. "Bg." and "wc." stand for background and wind-carrying respectively.	211
B.3	Vertical distribution of atmospheric aerosols. The extinction coefficient values refer to dry particles. The underlined values represent normalized extinction coefficients with respect to number density of 1 cm^{-3} and z is in unit of km.	217

Nomenclature

A	Area of the Earth (4)
A_a	Absorptance of aerosol layer (5)
A_c	Total cloud cover fraction (4)
A_{st}	Fraction of stratiform cloud cover (5)
a_w	Water activity (3)
B	Column burden, kg/m^2 (3)
	Beta function (5)
B_λ	Planck function, $\text{W}/(\text{m}^2\text{Sr}\mu\text{m})$ (5)
C	Covariance matrix of a random field (4)
C_{eq}	Gas-phase concentration required for equilibrium with droplet solution (3)
$C_{u,v,T,g,x,n}$	Contribution from subgrid convection (2)
C_∞	Gas-phase concentration in ambient air (3)
c	Central value (4)
	Slope for cloud condensation nuclei activation spectrum (5)
c_D, c_H	Drag coefficients for momentum and heat (8)
c_p	Heat capacity at constant pressure for air, $\text{J}/(\text{kgK})$ (8)
c_s	Specific heat capacity of soil, $\text{J}/(\text{kgK})$ (8)
c_v	Heat capacity at constant volume for air, $\text{J}/(\text{kgK})$ (2)
D_i	Particle or component diffusivity, m^2/s (3)
F_T	Solar constant, W/m^2 (4)
F_λ	Net downward monochromatic irradiance, $\text{W}/(\text{m}^2\mu\text{m})$ (5)
F_{T,q_1}	Vertical diffusion of temperature/water vapor (7)
f	Coriolis parameter, $f=2\Omega \sin \phi$, $1/\text{s}$ (2)
f_{ac}	Aerosol activation fraction (5)
$f(k)$	Probability density function of parameter k (4)
$f(\omega)$	Random variable (4)
G	Size growth factor (5)
GH	Ground heat flux, W/m^2 (7)
$G_{X,n}$	Mass transfer between gas-phase species and aerosols (2)
g	Asymmetry factor (3)
	Gravitational acceleration, m/s^2 (2)
H	Mixing layer height, m (5)
I	Mie intensity parameter in the Stokes matrix (3)
I_i	Uptake rate of species i , kg/s (2)
I_λ	Monochromatic radiance, $\text{W}/(\text{m}^2\text{Sr}\mu\text{m})$ (5)
J_λ	Monochromatic source function of radiative transfer (5)
K	Thermal diffusivity, m^2/s (8)
\mathbf{K}	Atmospheric eddy diffusivity tensor, m^2/s (2)
k	Y-offset for cloud condensation nuclei activation spectrum (5)
	Input uncertain parameter (4)
k_L	Mass transfer coefficient (3)
$k_{f,r}$	Forward/reverse reaction rate constant (3)
k_v	Vertical diffusion coefficient, m^2/s (7)
L	Aerosol lifetime in the atmosphere, s (3,4,5)
	Latent heat of evaporation of water, J/kg (8)

LH	Latent heat flux, W/m^2 (7)
LW	Long-wave flux, W/m^2 (7)
m	Mass coordinate vector, kg (2)
m	Refractive index (3)
m_0	Mass of dry particle, kg (3)
m_w	Mass of condensed water, kg (3)
N	Total number density, $1/m^3$ (3)
N_d	Cloud droplet number density, $1/m^3$ (5)
n	Refractive index (3)
$n(r)$	Aerosol size distribution, $1/m^4$ (2)
n_0	Refractive index of dry particle (3)
n_w	Refractive index of water (3)
n_i	Imaginary part of refractive index (2)
P	Phase function (3)
P_{T,q_i}	Contribution from subgrid precipitation (2)
P_λ	Phase function (5)
p	Number of input parameters (4)
	Pressure, pa (2)
Q	Aerosol source strength, kg/s (3,4,5)
$Q_{e,s,a}$	Extinction/scattering/absorption efficiency factors (3)
$q_i(i=1,2,3)$	Specific humidity of vapor/liquid/ice forms of water, kg/kg (2)
R	Gas constant of dry air, $J/(kgK)$, (2)
	Radiative flux, W/m^2 (7)
RH	Relative humidity (3)
$R_{95\%}$	Range of 95% confidence level (5)
R_a	Reflectance of aerosol layer (5)
R_{as}	Reflectance of aerosol layer and surface (5)
R_{ct}	Cloud top albedo (5)
R_i	Richard number (8)
R_s	Surface albedo (4)
R_T	Radiative flux divergence (2)
R_w	Gas constant of water, $J/(kgK)$, (2)
$R_{\chi,n}$	Contribution from chemical reactions (2)
r	Particle radius (2,3)
r_0	Dry particle radius (2)
r_1	Low limit of particle radius (3)
r_2	High limit of particle radius (3)
r_g	Geometric mean radius, m (3)
r_{min}	Radius of smallest aerosol activated (5)
r_s	Surface resistance to evaporation, $1/m$ (8)
SH	Sensible heat flux, W/m^2 (7)
SW	Short-wave radiative flux, W/m^2 (7)
S_{max}	Maximum supersaturation in cloud (5)
$S(\lambda)$	Monochromatic solar irradiance $W/(m^2\mu m)$ (5)
$S_{\chi,n}$	Contribution from source (2)
s	Particle radius, m (3)
T	Temperature, K (2)
	Atmospheric transmittance (4)

T_a	Transmittance of aerosol layer (5)
t	Time, s (2)
V	Volume, m^3 (3)
$V_{s,r}$	Stokes terminal velocity for particle of radius r , m/s (3)
V_w	Specific volume of water, m^3/kg (3)
\vec{V}	Velocity vector, m/s (2)
u	Velocity in the east-west direction, m/s (2)
	Uncertainty factor (4)
v	Velocity in the north-south direction, m/s (2)
W	Cloud liquid water content (5)
w^*	Effective vertical velocity, m/s (5)
w	Velocity in the vertical direction, m/s (2)
x	Output variable (4)
(x,y,z)	Cartesian spatial coordinates (2)
$(x,y,z)(\omega)$	Random variable (4)
Y	Fraction of sulfur dioxide converted to sulfate (3,4,5)
z_0	Roughness height, m (8)

Greek

α	Factor in Cunningham slip-flow correction (3)
	Surface albedo (8)
α_i	i th eigenfunction (4)
α_k, β_k	Coefficients of recurrence relations for orthogonal polynomials (4)
β	Coagulation kernel, m^3/s (2,3)
	Thermal contact coefficient, $JK/(m^2s^{1/2})$ (8)
$\bar{\beta}$	Backscattered fraction (4,5)
β_i	Random variable (4)
ϵ	Error bound (4)
ϵ_M	Fractional variance (4)
ε	Rate of energy dissipation per unit mass in turbulent eddy, m^2/s^3 (3)
η_a	Dynamic viscosity of air (3)
θ	Potential temperature, K (7)
	Scattering angle (3)
λ	Wavelength, μm (2)
λ_a	Mean free path of an air molecule, m (2)
λ_i	i th eigenvalue (4)
μ	Cosine of solar zenith angle (5)
	Mean (5)
ν_a	kinematic viscosity of air (3)
$\tilde{\omega}$	Single-scattering albedo (2,3)
ρ	Air density, kg/m^3 (2)
ρ_s	Soil density, kg/m^3 (2)
σ	Surface tension on the wet particle surface, N/m (3)
	Standard deviation (5)
$\sigma_{e,s,a}$	Extinction/scattering/absorption coefficients, 1/m (3)
σ_g	Geometric standard deviation (3)

τ	Optical depth (2)
$\vec{\tau}$	Momentum flux (8)
τ_c	Optical depth of cloud (5)
Ω	Probability space (4)
ω	Element of probability space (4)
ϕ	Azimuthal angle (5)
	Latitude (2)
χ_j	Mass of gas-phase species j per unit mass of dry air, kg/kg (2)
Ψ_e	Specific extinction coefficient, m ² /kg (3)

Acronym

AOP	Aerosol Optical Properties
BLM	Boundary Layer Model
CCM	Community Climate Model
CIT	California Institute of Technology and Carnegie Institute of Technology
DEMM	Deterministic Equivalent Modeling Method
DRF	Direct Radiative Forcing
EBM	Energy Balance Model
ECMWF	European Center for Medium-range Weather Forecast
GCM	General Circulation Model
GMT	Greenwich Mean Time
GSFC	Goddard Space Flight Center
IRF	Indirect Radiative Forcing
LLNL	Lawrence Livermore National Laboratory
MCM	Monte Carlo Method
NCAR	National Center for Atmospheric Research
NMC	National Meteorological Center
ODE	Ordinary Differential Equation
PDF	Probability density function
PST	Pacific Standard Time
RCM	Radiative Convective Model
SCAQS	Southern California Air Quality Study
UKMO	United Kingdom Meteorological Office
UTM	Universal Transverse Mercator

Chapter 1

Introduction

1.1 Thesis Statement

Tropospheric aerosols¹ have been studied for several decades in the research areas of meteorology, atmospheric chemistry, and remote sensing. Their environmental roles are achieved mainly through the interaction of aerosols and radiation field, and to a lesser degree through their participation in the chemical reaction pathways.

The effects of radiative forcing and chemical reactions involving atmospheric aerosols depend critically on their size distribution, shape, and chemical composition. The short lifetimes, inhomogeneous sources, and complicated physical and chemical transformations for atmospheric aerosols and their precursors demand fairly high resolution observational networks and sophisticated numerical models for their accurate study. Currently the lack of these networks and models adds large uncertainty to quantifying the spatial and temporal evolution of aerosol characteristics in the atmosphere.

Effects of aerosols are also dependent on their interactions and feedbacks with other components in the atmospheric system. An integrated modeling effort is therefore required to address the role of aerosols in the atmosphere.

Finally, since any modeling results are subject to uncertainty in the model structures and parameters, systematic uncertainty analysis is required in order to reach any quantitative conclusions.

This thesis addresses the role of aerosols in the troposphere in the context of radiative forcing, model response, and uncertainty analysis.

1.2 Background and Motivation

Atmospheric aerosols consist of suspended fine solid or liquid particles in air. They can be characterized by such properties as chemical composition, particle shape, size distribution and number density, which are in principle functions of both space and time. Chemical composition and number density are generally determined by production source type and strength. Particle shape and size distribution are dictated by the aerosol production and evolution mechanisms. The processes of transformation (coagulation, condensation, chemi-

¹Due to the high degree of atmospheric stability and the lack of clouds in the stratosphere, stratospheric aerosols have residence times of a year or more compared with days for tropospheric aerosols and were not the focus of this work.

cal conversion, and recycling through cloud droplets), transport (advection, convection, and turbulent mixing), and scavenging (wet and dry depositions) are the main factors to affect the spatial and temporal distributions of aerosol properties.

Table 1.1, adapted from d’Almeida *et al.* [36] and Hobbs [68], summarizes the sources, production mechanisms, particle components, and source strengths of typical atmospheric aerosols. The estimates for source strengths are rather crude. Nevertheless, two points can be drawn here: (1) natural source strengths are much larger than man-made ones; and (2) ocean, crust, gas-to-particle conversion, and clouds are the main sources for atmospheric aerosols.

Because of measuring techniques, aerosol components are usually classified into Aitken particles ($r < 0.1 \mu m$), large particles ($0.1 \mu m \leq r < 1 \mu m$), and giant particles ($r \geq 1 \mu m$). However, from the view of the production mechanisms, it is more appropriate to group aerosol particles into a nuclei mode ($r < 0.05 \mu m$), accumulation mode ($0.05 \mu m \leq r < 1 \mu m$), and coarse mode ($r \geq 1 \mu m$) [163, 39]. The particles in the nuclei mode are created from the condensation of vapor during combustion and nucleation of atmospheric species. The accumulation mode particles are produced by the coagulation of nuclei mode particles or vapor condensation on existing particles. The coarse particles are the direct products of surface sources such as deserts and oceans.

Source	Production mechanism	Aerosol component	Source strength (10^{12} g/yr)
Natural			
biomass burning	combustion	soot particles	200-450
biosphere	direct injection	pollen/spores/etc.	80
clouds	cloud evaporation	water-soluble	3000
crust/cryosphere	weathering	soil dust	2000
extraterrestrial	cosmic dust	meteoric dust	10
gas-to-particle conversion	nucleation	sulfate/nitrate/organics	345-1100
ocean/fresh water	bubble bursting	sea-salt	1000-2000
volcanoes	direct injection	water-insoluble	15-90
	nucleation	H ₂ SO ₄	
Man-made			
direct emission	direct injection	dust/soot/water-soluble	10-90
gas-to-particle conversion	nucleation	sulfate/nitrate/organics	175-325
biomass burning	combustion	soot particles	3-150

Table 1.1: Global sources, production mechanisms, components, and source strengths of atmospheric aerosols

Because of the interaction among aerosol particles in different size ranges, particles at a given time may be externally or internally mixed. In an external mixture, different components co-exist without coagulation; while in an internal mixture, different components coagulate with each other and result in a heterogeneous chemical structure. It is believed that after a given residence time in the atmosphere, most aerosol particles are internally mixed. Only freshly produced particles may possess an externally mixed structure.

Atmospheric aerosol research is motivated by the need to include aerosols in the study of remote sensing, air quality modeling, weather prediction and climate modeling. Both con-

ventional (e.g., lidar) and non-conventional (e.g., satellite) sensing of surface or atmospheric parameters require corrections for aerosol scattering and the absorption and emission of radiation. Therefore it is essential to improve our understanding of aerosol properties and their distributions to achieve accuracy in such measurements.

The influence of aerosols on air quality is manifested in the following three aspects. Aerosols can change the photolysis rate constant by scattering and absorbing the ultraviolet (UV) solar radiation. They can interact with gas-phase species through aerosol surface chemical conversions and aqueous chemistry. Finally they can modify meteorological fields, which in turn determine the diffusion, transport, and removal processes for chemical species in the atmosphere.

The aerosol-induced perturbation on the radiation budget and cloud condensation nuclei may affect both weather prediction and climate modeling. As we will discuss in the following section, results of previous sensitivity studies do indicate the importance of atmospheric aerosols for global climate. In response to possible global climate change due to rising trace gases, the last decade has witnessed considerable research effort on these gases. However, a similar effort is still lacking in the area of aerosol research. One of the reasons for this lack is that the complicated sources for aerosol particles and their precursors and their short lifetimes demand fairly high resolution observations and models and the inclusion of various physical, chemical, and dynamical processes in the models.

1.3 Objective

The objective of this study is to improve the understanding of the role of aerosols in the troposphere with the focus on the following questions:

1. What are the magnitude and distribution of the radiative forcing induced by natural and anthropogenic aerosols in the troposphere?
2. What are the mechanisms and magnitudes of meteorological and atmospheric chemical response to aerosol radiative forcings?
3. How can we quantify the uncertainty of the radiative forcing by anthropogenic sulfate aerosols? What are the parameters contributing most to the variance of estimates of this forcing?

1.4 Thesis Outline

The thesis is organized into 11 chapters. Chapter 2 which follows reviews the current understanding of aerosol effects in the troposphere and points out some of the remaining problems to be addressed in this thesis.

Chapter 3 describes the characterization of aerosol physical and optical properties and reviews the current status of aerosol modeling.

Chapter 4 presents the calculations of the radiative forcings by anthropogenic sulfate aerosols and climatological aerosols.

Chapters 5 to 7 address the aerosol effects in the atmosphere with different emphases. In Chapter 5 a one-dimensional radiative-convective equilibrium model is used to study the mechanism and magnitude of aerosol effects on climate. In Chapter 6 a mesoscale meteorological model is applied to a typical urban-rural complex. One-dimensional and

three-dimensional simulations with different aerosol loading scenarios are carried out to study the aerosol effect on mesoscale meteorological fields. Results are then used to evaluate the coupling between aerosol and meteorological processes. In Chapter 7 a photochemical air quality model is used to study the sensitivity of chemical species concentration to changes in meteorological fields.

Chapter 8 addresses the need for uncertainty analysis in atmospheric modeling and demonstrates the efficiency of the deterministic equivalent modeling method with collocation in performing parametric uncertainty analysis in complex models. Two applications are presented in Chapter 9 and 10, where uncertainty analyses are carried out to the direct and indirect radiative forcing by anthropogenic sulfate aerosols.

Chapter 11 summarizes the accomplishments of the thesis and outlines the remaining future work.

Chapter 2

Role of Aerosols in the Troposphere

In this chapter the equations which govern the meteorological, gas-phase chemical, and aerosol processes in the atmosphere will be described to clarify the role of aerosols, followed by a review of both observational and modeling evidence. After summarizing the current understanding of this issue, I will present the research problems and the corresponding strategies to copy with these problems.

2.1 Governing Equations

To understand the role of aerosols in the atmosphere, it is helpful to review the equations governing the physical and chemical processes in the atmosphere:

$$\frac{\partial u}{\partial t} = -\vec{V} \cdot \nabla u + fv - \frac{1}{\rho} \frac{\partial p}{\partial x} + \nabla \cdot \mathbf{K} \cdot \nabla u + C_u, \quad (2.1)$$

$$\frac{\partial v}{\partial t} = -\vec{V} \cdot \nabla v - fu - \frac{1}{\rho} \frac{\partial p}{\partial y} + \nabla \cdot \mathbf{K} \cdot \nabla v + C_v, \quad (2.2)$$

$$\frac{\partial w}{\partial t} = -\vec{V} \cdot \nabla w - g - \frac{1}{\rho} \frac{\partial p}{\partial z} + \nabla \cdot \mathbf{K} \cdot \nabla w, \quad (2.3)$$

$$\frac{\partial \rho}{\partial t} = -\nabla \cdot (\rho \vec{V}), \quad (2.4)$$

$$\frac{\partial T}{\partial t} = -\vec{V} \cdot \nabla T - \frac{RT}{c_v} \nabla \cdot \vec{V} + \nabla \cdot \mathbf{K} \cdot \nabla T + C_T + R_T + P_T, \quad (2.5)$$

$$p = \rho RT, \quad (2.6)$$

$$\frac{\partial q_i}{\partial t} = -\nabla \cdot (q_i \vec{V}) + \nabla \cdot \mathbf{K} \cdot \nabla q_i + C_{q_i} + P_{q_i}, \quad (2.7)$$

$$\frac{\partial \chi_j}{\partial t} = -\nabla \cdot (\chi_j \vec{V}) + \nabla \cdot \mathbf{K} \cdot \nabla \chi_j + C_{\chi_j} + R_{\chi_j} + S_{\chi_j} - G_{\chi_j}, \quad (2.8)$$

$$\begin{aligned} \frac{\partial n(\mathbf{m})}{\partial t} &= -\nabla \cdot (n(\mathbf{m}) \vec{V}) + \nabla \cdot \mathbf{K} \cdot \nabla n(\mathbf{m}) - \sum_{i=1}^s \frac{\partial}{\partial m_i} (n(\mathbf{m}) I_i) \\ &\quad + \frac{1}{2} \int_0^{m_1} \dots \int_0^{m_s} \beta(\mathbf{u}, \mathbf{m} - \mathbf{u}) n(\mathbf{m} - \mathbf{u}) n(\mathbf{u}) d\mathbf{u} - n(\mathbf{m}) \int_0^\infty \dots \int_0^\infty \beta(\mathbf{u}, \mathbf{m}) n(\mathbf{u}) d\mathbf{u} \\ &\quad + C_{n(\mathbf{m})} + R_{n(\mathbf{m})} + S_{n(\mathbf{m})} + G_{\chi_j}, \end{aligned} \quad (2.9)$$

where

$$i = 1, 2, 3$$

$$j = 1, 2, \dots, M,$$

$x, y, z, u, v, w, \vec{V}, \rho, p, T, f, c_v$, and R have the usual meteorological definitions, q_i is the specific humidity of the vapor, liquid, and ice forms of water, χ_j is the ratio of the mass of any gas-phase chemical species to that of air in the same volume omitting water, n is the size distribution for an s -component aerosol mass coordinate vector \mathbf{m} , \mathbf{K} is the atmospheric eddy diffusivity tensor, C and P represent the contribution from subgrid convection and precipitation. R_T in Equation 2.5 is the radiative flux divergence, and R_{χ_j} and $R_{n(\mathbf{m})}$ are the rate of generation of gas-phase species and aerosol particulates due to chemical reactions. S and G in Equations 2.8 and 2.9 denote the source and mass transfer between gas-phase species and aerosol particulates. In Equation 2.9, the third and fourth terms of the right-hand side represent the rate of generation due to aerosol growth and coagulation, where β is the coagulation kernel and I_i is the growth rate for the i th component (cf. Chapter 3).

The direct and indirect aerosol effects on radiation and hence meteorology results from perturbation of R_T and P_T in Equation 2.5. Aerosols affect chemistry through perturbing the photochemical reaction, R_{χ_j} , and the gas-to-particle conversion, G_{χ_j} , in Equations 2.8 and 2.9.

These equations are traditionally solved separately in the areas of meteorology (Equations 2.1 to 2.7), gas-phase chemistry (Equation 2.8), and aerosol physics (Equation 2.9). This approach implicitly assumes the interactions between meteorology, gas-phase chemistry, and aerosols are small. One of the questions to be addressed in this thesis is the strength of two-way coupling between aerosol and meteorological processes, which can be measured by the magnitude of aerosol-induced dynamical field changes, since any significant change in these dynamical fields would then affect the physical and chemical transformation of aerosols in the atmosphere.

2.2 Observational Evidence

Over the past two decades, observations of aerosol effects on near-clear sky radiation balance and the cloud top albedo have steadily accumulated.

The absorption and scattering of solar radiation by aerosols can cause heating in the aerosol layer and reduction of the radiative flux at the surface. Carlson and Benjamin [18] found typical heating rates in excess of $1^\circ\text{C}/\text{day}$ from the combined short and long wave spectrum for most of the atmosphere below 500 mb in a region with suspended Saharan Desert dust. Ackerman and Cox [1] determined that aerosols in the desert air over Saudi Arabia approximately doubled the clear sky short wave absorption and may play an important role in the maintenance of the heat low over the peninsula. For urban areas, Hänel [63] carried out *in situ* measurements in Frankfurt, Germany and Tucson, Arizona and concluded that maximum heating rates of about $10^\circ\text{K}/\text{day}$ were reached at the ground and up to about 15% of the incoming solar radiation can be absorbed within particles. Moreover, Ball and Robinson [9] have shown that the average annual solar irradiance is depleted by 7.5% at the surface in the eastern United States due to aerosols. For a daily mean surface irradiance of $200 \text{ W}/\text{m}^2$, the change in surface forcing would be $7.5 \text{ W}/\text{m}^2$ if about half of this depleted irradiance is lost to the atmosphere by reflection to space. Recently

Justus and Murphey [73] analyzed the temporal trends of surface irradiance at ultraviolet wavelengths in Atlanta from 1980 to 1984 and found out that the decrease of about 10% in Robertson-Berger (UVB) meter readings over this period appeared to be due to changes in aerosol concentrations.

Cloud-top albedo and cloud lifetime depend on the cloud condensation nuclei (CCN) density, which is determined by the density of available relevant aerosol particulates in the atmosphere. An increase in the cloud droplet concentration caused by aerosol-induced cloud condensation nuclei (CCN) was demonstrated by Leaitch [86] in the analysis of hundreds of cloud water samples taken over eastern North America. As first shown by Twomey [150], the increase in the cloud droplet concentration will lead to an increase of cloud albedo assuming the total liquid water content is unchanged. Tests of the so-called Twomey “CCN-cloud brightening theory” have been made possible by satellite and airborne observations of the enhanced droplet number concentrations in marine stratiform clouds due to emissions from ship stacks [29, 114] and due to contamination from polluted continental air [6]. Also there are some indications that increased CCN concentrations might prolong the lifetime of stratiform clouds [114, 6] and thus enhance their contribution to the planetary albedo.

2.3 Modeling Study

2.3.1 Direct Effect

Modeling of the direct radiative influence of aerosols on the atmosphere started with the pioneering work of Ångström in 1929 [8]. Since then, a full array of energy balance, radiative-convective, boundary layer, and general circulation models has been used in the study of aerosol effects on climate. A brief survey of some of these modeling studies is given in Table 2.1. Some factors considered include the aerosol vertical profile ($n(z)$), size distribution ($n(r)$), imaginary part of the refractive index (n_i), single-scattering albedo ($\tilde{\omega}$) and optical depth (τ) at $0.55 \mu m$, method for radiation calculation, form of the climate model, and surface temperature changes. As we see from Table 2.1, the predicted surface temperature change ΔT_s depends not only on aerosol characteristics (i.e., size distribution, refractive index, single-scattering albedo, optical depth) but also on its vertical distribution, method for radiation calculation and type of climate model used. At this point it is still quite difficult to distinguish the contribution by individual processes to the model response. Moreover, a detailed examination indicates that the results were not consistent. Specifically, the studies by Ackerman [2], Tanre et al. [142] and Coakley and Cess [30] show that the aerosol effect on surface temperature is insignificant. On the other hand, the recent study by Taylor and Penner [145] concludes that this effect is significant even for anthropogenic sulfate aerosols alone, which have a much smaller optical depth than natural aerosols.

2.3.2 Indirect Effect

Compared to studies of the direct effect of aerosols on the radiative balance in the atmosphere, modeling of the aerosol effect on clouds has a shorter history. Charlock and Sellers [21] studied the aerosol effect on the low level cloud albedo in the context of a radiative convective model and concluded that a doubling in the number of CCN gave a $0.9^\circ C$ decrease in the model surface temperature. The influence of cloud radiation absorption due to aerosols was studied by Ackerman and Baker [3] and Newiger and Bahnke [102]. They found that an increase in the absorption of solar radiation in a cloud due to aerosols can

Table 2.1: A survey of research on direct tropospheric aerosol effect on surface temperature change.

Authors	n(z)	n(r)	$n_i/\bar{\omega}$	τ	Radiative Transfer	Climate Model	ΔT_s (K)
Rasool/Schneider 1971 [117]	homogeneous	Junge 1952 [72]	/0.90 /0.99	0.2	SW/LW 2-S appx.	1d/EBM	-2.3 -3.4
Yamamoto/Tanaka 1972 [171]	Elterman's 1964 [45]	Deirmendjian 1964 [40]	/0.90 /0.99	0.2	SW Adding	1d/EBM	-2.4
Wang/Domoto 1974 [159]	Elterman's 1964 [45]	Deirmendjian 1964 [40]	$0(\lambda < 0.6)/$ linear/ $0.1(\lambda > 2)/$	0.25	2-S appx.	1d/RCM	-2.1
Reck 1976 [118]	Lower layers	Junge 1952 [72]	0.1/	0.26		1d/RCM	-1.0
Zdunkowski et al. 1976 [173]	Modeled 1952 [72]	Junge	0.048/0.72	0.8	Spherical Harmonics	1d/BLM Wet	-4/-17
Ackerman 1977 [2]	Measurement	bi-modal lognormal	0.04/	0.3	4-S appx.	1d/BLM dry	-0.1
Welch et al. 1978 [161]	Modeled	Junge 1952 [72]	0.048/0.72	0.8	Spherical Harmonics	2d/BLM Wet	-2/-7
Charlock/Sellers 1980 [22]	Toon/Pollack's 1976 [146]	Toon/Pollack 1976 [146]	/0.994	0.125		1d/RCM	-1.5
Coakley et al. 1983 [31]	homogeneous	Shettle/Fenn 1979 [132]	0.005/0.96	0.07- 0.16	SW	2d/EBM	-2.7- -3.0
Tanre et al. 1984 [142]	WCP-12 1980 [38]	WCP-12 1980 [38]			ECMWF scheme	ECMWF GCM	-0.15
Coakley/Cess 1985 [30]	Toon/Pollack's 1976 [146]	Shettle/Fenn 1979 [132]			2-S appx.	NCAR CCM	-0.08
Taylor/Penner 1994 [145]	Modeled	lognormal	0/1.0	0.04	SW	NCAR CCM1	-1.0

significantly modify the cloud heating rate and may affect the cloud dynamics. Recently, Ghan [55], using a general circulation model, revealed that not only cloud albedo but also cloud liquid water content and cloud lifetime could be enhanced by an increase of the CCN number. Charlson et al. [24] estimated that the globally averaged perturbation in short wave radiative forcing by clouds due to anthropogenic sulfate aerosols was approximately -1 W/m^2 for an assumed global-mean enhancement in cloud droplet number concentration of 15%¹. Jones et al. [70] introduced sulfate aerosol effect on cloud condensation nuclei into the United Kingdom Meteorological Office (UKMO) unified forecast/climate model and estimated that the indirect aerosol radiative forcing was approximately -1.3 W/m^2 in the global annual mean.

2.4 Current Understanding

The general conclusion from both the modeling and observational studies carried out to date can be summarized as follows:

- The aerosols can either decrease or increase the radiative energy received by the planet system and, thus, lead to either cooling or warming of the system; the cutoff

¹The sensitivity of global-mean surface temperature to radiative forcing at the top of the atmosphere was estimated to be $0.47 \pm 0.05 \text{ K}/(\text{W/m}^2)$ [20].

between the two cases depends on the aerosol optical properties (i.e., single-scattering albedo, phase function, and optical depth), the location of the aerosol layer, and the underlying surface reflectivity (cf. Chapter 4).

- In the aerosol layer itself the absorption of solar radiation leads to a warming of the layer. On the other hand, the aerosol absorption and emission in the atmospheric window (i.e., $8\ \mu\text{m}$ to $13\ \mu\text{m}$) increase the upward emission of the layer and produce a local radiative cooling. Both effects in an aerosol-rich environment can reach up to one to several degrees per day, which is comparable to the radiative effects due to tropospheric water vapor.
- The aerosol effects depend strongly on aerosol radiative characteristics, which are described by the complex refractive index, size distribution, and spatial and temporal distribution of the aerosols, and the relative humidity of the ambient air.
- The impact of aerosols on cloud structure and lifetime may also yield a cooling effect, which needs further study.

2.5 Research Targets

2.5.1 The Direct Radiative Forcing by Aerosols

Over recent years, the global mean direct radiative forcing² by anthropogenic aerosols, especially sulfate aerosols, has been estimated in several studies by Charlson et al. (1991) [23], Charlson et al. (1992) [24], Kiehl and Briegleb (1993) [77], Box and Trautmann (1994) [16], Penner et al. (1994) [107], and Taylor and Penner (1994) [145]. These estimates range from -0.28 to $-1.30\ \text{W}/\text{m}^2$. Since different model structures and parameters have been used in these studies, the causes for the large discrepancy have not been unveiled clearly. Therefore, further investigation of this issue is necessary.

On the other hand, as pointed out in Chapter 1, natural aerosols are important components of total aerosols in the atmosphere. Therefore studies of the direct radiative forcing by anthropogenic aerosols closely depend on the direct radiative forcings by total aerosols and natural aerosols. Although complete prognostic global aerosol fields are unlikely to be available in the near future, estimates of the global direct radiative forcing by total aerosols can be made based on our current knowledge. These estimates can be used to understand the role of aerosols in the global radiation budget and to identify the key processes.

2.5.2 Mechanism of Model Responses to Aerosol Radiative Forcing

The model responses to aerosol radiative forcing depend on not only the forcing itself but also the internal processes. These internal processes are represented by the physics and chemistry in specific models. Therefore, models with different treatment of physical and chemical processes in the system may give quite different results to the same forcing.

In the global climate model (GCM) studies of aerosol effects by Tanre et al. [142] and Coakley and Cess [30], the sea surface temperature is fixed and little change of surface

²The direct radiative forcing by aerosols is defined as the scattering or absorption of solar and terrestrial radiation, as opposed to the indirect radiative forcing by aerosols, whereby cloud optical properties are influenced by the available number concentration of cloud condensation nuclei. However, the radiative forcing will be referred as the direct radiative forcing throughout the thesis unless stated otherwise.

temperature due to changes in aerosol forcing is found. On the other hand, in the study by Taylor and Penner [145], a GCM is coupled to a 50 meter deep mixed-layer ocean model and the model response to anthropogenic sulfate aerosol forcing alone, which is much smaller than that in Tanre et al. [142] and Coakley and Cess [30], is found to be quite large.

Previous boundary layer model (BLM) studies have also reached different conclusions. Zdunkowski et al. [173] studied the effects of air pollution (defined by the NO_2 and aerosol concentration) on the planetary boundary layer (PBL) using a one-dimensional model. They found that the impact on the evolution of temperature and wind profiles is highly significant, with temperature decreases ranging from 4 to 17°C. They also found a maximum inversion height increase of more than 500 m due to heavy pollution. A maximum relative humidity change of 50% due to heavy pollution was also found.

In the two-dimensional boundary layer model by Welch et al. (1978) low-level pollution sources lead to a 2°C surface temperature decrease during the day and upper level sources lead to 7°C decreases under stagnant conditions in urban areas.

However, Ackerman [2] employed a one-dimensional two-layer boundary layer model with no hydrological cycle and simulated the temporal evolution of surface temperature, mixing layer height, and mean potential temperature in the mixed layer. He concluded that aerosols have a fairly small effect on urban temperature because of the self-stabilizing compensation within the surface-atmosphere system.

We conclude that the mechanisms underlying aerosol effects in the atmosphere need to be addressed in more rigorous models.

2.5.3 Coupling Between Aerosol and Meteorological Processes

The coupling between aerosol and meteorological processes determines how aerosol modeling should be carried out. The common approach of decoupling these processes in aerosol modeling, i.e., using meteorological fields from either observation or atmospheric models, stems from the traditional approach of air quality modeling, which solves the spatial and temporal distribution of chemical species. Because most gas-phase chemical species are not radiatively important in the troposphere or contribute only a small contribution to the energy budget in the atmosphere, their feedbacks may be negligible. However, aerosols differ from gas-phase species in several ways. Their effect on radiation covers wide spectral bands instead of the narrow bands covered by most radiatively active gases. As a result, the induced radiative perturbation may lead to a significant change in the radiation budget at the surface and the heating/cooling rates aloft, which will in turn affect the surface heat flux, temperature structure, and convective and turbulent mixing processes. Also aerosols may participate in cloud microphysical processes and modify its optical depth and precipitation efficiency and thus influence the atmospheric circulation, latent heat release, wet deposition and scavenging for chemical species.

Under the assumption of no compensation and feedbacks among different components in the system, sufficient conditions for decoupling aerosol and meteorological processes can be sought out in terms of the surface energy budget and heating/cooling rate in the atmosphere. On the surface, the aerosol-induced radiative flux change should be much smaller than the other components including radiative flux, latent and sensible heat flux and ground heat flux. In the atmosphere, the heating/cooling rate due to aerosols should be much smaller than those due to radiation, convection, diffusion, and latent heat release.

In reality interactions between different processes in the atmosphere may suppress an initially large forcing or amplify an initially small forcing. Without accurately accounting

these interactions, one cannot draw solid conclusions on the coupling strength.

2.5.4 Aerosol Effects on Modeling of Gas-phase Chemistry

Currently aerosols have not been included in most air quality modeling. The aerosol influence on photolysis rates, chemical conversions, and meteorological fields needs to be taken into account to model the temporal and spatial distributions of gas-phase species. This may require a modeling approach to integrate meteorology, gas-phase chemistry, and aerosol dynamics into one consistent framework. Although the effects of air pollution on the dispersion of chemical species have been studied in a preliminary way [12, 155, 141, 156], as we will discuss more detail in Chapter 3, the difficulty of solving size-resolved aerosol dynamics presents a major barrier to addressing comprehensively the aerosol effects on gas-phase chemistry.

2.5.5 Uncertainty Analysis of Radiative Forcing by Anthropogenic Aerosols

As listed in Table 1.1, anthropogenic aerosols consist of water-soluble inorganic species, organics, soot, and mineral dust. Previous estimates of the radiative forcing by anthropogenic sulfate aerosols [23] and by organic biomass-burning aerosols [108] show that this forcing is large enough to possibly offset the radiative forcing by anthropogenic greenhouse gases. However, these estimates are subject to large uncertainty due to our limited knowledge of aerosol physical and chemical processes in the atmosphere. These processes govern the spatial and temporal distributions of aerosol size distribution and chemical composition as well as the interactions of aerosols with water vapor and cloud condensation nuclei. Different models may represent these processes in very different manners.

In addition, these estimates also depend on how model parameters are specified. Since many model parameters can be adjusted in a certain range, model outputs are subject to the tuning of the parameters.

It appears that the radiative forcing by anthropogenic aerosols should be evaluated with different models subject to various model parameters. Therefore not only the uncertainties introduced by model parameters and model structures can be compared but also contributions to the model variance by individual parameters can be ranked.

2.6 Research Strategies

To clarify the causes for the large variation in the estimated radiative forcing by anthropogenic sulfate aerosols, I will develop an explicit radiative transfer model and carry out a series of sensitivity tests of the radiative forcing to different treatments. To calculate the global distribution of direct radiative forcing by total aerosols, I will use a state-of-art climatological aerosol data set and a proper radiative transfer scheme. Results will be given in terms of surface and top-of-the-atmosphere radiative flux changes for both short-wave and long-wave ranges. Sensitivity of these results to ambient relative humidity and boundary layer height will be analyzed.

To understand the mechanism of aerosol effects in the troposphere, I will use two types of one-dimensional models: a radiative-convective equilibrium model and a single-column mesoscale model. The first model is used to understand the mechanism of aerosol influence on the equilibrium climate. Since water vapor plays an important role in the climate system, the model is selected to have an explicit hydrological cycle. The second model is used to

understand the mechanism of aerosol influence on the transient meteorological fields. The choice of a mesoscale model is based on its more accurate treatment of processes in the boundary layer and the surface.

To evaluate the coupling strength between aerosol and meteorological processes, I will apply a mesoscale model to a real urban-rural complex with two different set of aerosol optical properties. These parameters are specified to simulate the possible range of aerosol loadings in the atmosphere. The differences in meteorological fields between aerosol and no-aerosol cases can be used as a first-order measure of the coupling strength. If the difference is significant, the interaction between aerosol and meteorological processes should be accounted in modeling of aerosol dynamics.

To estimate the aerosol radiative effect on the temporal and spatial distribution of gas-phase chemical species, I will use a three-dimensional photochemical air quality model. The model sensitivity to meteorological fields will be evaluated first and then the meteorological fields with or without aerosols will be used to drive the model. The change in the concentration of chemical species due to different meteorological fields will indicate the magnitude of the aerosol effect on gas-phase chemistry.

To address the last issue, I will apply models of different complexity and calculate the probability density functions of both the direct and the indirect radiative forcing by anthropogenic sulfate aerosols with respect to input parameters. These parameters will be kept as constant as possible so that parametric uncertainty in different models can be compared. Two types of uncertainty analysis techniques, the Monte Carlo method and the Deterministic Equivalent Modeling Method, will be used. Results can be used to deduce the relative importance of the structural and parametric uncertainties and to pinpoint the parameters which contribute most to the variance of the results.

Chapter 3

Aerosol Models and Optical Properties

The radiative forcing of aerosols is determined by their optical properties, which depend on their density, size distribution and refractive index. The size distribution and refractive index of aerosols is further controlled by the dynamical processes in the atmosphere. In this chapter, the multi-component aerosol dynamics will be briefly described, followed by a review of aerosol models in the literature. The optical properties of aerosols will be discussed in the end.

3.1 Multi-component Aerosol Dynamics

The governing equation for multi-component aerosol size distribution, $n(\mathbf{m})$, has been given in Equation 2.9. The evolution of size distribution is determined by advection, diffusion, source, removal, coagulation, and growth. Coagulation and growth terms distinguish Equation 2.9 from the dynamic equation of gas-phase chemistry (cf. Equation 2.8). As we will discuss in the following sections, the treatment of these two terms poses both numerical and thermodynamical challenges in size-resolved aerosol models.

3.1.1 Coagulation

Coagulation of aerosol particles results from the differences in the speed and/or direction of their movement in the atmosphere. Since the kinetic energy of aerosol particle collisions is very small, the sticking probability can be assumed to be nearly unity. If the distribution of particles is known, the coagulation rate is a function of the mechanism bringing the particles together. This mechanism can be characterized by the coagulation kernel, $\beta(x, y)$, which is defined as the probability of a collision between two particles of size x and y , respectively, occurring within a given volume. The coagulation kernel is determined by the mechanisms affecting the distributions, such as diffusion, turbulence, etc. The total rate of particle collisions may thus be represented in terms of mass by

$$F = \beta(m, u)n(m, t)n(u, t)dmdu, \quad (3.1)$$

where m and u are the masses of the two colliding particles. For a given size, coagulation acts as both a source and a sink; articles of size m are consumed by collisions with particles of all sizes and in the meantime produced by collisions between particles of mass u and $m - u$.

Therefore the total rate of change in number density due to coagulation can be obtained by integrating the above expression for F over the appropriate mass ranges, resulting in

$$\frac{dn(m, t)}{dt} = \frac{1}{2} \int_0^m \beta(m - u, u)n(m - u, t)n(u, t)du - n(m, t) \int_0^\infty \beta(m, u)n(u, t)du, \quad (3.2)$$

where the first term in the right-hand side Equation 3.2 represents the production and the second term represents the removal. The production term requires a factor of a half since formation is double counted.

Four mechanisms for coagulation are illustrated in Figure 3-1: Brownian diffusion, laminar shear, turbulent inertial, and gravitational settling. In the atmosphere, however, Brownian coagulation tends to dominate – laminar shear coagulation requires large velocity gradients usually found only very near surfaces, and sedimentation and turbulence driven forms are significant only for particles greater than a few microns in radius [112]. It should be pointed out, however, that the coagulation kernels are additive. Inclusion of additional mechanisms therefore requires adding the appropriate kernel to the total coagulation kernel.

3.1.2 Growth

Atmospheric aerosols are strongly linked to gas-phase chemical species since a vapor phase in contact with an aerosol may be absorbed and dissolved into a droplet. As shown in figure 3-2, these dissolved species may then be involved in a variety of aqueous phase processes, such as oxidation and acid-base equilibria. As a result, the net rate of adsorption into a particle may be limited by any of the following steps: diffusion of the vapor to the droplet, interfacial mass transport, diffusion of the dissolved species within the droplet, aqueous phase reaction, or dissolution into solution. Under the assumption of internal mixing, aqueous phase diffusion may be neglected since no gradients exist within the droplet.

Particle growth by adsorption differs from coagulation in that the total number density is conserved, though particle concentration for a given mass or radius may change.

In general diffusion limited growth dominates the effect of coagulation. However, for particles less than about 0.1μ in radius, the net rate of change in particle number due to coagulation may be several times greater than that induced by reaction limited condensation [120].

3.1.3 Sources

Atmospheric aerosols result from both natural processes and human actions. The source strength and composition of the resulting particles are functions of both the physical process generating the particles and the material source of the particles, such as sea water, soil, or volcanos. Particle sources may be further divided into two basic categories, direct and secondary. Direct sources emit already-formed particles into the atmosphere, such as dust, solution droplets, or other condensed forms. Secondary sources contribute vapors that may either condense on pre-existing particles or nucleate and/or react to form new condensed particles. Secondary sources are thus strongly dependent on surrounding gas-phase species.

Examples of secondary particle production include the formation of sulfuric acid droplets through binary homogeneous nucleation, and the reaction of $\text{NH}_3(\text{g})$ and $\text{HCl}(\text{g})$ to form a nonvolatile solid, $\text{NH}_4\text{Cl}(\text{s})$. In either case, estimation of the nucleation rate requires the knowledge of the critical radius, the smallest radius at which a stable droplet or particle may exist.

3.1.4 Sinks

Aerosols may be removed from the atmosphere through both dry deposition and rainout. Dry deposition, a continuous process, may be caused by gravitational settling or inertial impaction of particles onto the surface. Inertial impaction results from turbulent convection, molecular diffusion, and diffusiophoresis produced by evaporation or condensation at the surface. It is typically determined by the particle size and the target surface.

Wet removal processes involve the collision with and subsequent absorption of aerosol particles by a condensed phase, such as a water cloud droplet, rain drop, or ice cloud particle. The removal rate is a function of the fall velocity and size distribution of droplets and the collision efficiency between droplets and aerosol particles. Although the wet removal processes when acting are much more efficient than dry deposition, the long-term average contributions of each mechanism to particle removal are of similar magnitude since wet removal takes the form of transient events [135].

3.2 Dynamical Aerosol Models

Dynamical aerosol models simulate the processes affecting the temporal and spatial evolution of atmospheric aerosols. These processes can be grouped into four categories: sources, sinks, transport (advection, convection, and diffusion), and transformation (coagulation, condensation, chemical conversion, and gas-to-particle conversion).

Since solving the coagulation equation for multi-component systems is very challenging, only the concentration is simulated in most aerosol models. These models include the Washington University CAPITA model for man-made aerosols over North America [69], the Norwegian LRTAP model for long-range transport of sulfur over Europe [44, 105, 43], the French LMD model for dust particles [71], and global three-dimensional models for the tropospheric sulfur cycle [83, 11, 158]. All of these models are driven by either observational or modeled meteorological data. No complete feedback loop connecting aerosols and dynamical meteorology has been included.

Since aerosol physics is highly dependent on size distribution, accurate aerosol models should resolve not only aerosol composition but also aerosol size. Several methods available in the literature include multidimensional distribution splitting [147], the full multidimensional surface approach [78], the split composition distribution method [120], and multicomponent sectionalization [54, 162, 13].

Distribution splitting represents a multicomponent distribution in terms of single components. For example, a two-component aerosol size distribution containing two species, **a** and **b**, would be described by 4 parameters: the number densities for particles of pure **a**, pure **b**, and particles containing both **a** and **b**, and another number indicating the amount of **a** or **b** in the mixed particles. The problem with this method is that the number of one dimensional distributions required increases very rapidly with the number of species. Solving an s -component system would require the solution of $s2^{s-1}$ one-dimensional problems.

The method of multidimensional surfaces retains all composition information, preserving the continuity of the distribution and its derivatives. However, this method is computationally expensive due to numerous multi-dimensional integrations and interpolations. For a four component system, nearly 16 hours on SUN 386i is required for 10 seconds simulation with a median error of 8% [78].

The split composition distribution method separates the number density from the particle compositions with the compositions treated as random variables. This new repre-

sentation simplifies the multicomponent coagulation into several one dimensional integral equations for coagulation. Results from this method have been verified against the analytical solutions and full multidimensional surface solutions for two-component systems. However, more verification and validation of this method are required before it can be applied to a complete aerosol model.

The most successful method reported thus far is multicomponent sectionalization, which discretizes the size range into many sections and conserves the total mass. Despite the computational efficiency of this method, however, it is weak due to the assumptions of treating condensational process: the growth rate of each component in a section is independent of particle composition, and the average product of number density and species uptake rate equals the product of sectional averages. In reality, condensational growth via uptake of species is highly nonlinear and depends strongly on particle composition.

3.3 Static Aerosol Models

Although dynamical aerosol models simulate the temporal and spatial evolution of aerosols within the atmosphere, their success is still very limited. Besides the considerable computer time and memory requirements, all of the physical processes (e.g., sources, transformation, transport, and sinks) have to be understood and all of the modeling results have to be verified against the observations.

Given the present state of knowledge, a compromising approach has been adopted in the aerosol research community [146, 132, 39, 36]. This approach utilizes spatially or temporally averaged aerosol physical properties such as size distribution and refractive index based on current available observations from different locations and at different times.

Measurements show that atmospheric aerosols have a wide size range of $0.001 \mu m$ to $100 \mu m$. For the sake of convenience, suitable analytical functions are sought to accurately fit the observed size distributions. As stated in Whitby [163], a suitable size distribution function should have the following three criteria:

1. It should fit the observation over the entire size range.
2. The form of the function must be independent of the weighting (i.e., number, surface area, volume, and mass).
3. The function should have a physical basis.

Some commonly used functions, such as the power law function [72] and modified Gamma distribution function[40], are at best only empirical fits to the observed distribution and they do not meet the second and third criteria. The log-normal distribution function, first used by Davies [37], is one of the simplest functions satisfying all of the above criteria.

As argued by Whitby[163], if the formation mechanism of a distribution variable is such that the effect is proportional to the already achieved magnitude of the variable, then this distribution will be log-normal. Since in the atmosphere the governing mechanisms for the nuclei and accumulation modes, coagulation and condensation, are functions of attained size, log-normal distribution function gives the best fit. Although the above arguments are strictly valid only for a distribution of particles originating from a single source through a single production mechanism, a combination of several log-normal distributions representing

all individual sources can be used to fit $n(r)$, if one assumes that external mixing is a good approximation [39, 36]

$$n(r) = \sum_i \frac{N_i}{\sqrt{2\pi r \ln \sigma_{g_i}}} \exp - \frac{(\ln(r/r_{g_i}))^2}{2(\ln \sigma_{g_i})^2}, \quad (3.3)$$

where N_i , r_{g_i} and σ_{g_i} are number density, geometric mean radius and geometric standard deviation for the i th component for a given aerosol type.

In order to compute the aerosol optical properties, the shape and the refractive index of the aerosol particles must be specified along with the aerosol size distribution. If the shape of the particles is assumed to be spherical, one can apply Mie theory to make the calculations for aerosol optical properties [97].

The refractive index of aerosol particles can be either obtained from direct measurements or inferred from remote sensing measurements. Unless the chemical composition of aerosol particles is homogeneous, the refractive index is critically dependent on the nature of the mixing of the particles [4]. Following WCP-55 [39] and d'Almeida et al. [36], the aerosol particles are assumed to be externally mixed unless otherwise stated.

Because of the temporal and spatial averaging, this method suffers both geographical limitation and statistical representativeness. It is at best a diagnostic method with no variability in space and time once a specific aerosol type is chosen.

3.4 Aerosol Optical Properties

In the radiative transfer calculations, such quantities as attenuation coefficients, single-scattering albedos, phase functions, asymmetry factors, and backscattered fraction are required.

For a multi-component aerosol system, the attenuation coefficients $\sigma_{e,s,a}^i$ (including extinction(e), scattering(s), and absorption(a)), single scattering albedo $\tilde{\omega}$, phase function P^i , asymmetry factor g^i , and backscattered fraction for any aerosol component i can be calculated using Mie theory¹[97]:

$$\sigma_{e,s,a}^i(\lambda, z) = \int_{r_1}^{r_2} \pi r^2 Q_{e,s,a}^i(m_i(\lambda, z), r, \lambda) n_i(r, z) dr, \quad (3.4)$$

$$\tilde{\omega}^i(\lambda, z) = \frac{\sigma_s^i(\lambda, z)}{\sigma_e^i(\lambda, z)}, \quad (3.5)$$

$$P^i(\theta, \lambda, z) = \frac{\lambda^2}{\pi \sigma_s^i} \int_{r_1}^{r_2} I^i(\theta, m_i(\lambda, z), r, \lambda) n_i(r, z) dr, \quad (3.6)$$

$$g^i(\lambda, z) = \frac{1}{2} \int_0^\pi P^i(\theta, \lambda, z) \cos \theta \sin \theta d\theta, \quad (3.7)$$

$$\bar{\beta}^i(\lambda, z) = \frac{1}{2\pi} \int_0^\pi P^i(\theta, \lambda, z) \theta \sin \theta d\theta, \quad (3.8)$$

where λ is the wavelength, r is the particle radius, θ is the scattering angle, z is the vertical height, m is the refractive index, Q is the efficiency factors, I is the Mie intensity parameter

¹Since most atmospheric particulates (except unaged dust and soot) consist in part of hygroscopic material, the shape of particles may be assumed to be spherical so that Mie theory applies. For non-spherical particles, other methods [109, 111] have to be applied to determine their optical properties.

in the Stokes matrix, r_1 and r_2 are the low and upper limits of particle radius, and n is the particle size distribution. A computer code in Fortran 77 for computing these optical properties is provided in Appendix A.

The extinction coefficient σ_e is defined as the fraction of energy removed, per unit path length, from an incident wave with a unit of energy flux density by a collection of aerosol particles characterized by their size distribution. The scattering coefficient σ_s and absorption coefficient σ_a measure the fraction of energy due to scattering and absorption respectively. The single-scattering albedo $\tilde{\omega}$ is the ratio of scattered energy and total energy removed. A zero single-scattering albedo implies a perfect absorber and a unit single-scattering albedo implies a pure scatter. The phase function describes the angular distribution of the scattered energy. The asymmetry factor g measures the difference between forward and backward scattering along the direction of incident beam. The asymmetry factor varies between -1 and 1. The asymmetry factor equals zero for isotropic scattering. For scattering with a positive asymmetry factor, the corresponding backscattered fraction satisfies [166],

$$\frac{1}{2}(1 - g) \leq \bar{\beta} \leq \frac{1}{2}\left(1 - \frac{3}{4}g\right). \quad (3.9)$$

Under the assumption of external mixing the total attenuation coefficients, single scattering albedo, asymmetry factor, and backscattered fraction are defined as

$$\sigma_{e,s,a}(\lambda, z) = \sum_i \sigma_{e,s,a}^i(\lambda, z), \quad (3.10)$$

$$\tilde{\omega}(\lambda, z) = \frac{\sum_i \sigma_e^i(\lambda, z) \tilde{\omega}^i(\lambda, z)}{\sigma_e(\lambda, z)}, \quad (3.11)$$

$$g(\lambda, z) = \frac{\sum_i g^i(\lambda, z) \sigma_s^i(\lambda, z)}{\sigma_s(\lambda, z)}, \quad (3.12)$$

$$\bar{\beta}(\lambda, z) = \frac{\sum_i \bar{\beta}^i(\lambda, z) \sigma_s^i(\lambda, z)}{\sigma_s(\lambda, z)}. \quad (3.13)$$

The aerosol optical depth at any height can be computed as

$$\tau(\lambda, z) = \int_z^\infty \sigma_e(\lambda, z) dz. \quad (3.14)$$

Since the vertical distribution of aerosol optical properties is very difficult to obtain, it is often assumed to be uniform within certain layers (boundary layer, free troposphere, stratosphere, etc.). It is sometimes convenient to relate the total optical depth $\tau(\lambda, 0)$ for a given layer with its column burden B and specific extinction coefficient $\Psi_e(\lambda)$:

$$\tau(\lambda, 0) = B\Psi_e(\lambda), \quad (3.15)$$

$$B = \int_0^\infty dz \int_0^\infty \frac{4}{3} \pi r^3 \rho n(r) dr, \quad (3.16)$$

$$\Psi_e(\lambda) = \frac{\sigma_e(\lambda)}{\int_0^\infty \frac{4}{3} \pi r^3 \rho n(r) dr}. \quad (3.17)$$

The column burden measures the species mass per unit area (i.e., g/m^2) and can be obtained by integrating vertically the species volume concentration (i.e., g/m^3), which is the normal variable simulated in chemical models or measured *in situ*. It can be estimated

using the aerosol source strength Q and lifetime L over a specific area A . For example, in Charlson et al. [24], the column burden for sulfate aerosols is estimated as

$$B = \frac{3YLQ}{A}, \quad (3.18)$$

where Y is the fraction of sulfur dioxide converted to sulfate aerosols.

The specific extinction coefficient, which has a unit of m^2/g , measures the extinction per unit mass. Together with the column burden, the specific extinction coefficient will be used in Chapter 4 for computing aerosol optical properties for sulfate aerosols.

Previous observations [17, 47, 49, 113] have shown that the aerosol optical properties are strongly dependent on ambient relative humidity. One common approach is to parameterize this dependence based on the method of Hänel [62] and Shettle and Fenn [132]. This method assumes that (1) the mean values obtained from aerosol samples represent the behavior of all these particles together; (2) during changes of relative humidity the particles do not experience coagulation, addition or removal processes; (3) thermodynamic equilibrium exists between the particles and the ambient moist air. Under these assumptions, the change of particulate size and complex refractive index due to a relative humidity variation is given by

$$r(RH) = r_0 \left[1 + \frac{\rho_0 m_w (a_w)}{\rho_w m_0} \right]^{1/3}, \quad (3.19)$$

$$a_w = RH \times \exp\left(\frac{2\sigma V_w}{R_w T r}\right), \quad (3.20)$$

$$n(RH) = n_w + (n_0 - n_w) \times \left[\frac{r_0}{r(RH)} \right]^3, \quad (3.21)$$

where r is the particle radius, RH is the relative humidity, r_0 is the dry particle radius, ρ_0 and ρ_w are the density of water and particle respectively, m_0 and m_w are the mass of dry particle and condensed water respectively, a_w is the water activity, σ is the surface tension on the wet particle surface, V_w is the specific volume of water, R_w is specific gas constant for water, T is the absolute temperature, and n , n_0 , and n_w are the complex refractive indices for wet particles, dry particles and water respectively.

Following Hänel [63] Equation 3.20 is approximated by

$$a_w = RH \times \exp\left(\frac{-0.001056}{r(a_w)}\right), \quad (3.22)$$

which leads to errors of less than 2% for particle radii $r > 0.01\mu m$.

In the following chapters where Equations 3.19, 3.21 and 3.22 are applied, the particle density relative to that of water $\frac{\rho_0}{\rho_w}$ and the water uptake per unit mass of dry material $\frac{m_w}{m_0}$ are taken from Table 4 of Hänel [63]. As in Shettle and Fenn [132], the complex refractive index of water is following that of Hale and Query [61].

The difficulty with this approach lies in the measurement of $\frac{m_w}{m_0}$ vs. a_w for a specific aerosol type. An alternative to accounting for the condensation effect is to use empirical measurements of aerosol optical properties at different relative humidities. At a specific relative humidity RH the aerosol optical properties can be related to those at a reference relative humidity RH_r as follows:

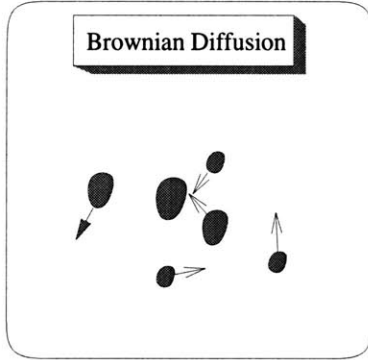
$$\Psi_e(\lambda, RH) = f_{\Psi_e}(\lambda, RH) \Psi_e(\lambda, RH_r), \quad (3.23)$$

$$\omega(\lambda, RH) = f_\omega(\lambda, RH)\omega(\lambda, RH_r), \quad (3.24)$$

$$g(\lambda, RH) = f_g(\lambda, RH)g(\lambda, RH_r), \quad (3.25)$$

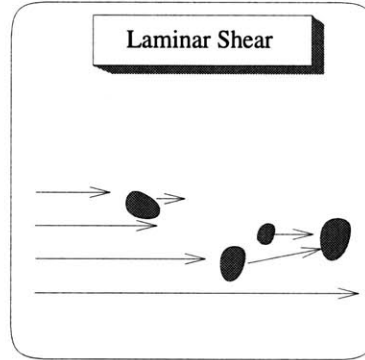
$$\bar{\beta}(\lambda, RH) = f_{\bar{\beta}}(\lambda, RH)\bar{\beta}(\lambda, RH_r), \quad (3.26)$$

where empirical functions, f_{ψ_e} , f_ω , f_g , and $f_{\bar{\beta}}$ can be inferred from observation.



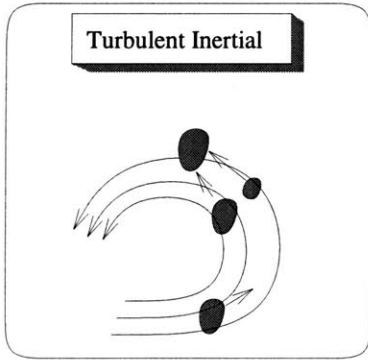
Brownian Diffusion

$$\beta(r, s) = \frac{2kT}{3\eta_a}(r + s) \left[\frac{1}{r} + \frac{1}{s} + \lambda_a \left(\frac{\alpha(r)}{r^2} + \frac{\alpha(s)}{s^2} \right) \right]$$



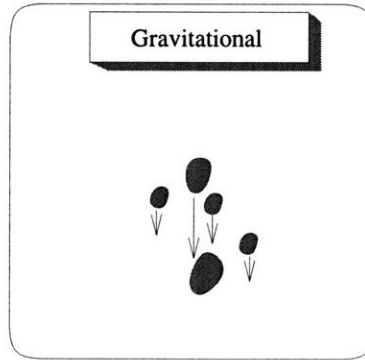
Laminar Shear

$$\beta(r, s) = \frac{4\Gamma}{3}(r + s)^3$$



Turbulent Inertial

$$\beta(r, s) = A(r + s)^3(\varepsilon/\nu_a)^{\frac{1}{2}}$$



Gravitational

$$\beta(r, s) = \frac{\pi}{2}s^2(V_{S,r} - V_{S,s})$$

Figure 3-1: Four mechanisms for coagulation [112]. Nomenclature: r, s = particle radii, k = Boltzmann's constant, T = temperature, η_a = dynamic viscosity of air, $\alpha = 1.257 + 0.4 \exp(-1.10r/\lambda_a)$ (from Cunningham slip-flow correction), λ_a = mean free path of air, Γ = shear rate, $\varepsilon = O(10) \text{ cm}^2/\text{s}^3$ rate of energy dissipation per unit mass for turbulent eddies, ν_a = kinematic viscosity of air, and $V_{S,r}$ = Stokes terminal velocity for particle of radius r .

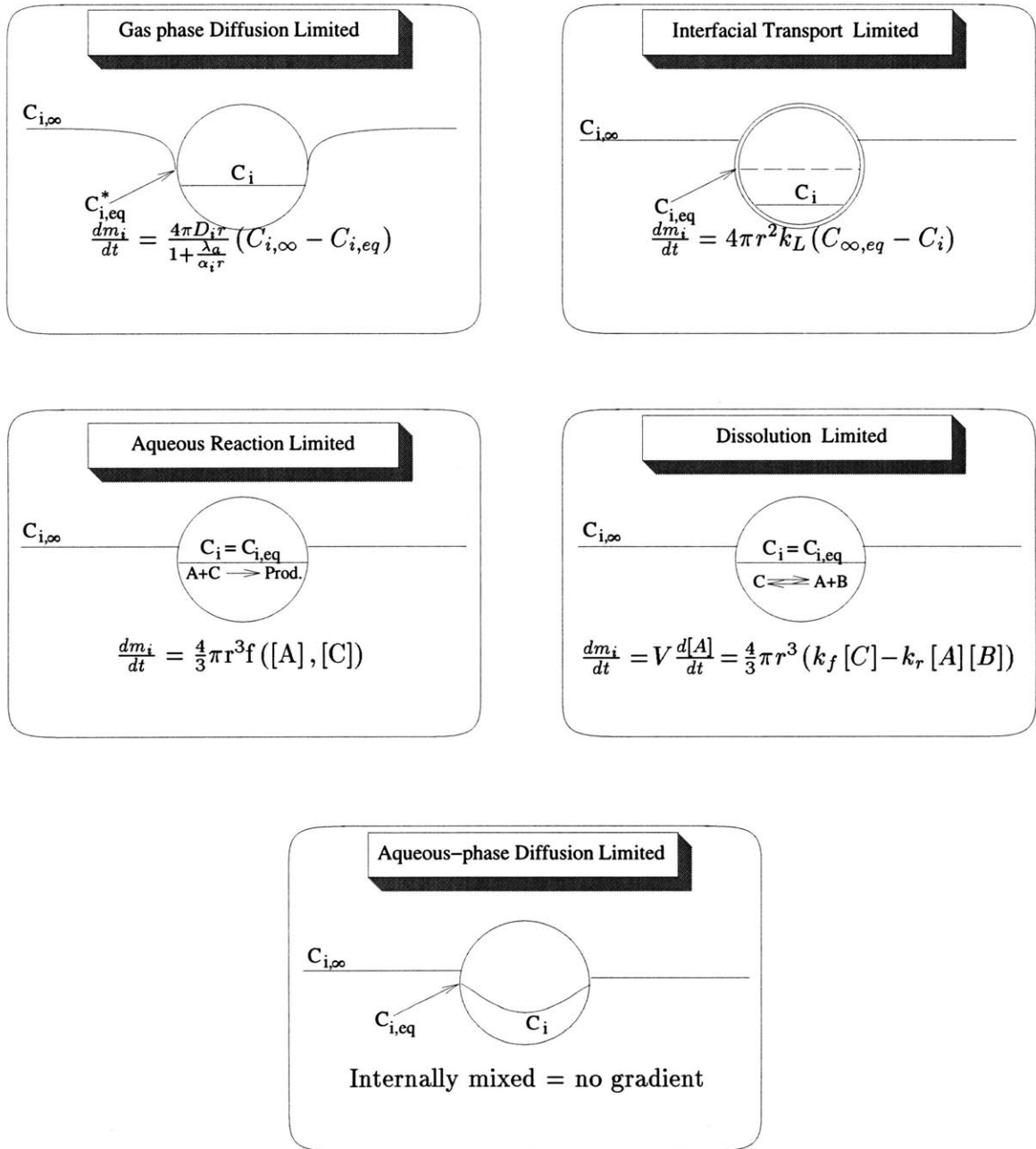


Figure 3-2: Different mechanisms that may act as the rate limiting step for droplet growth and the corresponding expressions for the mass growth rate [120]. Symbols are defined in Nomenclature.

Chapter 4

Radiative Forcing by Aerosols

The role of aerosols is mainly achieved through their participation in the radiative transfer in the atmosphere. The radiative forcing by aerosols is governed by the spatial and temporal distributions of their optical properties. Given the current knowledge of aerosol processes in the atmosphere, only limited knowledge regarding these distributions is available. In this chapter, I will first review some background information on the radiative transfer in the presence of aerosols and then present the calculations of radiative forcings by both anthropogenic sulfate aerosols and climatological aerosols.

4.1 Radiative Transfer in the Presence of Aerosols

The general radiative transfer equation for calculating the radiance I along direction μ (cosine of solar zenith angle) and ϕ (azimuthal angle) at optical depth $\tau(\lambda)$ (measured perpendicular to the surface of the medium) is

$$\mu \frac{dI(\tau(\lambda), \mu, \phi)}{d\tau(\lambda)} = I(\tau(\lambda), \mu, \phi) - J(\tau(\lambda), \mu, \phi). \quad (4.1)$$

The source function $J(\tau(\lambda), \mu, \phi)$ is given by

$$\begin{aligned} J(\tau(\lambda), \mu, \phi) &= (1 - \tilde{\omega}(\lambda))B(\lambda) + \\ &\quad \frac{\tilde{\omega}(\lambda)}{4\pi} \int_{\mu} \int_{\phi} P(\mu, \phi; \mu', \phi') I(\tau(\lambda), \mu', \phi') d\mu' d\phi' + \\ &\quad \frac{\tilde{\omega}(\lambda)}{4\pi} (\pi I_0(\lambda)) P(\mu, \phi; -\mu_0, \phi_0) e^{-\tau(\lambda)/\mu_0}. \end{aligned} \quad (4.2)$$

where λ is the wavelength, $\tau(\lambda)$ is related to the extinction coefficient $\sigma_e(\lambda)$ and height z by $d\tau(\lambda) = -\sigma_e(\lambda)dz$, $\tilde{\omega}(\lambda)$ is the single-scattering albedo, $B(\lambda)$ is the Planck function, $P(\mu, \phi; \mu', \phi')$ is the phase function, and $I_0(\lambda)$ is the direct monochromatic radiance incident at direction (μ_0, ϕ_0) . The three terms on the right hand side of Equation 4.2 represent respectively the thermal emission in local thermodynamic equilibrium, the diffusion of light by multiple scattering, and the scattering of the direct radiation.

The net downward monochromatic irradiance $F(\tau(\lambda))$ is related to the monochromatic

radiance $I(\tau(\lambda))$ by

$$F(\tau(\lambda)) = \mu_0 \pi I_0(\lambda) e^{-\tau(\lambda)/\mu_0} + 2\pi \int_{\mu} \int_{\phi} I(\tau(\lambda), \mu' \phi') \mu' d\mu' d\phi'. \quad (4.3)$$

The radiative heating and cooling rates are proportional to the vertical divergence of irradiance:

$$\frac{\partial T(z)}{\partial t} = -\frac{1}{\rho c_p} \int_{\lambda} \frac{\partial F(\tau(\lambda))}{\partial z} d\lambda, \quad (4.4)$$

where ρ and c_p are density and specific capacity at constant pressure of air.

To calculate the irradiance accurately, one has to take into account molecular scattering, gaseous absorption, and the scattering and absorption due to aerosols and clouds. This may require quite sophisticated radiation schemes.

Figure 4-1 shows the clear sky radiative flux and heating rate for five standard atmospheric profiles defined in McClatchey et al. [91] using the radiation scheme developed by Fu and Liou [51]. Although the radiative flux and heating rate are sensitive to surface albedo and solar zenith angle, surface albedo and cosine of solar zenith angle are set to 0.15 and 0.5, respectively, with no spatial and temporal variation for the purpose of illustration. In the lower troposphere, the magnitude of the radiative cooling rate is a factor of 2 to 3 times larger than that of the radiative heating rate; whereas the stratosphere appears to be in radiative equilibrium. At the surface, the incoming short wave flux dominates the net outgoing long wave flux, indicating the importance of surface sensible and latent heat flux in reaching surface energy balance.

Under some circumstances, the radiative forcing by aerosols can be obtained approximately in explicit forms, which may help us understand the nature of the problem.

Based on the adding method for radiative transfer in a scattering atmosphere [153], the monochromatic reflectance of a system consisting of a homogeneous *thin* aerosol layer overlying a surface, R_{as} , for radiation incident at solar zenith angle of $\arccos \mu_0$, is given by

$$R_{as}(\lambda, \mu_0) = R_a(\lambda, \mu_0) + \frac{T_a^2(\lambda, \mu_0) R_s(\lambda)}{1 - R_a(\lambda) R_s(\lambda)}, \quad (4.5)$$

where $R_s(\lambda)$ is the surface albedo, and $R_a(\lambda, \mu_0)$ and $T_a(\lambda, \mu_0)$ are the aerosol monochromatic reflectance and transmittance of the aerosol layer.

The change in the reflectance of the system due to the aerosol layer is

$$\Delta R_{as}(\lambda, \mu_0) = R_a(\lambda, \mu_0)(1 - R_s^2) - 2R_s A_a(\lambda, \mu_0), \quad (4.6)$$

with $A(\lambda, \mu_0)$ is the monochromatic absorptance of the aerosol layer.

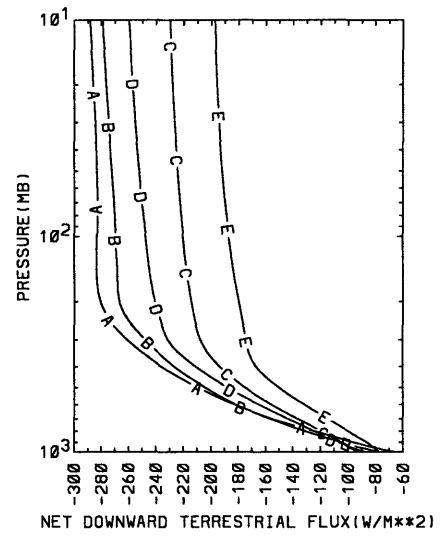
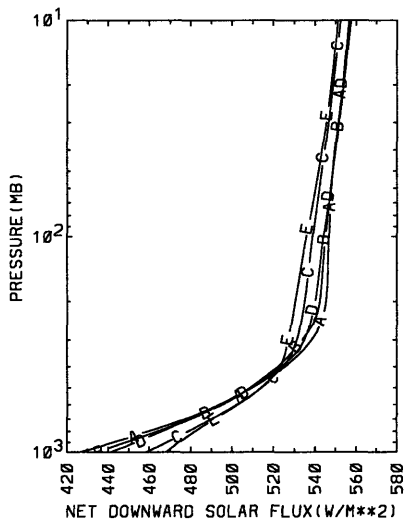
If the optical depth of the aerosol layer is small, the reflectance, transmittance, and absorptance of the aerosol layer can be related to the AOPs and solar zenith angle in the following simple forms,

$$R_a(\lambda, \mu_0) = \beta(\lambda, \mu_0) \tilde{\omega}(\lambda) \tau(\lambda) / \mu_0, \quad (4.7)$$

$$T_a(\lambda, \mu_0) = 1 - (\beta(\lambda, \mu_0) \tilde{\omega}(\lambda) - \tilde{\omega} \lambda + 1) \tau(\lambda) / \mu_0, \quad (4.8)$$

$$A_a(\lambda, \mu_0) = (1 - \tilde{\omega}(\lambda)) \tau(\lambda) / \mu_0, \quad (4.9)$$

where β is the backscattered fraction for monodirectional radiation and relates to $\bar{\beta}$ [166]



- A- TROPICAL ATMOSPHERE
- B- MID-LATITUDE SUMMER
- C- MID-LATITUDE WINTER
- D- SUBARCTIC SUMMER
- E- SUBARCTIC WINTER

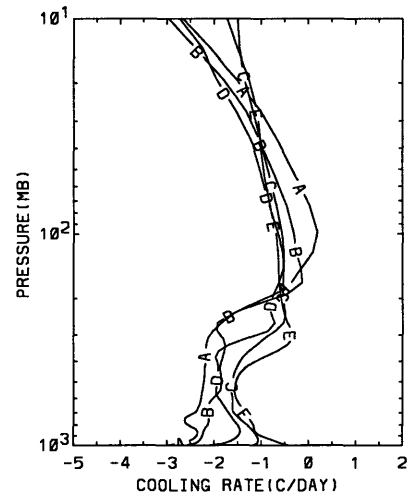
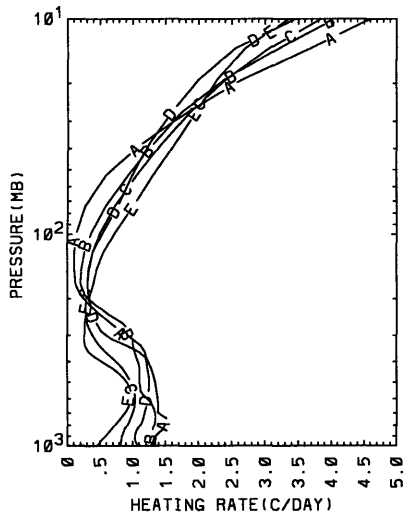


Figure 4-1: Clear sky radiative flux and heating rates for 5 atmospheric types.

as

$$\bar{\beta}(\lambda) = \int_0^1 \beta(\lambda, \mu_0) d\mu_0. \quad (4.10)$$

The corresponding aerosol induced radiative forcing is

$$\Delta F = \frac{1}{2}(1 - Ac)T^2 \int S(\lambda) d\lambda \int_0^1 \mu_0 \Delta R_{as}(\lambda, \mu_0) d\mu_0, \quad (4.11)$$

where $S(\lambda)$ is solar irradiance at wavelength λ , A_c is the fraction of cloud cover, and T is the atmospheric transmittance above the aerosol layer.

In terms of AOPs, Equation 4.11 can be written as

$$\Delta F = \frac{1}{2}(1 - Ac)T^2 [(1 - R_s)^2 \int S(\lambda) \bar{\beta}(\lambda) \bar{\omega}(\lambda) \tau(\lambda) d\lambda - 2R_s \int S(\lambda) (1 - \bar{\omega}(\lambda)) \tau(\lambda) d\lambda]. \quad (4.12)$$

The assumptions in the use of Equation 4.12 are:

1. Aerosols are well-mixed in the boundary layer, which means that AOPs are height independent;
2. T and R_s are assumed wavelength independent;
3. τ is very small ($\ll 1$).

If all the spectral dependent variables can be approximated by those at a wavelength of $0.55 \mu m$, Equation (4.12) is reduced to Equation (3) in Charlson et al. [24],

$$\Delta F = \frac{1}{2} S_0 (1 - Ac) T^2 (1 - R_s)^2 \bar{\beta} \tau, \quad (4.13)$$

where S_0 is the solar constant.

Equation 4.6 relates the aerosol radiative forcing to surface albedo, solar zenith angle, and AOPs. The relationship between A_a/R_a and R_s for zero forcing is shown in Figure 4-2. It illustrates that aerosols can either heat or cool the climate system, depending on AOPs and surface albedo. For example, weak absorptive aerosols such as sulfate aerosols with very small A_a/R_a tend to cool the system globally; whereas strong absorptive aerosols such as soot with large A_a/R_a cause cooling in the lower latitude and heating in the higher latitude. At a specific location, heating or cooling depends on AOPs.

4.2 Radiative Forcing by Anthropogenic Aerosols

The direct radiative forcing (DRF) by anthropogenic sulfate aerosols has been addressed in several studies by Charlson et al. (1991) [23], Charlson et al. (1992) [24], Kiehl and Briegleb (1993) [77], Box and Trautmann (1994) [16], Penner et al. (1994) [107], and Taylor and Penner (1994) [145]. These studies will be identified hereafter by C91, C92, KB, BT, P, and TP, respectively. A summary of these results is shown in Figure 4-3, along with the radiative forcing by carbon dioxide and total greenhouse gases from preindustrial time to 1990 [133]. To facilitate the comparison, only the magnitude of the radiative forcing is shown. It is seen from Figure 4-3 that the estimated forcing by anthropogenic sulfate aerosols has a large variation.

As stated in KB, the radiative forcing in C91 is overestimated by a factor of 2 because the spectral dependence of AOPs is not taken into account. However, after the spectral

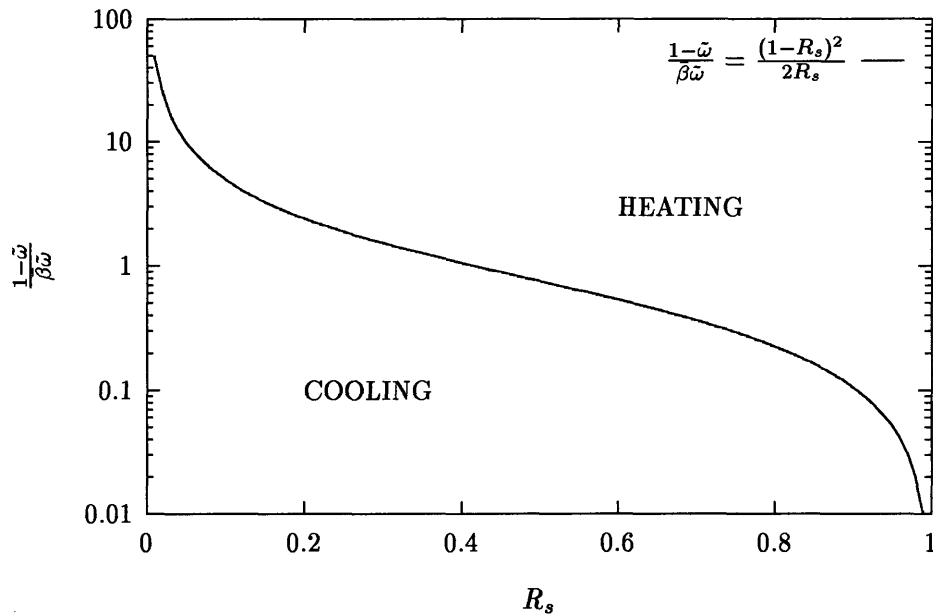


Figure 4-2: The relationship between the A_a/R_a and surface albedo for zero forcing of the atmosphere-surface system.

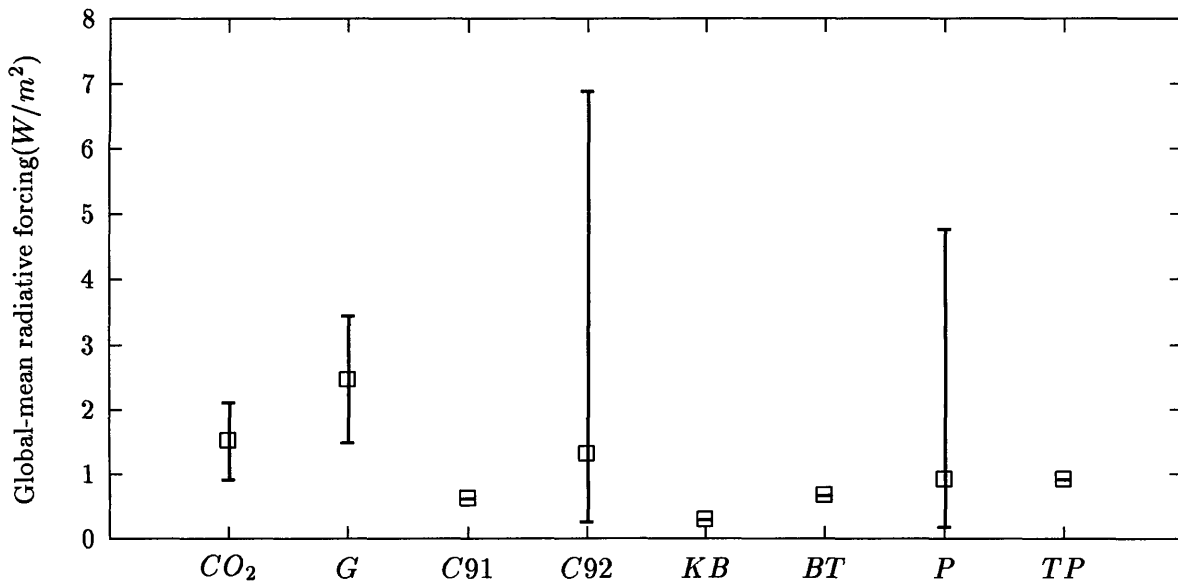


Figure 4-3: Comparison of global-mean DRF by anthropogenic sulfate aerosols estimated by various studies, along with the increased radiative forcing caused by the increases in carbon dioxide (CO_2) and total greenhouse gases (G) from preindustrial time to 1990. C91, C92, KB, BT, and P are defined in the text, and error bars indicate the ranges of the forcing for 95% confidence where they apply. Only the magnitudes of the forcings are shown here.

dependence of AOPs and $f_{\Psi_e}(\lambda, RH)$ are both included in the calculation, BT found that their estimate is close to that in C91. Therefore they suggest that since the specific extinction is scaled using $f_{\Psi_e}(0.55\mu m, RH)$ in KB, a wavelength-dependent $f_{\Psi_e}(\lambda, RH)$ may bring KB's result back to that of C91.

One problem arising from these arguments is that different results come from quite different models, where both the model structures and model parameters are not the same. Therefore, the real causes are sometimes hard to sort out. In the following, I will reexamine these two issues using Equation 4.12.

In my calculations, the surface albedo, cloud fraction, and relative humidity are from a 5-year (March 1985 through February 1990) global, gridded 4-D assimilated atmospheric data set produced by the Laboratory for Atmospheric Data Assimilation Office (DAO) at NASA/GSFC. This data set assimilated rawinsonde reports, satellite retrievals of geopotential thickness, cloud-motion winds, aircraft, ship and rocketsonde reports with model forecasts employing version 1 of the Goddard Earth Observing System (GEOS-1) GCM. The data are archived at the GSFC Distributed Active Archive Center (DAAC), accessible through anonymous ftp. The column burden of anthropogenic sulfate aerosols, obtained from Langner and Rohde [83], is simulated in a global three-dimensional chemical model of the tropospheric sulfur cycle. The model treats three sulfur species as prognostic variables: dimethyl sulfide (CH_3SCH_3), sulfur dioxide as gases (SO_2), and sulfate as aerosols (SO_4^{2-}). These species are transported by climatological monthly mean windfields with emission, chemistry, and removal processes represented properly.

Figures 4-4 to 4-6 show the monthly averaged surface albedo, cloud fraction, and boundary layer relative humidity for January and July of 1989. Low relative humidity occurs in the desert areas of Sahara, Namib, and Australia due to the limited water vapor content. High relative humidity occurs in the summer of north Antarctica and winter-time Siberia region due to the extreme cold temperature. In the vast area of oceans the relative humidity is about 80%. Figure 4-7 shows the column burden of anthropogenic sulfate aerosols for January and July. Higher values of contours are seen mainly in several regions of the northern hemisphere. The seasonal variation is small.

Figure 4-8 shows the resulting DRF at the top of the atmosphere for January and July. In my calculations the monthly averaged surface albedo, cloud fraction, and boundary layer relative humidity are scaled such that their annual global means are 0.15, 0.61, and 0.75, respectively, identical to those in C91. The annual global mean is -0.24 W/m^2 , compared with -0.28 W/m^2 in KB and -0.60 W/m^2 in C91. Our result is 15% smaller than that in KB, due to the humidity effect on backscattered fraction and single-scattering albedo in our calculation, as will be shown in the sensitivity studies of Table 4.1.

Cases 1 to 3 in Table 4.1 shows the annual global mean DRF by anthropogenic sulfate aerosols (ΔF) using different AOPs with constant humidity scaling functions. All the other parameters are the same as in Table 9.2. In Case 1 ΔF is computed using the same parameters as in P (cf. Table 9.2). In Case 3, AOPs are computed from the same size distribution and refractive index as in KB. In Case 2, a similar calculation as in Case 1 is made except that the backscattered fraction is replaced by a value at $0.55 \mu m$ from Case 2. Results show that taking into account of the spectral dependence of AOPs leads to about a 50% decrease in the magnitude of ΔF and that a backscattered fraction computed from the size distribution contributes about half of the decrease.

To examine the second issue, one has to compute the AOPs at an ambient relative humidity of 75% from the size distribution and refractive index. Since the humidity effect

on AOPs depends on aerosol composition, the size growth factor,

$$G = r_g(RH)/r_g(RH_r),$$

for H_2SO_4 and $(NH_4)_2SO_4$ in d'Almeida et al. [36] is adopted. A combined growth factor, which takes the form of

$$G = 0.57G_{(NH_4)SO_4} + 0.43G_{H_2SO_4},$$

is found to give a $f_{\Psi_e}(0.55\mu m) = 1.7$. Comparing the result in Case 4 with that in Case 3, we see that the spectral dependence of $f_{\Psi_e}(\lambda, RH)$ barely change the result, provided that $f_{\Psi_e}(0.55\mu m)$ is kept as the observed one. This is in contrast to the conclusion in BT. In Case 5, all the AOPs (i.e., $\Psi_e(\lambda)$, $\tilde{\omega}(\lambda)$, and $\tilde{\beta}(\lambda)$) are corrected based on humidity effect according to the size growth factor. The forcing decreases by 15% because of the change of backscattered fraction and single scattering albedo.

If the monthly averaged sulfate burden is the same as in Langner and Rohde [83] instead of being scaled such that its annual global mean is $3.2 \times 10^{-3} g/m^2$ as in C92 and P, ΔF will further decrease by 25%. On the other hand, if the column burden is the same as in C92, which uses a larger value of lifetime, the result will be close to that in C92 (cf. Case 7).

Therefore it is concluded that the DRF by anthropogenic sulfate aerosols is very sensitive to their optical properties and column burden. Aerosol column burden and optical properties contribute about equally to the discrepancy in the literature. The use of constant scaling functions for humidity effects on aerosol optical properties is a good approximation, provided that their values are kept the same as the observed ones in the visible range. Neglecting the humidity effect on the backscattered fraction and single-scattering albedo will only overestimate the result by 10%.

Finally it should be noted that the above conclusions are subject to the accuracy of the column burden data and the single mode assumption of aerosol size distribution.

4.3 Radiative Forcing by Climatological Aerosols

In this section a climatological aerosol data set [36] will be used to calculate the radiative forcing by total aerosols, including both anthropogenic and natural aerosols. A detailed description of this data set can be found in Appendix B.

The global distributions of monthly averaged aerosol number density in January and July are given in Figure 4-9. Large number concentration is found over land areas. Although large optical depth is observed in the Saharian area as shown in Figure 4-14, the number concentration is small due to the large size of mineral dust. The seasonal variation is not significant.

Figures 4-10 to 4-14 show the global distributions of monthly averaged optical properties at $0.5 \mu m$ and a hypothetical relative humidity of 0% in January and July. The distributions of attenuation coefficients follow the patterns of number density with lower values in the polar region and clean-maritime environments and higher values in continental areas. The high attenuation coefficient contour lines correspond to several urban areas. The values of single scattering albedo are generally higher than 0.9 except in the arid and semi-arid regions. The asymmetry factors are between 0.6 and 0.85 with the lower values occurring in the continental environment and the higher values in the polar and maritime regions. The optical depth at the surface lies between 0.01 and 1.5 and its seasonal variation is small.

Table 4.1: Sensitivity of the annual global mean DRF by anthropogenic sulfate aerosols to AOPs, humidity scaling functions, and column burden.

Case #	$\Psi_e(\lambda)$ (m ² /g)	$\bar{\beta}(\lambda)$	$\tilde{\omega}(\lambda)$	$f_{\Psi_e(\lambda)}$ (RH=75%)	$f_{\bar{\beta},\tilde{\omega}}(\lambda)$ (RH=75%)	\bar{B} (mg/m ²)	$\overline{\Delta F}$ (W/m ²)
1	5.0	0.3	1.0	1.7	1.0/1.0	3.2	-0.90
2	„	0.223	„	„	„	„	-0.67
3	$\Psi_e(\lambda)$ 5(.55)	$\bar{\beta}(\lambda)$.223(.55)	$\tilde{\omega}(\lambda)$ 1(.55)	„	„	„	-0.47
4	„	„	„	$f_{\Psi_e(\lambda)}$ 1.7(0.55)	„	„	-0.48
5	„	„	„	„	$f_{\bar{\beta},\tilde{\omega}}(\lambda)$ 0.85/1.0(0.55)	„	-0.41
6	„	„	„	„	„	1.8	-0.24
7	5.0	0.3	1.0	1.7	1.0/1.0	4.6	-1.29

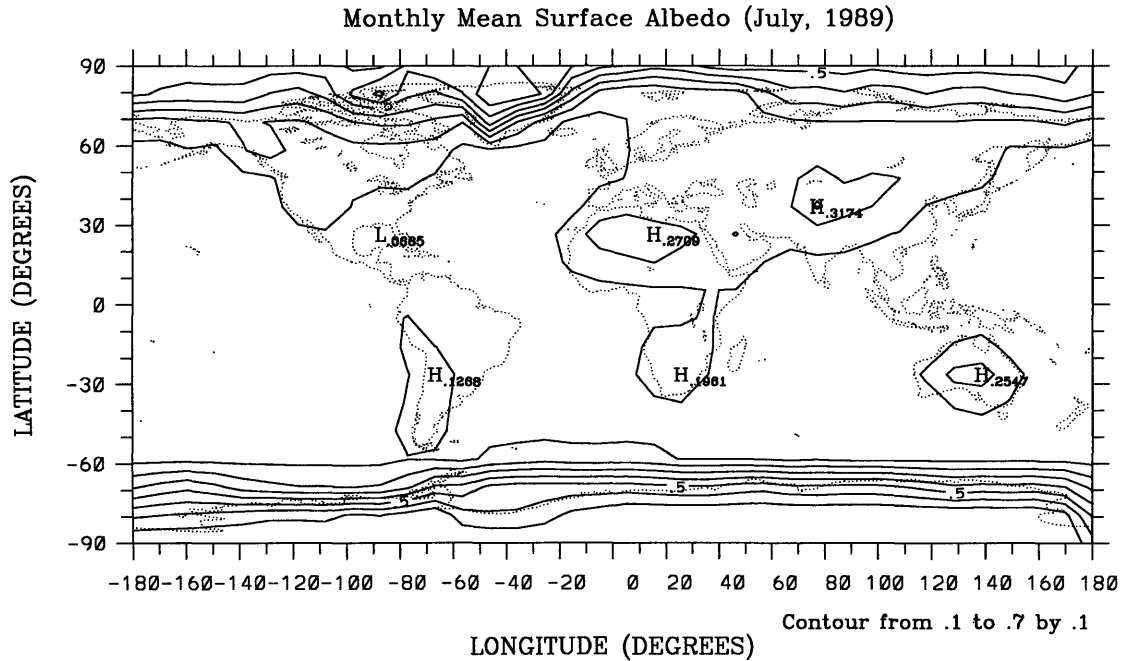
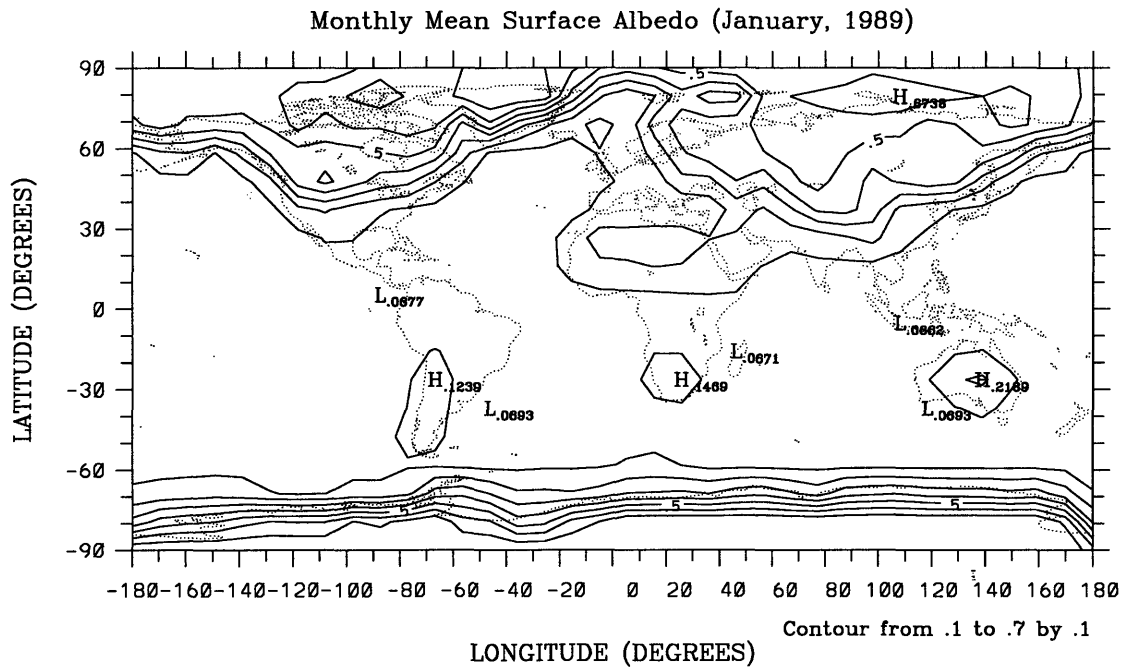


Figure 4-4: Monthly averaged surface albedo.

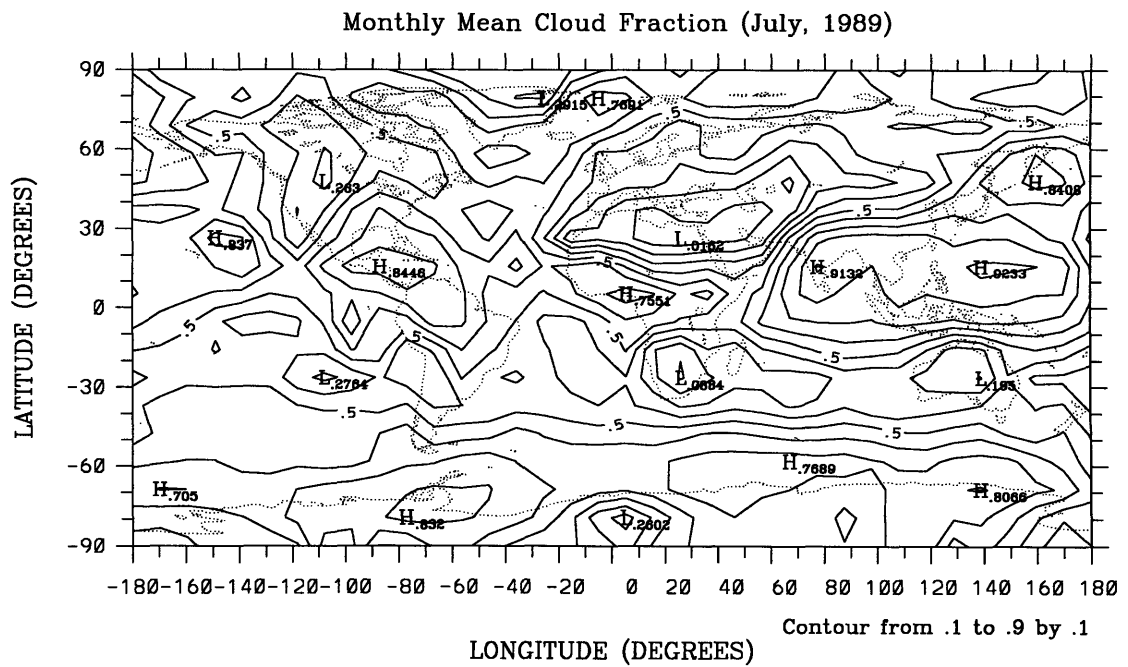
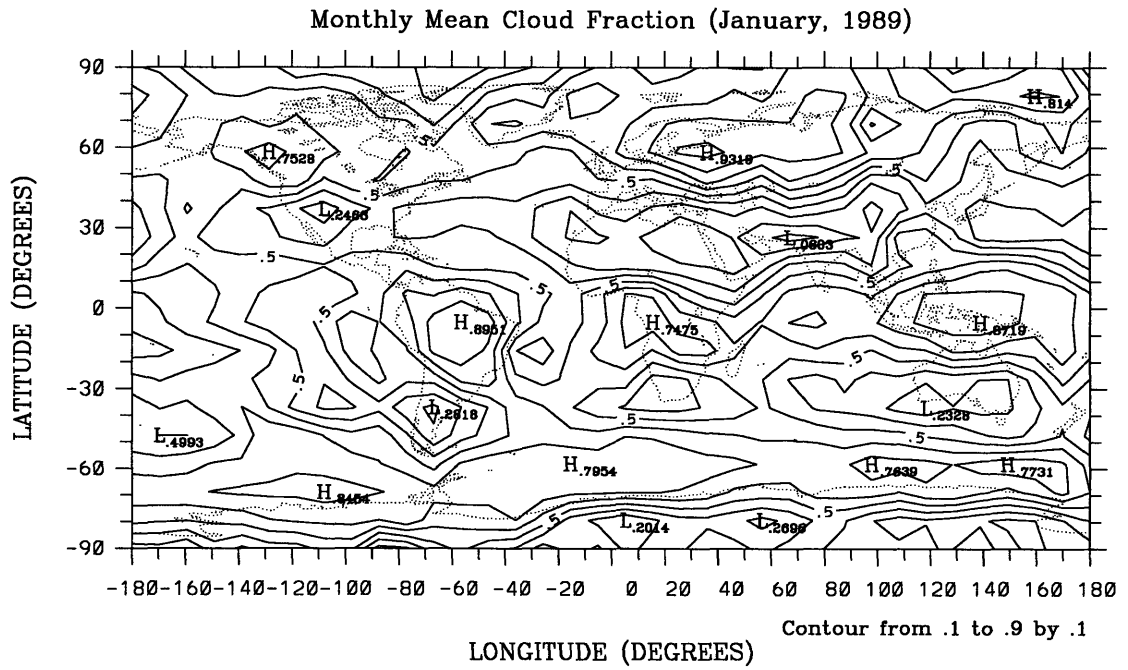


Figure 4-5: Monthly averaged cloud fraction..

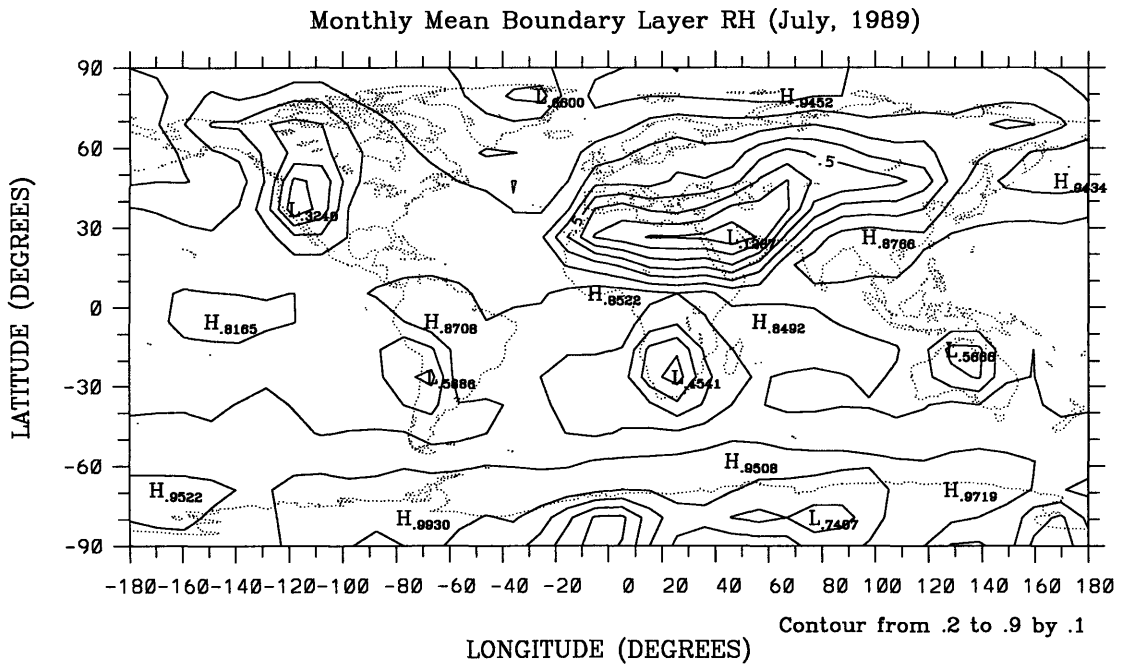
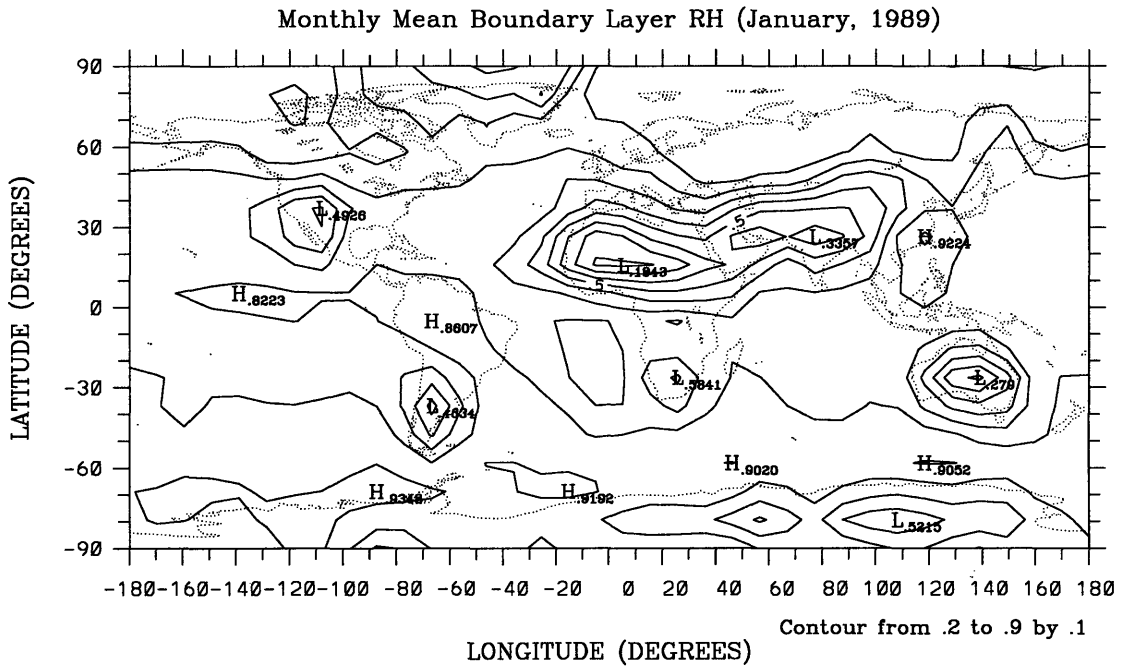


Figure 4-6: Monthly averaged boundary layer relative humidity.

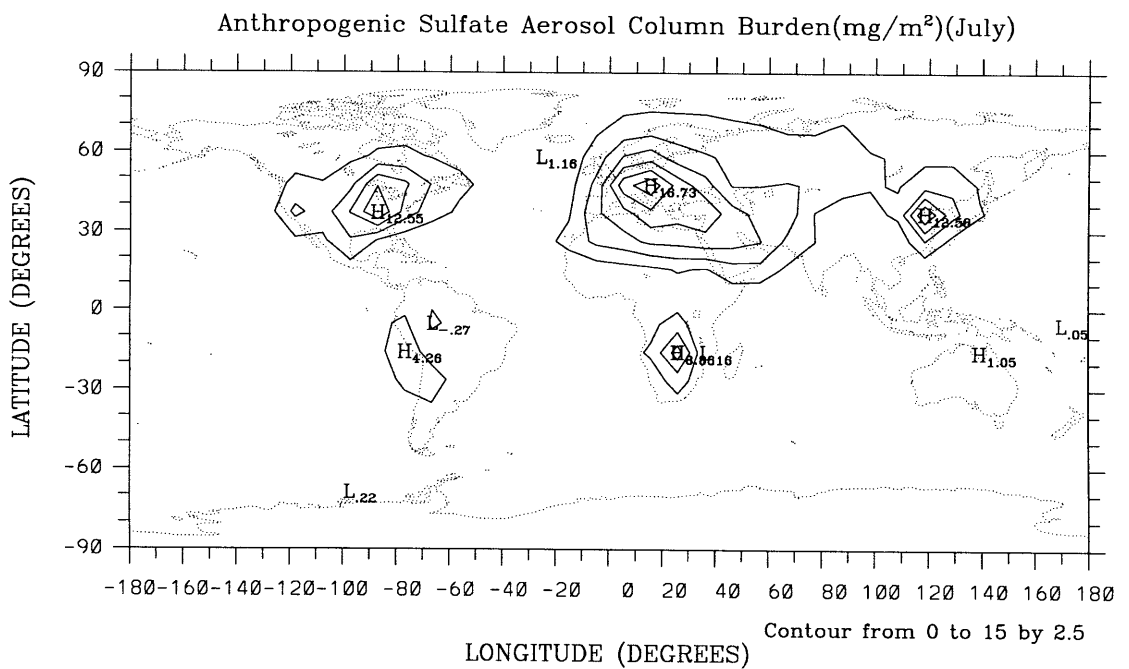
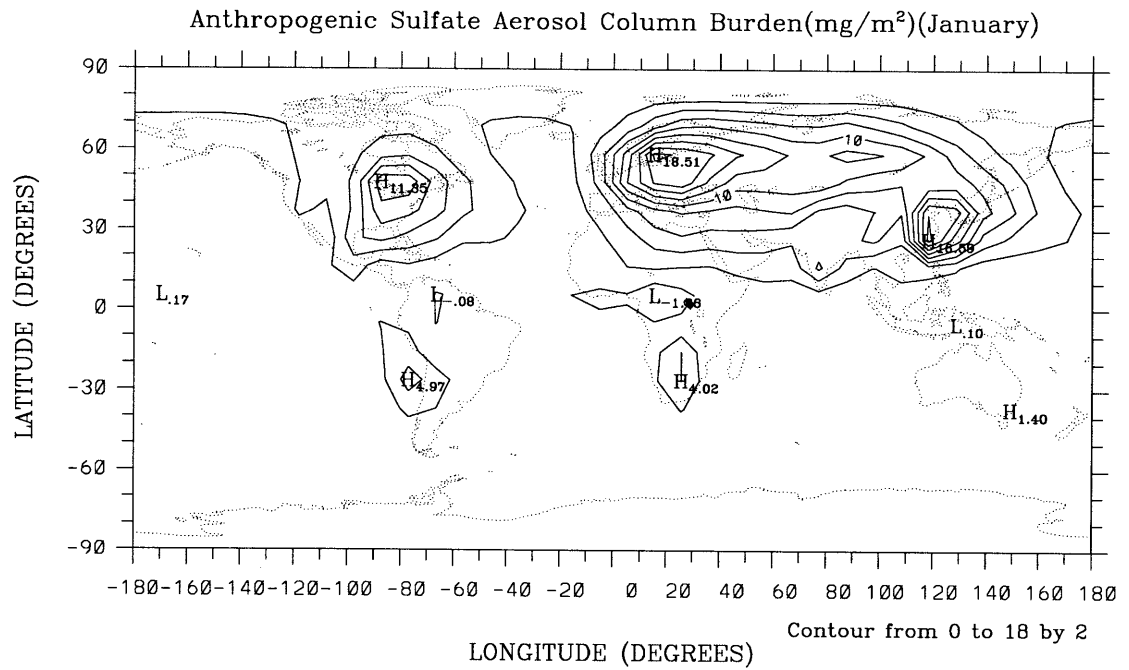


Figure 4-7: Monthly averaged column burden of anthropogenic sulfate aerosols.

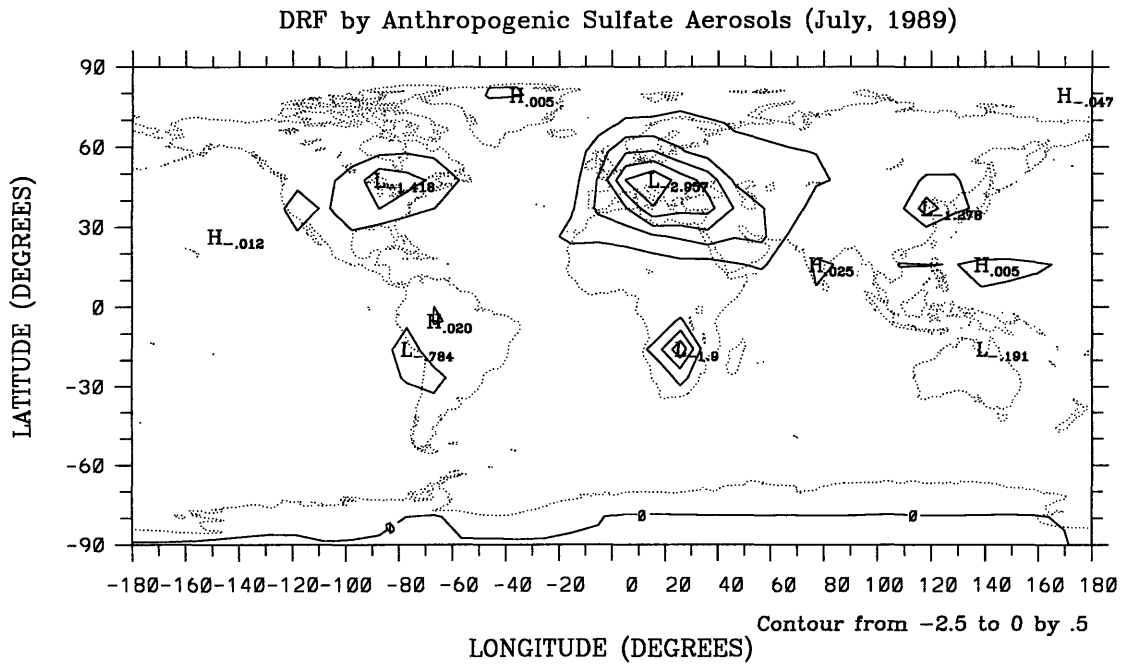
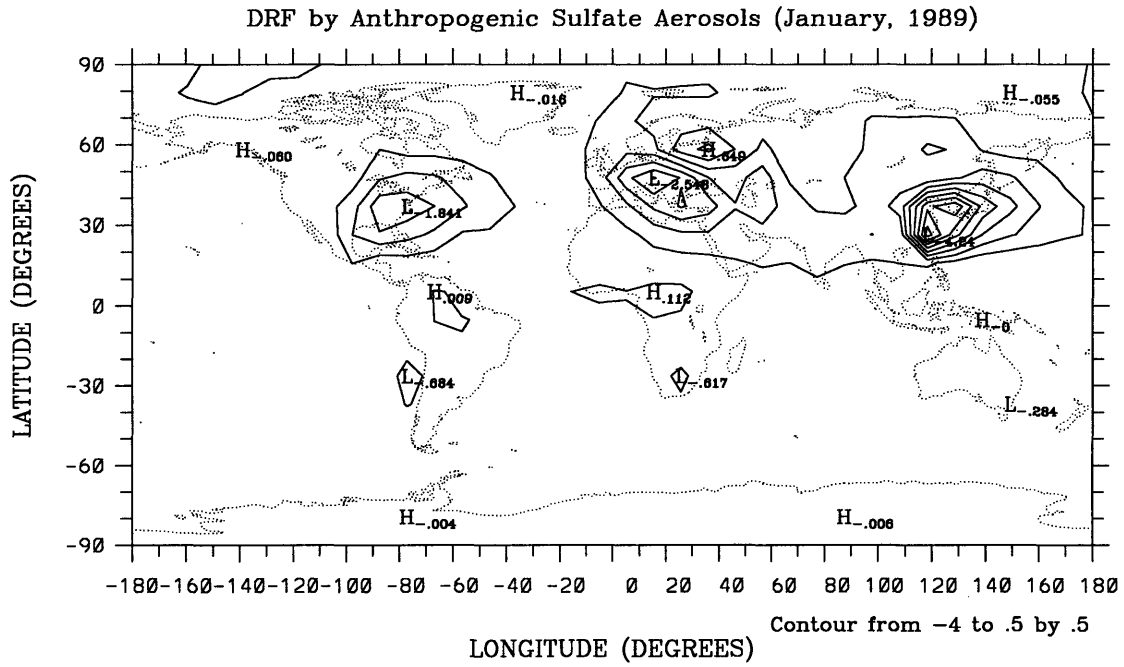


Figure 4-8: Monthly averaged direct radiative forcing by anthropogenic sulfate aerosols: top-January; bottom-July.

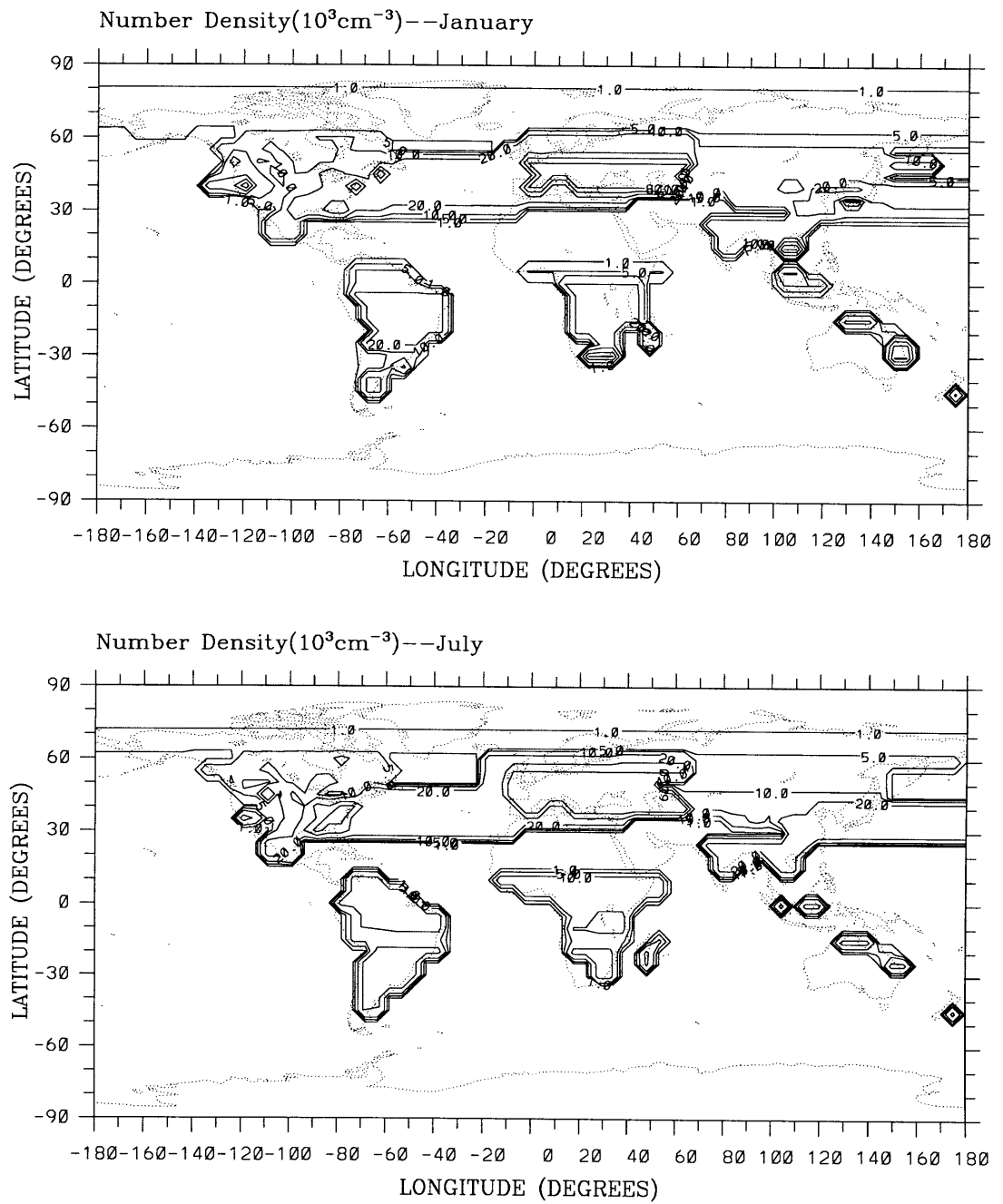


Figure 4-9: Monthly averaged aerosol number density at surface.

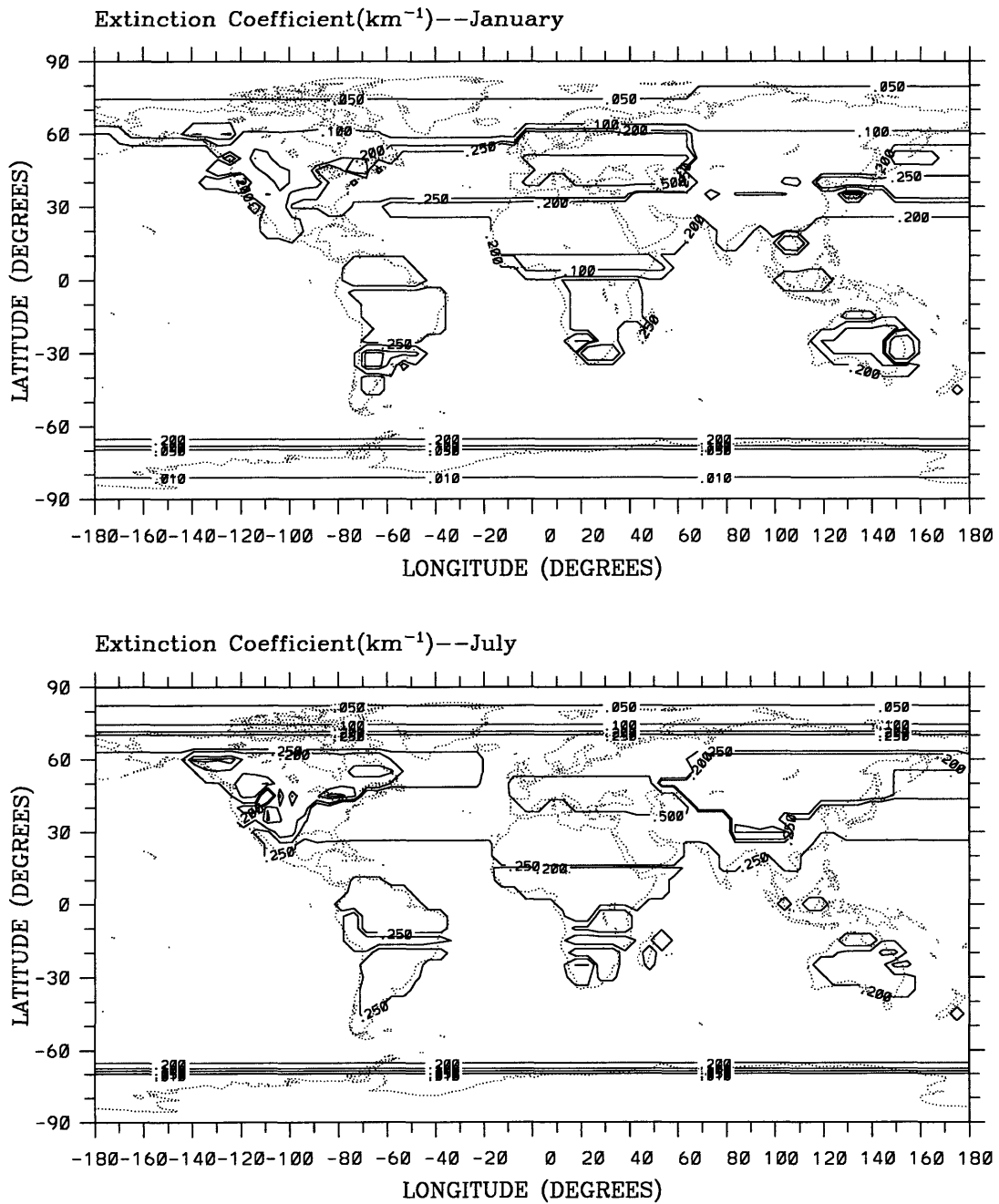


Figure 4-10: Monthly averaged aerosol extinction coefficient at surface for $0.5 \mu\text{m}$ and a hypothetical relative humidity of 0 %.

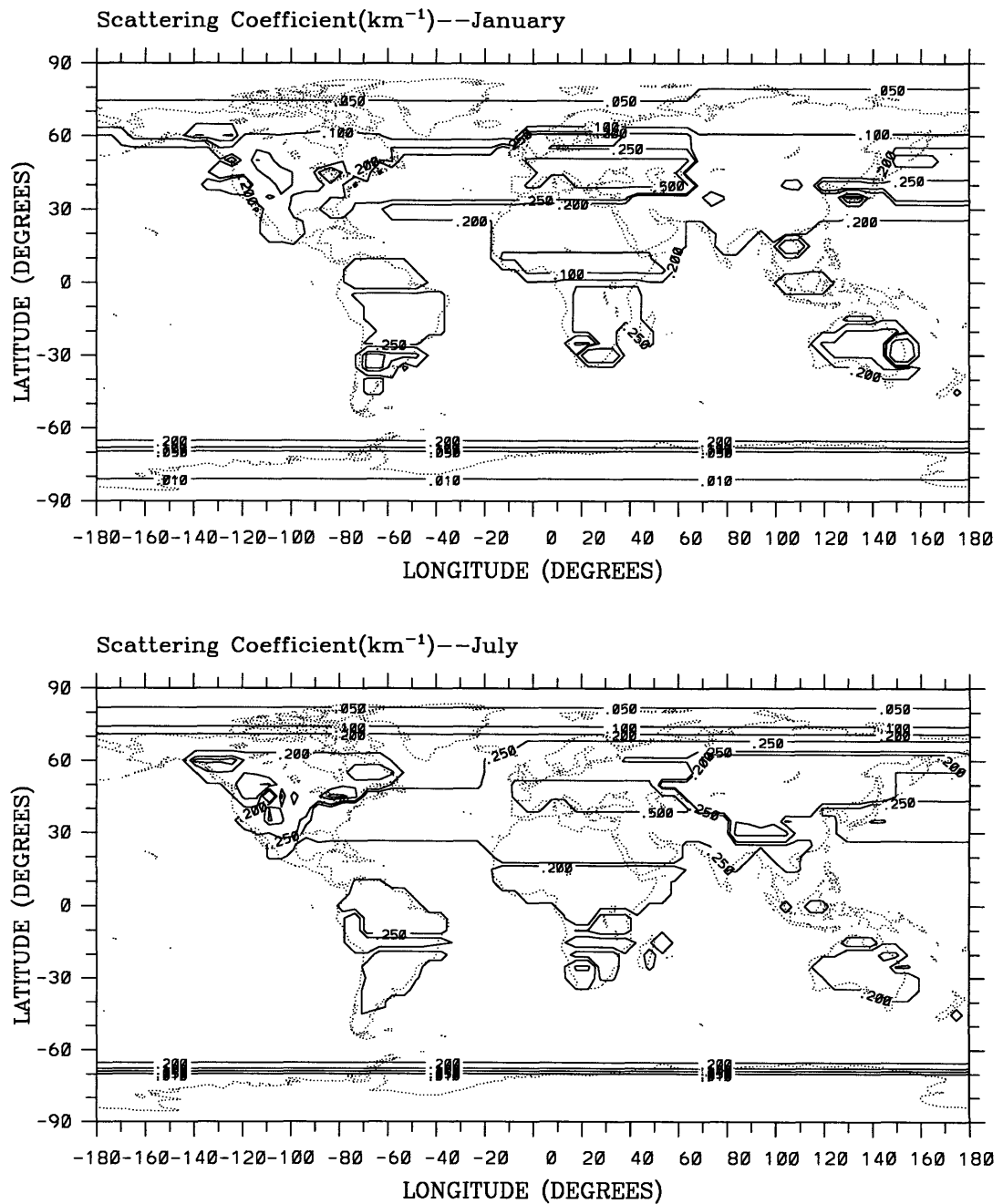


Figure 4-11: Monthly averaged aerosol scattering coefficient at surface for $0.5 \mu\text{m}$ and a hypothetical relative humidity of 0 %.

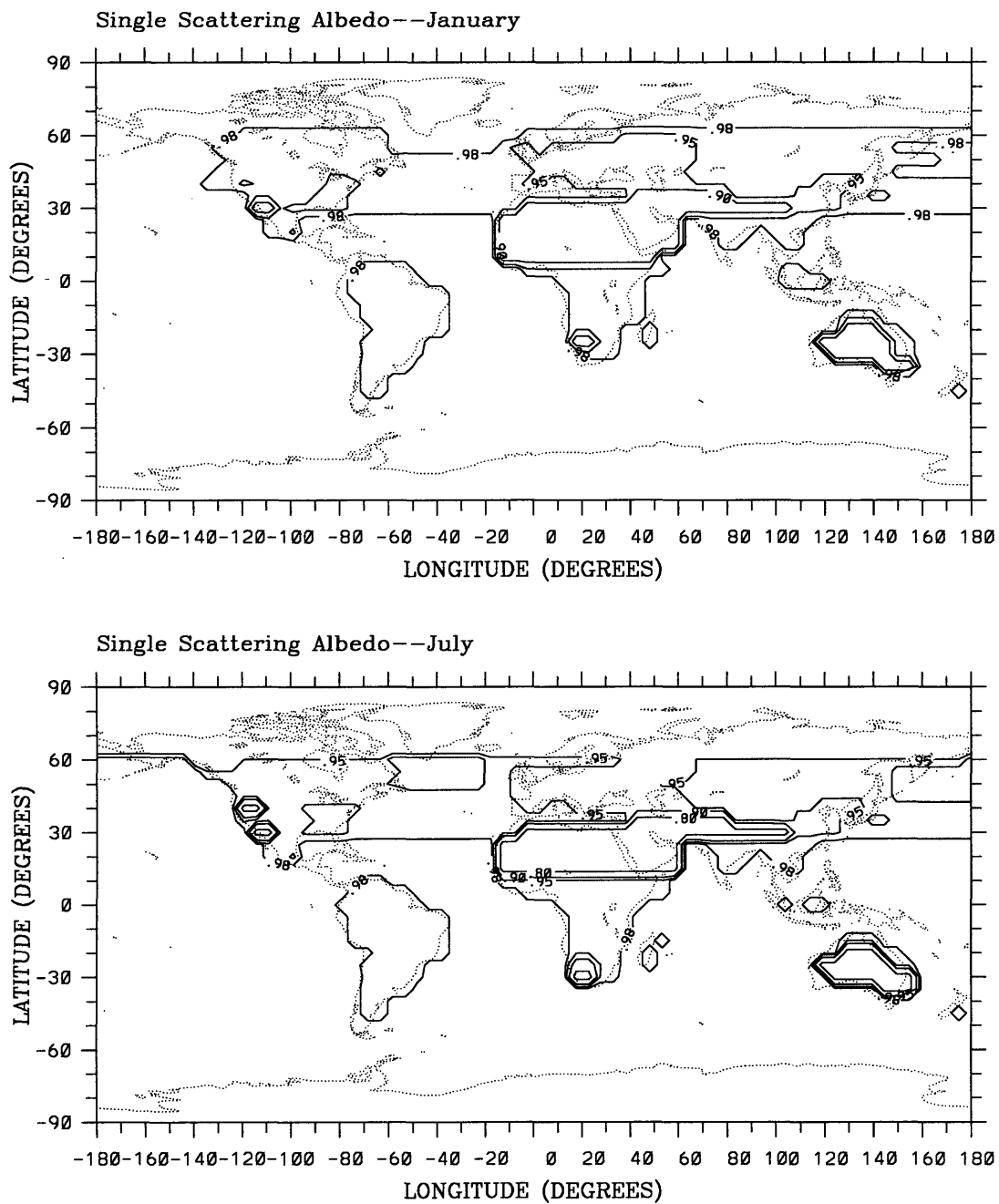


Figure 4-12: Monthly averaged aerosol single scattering albedo at surface for $0.5 \mu\text{m}$ and a hypothetical relative humidity of 0 %.

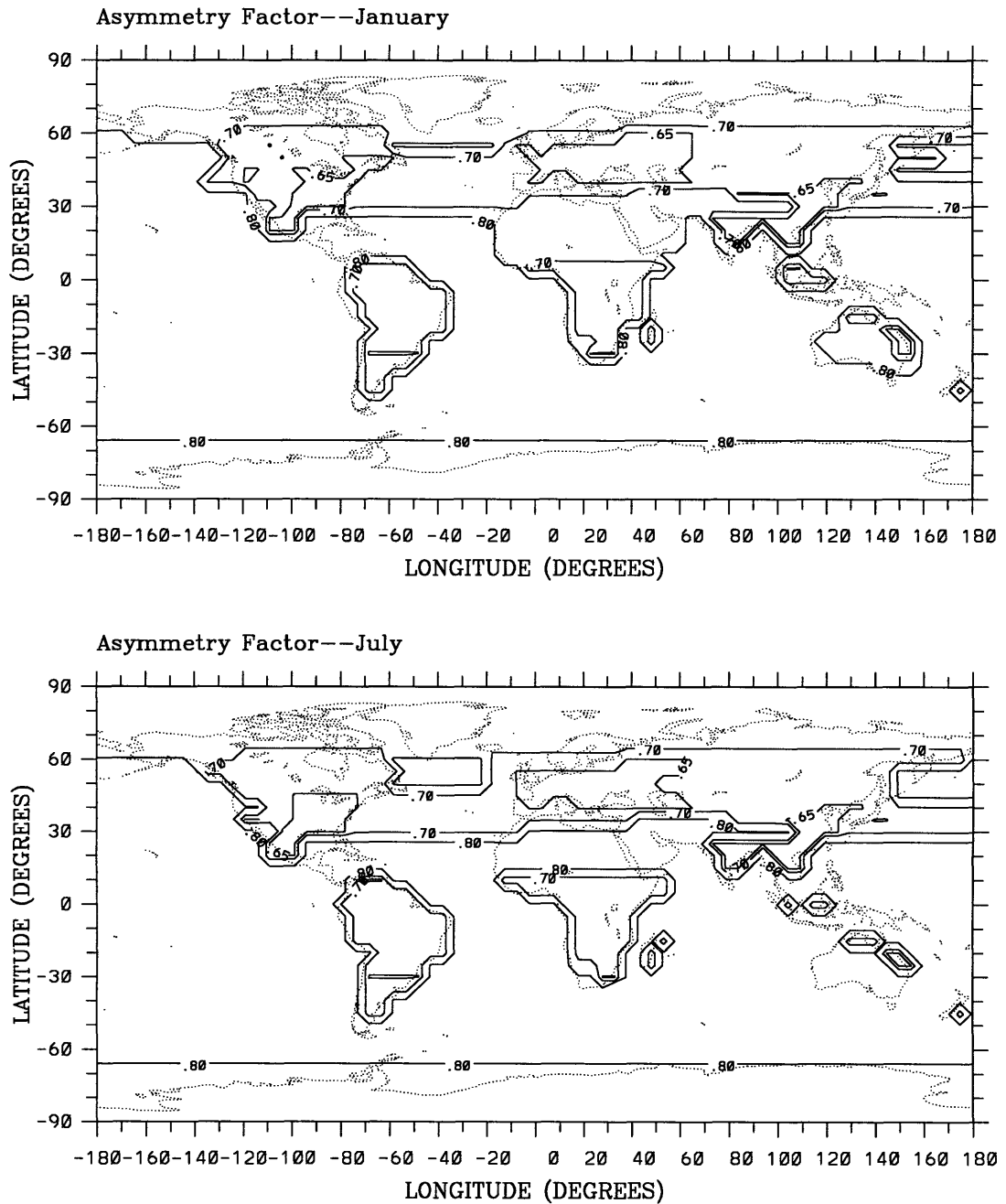


Figure 4-13: Monthly averaged aerosol asymmetry factor at surface for 0.5 μm and a hypothetical relative humidity of 0 %.

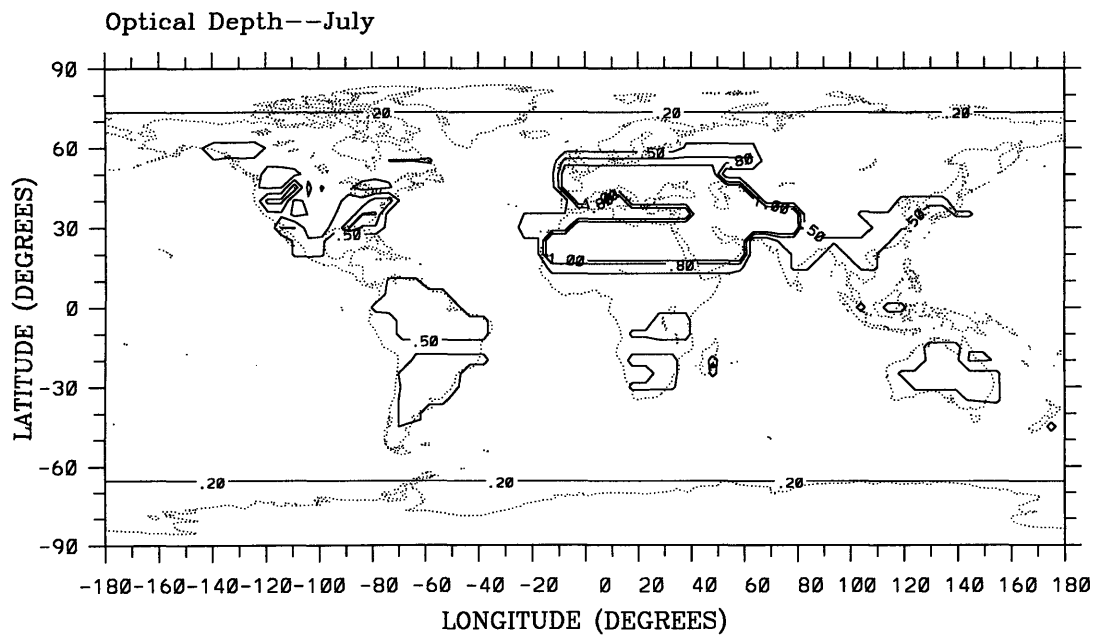
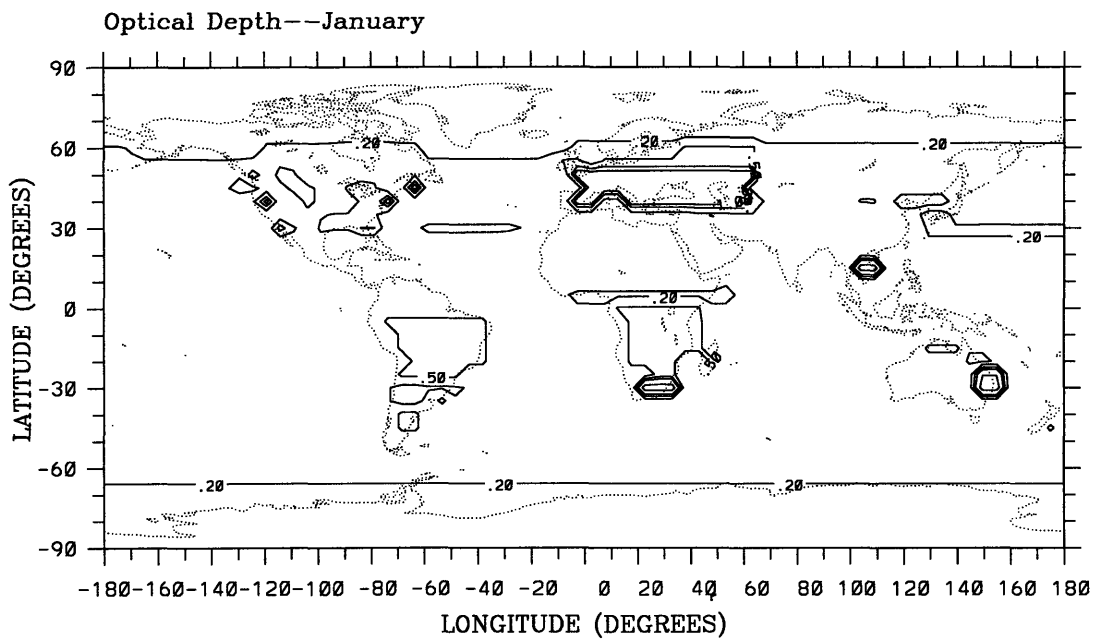


Figure 4-14: Monthly averaged aerosol optical depth at surface for $0.5 \mu m$ and a hypothetical relative humidity of 0 %.

The aerosol optical properties with the correction of boundary layer relative humidity are shown in Figures 4-15 to 4-19. Compared with the dry case, the aerosol optical properties show higher spatial variability following the spatial variation of relative humidity. Both attenuation coefficients and optical depth increase significantly in high relative humidity region. Single scattering albedo and asymmetry factor show small variation compared with those in the dry case, except in winter polar region where high relative humidity occurs.

To account for the short-wave and long-wave radiative forcing by aerosols, I have used the radiative transfer scheme developed by Fu and Liou [51]. For short-wave radiation, this scheme includes the Rayleigh scattering and the absorption and scattering due to ozone, oxygen, carbon dioxide, water vapor, clouds, and aerosols. For long-wave radiation, this scheme includes the scattering and absorption due to water vapor, ozone, carbon dioxide, methane, nitrous oxide, clouds, and aerosols. The solar spectrum is divided into 6 bands and the infrared spectrum is divided into 12 bands, within which the optical properties of clouds and aerosols are treated as constant, based on the correlated k -distribution method. The radiative transfer equation in a vertically nonhomogeneous path is then solved using the delta-four-stream discrete-ordinate approximation [87]. The required aerosol optical properties for the scheme are optical depth, single-scattering albedo, and asymmetry factor in each vertical layer. By using a variety of atmospheric profiles and spectral intervals containing principal absorbing gases, our calculated fluxes and heating rates are compared with those based on line-by-line calculations[51]. In the solar region, errors in fluxes and heating rates are within 0.05% and 0.01 K/day, respectively; in the thermal infrared region, errors are less than 0.2% for all the principal absorbing gases except O₃(for which, the error is about 2%) and .01K/day below 30 km(above which, the error is about 0.1 K/day), respectively.

The changes of vertical radiative flux and heating rate relative to those in clear sky condition (i.e., Figure 4-1) for 7 aerosol types are shown in Figure 4-20. The aerosol number densities are given in Table 5.2. The magnitude of the change of solar radiative flux and heating rate is about a factor of ten larger than that of the terrestrial counterparts. On a daily average, the maximum radiative heating rate peaks near the top of the boundary layer, varying from 0.1 to 1.2°C/day.

Figures 4-21 to 4-26 show the January global distribution of short-wave and long-wave flux at the top of the atmosphere and at surface for three aerosol cases relative to the base case (i.e., without aerosols). The first case is for dry aerosols with fixed boundary layer height given in Table B.3. The second case is the same as the first case except with the boundary layer averaged relative humidity as shown in Figure 4-6. The third case is the same as the second case except the actual boundary height is used. Figures 4-27 to 4-32 show the same plots except for July. The corresponding annual global means of radiative flux changes are listed in Table 4.2.

At the top of the atmosphere, the presence of aerosols decreases the net downward short-wave flux except in several arid regions, where the higher absorption-to-reflection ratio due to mineral aerosols heats the system as shown in Figure 4-2, and increases the net downward long-wave flux. As in the column calculations, the solar radiative flux change dominates the terrestrial flux change. The interaction between water vapor and aerosols increases the flux change by almost a factor of 2. The use of actual boundary layer heights tends to underestimate the aerosol effect by about a factor of 2, indicating the boundary layer height used in Table B.3 seems to be about a factor of 2 larger than observations. On the other hand, if total aerosol number concentrations or total optical depths are preserved according to fixed boundary heights, heating rates with actual boundary layer heights would increase by

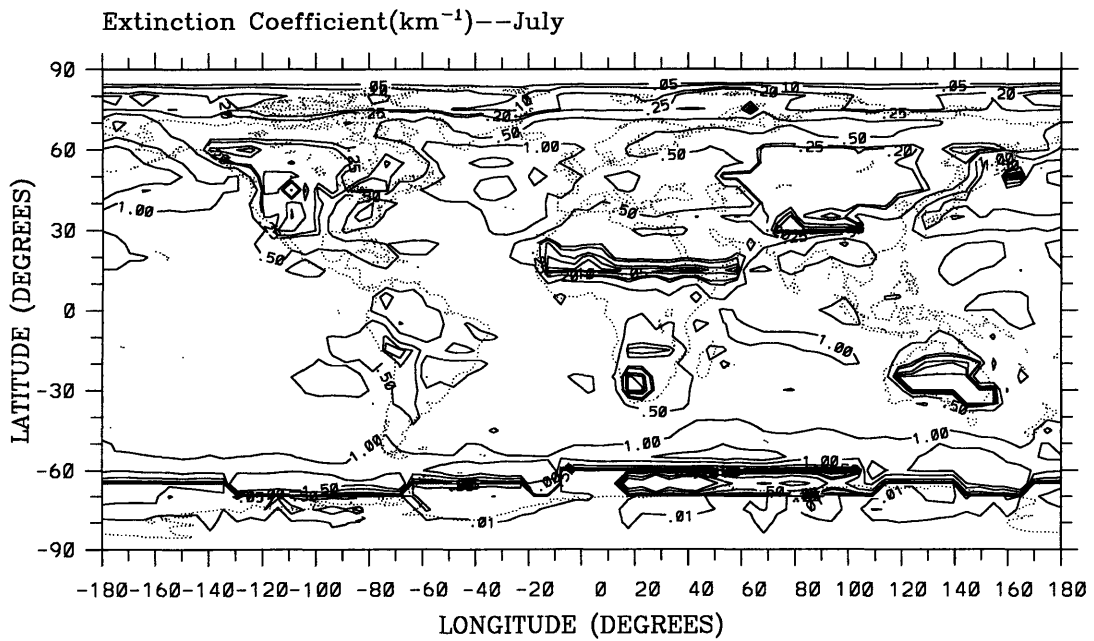
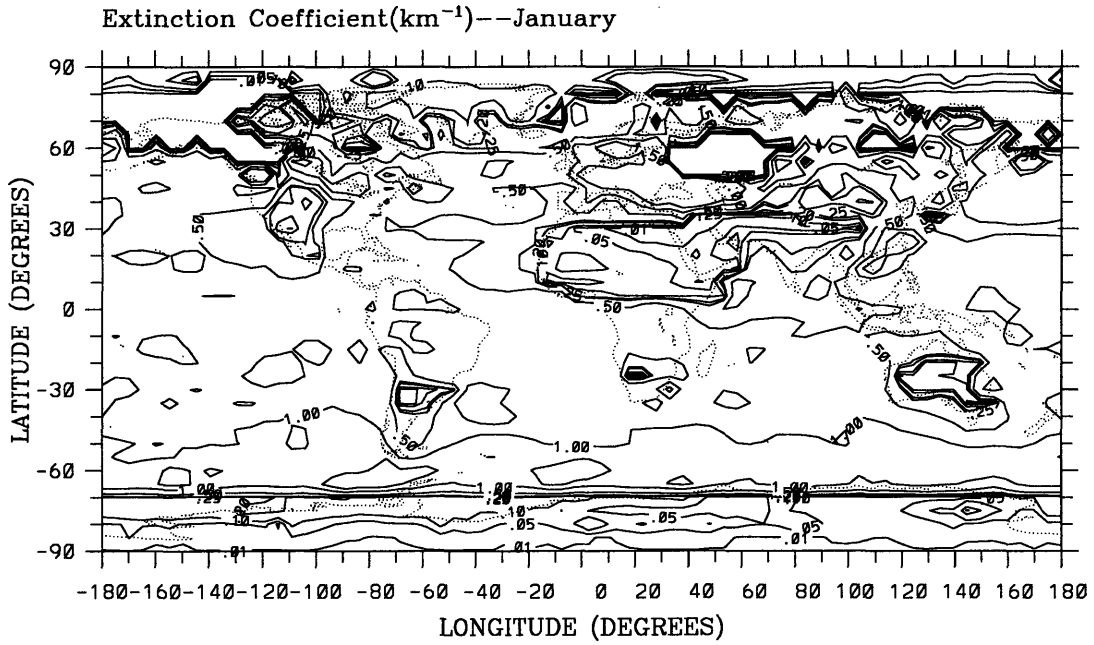


Figure 4-15: Monthly averaged aerosol extinction coefficient at surface for $0.5 \mu\text{m}$ and a boundary layer relative humidity from Figure 4-6.

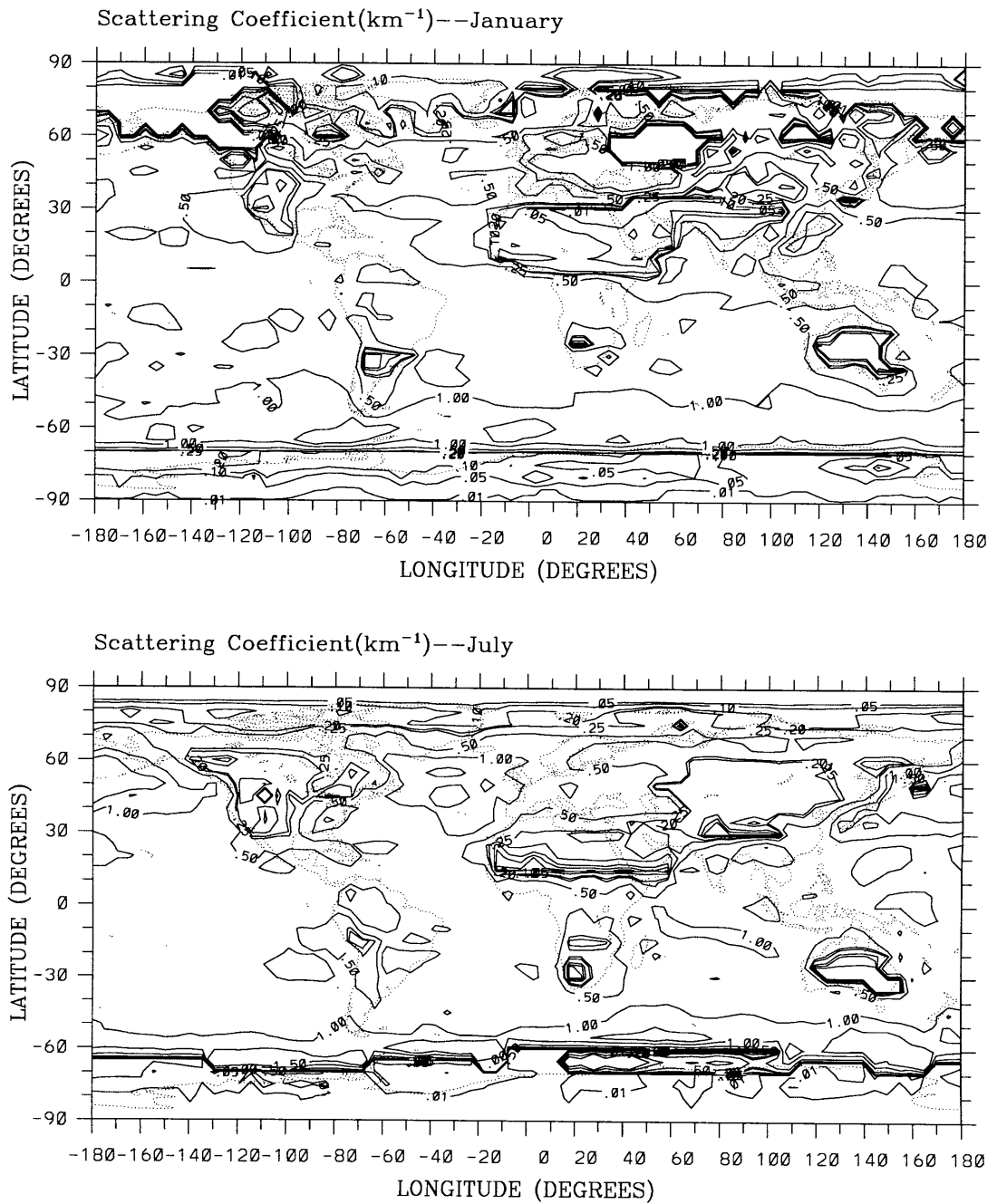


Figure 4-16: Monthly averaged aerosol scattering coefficient at surface for $0.5 \mu m$ and a boundary layer relative humidity from Figure 4-6.

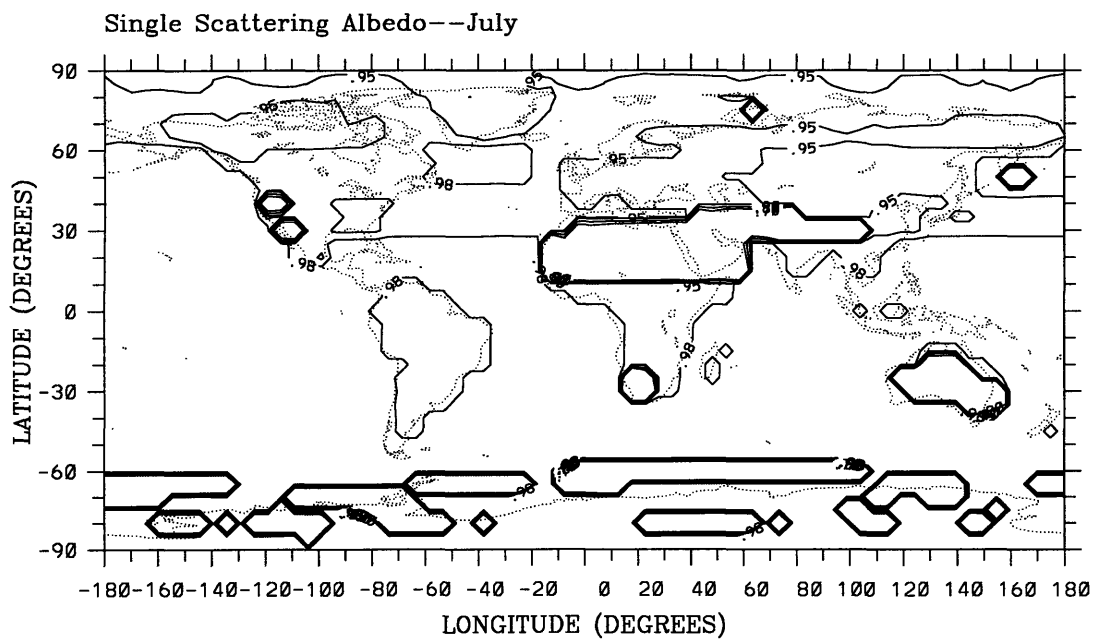
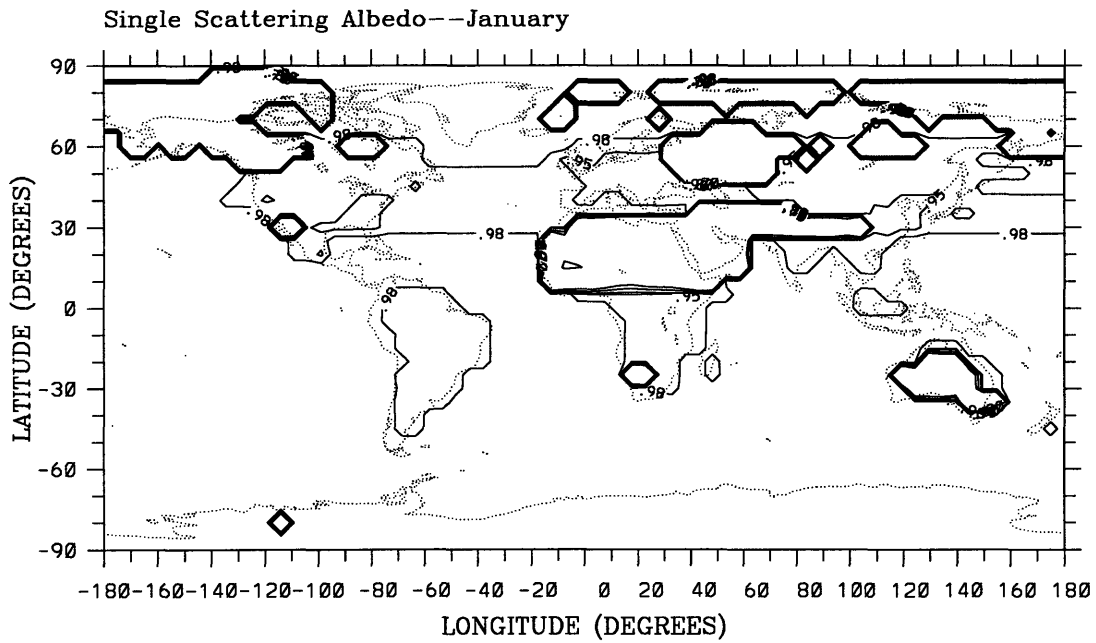


Figure 4-17: Monthly averaged aerosol single scattering albedo at surface for $0.5 \mu m$ and a boundary layer relative humidity from Figure 4-6.

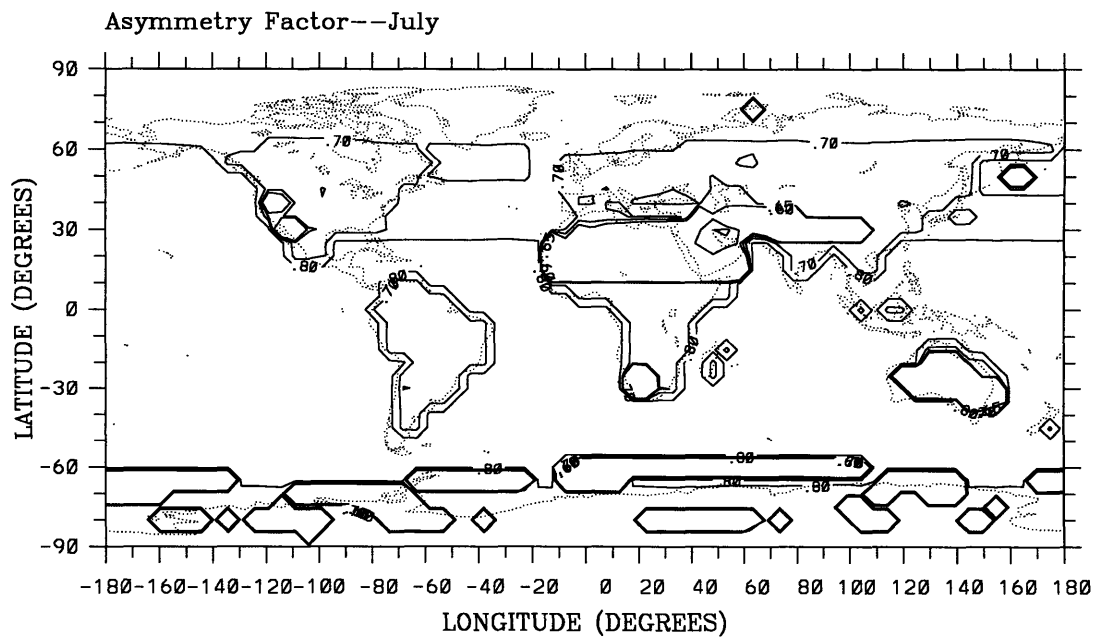
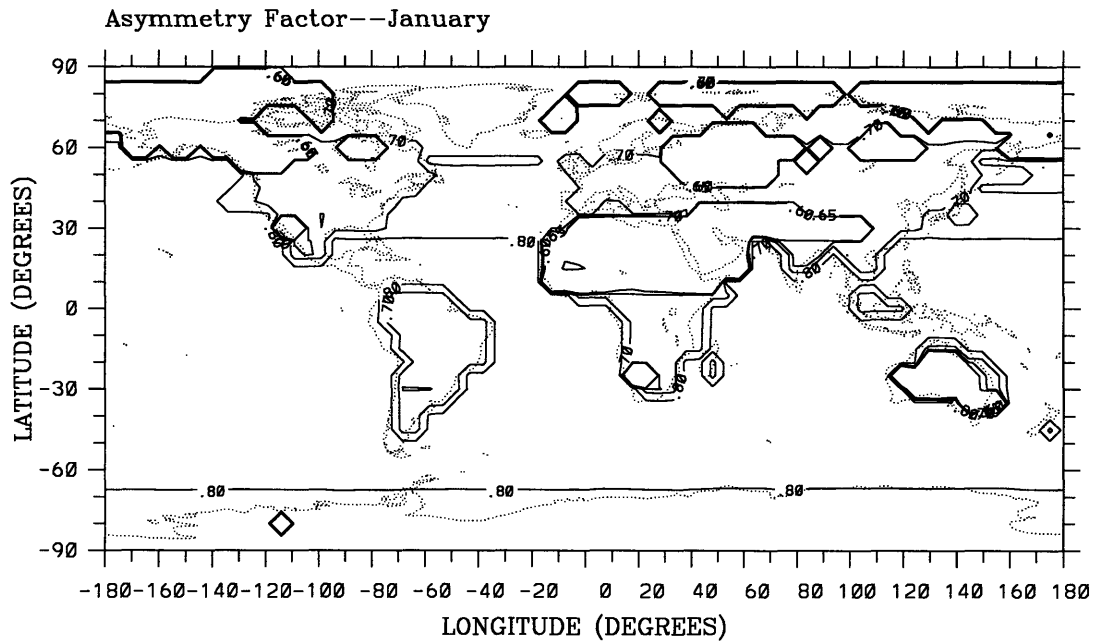


Figure 4-18: Monthly averaged aerosol asymmetry factor at surface for $0.5 \mu m$ and a boundary layer relative humidity from Figure 4-6.

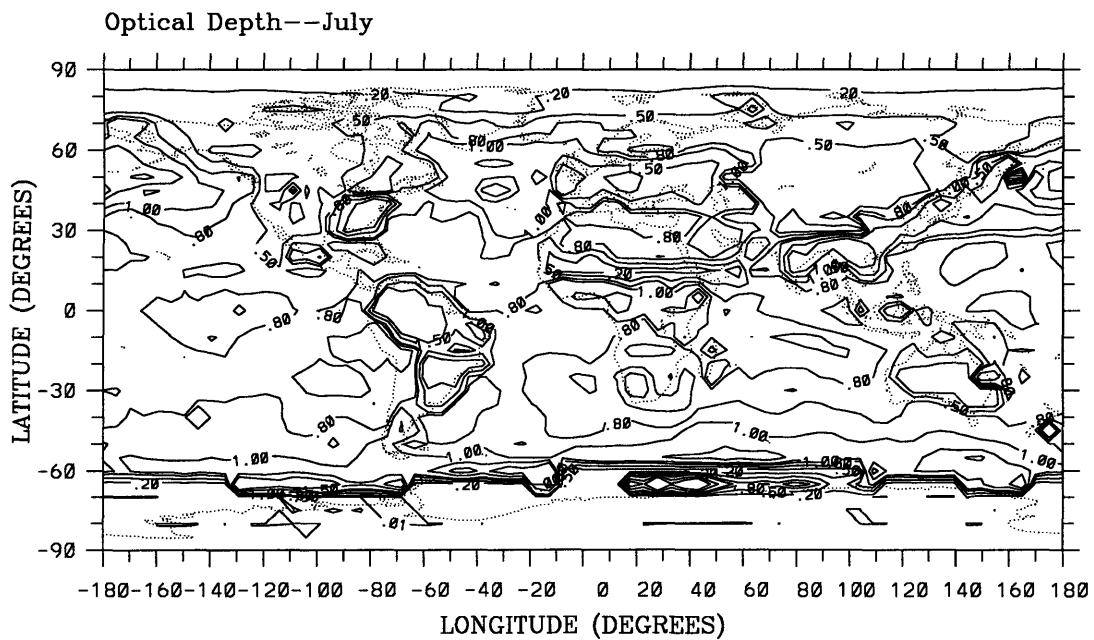
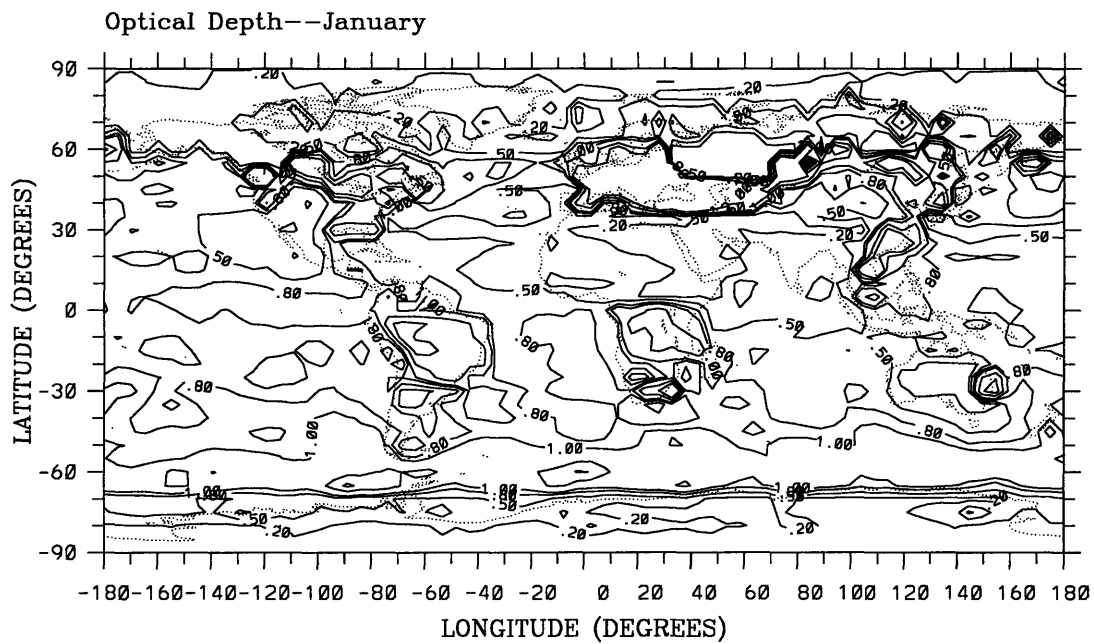
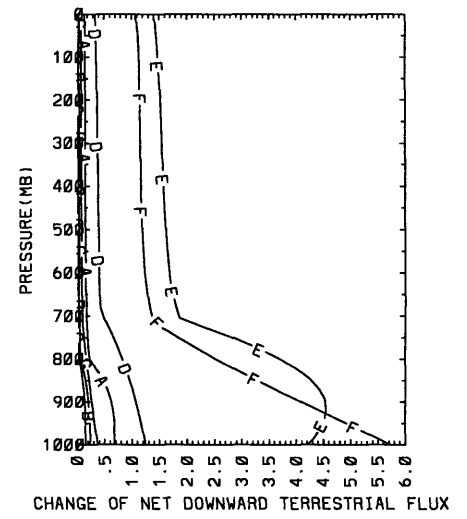
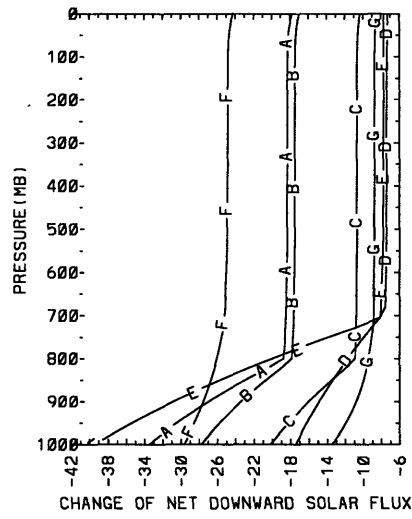


Figure 4-19: Monthly averaged aerosol optical depth at surface at surface for $0.5 \mu m$ and a boundary layer relative humidity from Figure 4-6.



- A- CL. CONT.
- B- AV. CONT.
- C- URBAN
- D- DESERT(WIN.)
- E- DESERT(SUM.)
- F- MARITIME CLEAN
- G- MARITIME POLL.

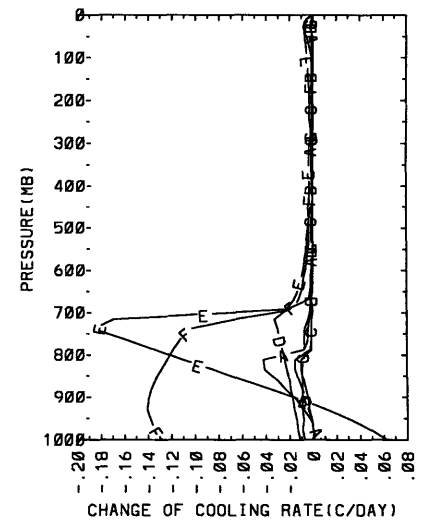
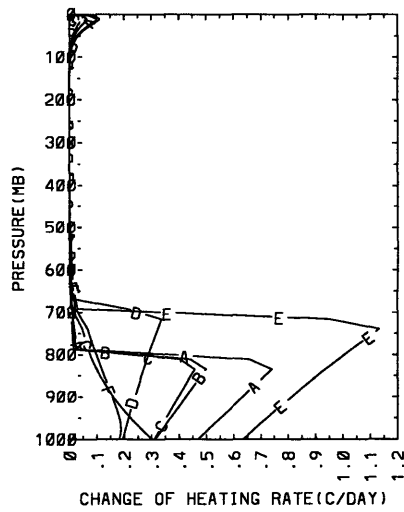


Figure 4-20: Change of radiative flux and heating rates for 7 aerosol types.

Table 4.2: The annual global mean of radiative flux changes by climatological aerosols for different cases.

Humidity Effect	Aerosol Density Profile(z)	$\Delta F(W/m^2)$ (Net Downward)			
		Top of Atmosphere		Surface	
		SW	LW	SW	LW
No	Constant in specified layers	-5.66	0.39	-10.32	1.50
$RH_{BL}(x, y)$	„	-10.46	0.59	-18.37	4.00
„	Constant in BL(x, y)	-4.39	0.31	-10.77	1.82

about a factor of 2.

At the surface, when humidity effects on aerosol optical properties are excluded, net downward short-wave flux decreases by less than $10 W/m^2$ in polar regions and by more than $50 W/m^2$ in several other regions. Net downward long-wave flux increases by less than $5 W/m^2$ in most of the globe except in the Saharian and Australian deserts, where an increase of more than $10 W/m^2$ is observed. The humidity effects increase the flux change by about a factor of 2 in most area. The sensitivity of surface flux change to boundary height is similar to that of flux change at the top of atmosphere.

The seasonal variations of the radiative forcing at both the top of the atmosphere and the surface are clear, due mainly to the variations in the meteorological fields. Large radiative forcings are seen in the Saharian desert and several urban regions.

4.4 Conclusions

The sensitivity of the radiative forcing by anthropogenic sulfate aerosols to aerosol burden, optical properties, and humidity effects has been calculated with an explicit radiative transfer model. Results show that the current discrepancy of this forcing are caused almost equally by differences in aerosol column burden and optical properties. The use of constant humidity scaling functions of humidity effect is a good approximation, provided that their values are kept as the observed one in the visible range. Neglecting the humidity effect on single-scattering albedo and asymmetry factor will only overestimate the result by 10%.

The magnitude of the radiative forcing by climatological aerosols is more than an order of magnitude larger than that from the anthropogenic sulfate aerosols. At the top of the atmosphere and the surface, the short-wave flux change dominates the long-wave flux change. The results vary by about a factor of 2 to the changes in the ambient relative humidity and the boundary layer height. Since the transformation of aerosols in the atmosphere is also highly dependent on ambient meteorological fields, it appears that accurate investigations may rely on how dynamical aerosol models interact with global climate models.

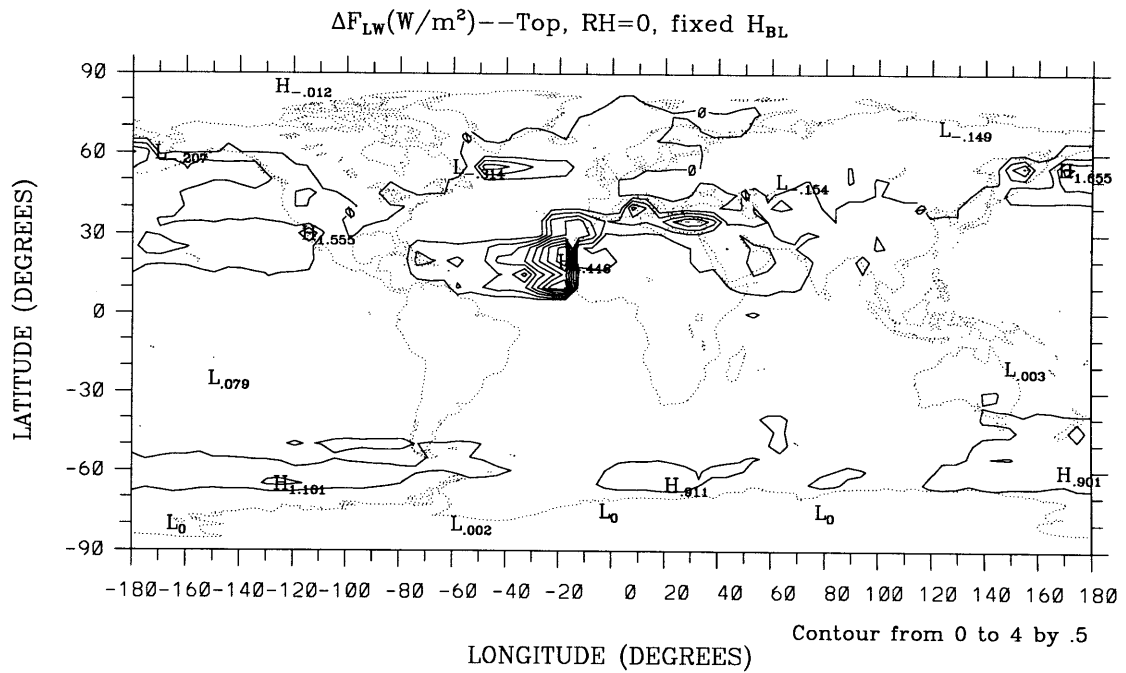
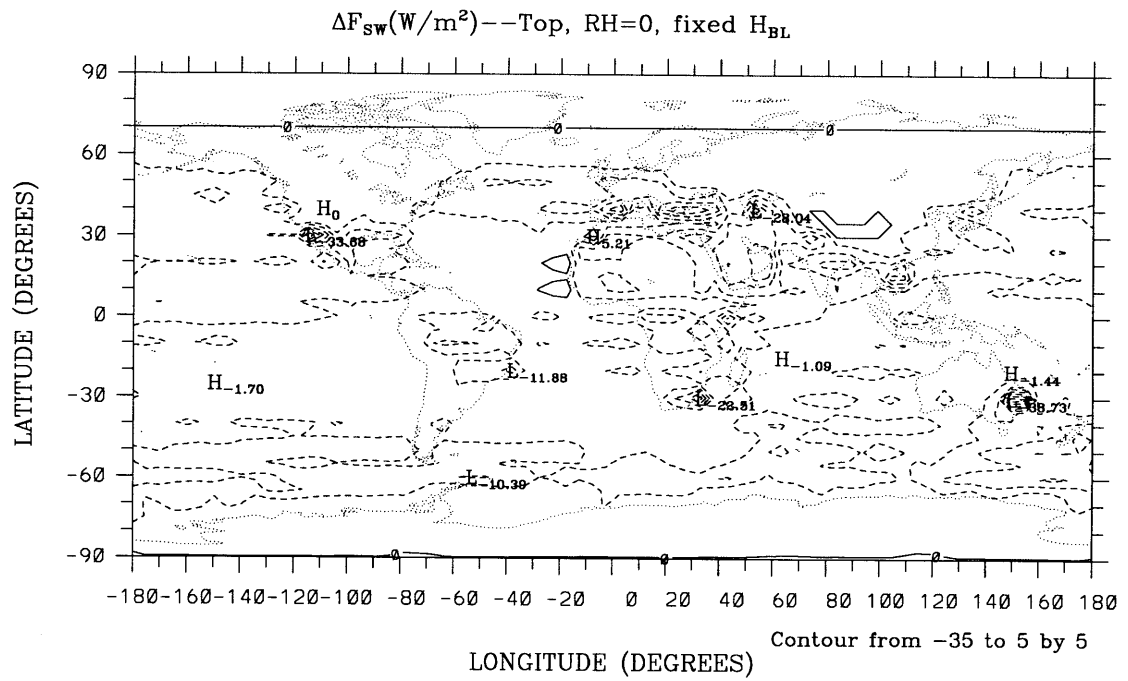


Figure 4-21: Radiative flux change at the top of the atmosphere in January using a hypothetical relative humidity and a fixed boundary layer height: top-short-wave; bottom-long-wave.

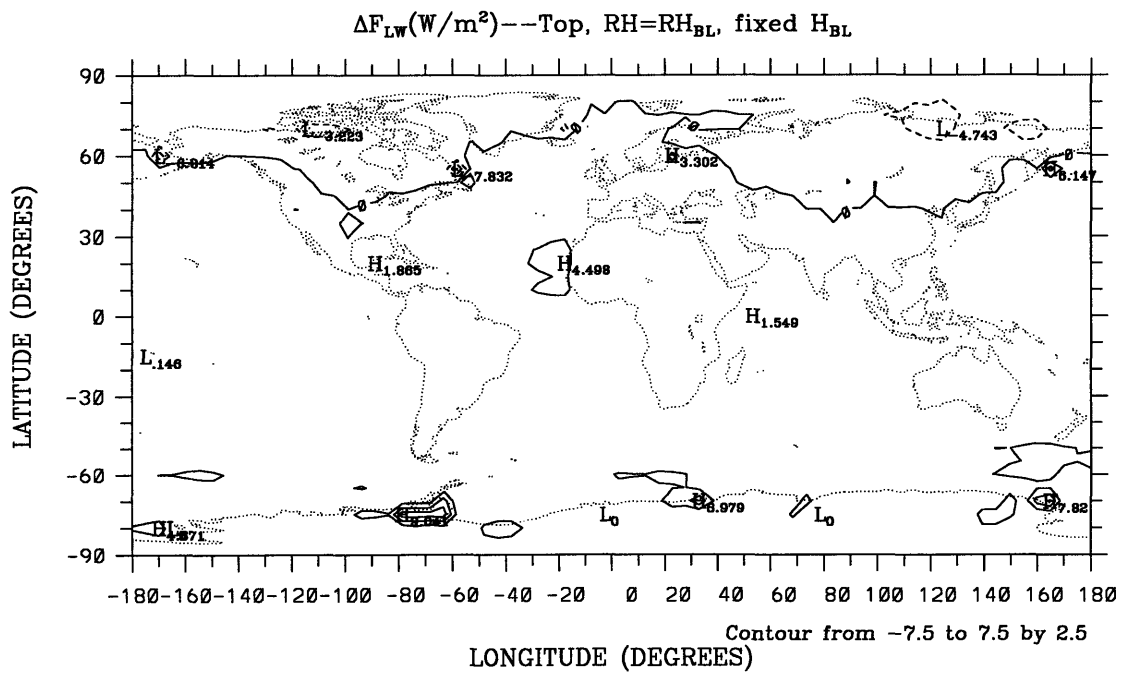
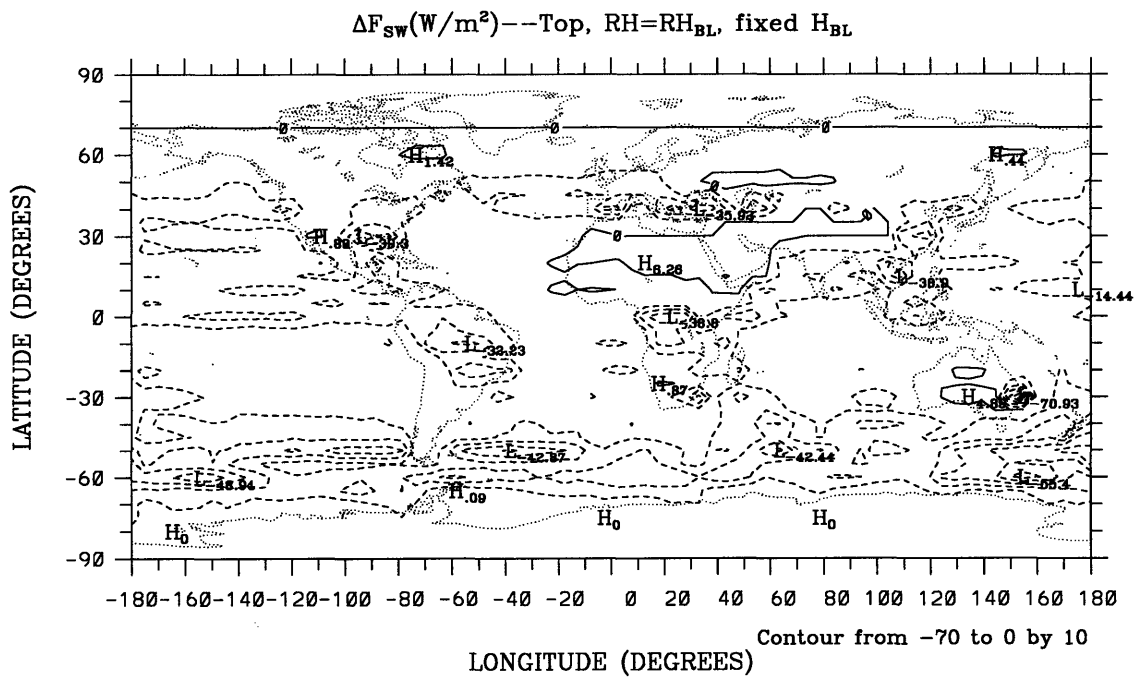


Figure 4-22: Radiative flux change at the top of the atmosphere in January using a fixed boundary layer height and a relative humidity from Figure 4-6: top-short-wave; bottom-long-wave.

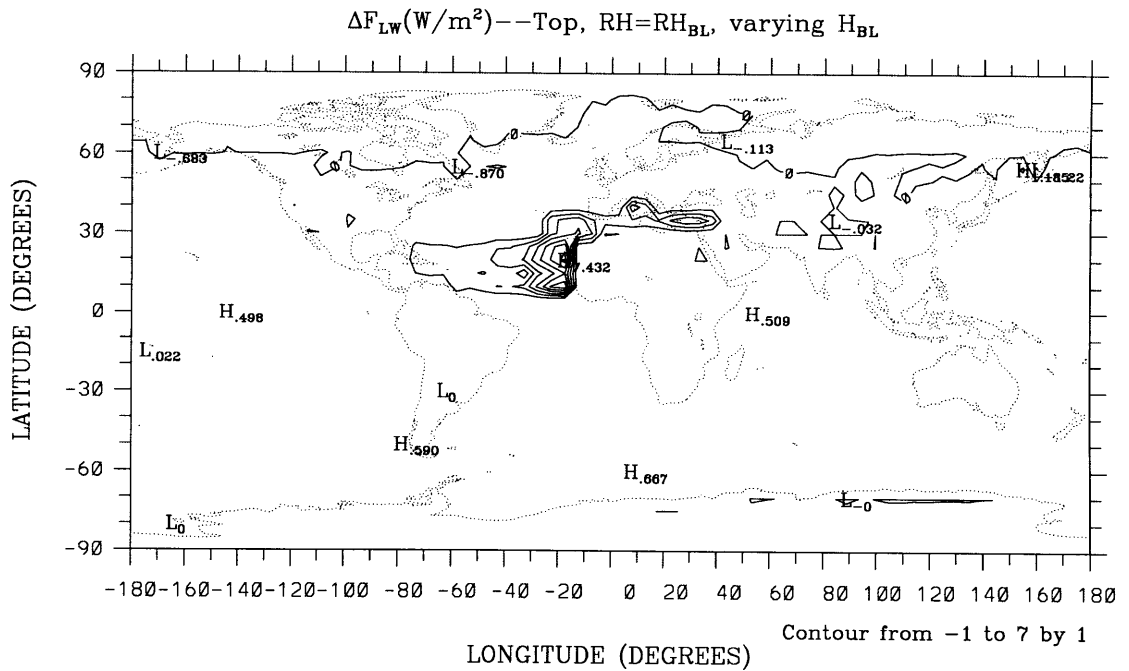
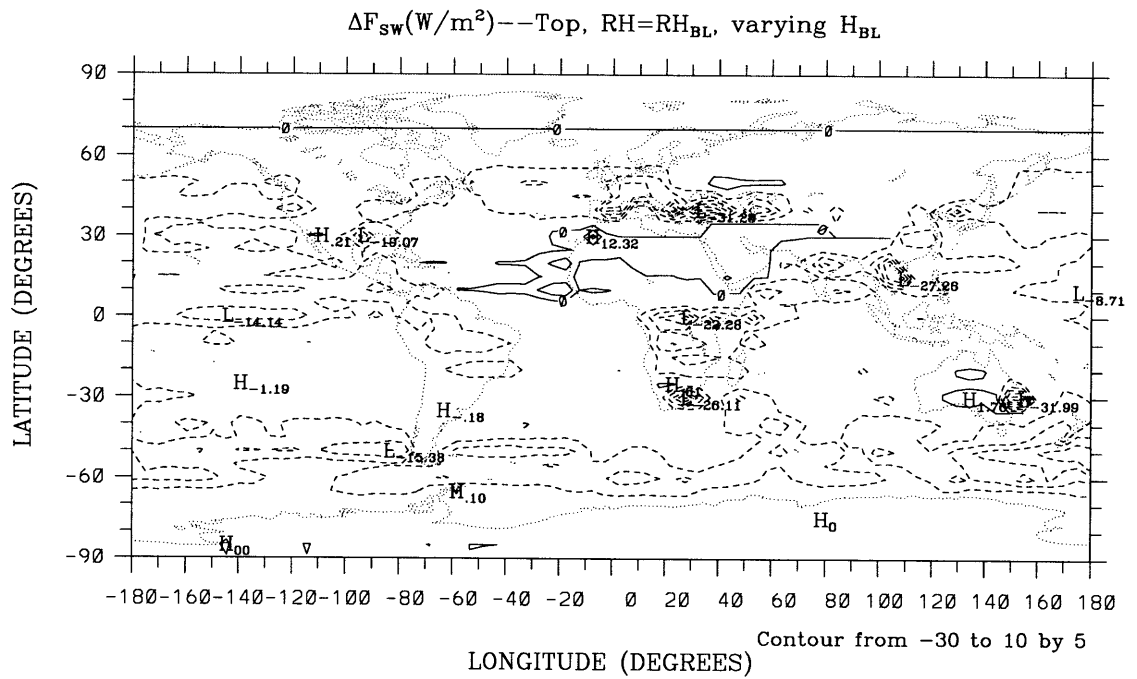


Figure 4-23: Radiative flux change at the top of the atmosphere in January using a varying boundary layer height and a relative humidity from Figure 4-6: top-short-wave; bottom-long-wave.

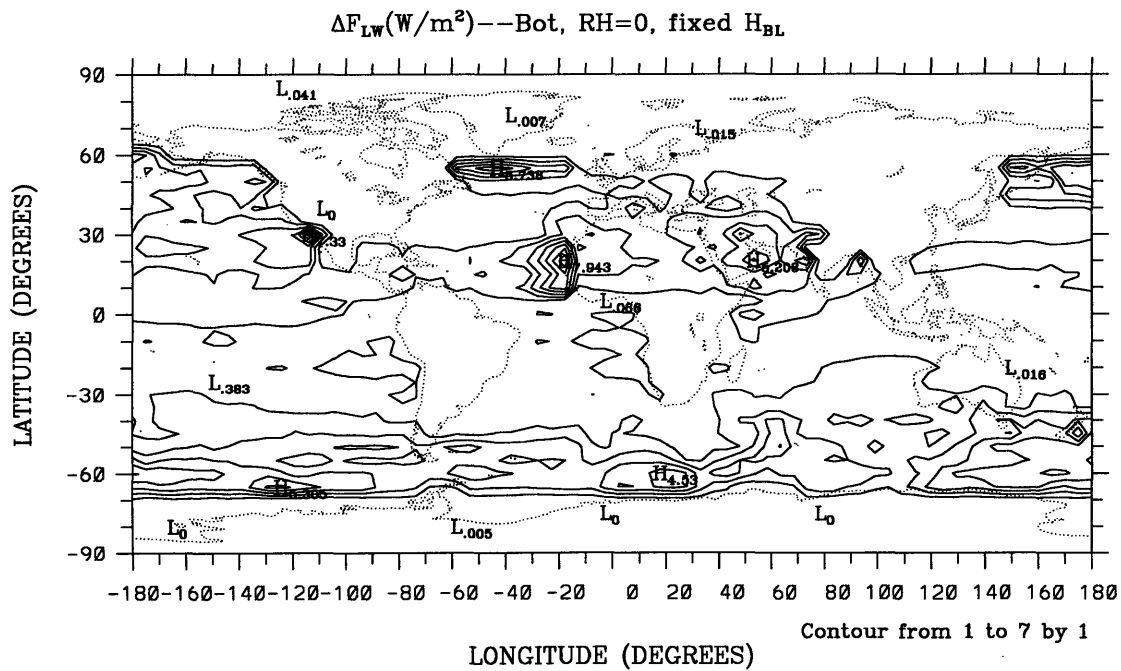
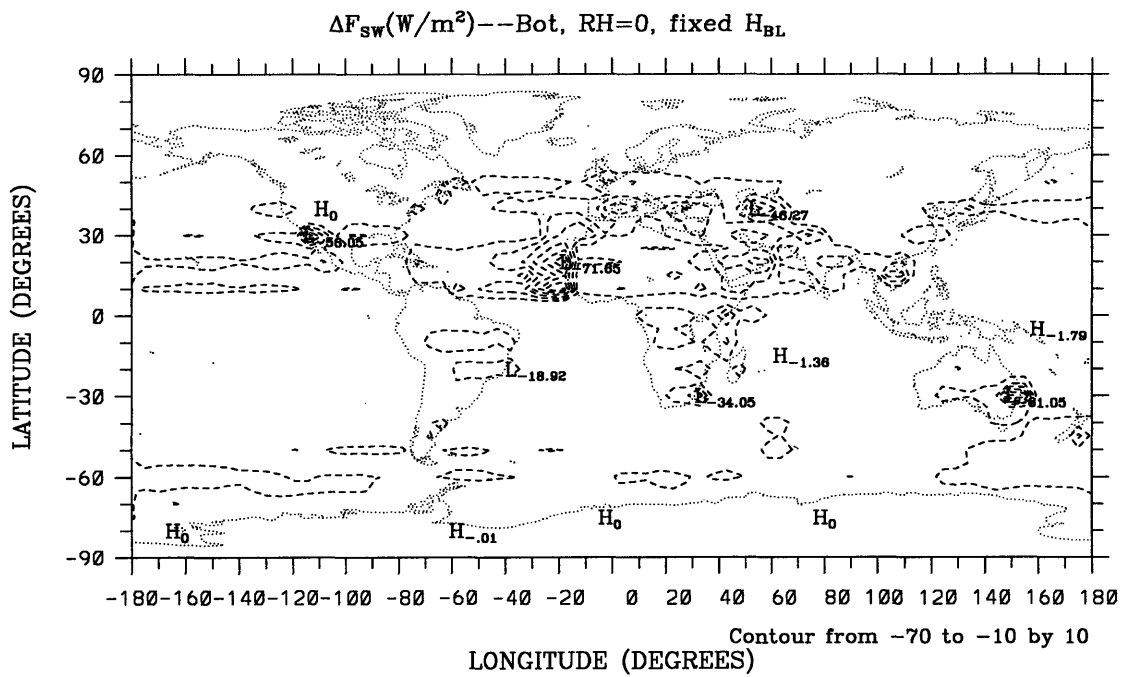


Figure 4-24: Radiative flux change at the surface in January using a hypothetical relative humidity and a fixed boundary layer height: top-short-wave; bottom-long-wave.

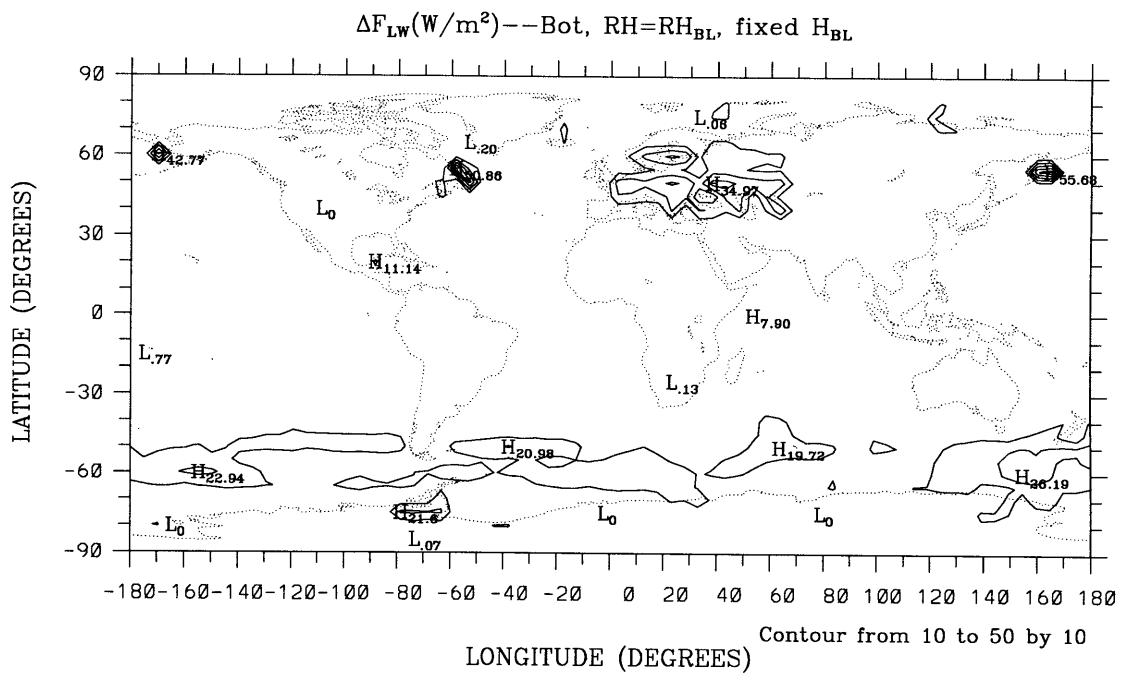
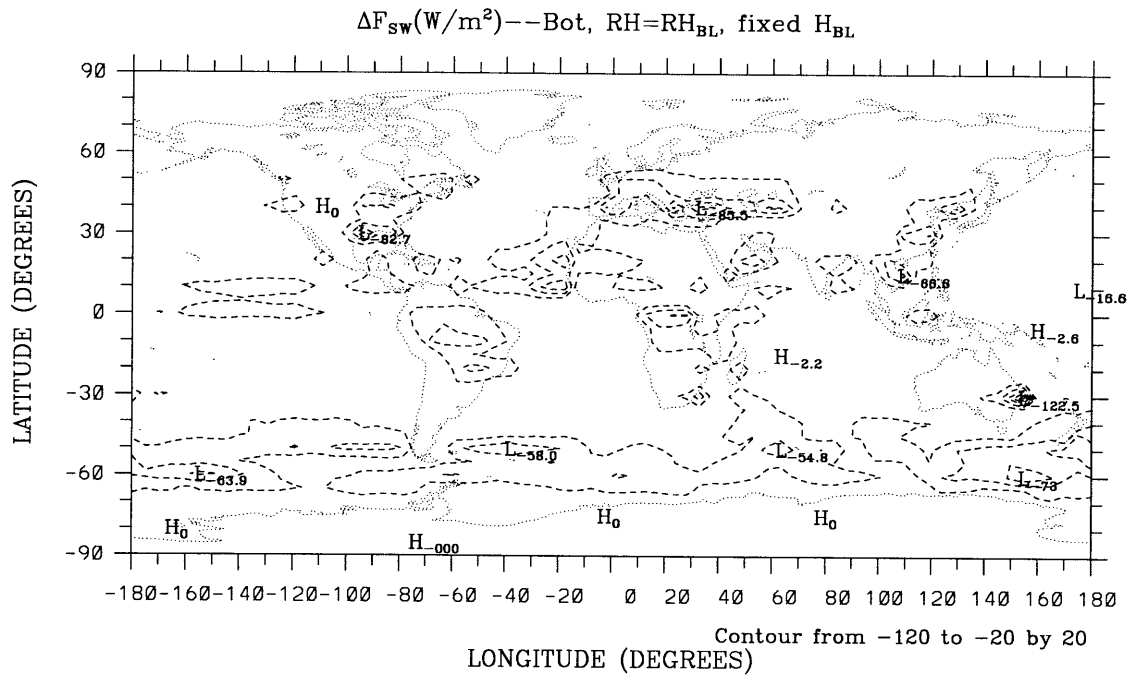


Figure 4-25: Radiative flux change at the surface in January using a fixed boundary layer height and a relative humidity from Figure 4-6: top-short-wave; bottom-long-wave.

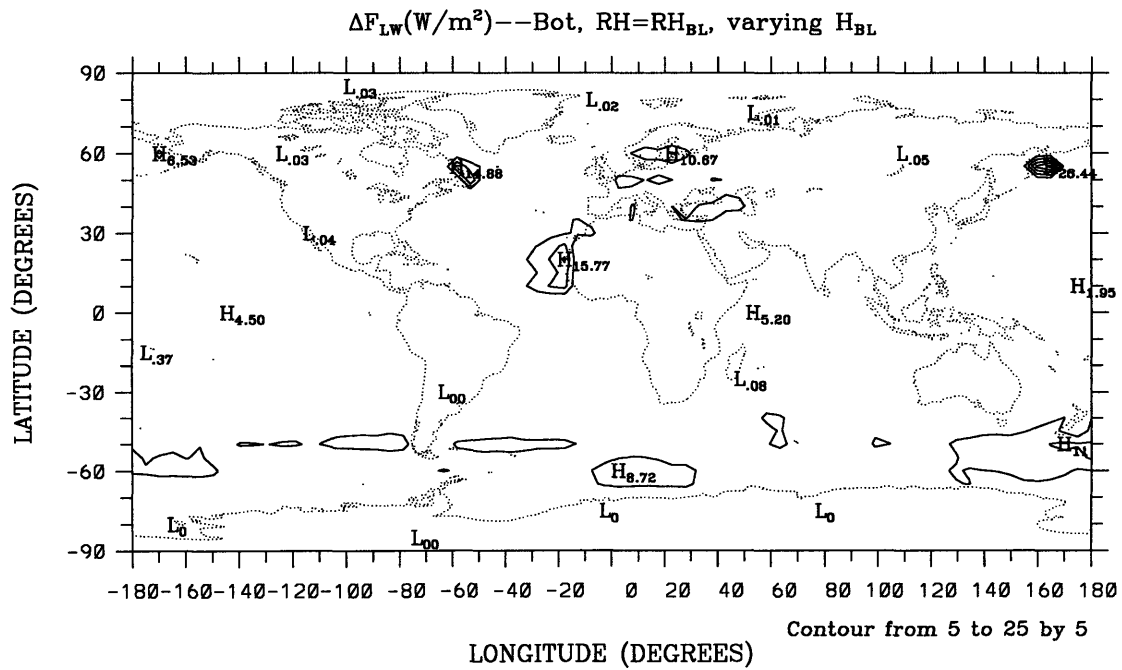
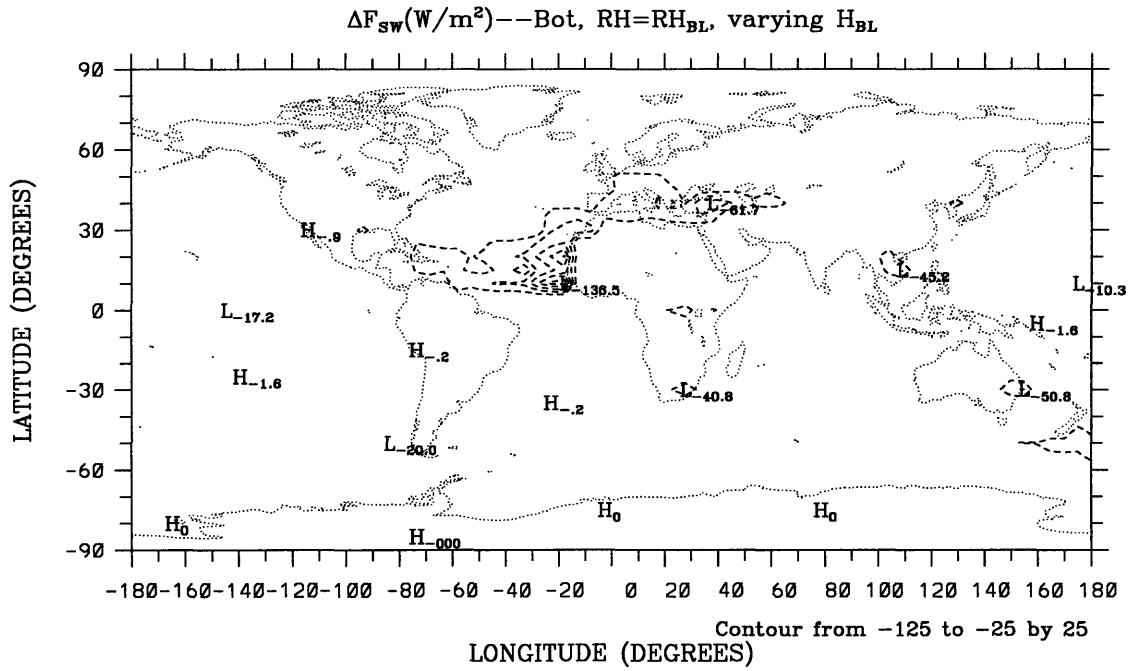


Figure 4-26: Radiative flux change at the surface in January using a varying boundary layer height and a relative humidity from Figure 4-6: top-short-wave; bottom-long-wave.

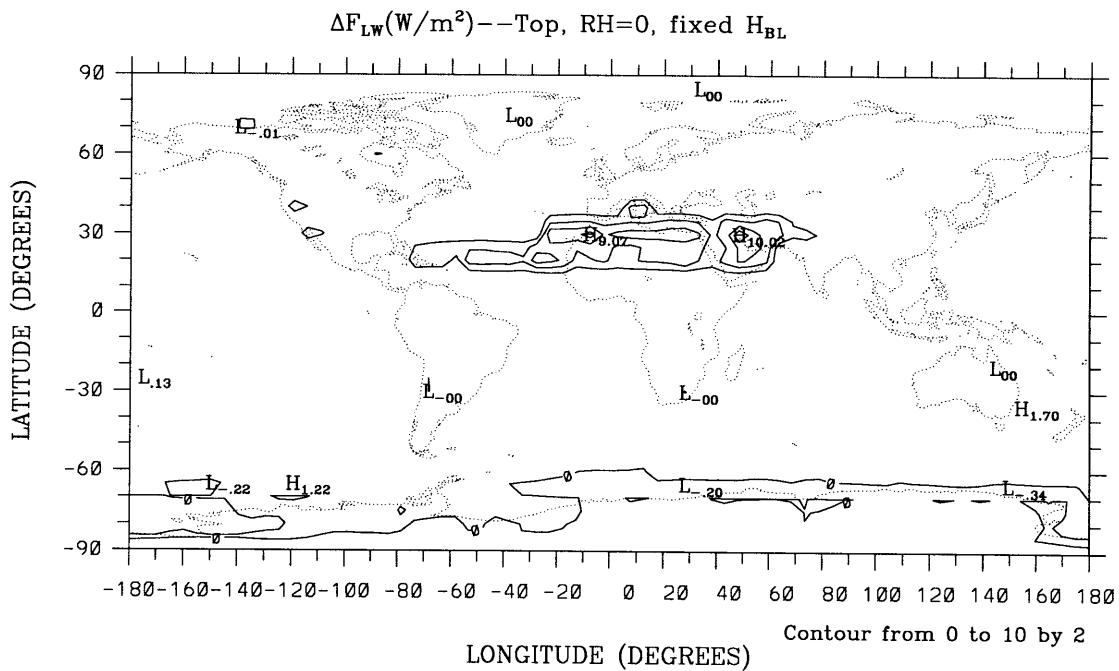
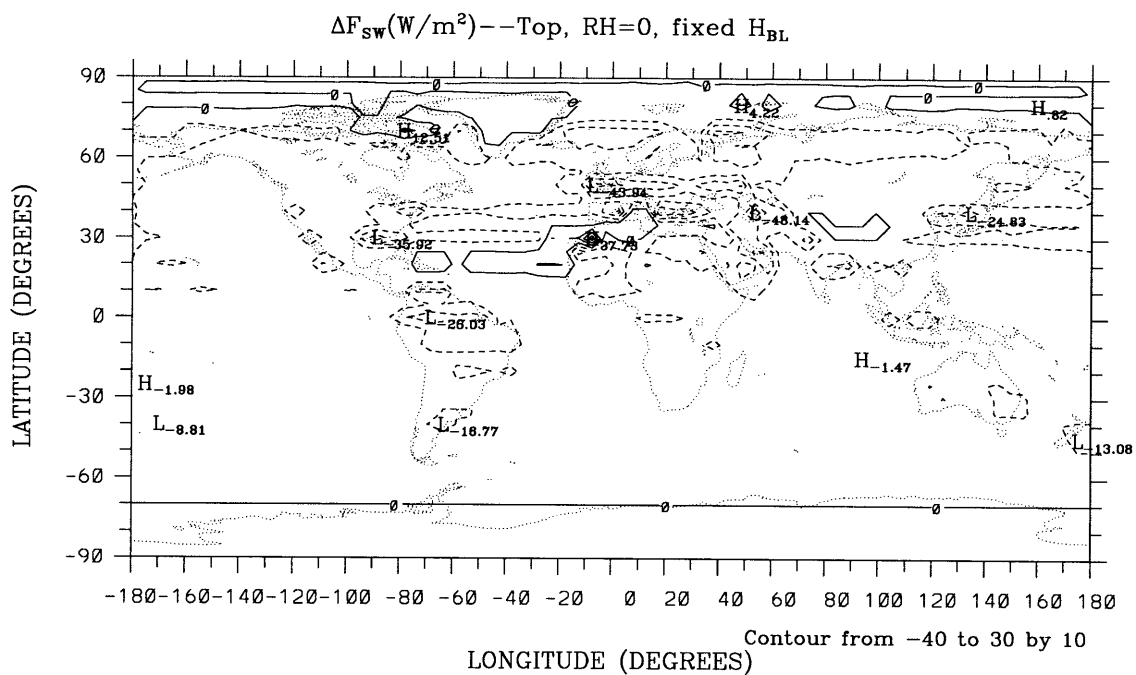


Figure 4-27: Radiative flux change at the top of the atmosphere in July using a hypothetical relative humidity and a fixed boundary layer height: top-short-wave; bottom-long-wave.

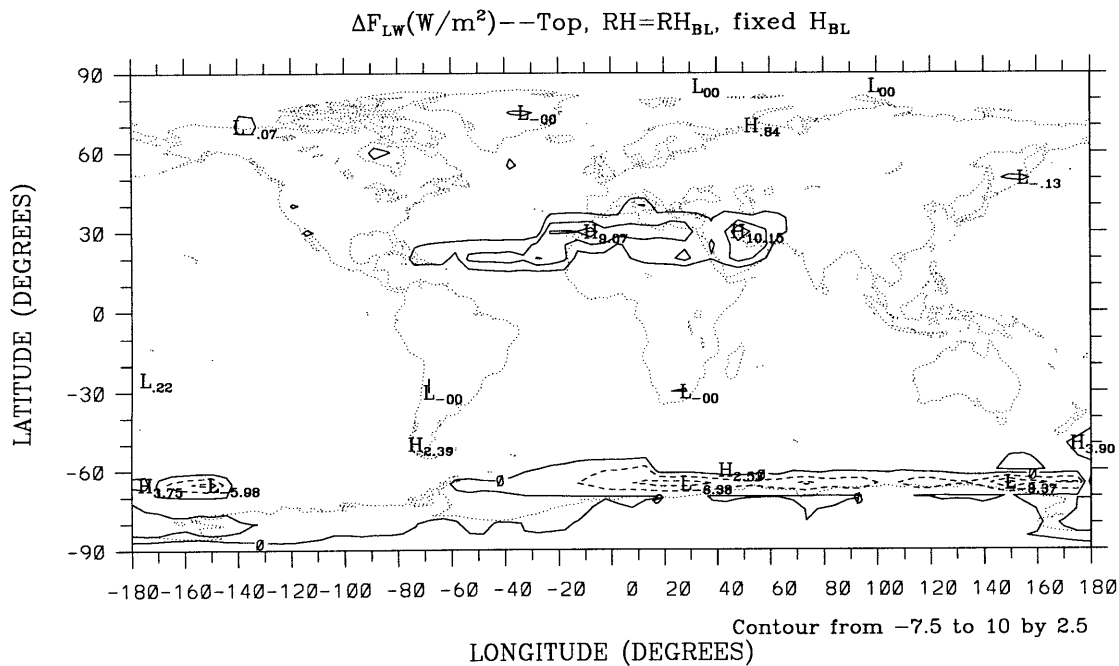
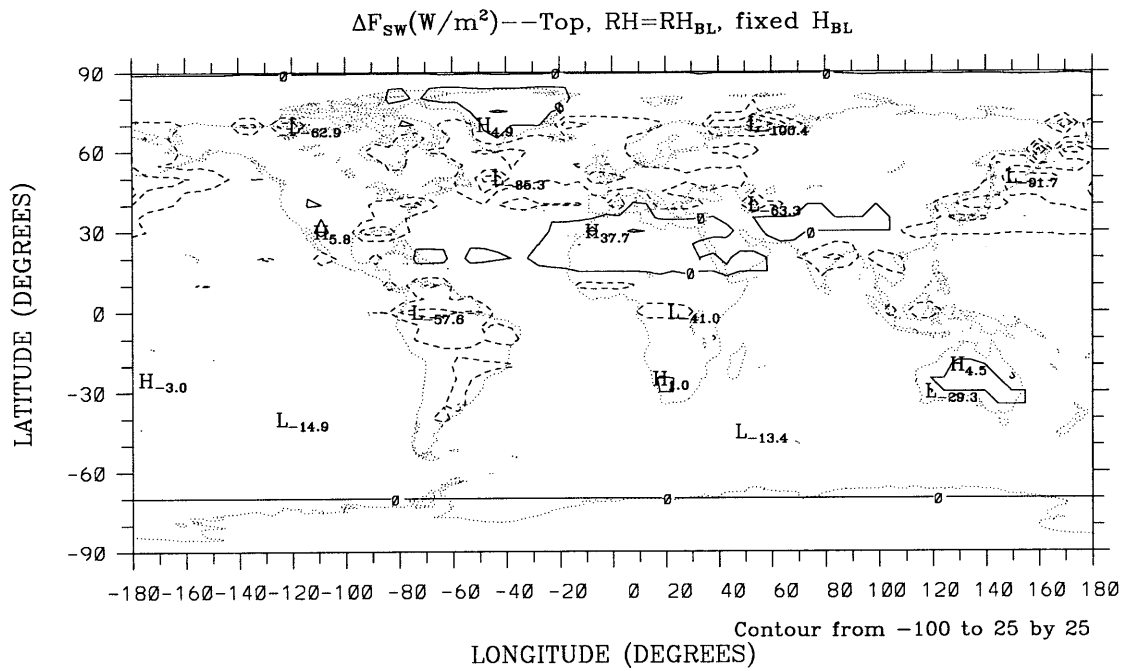


Figure 4-28: Radiative flux change at the top of the atmosphere in July using a fixed boundary layer height and a relative humidity from Figure 4-6: top—short-wave; bottom—long-wave.

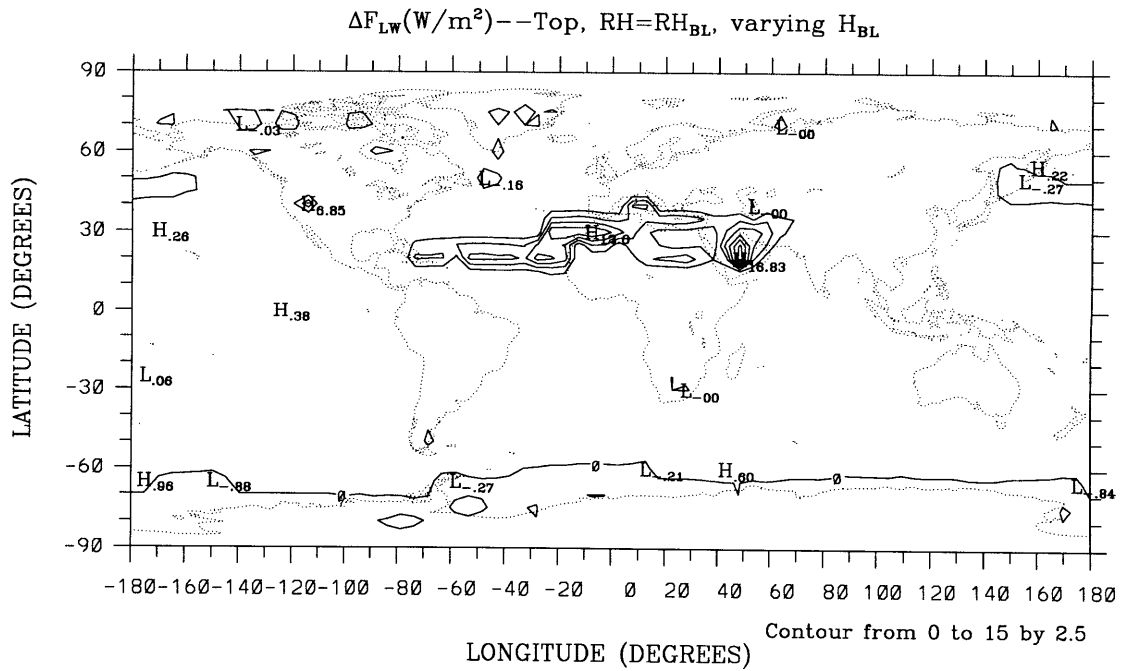
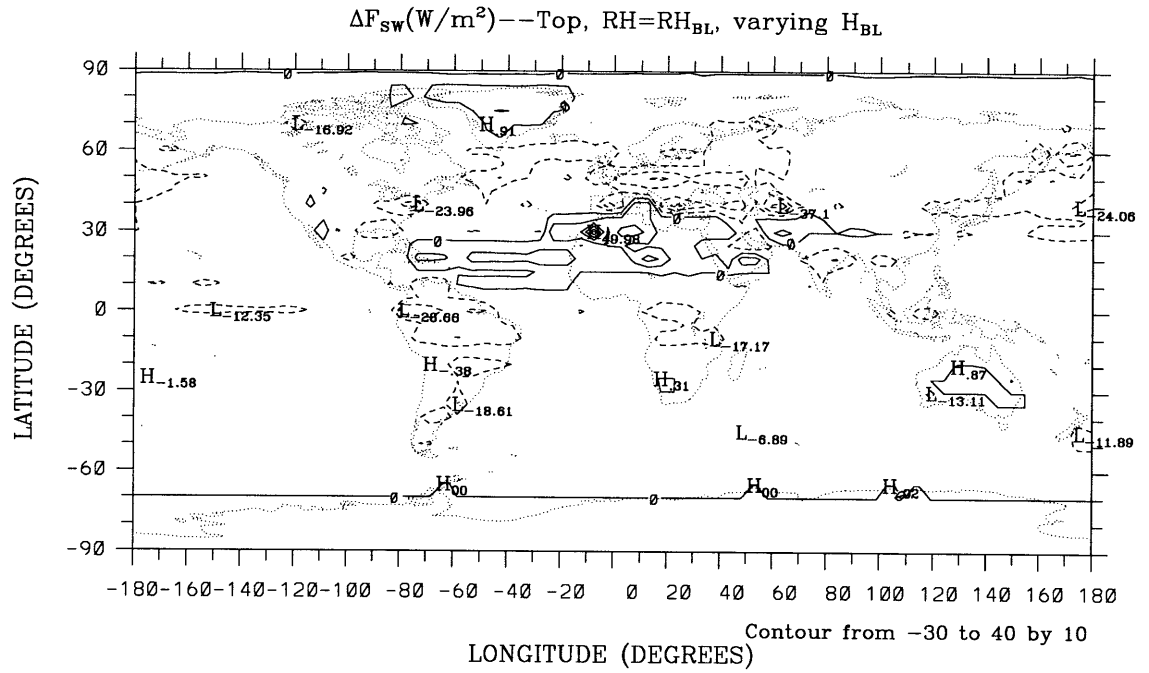


Figure 4-29: Radiative flux change at the top of the atmosphere in July using a varying boundary layer height and a relative humidity from Figure 4-6: top-short-wave; bottom-long-wave.

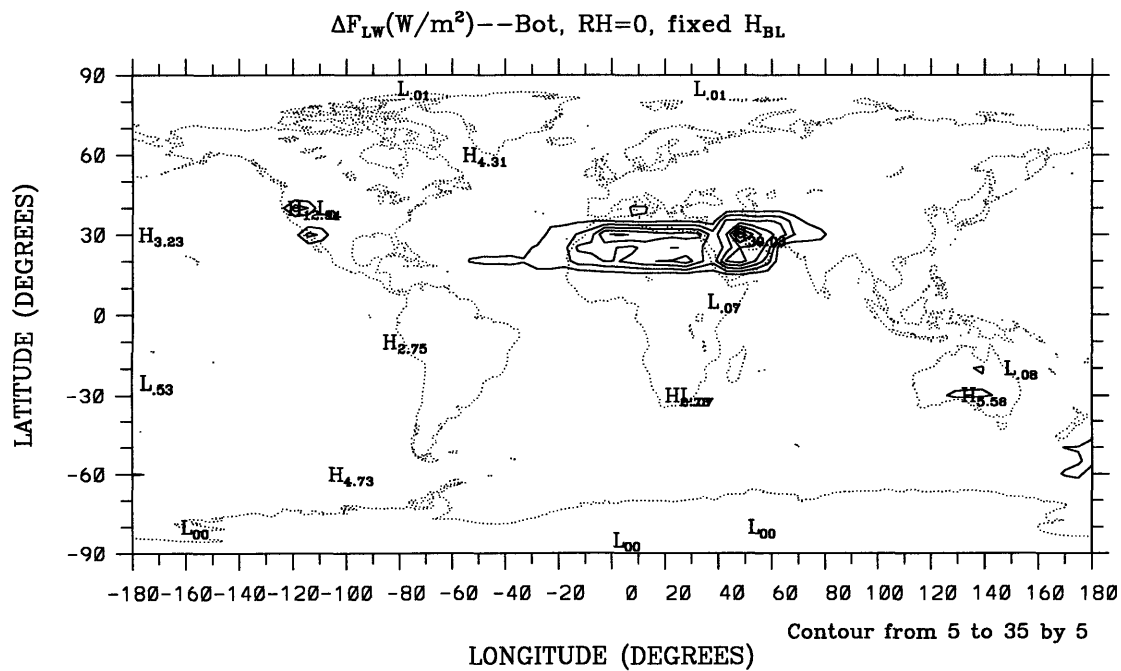
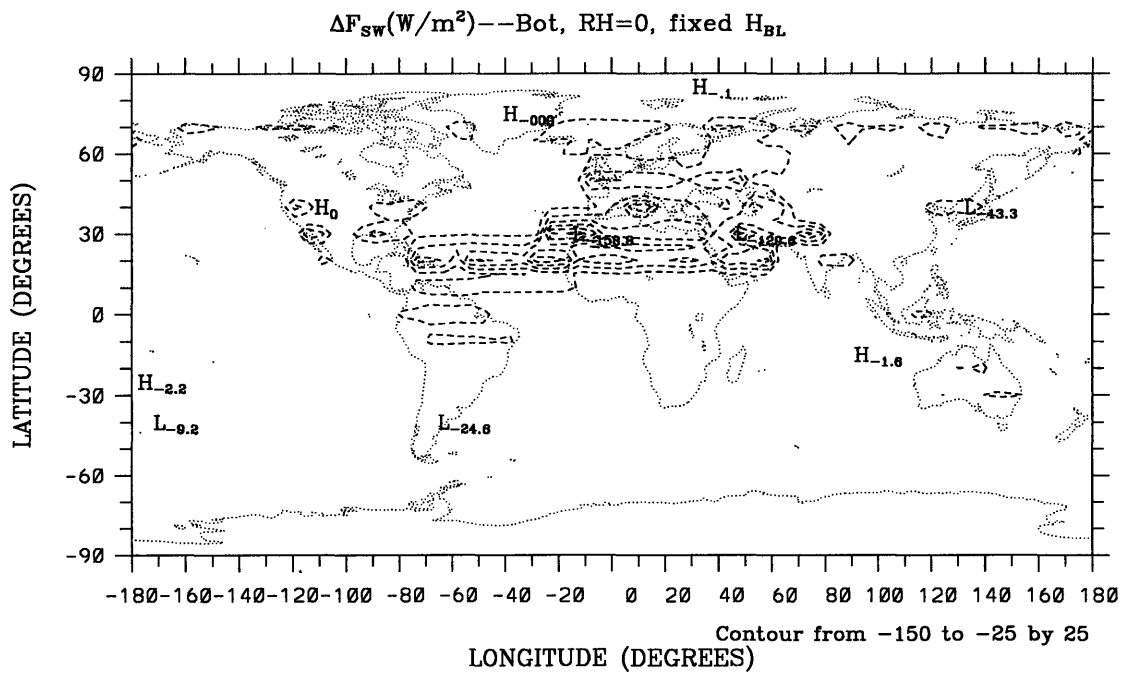


Figure 4-30: Radiative flux change at the surface in July using a hypothetical relative humidity and a fixed boundary layer height: top—short-wave; bottom—long-wave.

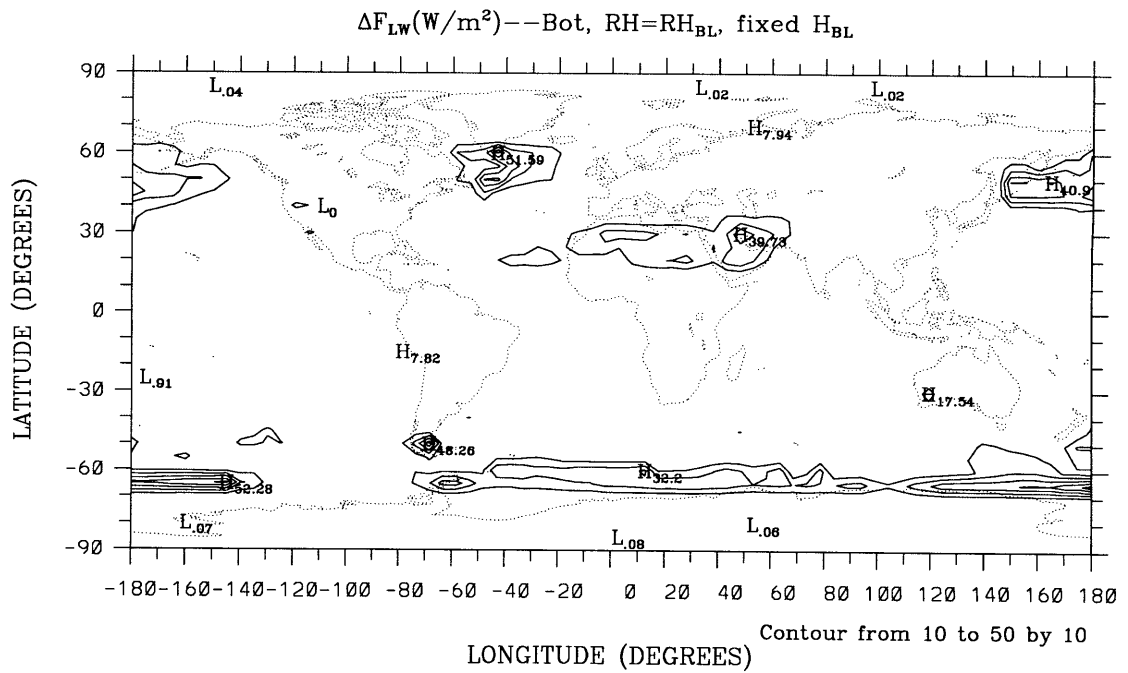
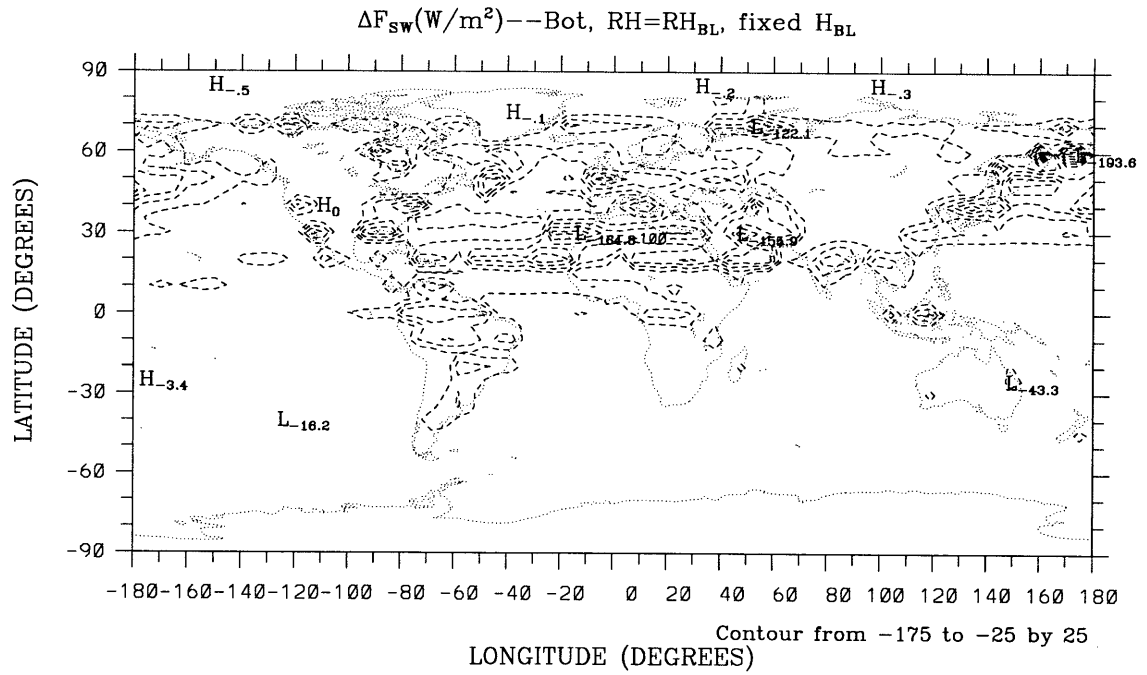


Figure 4-31: Radiative flux change at the surface in July using a fixed boundary layer height and a relative humidity from Figure 4-6: top-short-wave; bottom-long-wave.

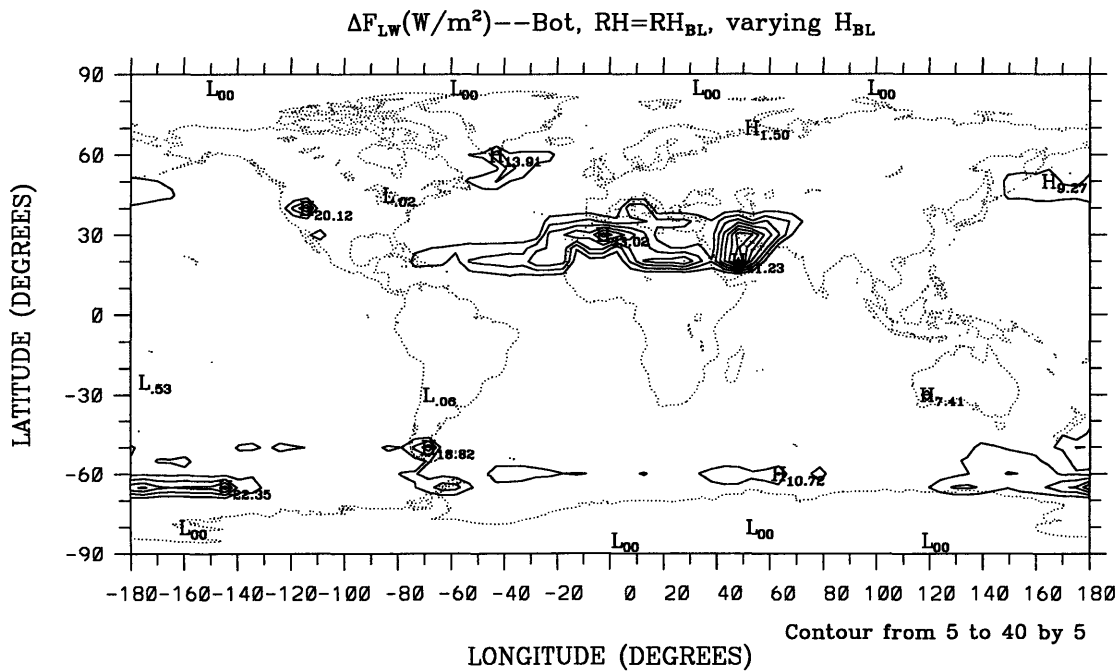
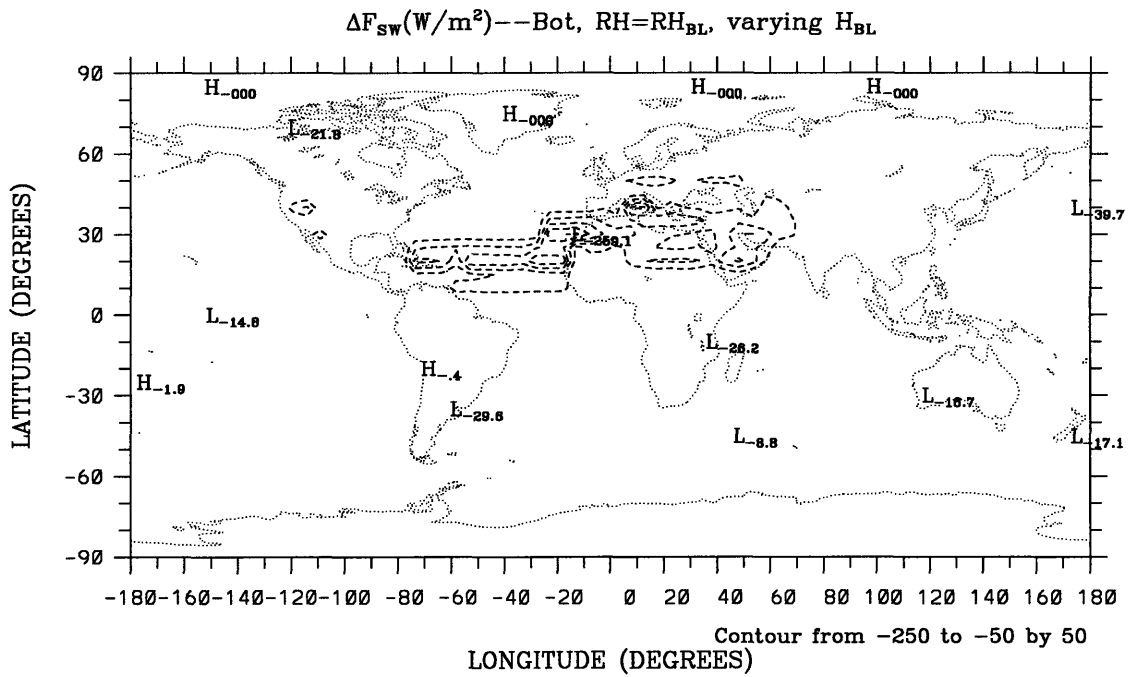


Figure 4-32: Radiative flux change at the surface in July using a varying boundary layer height and a relative humidity from Figure 4-6: top-short-wave; bottom-long-wave.

Chapter 5

Model Responses to Aerosol Radiative Forcing: 1. Radiative-convective Equilibrium

In the following chapters, three different models are used to study the aerosol radiative effects: a one-dimensional radiative-convective model (RCM), a mesoscale model, and a photochemical air quality model. The RCM addresses the magnitude and mechanism of aerosol effects in an equilibrium and global average sense. The mesoscale model simulation focuses on aerosol effects in a realistic urban-rural complex and the coupling strength between aerosol and meteorological processes. The photochemical model simulates the possible changes of spatial distributions of chemical species due to aerosol-induced changes in mesoscale meteorological fields.

5.1 Introduction

One-dimensional RCMs simulate the vertical distributions of atmospheric variables, such as temperature and water vapor mixing ratio, and surface variables in a horizontally averaged sense. They are good tools for studying the climate sensitivity to perturbations in radiative forcing and for assessing feedback processes (except of course feedbacks involving horizontal advection) in the atmosphere. In RCMs, parameterization of key physical processes (radiation, turbulence, convection, cloudiness) can be as comprehensive as in general circulation models (GCMs). And model response is highly dependent on the specific treatment of the key physical processes.

As reviewed by Ramanathan et al. [116], model responses induced by a doubled CO_2 concentration are extensively and thoroughly studied in 1-D RCMs. Key feedback processes (i.e., water vapor, lapse rate, surface albedo, and cloud) are identified, although the mechanism and magnitude of these feedback processes depend on how physical processes are handled in a specific model.

On the other hand, studies on aerosol effects in 1-D RCMs are extensive but far from conclusive [39]. Unlike trace gases which appear uniform over the globe due to their long lifetime, aerosol concentrations are highly variable in space and in time as a result of their shorter lifetime and regional sources. Since 1-D RCMs can only simulate atmospheric conditions in a horizontally averaged sense, they do not provide a quantitative estimate of aerosol effects in the atmosphere.

In addition, trace gases and aerosols affect the radiation budget in different ways. Namely, trace gases warm the surface by increasing the opacity of the atmosphere for long-wave radiation and thus reducing the outgoing long-wave radiation to space. Aerosols act similarly in the long-wave radiation range, but in the meantime they may either decrease or increase the radiative energy received by the planet system, depending on their optical properties and the underlying surface reflectivity, as discussed in Chapter 4.

Nevertheless, 1-D radiative-convective models can be used to investigate qualitatively the mechanism of how the climate system responds to an increase in atmospheric aerosols provided that they can account for the water vapor feedback in the atmosphere. A good candidate for such a model has been developed by Renno [119].

5.2 Model Description and Sensitivity

The Renno [119] model simplifies the equations for energy (Equation 2.5) and water vapor (Equation 2.7) as follows:

$$\frac{\partial \theta(t, p)}{\partial t} = C_T(t, p) + R_T(t, p) + F_T(t, p), \quad (5.1)$$

$$\frac{\partial q(t, p)}{\partial t} = C_q(t, p) + F_q(t, p), \quad (5.2)$$

where time t and pressure p are independent variables, while potential temperature θ and water vapor mixing ratio q are dependent variables. C_T and C_q represent the heat and moisture sources due to cumulus convection, which is dependent on the cumulus convection scheme. R_T stands for the net radiative heating and is computed using the scheme developed by Fu and Liou [51] as described in Chapter 4. F_T and F_q are vertical diffusion of temperature and moisture respectively, and are computed using the K -theory as

$$F_T = \rho^2 g^2 k_v \frac{\partial^2 \theta}{\partial p^2}, \quad (5.3)$$

$$F_q = \rho^2 g^2 k_v \frac{\partial^2 q}{\partial p^2}, \quad (5.4)$$

where k_v is the vertical diffusion coefficient, ρ is the air density, and g is the gravitational acceleration.

The model surface is assumed saturated with zero heat capacity and infinite moisture supply. Surface fluxes are computed with the bulk aerodynamic formulae,

$$SH = \rho c_p c_H |\vec{V}_a| (\theta_s - \theta_a), \quad (5.5)$$

$$LH = \rho L c_H |\vec{V}_a| (q_s(T_s) - q_a), \quad (5.6)$$

where SH and LH represent the sensible and latent heat fluxes, c_p is the specific heat capacity at constant pressure of dry air, \vec{V}_a is the wind at the anemometer level, c_H is the exchange coefficients for heat, and q_s is the saturated water vapor mixing ratio.

The chosen cumulus parameterization scheme is based on the dynamics and microphysics of convection as disclosed by recent detailed aircraft observations [46]. This scheme assumes that the fundamental entities in cumulus convection are the sub-cloud-scale drafts rather than the clouds themselves. Whenever the environment is unstable to a parcel in reversible

Table 5.1: Key parameters used in the 1-D RCM. ϵ_i are the precipitation efficiencies in Emanuel’s cumulus convection scheme.

model levels in the troposphere	NL_{trp}	16
model levels in the stratosphere	NL_{str}	10
time step for the integration(s)	Δt	900
short wave surface albedo	A_s	0.102
long-wave surface albedo	A_l	0
diurnally average solar constant(W/m^2)	S_0	680
cosine of tropical diurnally average solar zenith angle	$\cos z$	0.5
surface drag coefficient	c_H	0.025
wind speed at the anemometer level(ms^{-1})	$ \vec{V}_a $	5
vertical diffusion coefficient(m^2s^{-1})	k_v	2
fractional area covered by unsaturated downdraft	σ_d	0.01
fractional of precipitation falling outside of cloud	σ_s	0.15
critical draft thickness below which ϵ_i is zero(mb)	PB_{crit}	150
critical draft thickness above which ϵ_i is unity	PT_{crit}	500

adiabatic ascent from the surface, convection occurs. The convection-induced vertical transport is accomplished by saturated updrafts and downdrafts, a single unsaturated downdraft created by evaporation of the falling precipitation, and the compensating subsidence. A detailed description and evaluation of this scheme has been given in Emanuel [46].

The model was originally developed to study the sensitivity of climate equilibria to various cumulus convection schemes. In this work it is used to address the sensitivity of climate equilibria to the radiative forcing by various aerosol types.

Table 5.1 lists the key parameters used in this study. The model sensitivity is 0.43 K/(W/m²) for clear sky, which is obtained from perturbing the mean temperature by ± 0.5 K. It is compared with the the clear sky average of 0.47 ± 0.05 K/(W/m²) in the study of 19 GCMs by Cess et al. [20].

5.3 Model Responses to Aerosol Radiative Forcing

To study the model response to aerosol forcing, a so-called “clean continental” aerosol model is used. The aerosol model consists of two components, dust-like and water soluble, each with a log-normal size distribution (cf. Tables B.1 and B.2). The size distributions are shown in Figure B-3. The aerosols are assumed to be well-mixed in the lowest 2 km with a number density of 10^4 cm⁻³, a typical value for a clean continental situation [36]. Humidity effects are excluded.

The model has been run with or without aerosols using the parameters listed in Table 5.1 except for S_0 , which is tuned to give a tropical mean surface temperature of 300 K for the no aerosol case. The resulting vertical profiles of equilibrium temperature and water vapor mixing ratio are shown in Figure 5-1. Aerosol cools and dries the model atmosphere with the largest change of temperature in the upper troposphere and the largest change of water vapor mixing ratio in the lower troposphere.

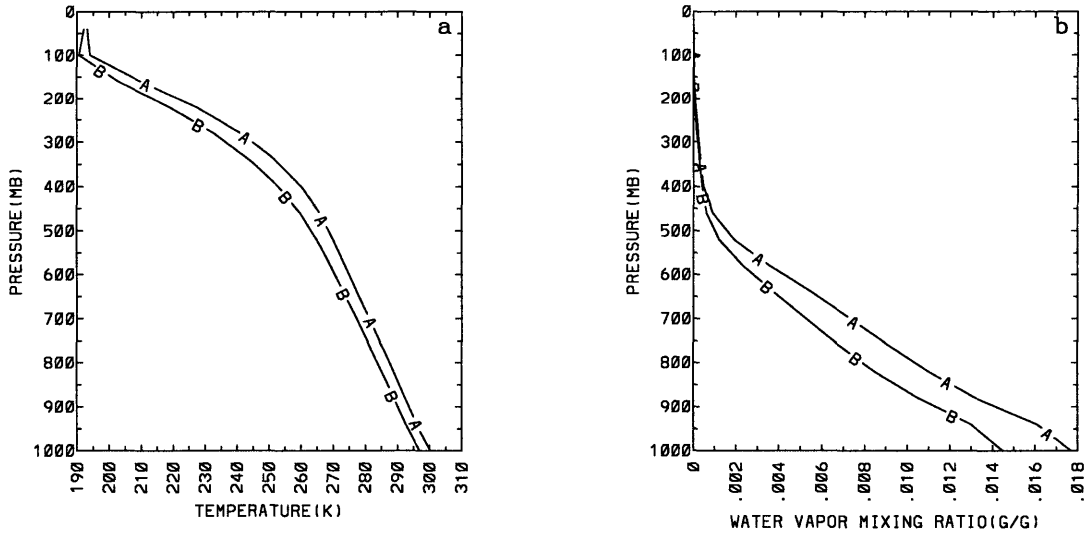


Figure 5-1: Vertical profiles of equilibrium variables without aerosols (A) and with aerosols (B): a. Temperature; b. Absolute humidity.

The vertical profiles of heating and moistening rates at equilibrium are shown in Figure 5-2. Although the aerosol initially perturbs only the short-wave heating in the lower boundary layer (cf. Figure 4-20), both upper air short-wave cooling and long-wave heating are observed at equilibrium due to the decrease of water vapor content in the model atmosphere. The combined cooling in the upper troposphere is compensated by the decrease of convective heating since the long-wave heating change dominates the short-wave cooling (cf. Figure 5-2a and b).

Table 5.2 summarizes the net flux change at the model tropopause and the temperature change at the surface for various aerosol types as discussed in Chapter 4 as well as the resulting model sensitivity to external forcing. The number density is chosen as in d’Almeida [36]. A doubled CO_2 concentration experiment is given for comparison. The change in the net radiative flux at the tropopause has been suggested by Ramanathan et al.[116] as a straightforward method to evaluate the climate change to external radiative forcing. It follows the fact that the vertical distribution of the tropospheric temperature change (therefore the surface temperature change) is largely determined by dynamical processes such as convective mixing of sensible and latent heat and large-scale motions. However, results in Table 5.2 imply the importance of the nature of the external forcing and the internal feedbacks. This will be discussed in detail in the following section.

5.4 Mechanism of Model Responses

The mechanism of model response to aerosol radiative forcing can be understood in Figure 5-5 where double arrows indicate the feedback between processes. Aerosols decrease the short-wave flux and increase the long-wave flux absorbed by the surface. In the meantime, they generate short-wave heating and long-wave cooling in the atmosphere. These changes can be viewed as the aerosol-induced external forcing (ΔR_{ext}) of the surface-atmospheric system. The short-wave forcing usually dominates the long-wave forcing. In addition, except for high

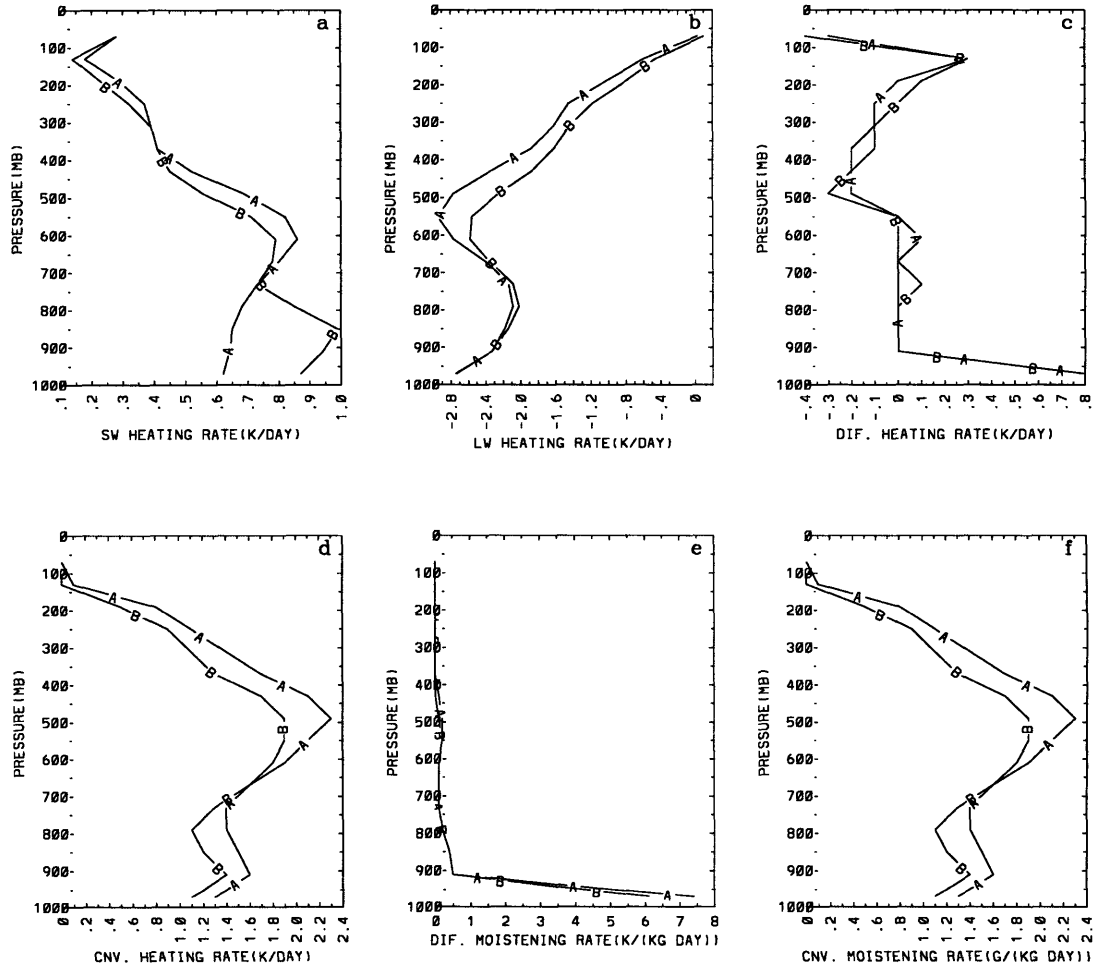


Figure 5-2: Vertical profiles of equilibrium heating rate without aerosols (A) and with aerosols (B): a: short-wave (SW) heating rate; b: long-wave (LW) heating rate; c: heating rate due to diffusion; d: heating rate due to convection; e: moistening rate due to diffusion; f: moistening rate due to convection.

Table 5.2: Net radiative flux change at model tropopause, and temperature change at surface at equilibrium as well as the resulting model sensitivity for various radiative forcing perturbation scenarios in the 1-d RCM, where a number density of 5 /cm³ for the mineral aerosols aloft is assumed for minerals above CM and MP.

Perturbation Experiments	Number Density (cm ⁻³)	ΔR_t (W/m ²)	ΔT_s (K)	$\frac{\Delta T_s}{\Delta R_t}$ (K/(W/m ²))
2× CO ₂	/	5.46	1.64	0.30
Sulfate	1500	-1.64	-0.54	0.33
Clean Continental	10000	-10.45	-3.34	0.33
Average Continental	„	-9.90	-3.14	0.32
Urban	„	-6.21	-1.50	0.24
Desert Winter	100	-3.87	-0.66	0.17
Desert Summer	„	-4.12	-0.54	0.13
Clean Maritime(CM)	1000	-12.50	-4.90	0.39
Polluted Maritime(PM)	10000	-4.93	-1.77	0.36
Mineral above CM	600	-7.49	-2.41	0.32
Mineral above PM	20000	-9.37	-3.06	0.33

absorptive aerosols or high reflective surfaces, aerosols lead to an initial decrease of surface temperature in the short-wave (cf. Figure 4-2). This decrease results in the reduction of upward long-wave radiation and surface heat fluxes and hence the cooling and drying of the atmosphere and the corresponding change of the downward long-wave radiation flux. Therefore the magnitude of the surface temperature decrease depends on not only the external radiative forcing but also the internal processes within the system, which include the surface latent, sensible, and ground heat fluxes and the downward long-wave radiative flux.

Mathematically, the surface temperature change satisfies

$$\frac{dT_s}{dt} = R(dn) - \sigma T_s^4 - LH - SH - GH, \quad (5.7)$$

where LH, SH, and GH are the latent, sensible, and ground heat flux, R(dn) is the downward radiation, including the downward long-wave flux and absorbed short-wave flux.

Therefore the transient response ΔT_s can be expressed in terms of the equilibrium response $(\Delta T_s)_{eq}$ and time scale C as follows,

$$\Delta T_s = (\Delta T_s)_{eq}(1 - e^{-\frac{t}{C}}), \quad (5.8)$$

$$(\Delta T_s)_{eq} = \frac{1}{4\sigma T_s^3} \frac{\Delta R_{ext}(dn)}{1 - (f_- + f_+)}, \quad (5.9)$$

$$C = \frac{\rho_s c_s \Delta Z}{4\sigma T_s^3 (1 - (f_- + f_+))}, \quad (5.10)$$

$$f_- = -\frac{1}{4\sigma T_s^3} \left(\frac{dLH}{dT_s} + \frac{dSH}{dT_s} + \frac{dGH}{dT_s} \right), \quad (5.11)$$

Table 5.3: Surface temperature and energy budget for clear sky and clean continental aerosol experiments.

Experiment	T_s (K)	T_a (K)	LH(W/m ²)	SH(W/m ²)	LW↓(W/m ²)
clear	300.19	297.69	163.14	-1.52	413.37
clean cont.	296.82	294.33	137.01	-1.29	382.29
difference	-3.38	-3.36	-26.13	0.23	-31.08

$$f_+ = \frac{1}{4\sigma T_s^3} \frac{\Delta R_{int}(dn)}{dT_a}, \quad (5.12)$$

where ρ_s , c_s , and ΔZ are surface density, heat capacity, and thickness, f_- and f_+ are feedback coefficients, accounting for the effect of surface and atmospheric temperature changes on surface heat fluxes and downward long-wave radiation (R_{int}).

The equilibrium temperature change depends on the delicate balance between the external forcing and internal feedbacks. On the other hand, the time scale, which characterizes how fast the temperature change approaches the equilibrium one, depends both the internal feedbacks and surface properties. The negative feedback, f_- , represents the process whereby any increase of surface temperature will cause more sensible and latent heat flux into the atmosphere and therefore stabilize the initial temperature increase and vice versa. The positive feedback, f_+ , states that any increase of surface temperature will cause warming and moistening of the atmosphere and therefore amplify the initial temperature perturbation by adding to the downward radiative flux to the surface and vice versa.

For example, the direct solar radiative forcing due to clean continental aerosol at the surface is about -18 W/m² and the IR radiative forcing is about 2 W/m². Therefore $\Delta R_{ext}(dn)$ is -16 W/m². Table 5.3 lists the surface temperature and energy budget for clear and clean continental aerosol cases. The difference shows the aerosol-induced effect. Using data in Table 5.3, one can deduce that the downward radiative flux due to internal processes, $\Delta R_i(dn)$, is about -30 W/m². Therefore the feedback factors, f_1 and f_2 , are -1.23 and 1.43 respectively.

Figure 5-3 shows the time series of $\Delta T_s/\Delta R_{ext}(dn)$, f_- , and f_+ for different aerosols with fixed absolute humidity. The magnitude of f_- decays with time and the initial value is about a factor of 4 to 5 larger than the equilibrium one, which is dependent on the nature of aerosol forcing. In the meantime, f_+ increases from zero to 0.8 at the equilibrium, with little dependence on the nature of aerosol forcing. As a result, the sensitivity of the surface temperature change to surface radiative forcing depends on the nature of aerosol forcing and increases by about a factor of 4 to 5 from the initial value to the equilibrium one. Similar results using different water vapor treatments under the low-level averaged-continental aerosol radiative forcing are shown in Figure 5-4. As one may expect, f_+ is highly dependent on different water vapor treatments.

Equation 5.8 implies that for a given magnitude of aerosol radiative forcing, the transient and equilibrium surface temperature changes are quite different, depending on the time scale C . For the 1-D RCM used here, this difference reaches up to about a factor of 4 to 5.

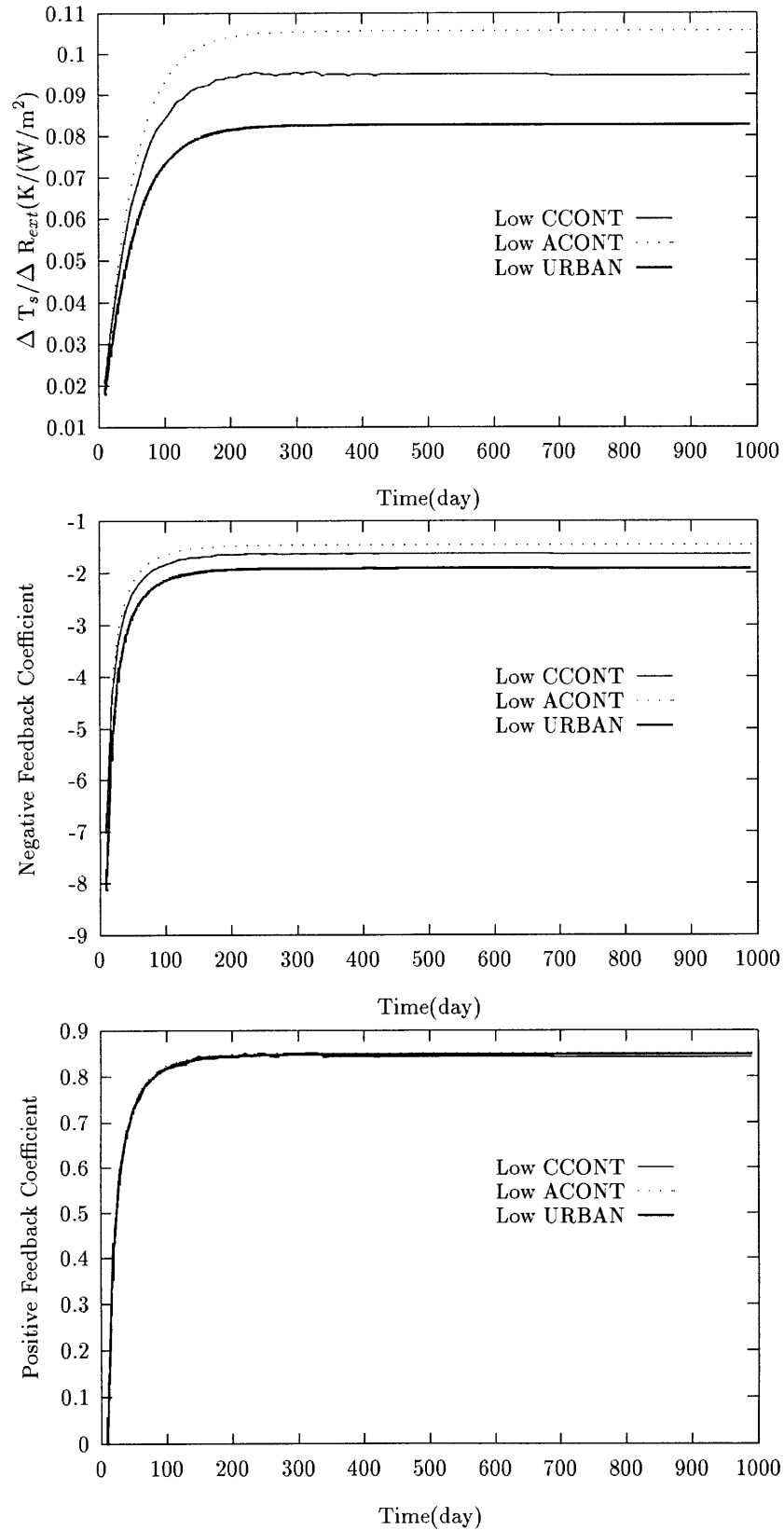


Figure 5-3: Time series of $\Delta T_s / \Delta R_{ext}(dn)$, f_- , and f_+ for different aerosols with fixed absolute humidity.

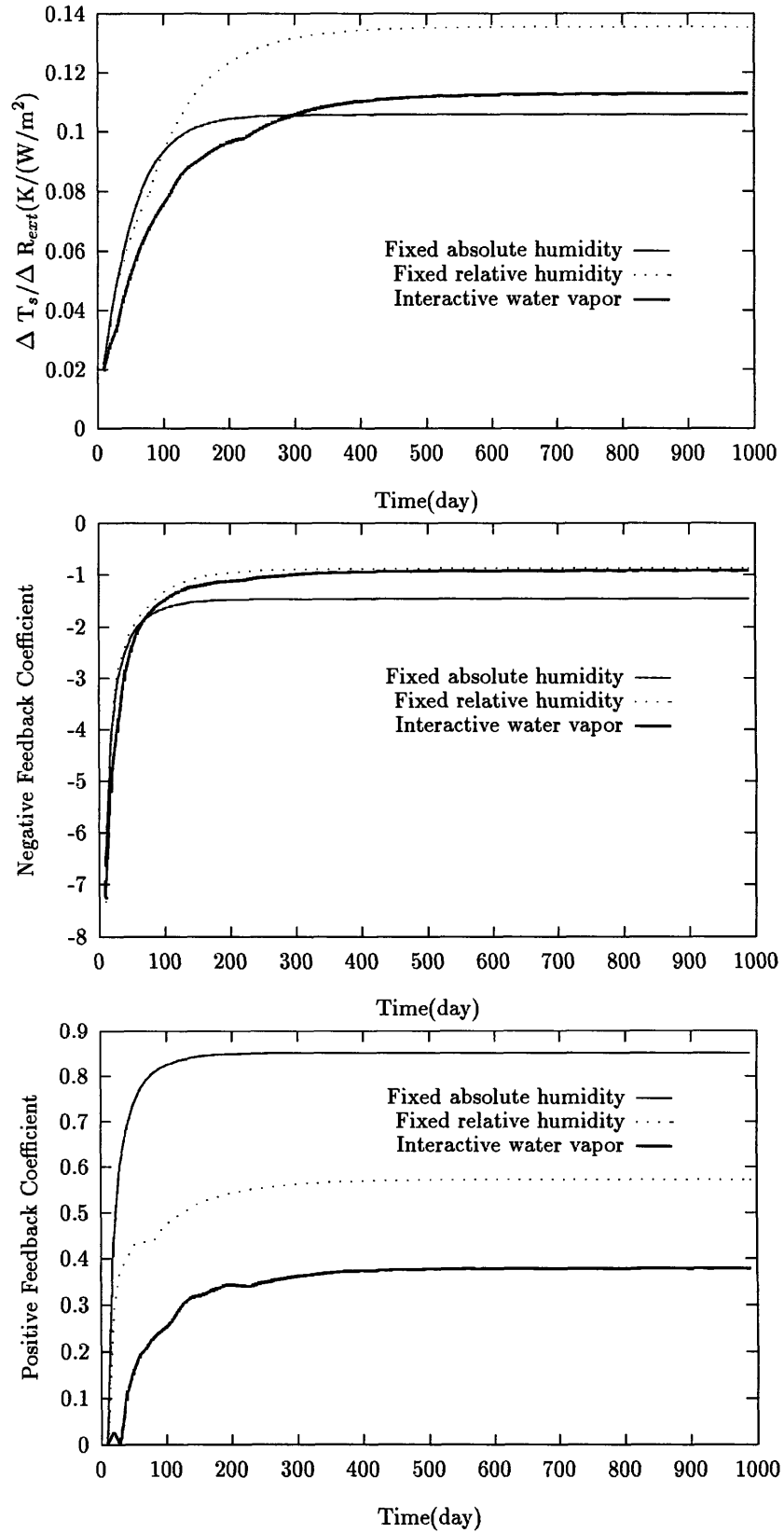


Figure 5-4: Time series of $\Delta T_s / \Delta R_{ext}(dn)$, f_- , and f_+ for different water vapor treatments with low-level averaged-continental aerosols.

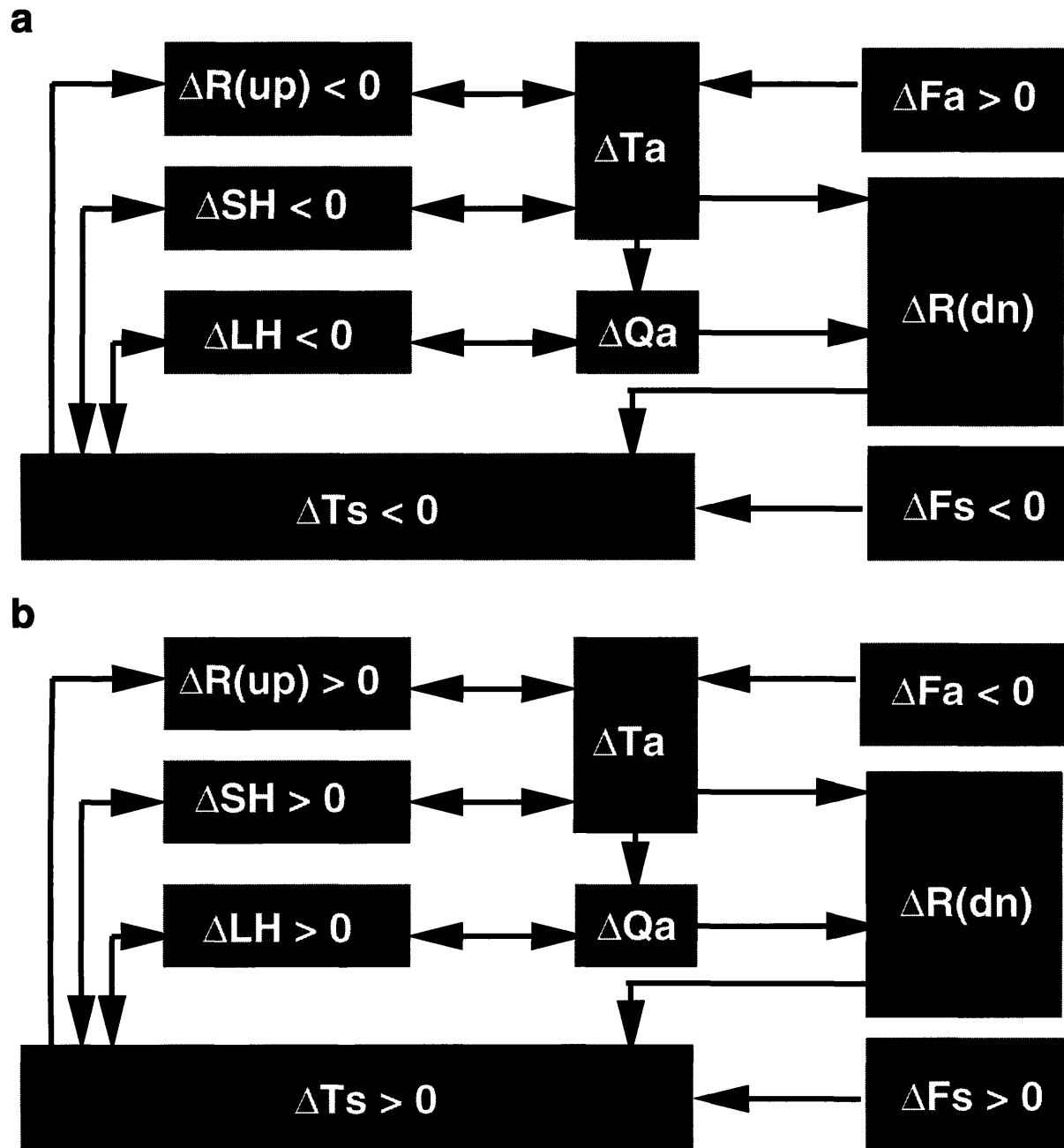


Figure 5-5: A schematic diagram showing how surface temperature change depends on both aerosol radiative forcing and internal processes in the model: a. short-wave; b. long-wave. Symbols are defined in the text.

5.5 Conclusions

A one-dimensional radiative-convective model has been used to simulate the aerosol radiative effect on climate equilibrium. Aerosols directly cause short-wave heating in the lower troposphere and indirectly cause long-wave heating in the upper troposphere as a result of the decrease of water vapor content in the atmosphere. In the new equilibrium the radiative perturbation is balanced by the decrease in the convective heating throughout the model atmosphere. The atmosphere under the new equilibrium is colder and drier than the control atmosphere.

The sensitivity of surface temperature change to radiative forcing at the model tropopause varies as different aerosol types are introduced into the model. The surface energy balance analysis shows that the temperature change depends not only on the external forcing but also on the internal feedbacks, which are solely represented by the model physics. A negative feedback is established between the changes of temperature and sensible and latent heat fluxes. The decrease in the surface temperature causes drying of the atmosphere and further reduces the initial temperature perturbation by decreasing the downward infrared flux to the surface. This represents a positive feedback between temperature and water vapor.

These feedbacks depend on external forcings and model formulations. The surface temperature response of the equilibrium is about a factor of 4 to 5 larger than that of the beginning.

Chapter 6

Model Responses to Aerosol Radiative Forcing: 2. Mesoscale Meteorology

The goal of this chapter is to investigate the sensitivity of mesoscale models to aerosol radiative forcing. As an initial and practical step, the climatological aerosol data described in Chapter 4 will be incorporated. Spatial variability is simulated through a simple dependence of aerosol types on land use properties. The range of the model response is evaluated using the lower and higher limits of aerosol burden in the atmosphere.

6.1 Model Description

The model used in this study is the latest version of the fully compressible and non-hydrostatic mesoscale model developed by the United Kingdom Meteorological Office (UKMO) [143, 19, 57]. It predicts wind, Exner pressure, liquid water potential temperature, and total water in a terrain-following Cartesian coordinate system. A staggered grid is used to minimize averaging in the divergence calculation. Horizontal wind components are on a “C” grid and vertical velocities are on mid-levels.

The linearized sound and gravity wave terms are treated implicitly with nonlinear terms integrated explicitly [143, 34]. The advection is formulated using a third-order semi-Lagrangian scheme [137]. The upstream departure point is located using the method described by McGregor [92]. A Hermite polynomial with optional monotone corrections to the derivatives is used for the interpolation according to Williamson and Rasch [165].

The model can be integrated using either fixed or time dependent boundaries. Two techniques are included to suppress resonant sound and gravity waves: (1) asymmetrically weighting the implicit scheme and, (2) imposing a Newtonian damping zone in the upper or the lateral boundaries.

The subgrid-scale physical processes are parameterized specifically for mesoscale simulation. Turbulent mixing is parameterized using a level 2.5 scheme [170]. The mean and turbulent quantities are truncated after second order with only the time rate of change of turbulent kinetic energy (TKE) retained. Cloud water and cloud fraction are diagnosed using the mean and variance of relative humidity together with the TKE and the saturation mixing ratio curve for water. Rain and ice are generated by microphysical interactions within the cloud [33] and are then advected separately.

For coarse resolution runs, the subgrid-scale deep convection scheme is based on that of Fritsch and Chappell [50]. Instability to convection is diagnosed every 15 minutes by lifting each grid volume which has a mean upward velocity and a cloud fraction of at least one-tenth. If it is unstable at the next layer, convection is parameterized using a one-dimensional entraining plume model for updraft and downdraft with the corresponding mass fluxes related to the cloud depth. Each cloud is advected with its mid-level wind and lasts for an hour.

A five band long wave radiation scheme [121] and a single band short wave scheme [136] are modified to incorporate the cloud fraction and the mixing ratios of cloud water and ice. At the surface, a two-layer soil model is coupled to the surface heat budget. The fluxes of sensible heat (SH), latent heat (LH) and momentum (τ) into the atmosphere are computed using the drag law expressions:

$$SH = \rho c_p c_H(z_0, R_i) |\vec{V}_{10}| (T_s - T_{10}), \quad (6.1)$$

$$LH = \rho L c_H(z_0, R_i) |\vec{V}_{10}| (q_s - q_{10}), \quad (6.2)$$

$$\vec{\tau} = \rho c_M |\vec{V}_{10}| \vec{V}_{10}, \quad (6.3)$$

where ρ and c_p are the density and specific heat capacity at constant pressure of dry air, L is the latent heat of evaporation of water, \vec{V}_{10} , T_{10} and q_{10} are horizontal wind, temperature and specific humidity at the first level (10m), T_s and q_s are surface temperature and specific humidity, and c_M and c_H are the drag coefficients for momentum and heat, which are pre-computed from Monin-Obukhov similarity theory as a function of roughness length¹ (z_0) and Richardson number (R_i). The Richardson number is computed as

$$R_i = \frac{z_{10} g}{|\vec{V}_{10}|} \left(\frac{\theta_{10} - \theta_s}{\theta_{10}} + \frac{q_{10} - q_s}{q_{10} + 0.61} \right), \quad (6.4)$$

where g and θ are gravitational constant and potential temperature respectively.

In computing the latent heat flux, since q_s is unknown, it is eliminated using the specified surface resistance to evaporation (r_s) [100]:

$$LH = \frac{\rho (q_*(T_s) - q_s)}{r_s}, \quad (6.5)$$

where $q_*(T_s)$ is the saturated specific humidity at surface temperature of T_s . Combining Equations 6.2 and 6.5, one can obtain

$$LH = \frac{\rho L c_H(z_0, R_i) |\vec{V}_{10}| (q_*(T_s) - q_{10})}{1 + L c_H(z_0, R_i) |\vec{V}_{10}| r_s}. \quad (6.6)$$

The ground flux, GH , is obtained from the diffusion equation:

$$GH = \rho_g c_g \sqrt{K} \left(h_1 \frac{\partial T_g}{\partial t} + h_2 \frac{\partial T_s}{\partial t} \right), \quad (6.7)$$

$$h_2 \frac{\partial T_g}{\partial t} = \lambda (T_s - T_g), \quad (6.8)$$

where ρ_g , c_g , and K are the density (kg/m^3), specific heat capacity ($Jkg^{-1}K^{-1}$), and

¹The surface roughness height is defined as the height of the momentum sink above the surface.

thermal diffusivity (m^2s^{-1}) of the soil, and h_1 , h_2 , and λ are empirical constants. The multiplicative constant $\rho_g c_g \sqrt{K}$ is also called the thermal contact coefficient², β ($Jm^{-2}Ks^{-1/2}$).

The model can be initialized from either a single sounding or gridded analysis. In the first approach, the pressure field is obtained from the observed pressure and wind using the geostrophic balance. Horizontal wind fields are set the same as the sounding. Vertical wind is set to zero. These variables are then interpolated to the model levels. The temperature fields are computed from the hydrostatic balance. A fixed boundary condition is applied in this approach.

In the second approach, the variables on the coarse resolution grid are interpolated onto the fine resolution grid. Pressures are constructed from temperatures and hydrostatic balance. Horizontal wind fields are adjusted to be non-divergent. This approach is usually applied with time varying lateral boundary conditions.

6.2 Model Sensitivity and Validation

The model is applied to the Southern California Air Quality Study (SCAQS) region³. It is set up on a Universal Transverse Mercator (UTM) projection plane of 80×30 with horizontal resolution of 5 km. The vertical levels above the topography are assigned as

$$\eta_k = \eta_{k-1} + (k - 1) * 100$$

with $\eta_1=10$ m and $k=1,2,3,\dots,18$.

Figure 6-1 shows both the contour plot and the 3-D surface plot of the topography of the SCAQS region on the UTM projection plane. Retrieved from the Defense Mapping Agency's 1:1,000,000-scale Digital Chart of the World (DCW) contour and hydrology data, the topographic data are archived at the Data Support Section (DSS) of the National Center for Atmospheric Research (NCAR). The SCAQS topography is a complex one, including the coastal ocean, several islands, urban regions, a lake area, and high mountains with peaks around 2500 m. Also, a large gradient of elevation is seen in several parts of the region.

Thirty-two land use categories are recognized in the region as in Table 9.1 of McRae et al.[94]. Surface characteristic parameters of roughness height, resistance to evaporation, albedo, and thermal contact coefficient are assigned accordingly in Table 6.2 [7].

According to the SCAQS land use categories, four aerosol types, defined in d'Almeida et al. [36], are resolved: clean continental (CCONT), average continental (ACONT), urban (URBAN), and clean maritime (CLMAR). Their optical properties have been discussed in Section B and are listed in Table 6.2 at two selected wavelengths. The ranges of the extinction coefficient correspond to the variability in aerosol number concentrations, which are assumed well-mixed in the boundary layer for CCONT, ACONT and URBAN aerosol types and decays exponentially from the surface with a scale height of 1 km for CLMAR aerosol type. The sulfate aerosol is used in the single-column simulations in the next section.

Given the grid area percentage (f_i) covered by each land use category [94], the grid cell

²The thermal contact coefficient β determines the strength of ground heat flux and is a function of surface soil type. The typical value of β varies from 900-1500 $Jm^{-2}Ks^{-1/2}$ [160].

³The 1987 SCAQS is the largest air quality study conducted in California and consisted of 11 intensive sampling days in the summer and six intensive sampling days in the fall, with five sampling periods per day. It has since developed and archived a comprehensive air quality and meteorological data base for the Los Angeles basin and its surrounding areas

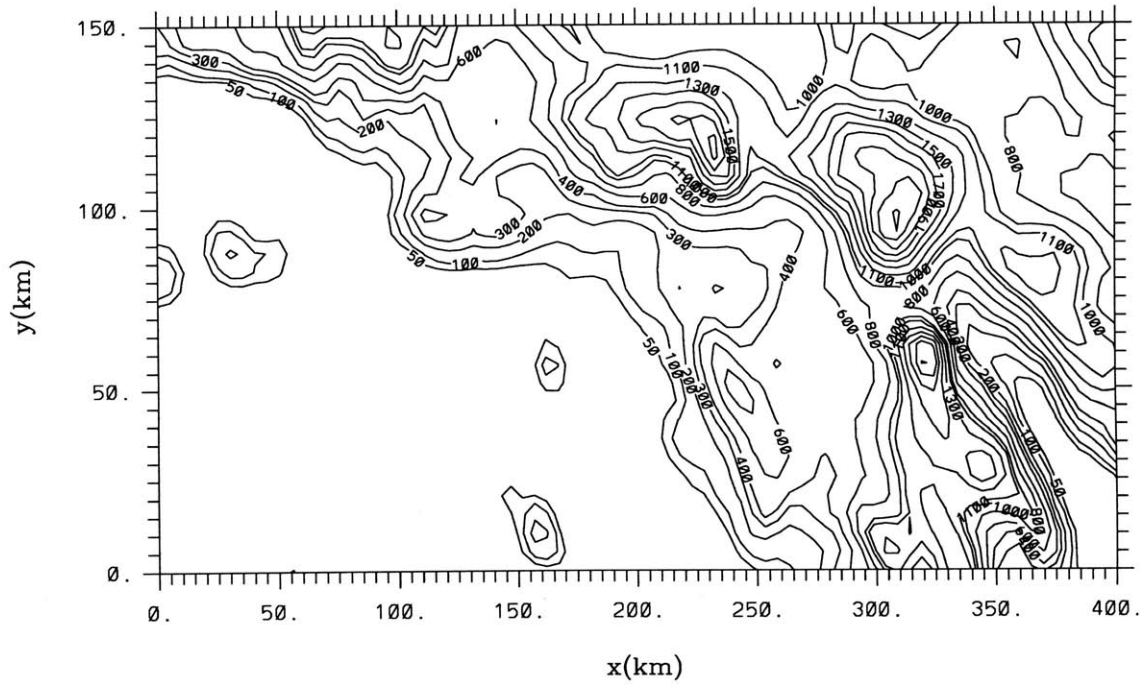
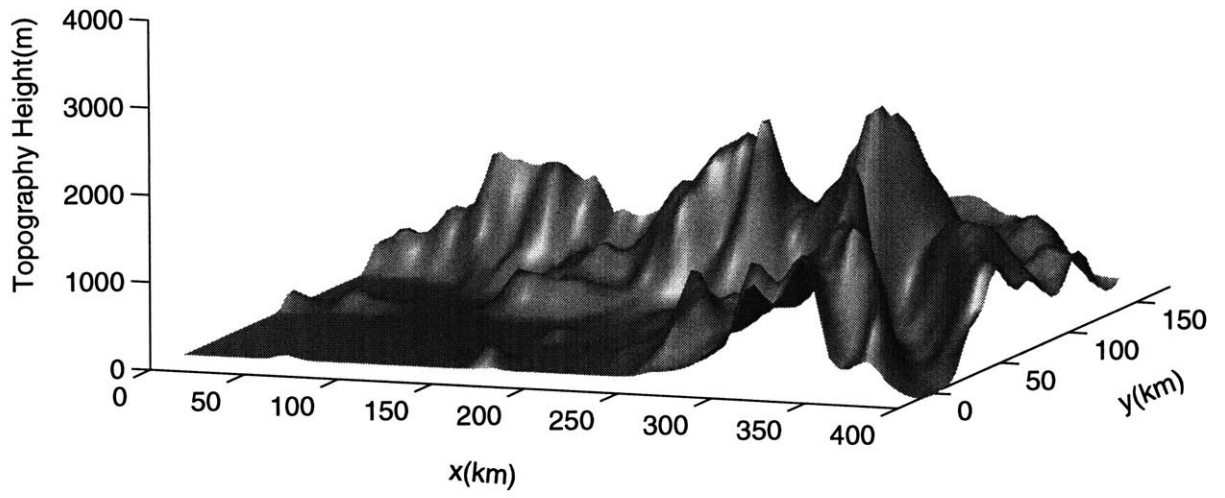


Figure 6-1: Topography height of the SCAQS region on the UTM projection plane.

Table 6.1: Land use categories and their corresponding surface roughness $z_0(\text{m})$, albedo α , resistance to evaporation $r_s(\text{m}^{-1})$, soil thermal contact coefficient $\beta(\text{Jm}^{-2}\text{Ks}^{-1/2})$, and aerosol type.

No.	Land use category	z_0	α	r_s	β	Aerosol type
1	Highrise urban	5	0.15	500	3000	URBAN
2	Residential	2	0.18	500	2500	URBAN
3	Commercial/services	3	0.18	500	3000	URBAN
4	Industrial	3	0.12	500	3000	URBAN
5	Transport/communications utilities	0.3	0.12	500	2500	URBAN
6	Industrial/commercial complexes	3	0.15	500	3000	URBAN
7	Mixed urban/built up land	2.5	0.16	500	2500	URBAN
8	Other urban/built up land	2.5	0.16	500	2500	URBAN
9	Cropland/pasture	0.1	0.20	100	900	ACONT
10	Orchards/groves/vineyards	0.45	0.18	75	900	ACONT
11	Confined feeding operations	0.3	0.20	100	900	ACONT
12	Other agricultural land	0.1	0.20	100	900	ACONT
13	Herbaceous rangeland	0.1	0.20	75	900	ACONT
14	Shrub/brush rangeland	0.25	0.20	75	900	ACONT
15	Mixed rangeland	0.25	0.20	75	900	ACONT
16	Deciduous forest land	1	0.17	50	900	CCONT
17	Evergreen forest land	1	0.14	50	900	CCONT
18	Mixed forest land	1	0.15	50	900	CCONT
19	Ocean	0.0001	0.06	0	1600	CLMAR
20	Streams/canals	0.002	0.06	0	1600	CCONT
21	Lakes	0.0001	0.06	0	1600	CCONT
22	Reservoirs	0.0001	0.06	0	1600	CCONT
23	Bays/estuaries	0.0001	0.06	0	1600	CCONT
24	Forested wetlands	1	0.15	50	1200	CCONT
25	Non-forested wetlands	0.15	0.1	25	1200	ACONT
26	Dry salt flats	0.00004	0.3	100	1200	ACONT
27	Beaches	0.0004	0.25	250	2500	ACONT
28	Sandy areas other than beaches	0.0004	0.3	250	2000	ACONT
29	Bare exposed rock	0.1	0.2	250	2400	ACONT
30	Strip mines/quarries/gravel pits	0.1	0.15	250	2000	ACONT
31	Transitional areas	0.002	0.2	250	2000	ACONT
32	Mixed barren land	0.002	0.2	250	2000	ACONT

Table 6.2: Variability range of aerosol optical properties of different dry aerosol types at two selected wavelength.

Aerosol Types	0.5 μm			10.0 μm		
	$\sigma_e(\text{km}^{-1})$	$\tilde{\omega}$	g	$\sigma_e(\text{km}^{-1})$	$\tilde{\omega}$	g
Clean Continental	0.0193-0.283	0.952	0.654	0.00503-0.0193	0.503	0.645
Average Continental	0.270-0.362	0.966	0.644	0.00352-0.00477	0.15	0.394
Urban	0.204-0.873	0.941	0.642	0.00256-0.0110	0.094	0.229
Clean Maritime	0.103-0.145	1.000	0.794	0.0782-0.109	0.737	0.861
Sulfate	0.039	1.000	0.699	0.0022	0.0175	0.0793

average of surface roughness height over land is computed as [94]:

$$z_0 = \exp \left(\sum_{i=1}^{32} f_i \ln(z_{0,i}) \right). \quad (6.9)$$

Over the ocean surface, the wind speed dependent formula of Charnock (1955) [25] is actually used in the model:

$$z_0 = k |\vec{V}_{10}|^2 / g \quad (6.10)$$

with $k = 0.0185$ [169].

The grid cell averages of other surface parameters (i.e., surface resistance to evaporation, surface albedo, and soil thermal contact coefficient) are arithmetic summations of surface parameters of different land use categories, weighted by their grid area percentage. The grid cell average of aerosol types are assigned to the land use category which has the largest grid area percentage.

In the single sounding initialization, a sounding from the SCAQS measurement at El Monte-9528 Telstar (EMUA) is used. Since it only extends to the top of boundary layer as most of the SCAQS soundings do, a complete profile is obtained by adding an appropriate vertical profile from the ECMWF analysis on top of the observed one.

In the full field initialization, the initial and boundary data (u , v , w , T , and RH) are taken from the European Center for Medium-Range Weather Forecast (ECMWF) global analyses (twice a day in spherical harmonic representation), which are also archived at DSS of NCAR. The data are first converted to a 320×160 grid on 14 pressure levels with about 1.125 degree in longitude and 160 Gaussian latitudes and then interpolated to the fine resolution UTM grid and vertical η -levels. A corresponding shell script is provided in Appendix C. Figure 6-2 shows some meteorological fields from the ECMWF global analysis on the SCAQS UTM projection plane at 06 GMT of August 27, 1987.

To validate the model performance and determine its sensitivity to key parameters and initial conditions, the SCAQS hourly averaged observations of surface temperature and wind of August 27 are used, although more meteorological fields are available [84]. Figures 6-3 and 6-4 show the observations for surface temperature and wind at two specific times during the day. Diurnal variation of surface temperature ranges up to 10°C . A sea-breeze

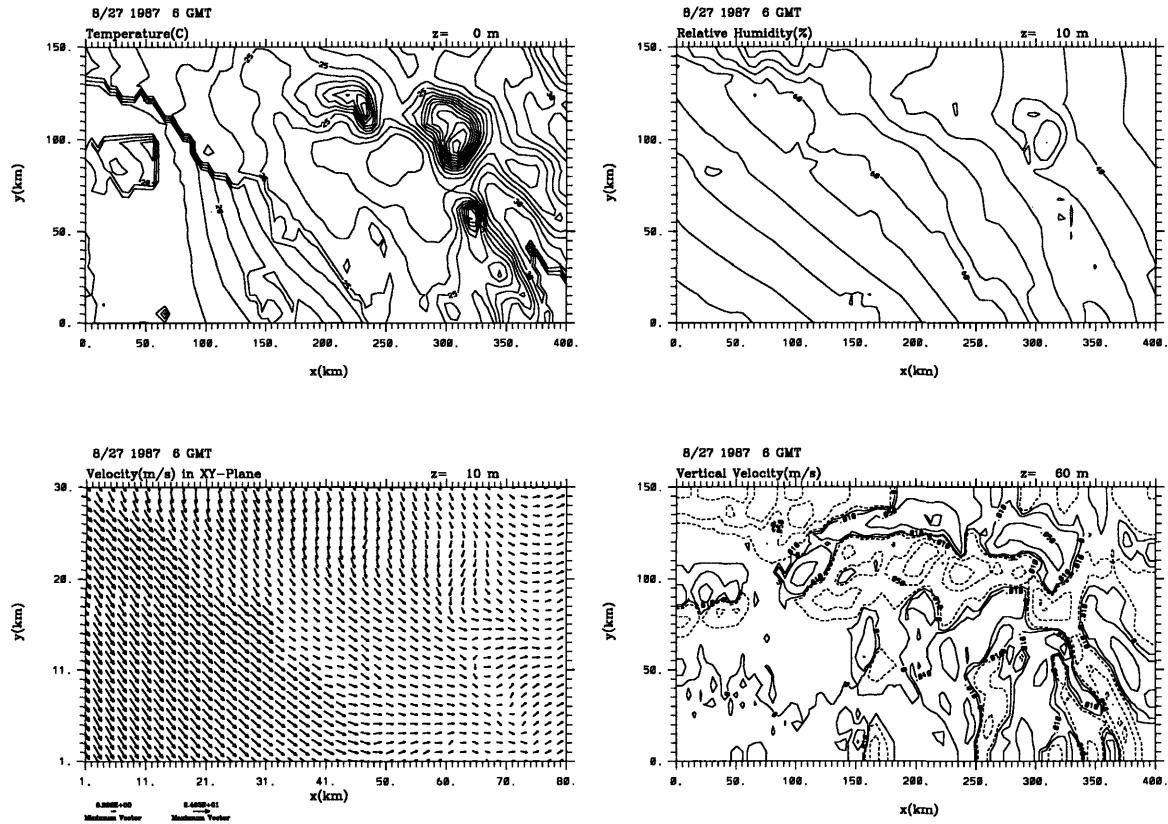


Figure 6-2: The analyzed meteorological fields from ECMWF on the SCAQS UTM projection plane at 06 GMT of August 27, 1987.

is well-established in the early afternoon.

Simulations have been carried out with a time step of 1 min to keep the maximum Courant number less than 0.5. The computational time required for 1 day simulation is about 4 hours on a SGI Indigo2 and half an hour on a Cray C-90.

Sensitivity tests to various surface parameters have been performed using the ECMWF analysis at 32 GMT of August 26, 1987 as the initial condition.

Figure 6-5 shows the mean and root mean square (RMS) errors of the resulting surface temperature. Doubling surface albedo decreases surface temperature by 1 to 2°C, with a larger temperature drop during the day and a smaller temperature drop during the evening, which is a result of the decrease in the incoming solar radiation. Doubling the thermal contact coefficient increases night-time surface temperature and decreases day-time surface temperature by 1 to 2°C. Since the soil layer acts as a heat capacitor, storing heat during the day and releasing heat during the evening, an increase in the thermal contact coefficient leads to more heat loss from the surface during the day and more heat transfer to the surface during the evening. The model tends to over-predict the surface temperature by about 3 ± 6 °C using the ECMWF analysis. The reason for this overprediction will be discussed later in this section.

The mean and root mean square (RMS) errors of the wind speed and direction at the first level (10 m) are shown in Figure 6-6 and 6-7. Wind speed is less sensitive to surface parameter changes than wind direction. Doubling thermal contact coefficient has profound effect on the simulated wind direction. For both wind speed and wind direction, minimum errors occur during the early afternoon, when the differential heating maximizes resulting in a well-established sea breeze circulation. The reason for this trend may relate to the fact that mesoscale models are usually formulated to predict the deviation on a synoptic average. Therefore, they tend to be more reliable when the mesoscale forcing is large and less reliable when the forcing is small.

The mean and root mean square (RMS) errors of simulated surface temperature and the first level wind speed and wind velocity using different initial conditions are shown in Figure 6-8 to 6-10. The ECMWF result, denoted by solid lines with diamonds, is a simple temporal interpolation from the 6-hour original analysis without performing any mesoscale simulations. Therefore it represents the error with least effort and it indeed carries the largest error for the surface temperature. However, errors for the wind speed and wind direction are larger than the model predictions only during the day, an indication that the large scale simulation fails to capture the strong mesoscale meteorological feature such as sea breeze. The errors using the full initial fields are smaller than those using the single sounding initialization, as shown in the curves denoted by -2Z and -2Z/LAX/ECMWF. The simulation started at 00 GMT of August 26 carries larger errors than that started at 06 GMT of August 27. The best surface temperature simulation is achieved with the SCAQS sounding at EMUA for the boundary layer and ECMWF vertical profile for the upper layers since this combined vertical profile consists of boundary layer information closer to the observations. The profiles for temperature, relative humidity and horizontal wind from the SCAQS observations are compared with those from the ECMWF at LAX in Figure 6-11.

In view of the above comparisons, the following facts should be noted:

- The simulation results represent a 25 km^2 area average; whereas the observations represent the values at specific stations.
- The screen level (1.25 m) temperature from the simulation is interpolated from the surface and first level (10 m) temperatures. And the surface wind from the simulation

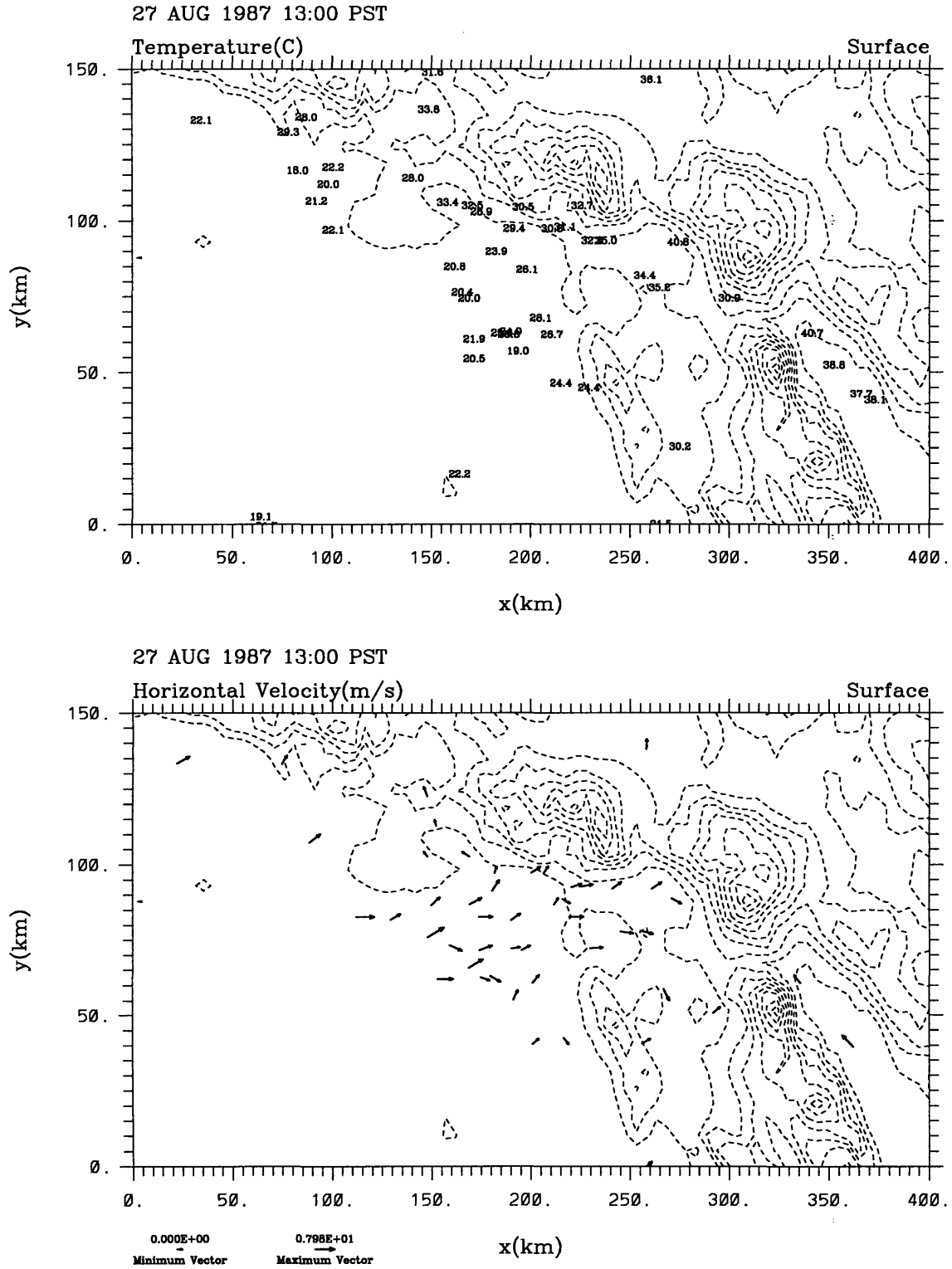


Figure 6-3: Observed surface temperature and wind for 13 PST of August 27, 1987. Dashed contours show the topography.

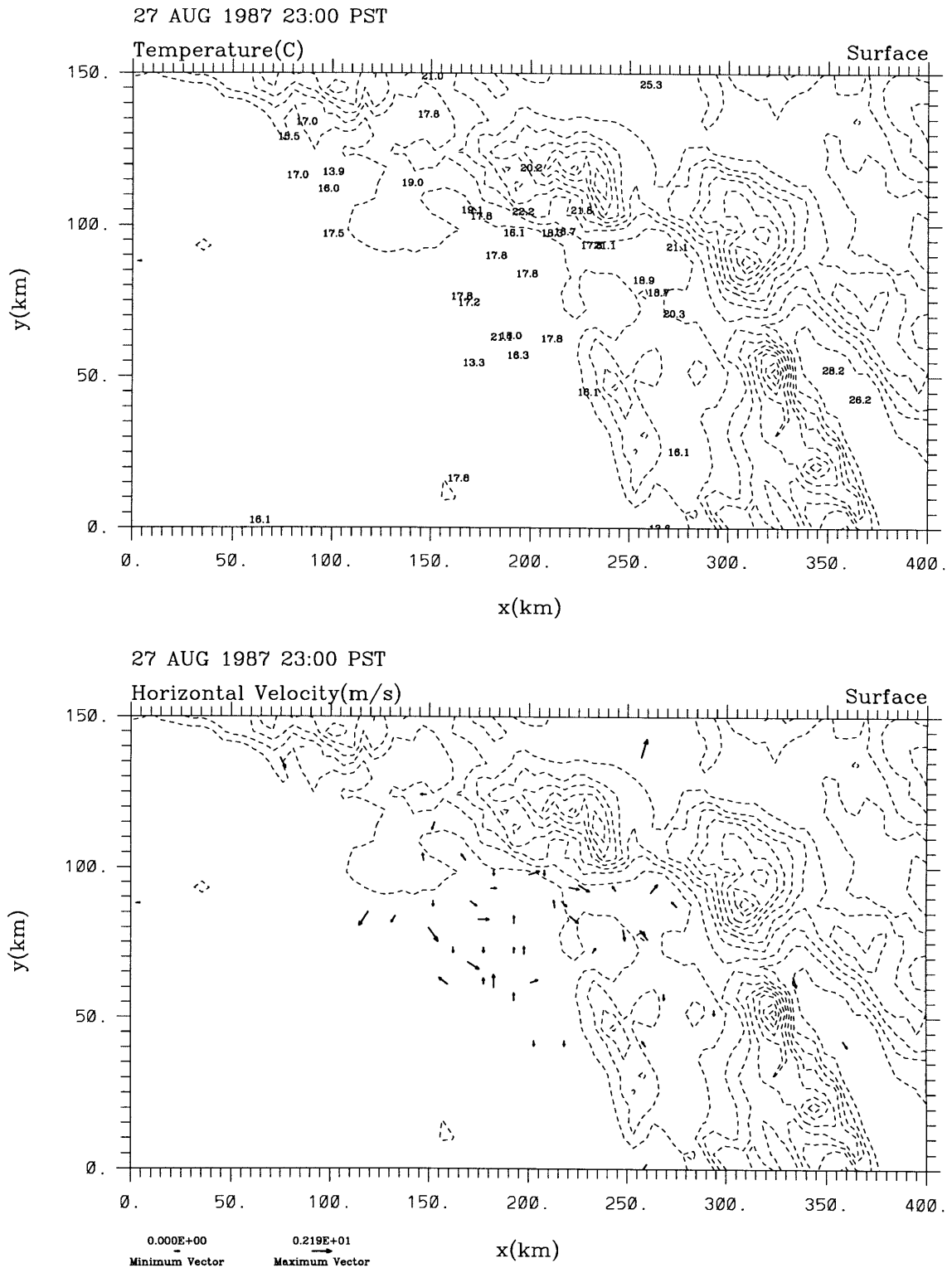


Figure 6-4: Observed surface temperature and wind for 23 PST of August 27, 1987. Dashed contours show the topography.

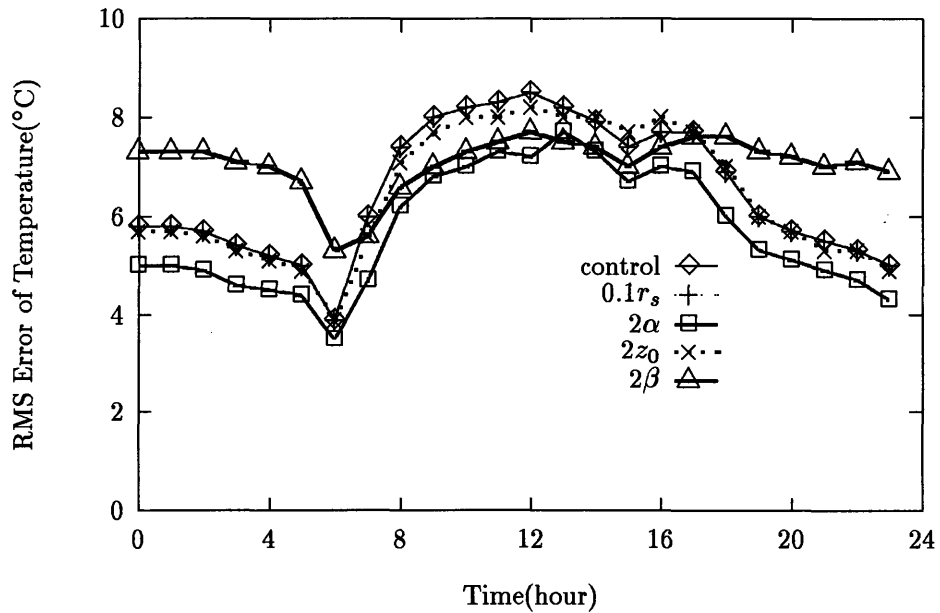
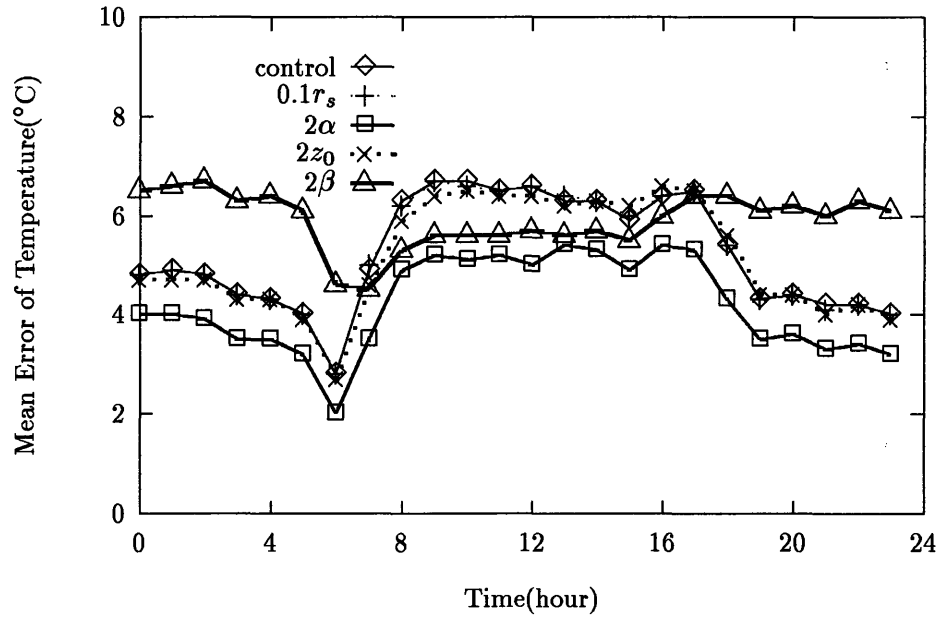


Figure 6-5: Mean and RMS errors of simulated surface temperature using different surface parameters for August 27, 1987. Nomenclature: $0.1r_s$ -reducing r_s by a factor of 10; $2\alpha/2z_0/2\beta$ -doubling α , z_0 and β .

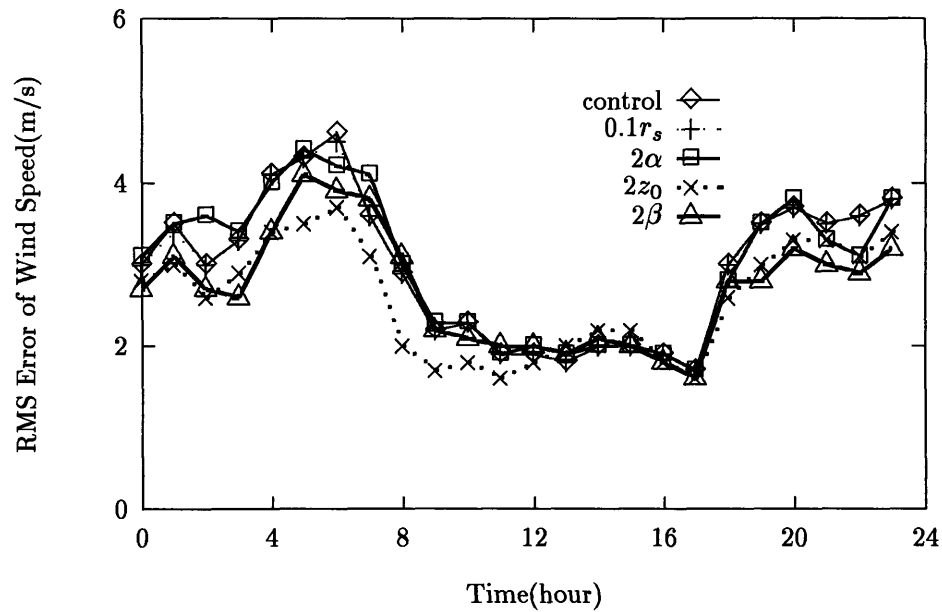
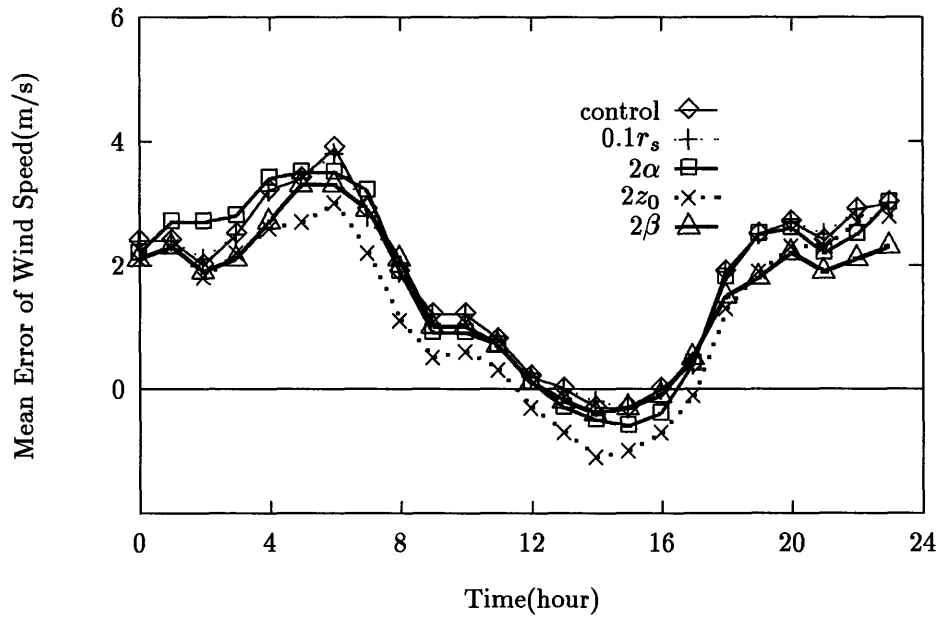


Figure 6-6: Mean and RMS errors of simulated surface wind speed using different surface parameters for August 27, 1987. Nomenclature: $0.1r_s$ —reducing r_s by a factor of 10; $2\alpha/2z_0/2\beta$ —doubling α , z_0 and β .

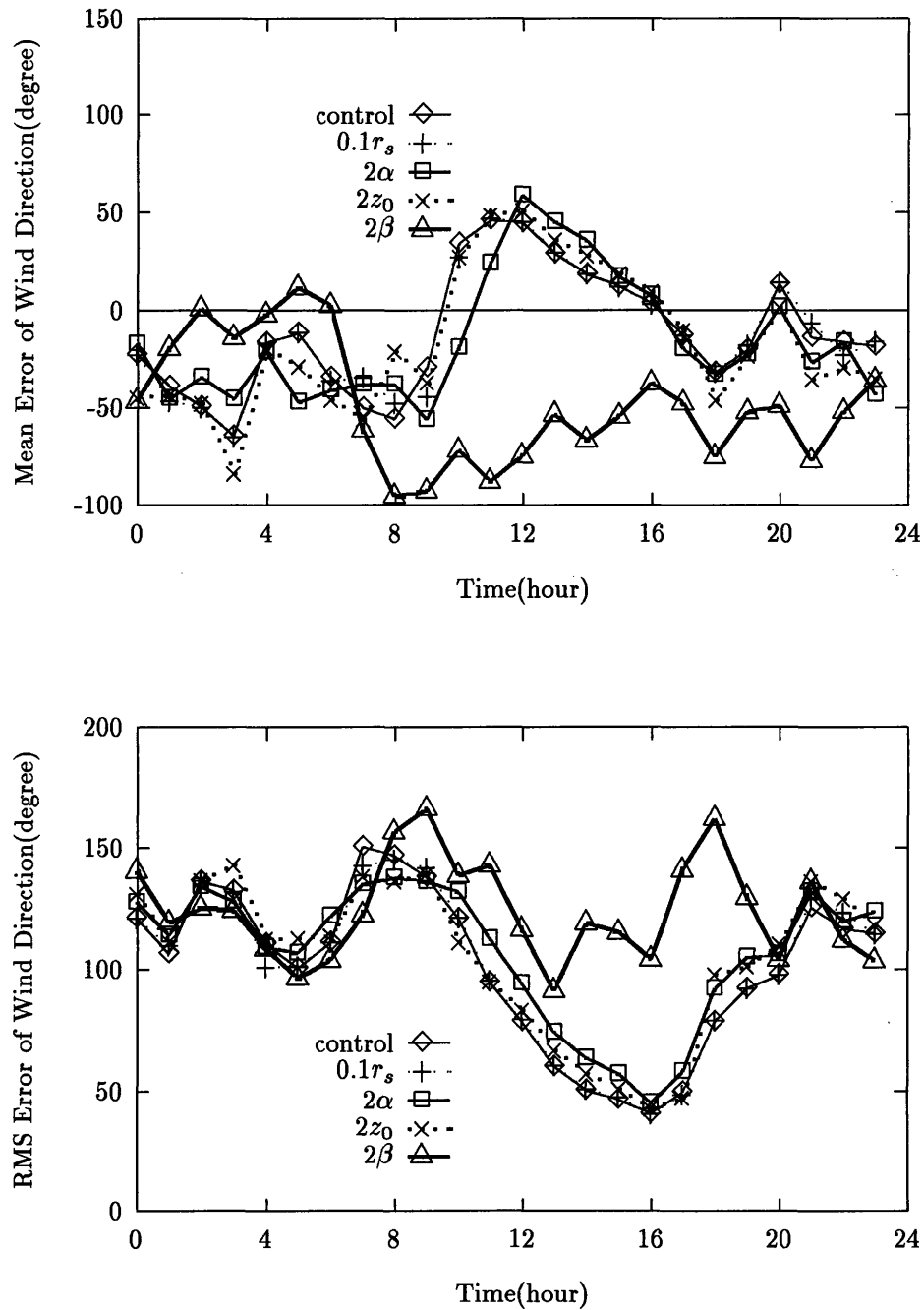


Figure 6-7: Mean and RMS errors of simulated surface wind direction using different surface parameters for August 27, 1987. Nomenclature: $0.1r_s$ —reducing r_s by a factor of 10; $2\alpha/2z_0/2\beta$ —doubling α , z_0 and β .

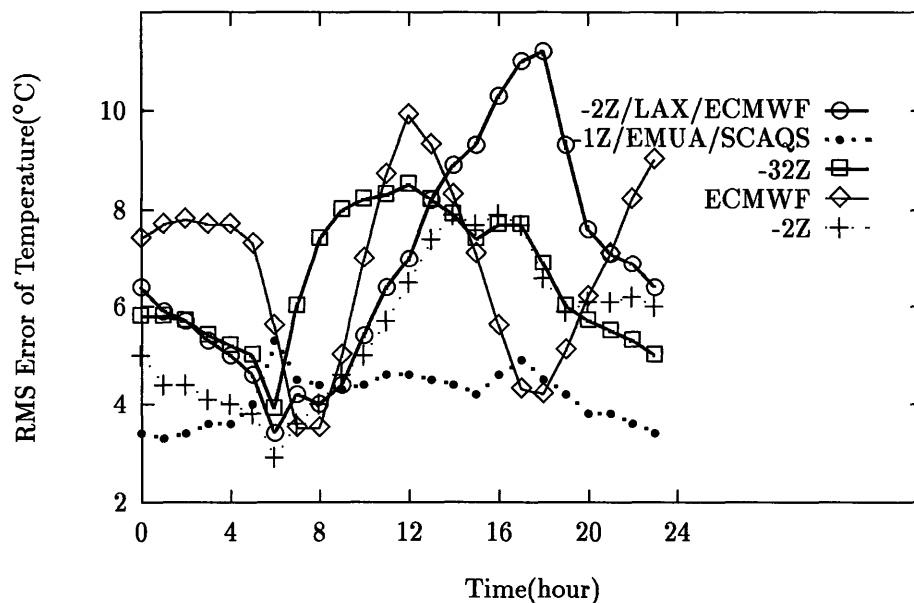
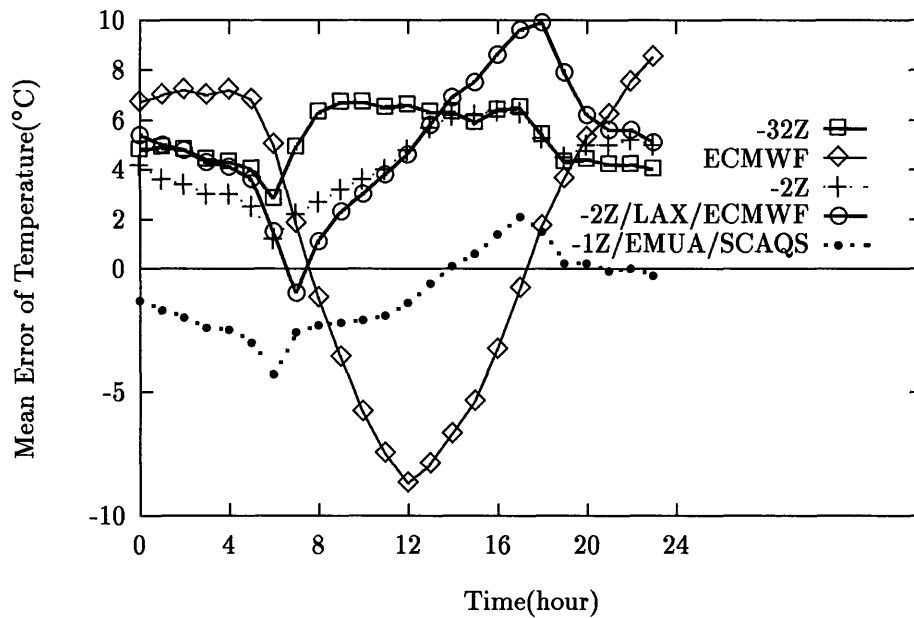


Figure 6-8: Mean and RMS errors of simulated surface temperature using different initial conditions for August 27, 1987. Nomenclature: ECMWF-ECMWF analysis; LAX/ECMWF-ECMWF vertical profiles at Los Angeles International Airport; EMUA/SCAQS-SCAQS soundings at El Monte-9528 Telstar for boundary layer and LAX/ECMWF for upper layers; -2Z/-32Z/-1Z-2, 32, or 1 hour earlier than the time origin.

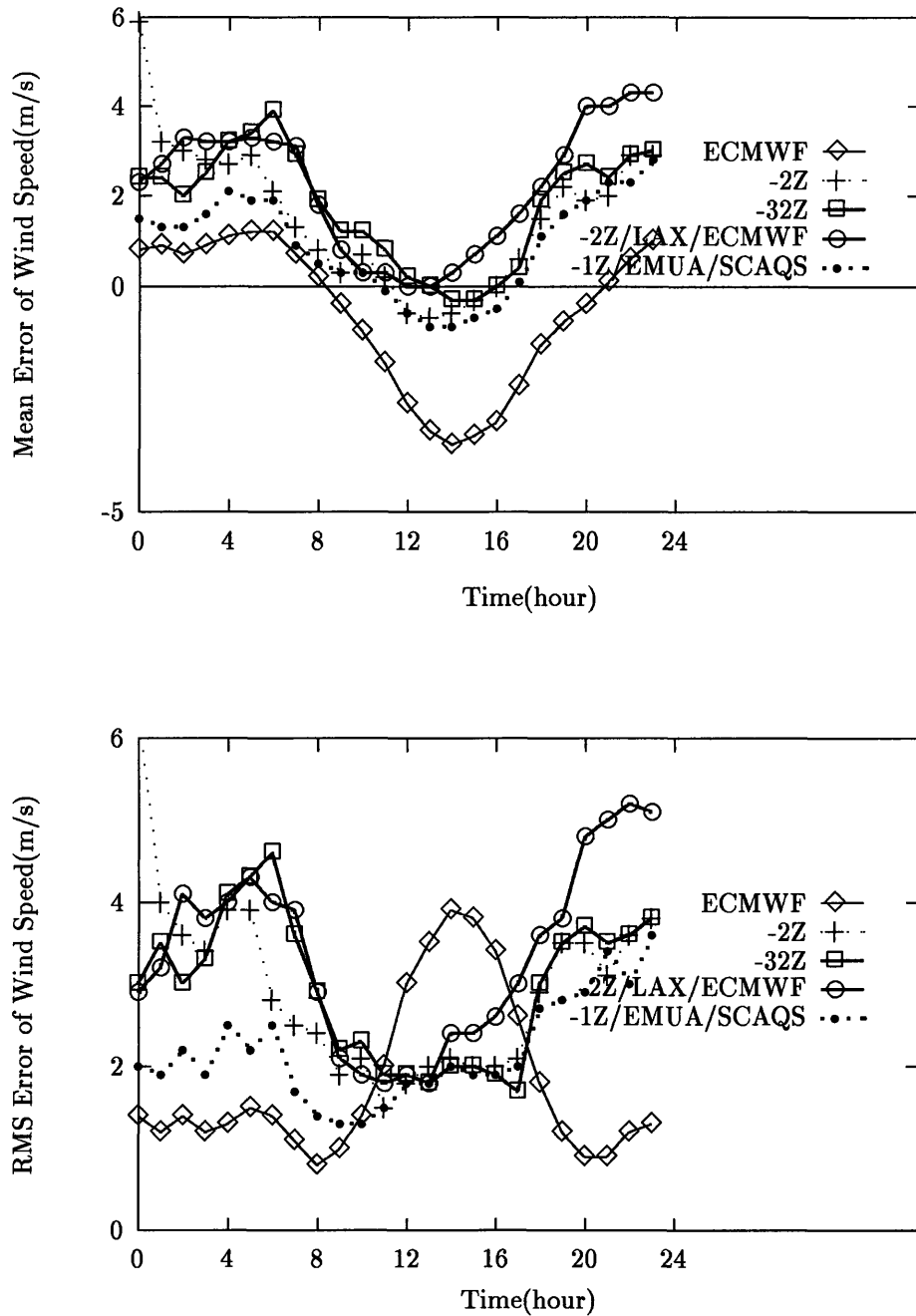


Figure 6-9: Mean and RMS errors of simulated surface wind speed using different initial conditions for August 27, 1987. Nomenclature: ECMWF–ECMWF analysis; LAX/ECMWF–ECMWF vertical profiles at Los Angeles International Airport; EMUA/SCAQS–SCAQS soundings at El Monte-9528 Telstar for boundary layer and LAX/ECMWF for upper layers; -2Z/-32Z/-1Z–2, 32, or 1 hour earlier than the time origin.

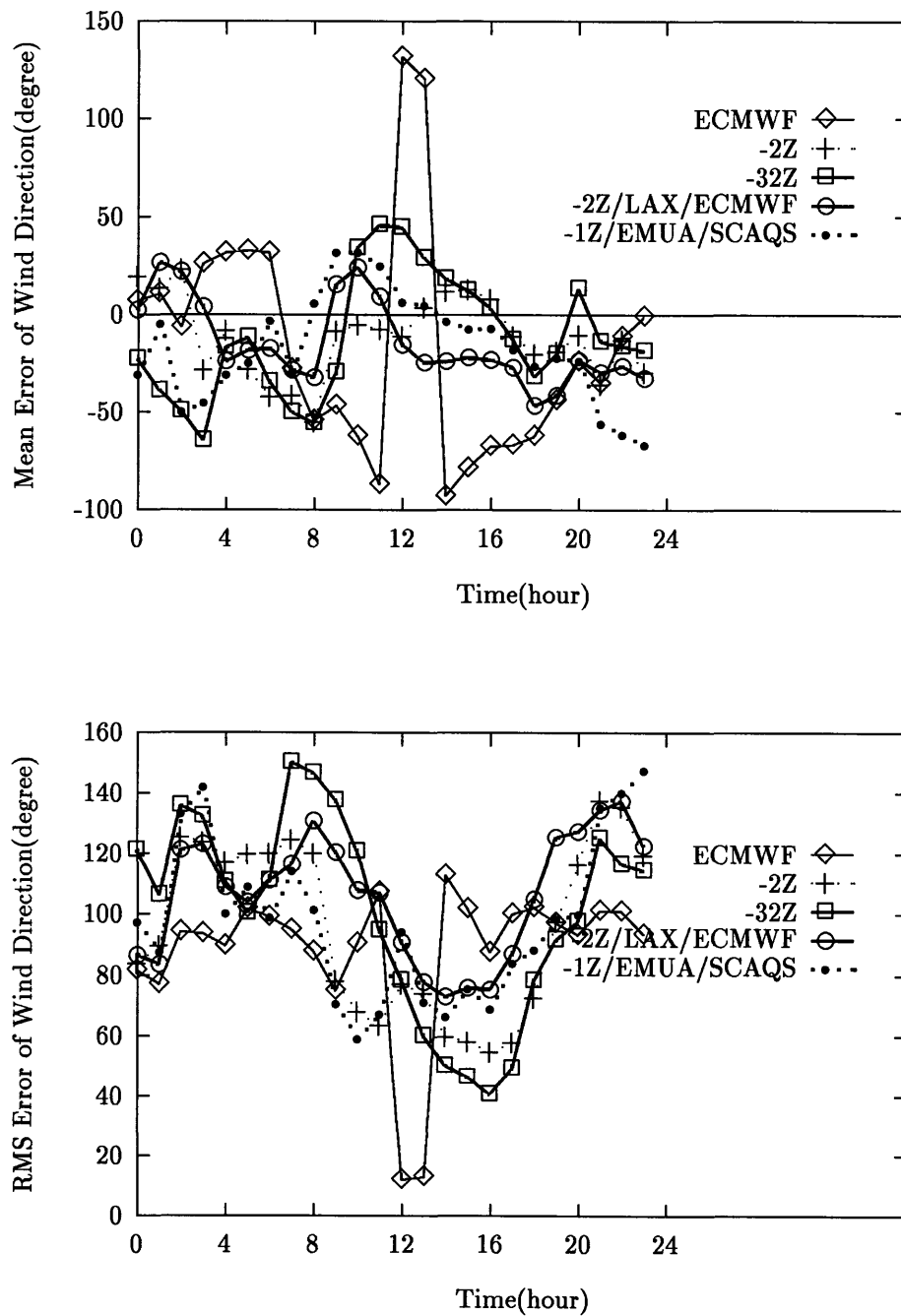


Figure 6-10: Mean and RMS errors of simulated surface wind direction using different initial conditions for August 27, 1987. Nomenclature: ECMWF–ECMWF analysis; LAX/ECMWF–ECMWF vertical profiles at Los Angeles International Airport; EMUA/SCAQS–SCAQS soundings at El Monte-9528 Telstar for boundary layer and LAX/ECMWF for upper layers; -2Z/-32Z/-1Z-2, 32, or 1 hour earlier than the time origin.

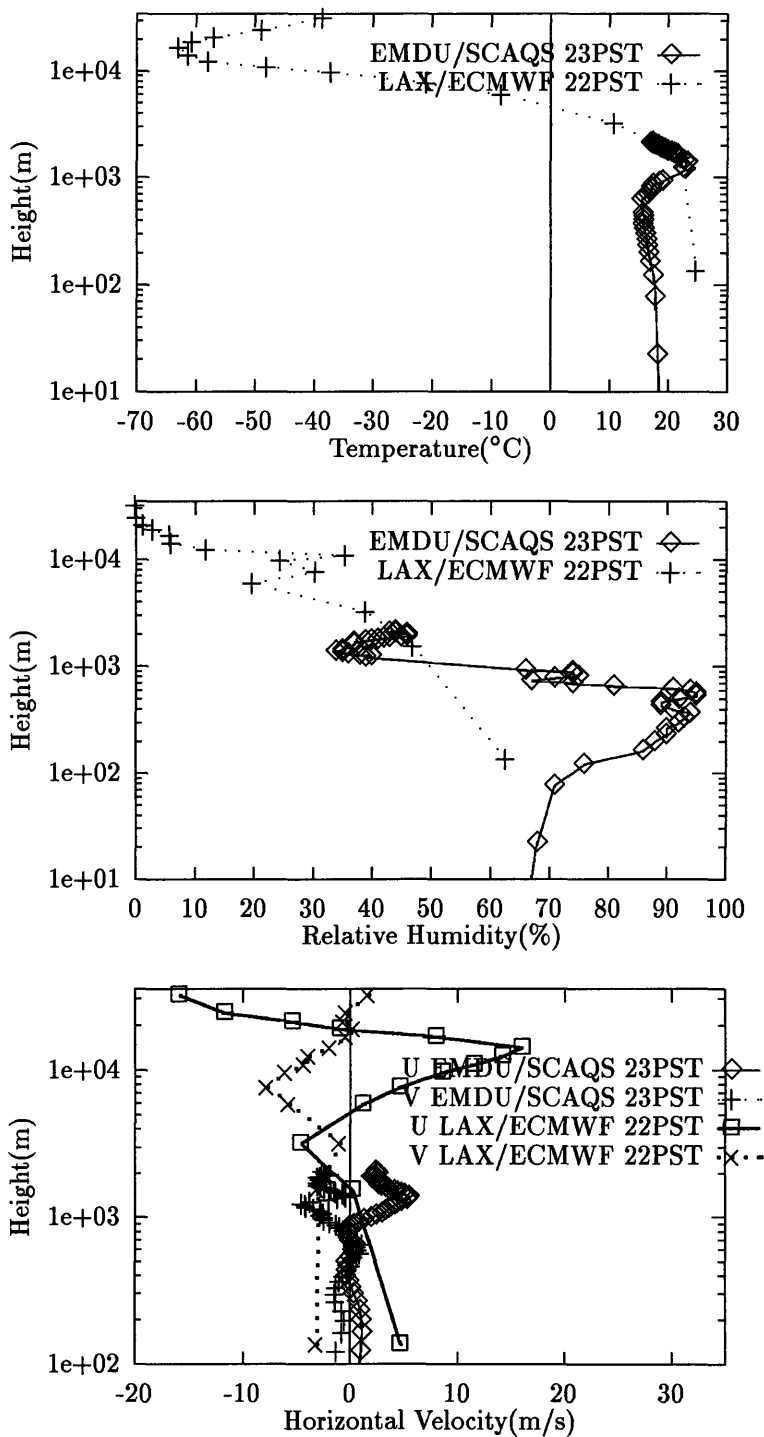


Figure 6-11: Comparison of vertical profiles of temperature, relative humidity, and horizontal velocity from ECMWF analysis and SCAQS observation at two stations, Los Angeles International Airport (LAX) and El Monte-9528 Telstar (EMDU), which are close to each other.

is at 10 m level. There may be a difference between these heights and those for the observations.

- The simulation results represent the instantaneous values; whereas observational values represent hourly averages.

Although the simulation using the combined vertical profiles at 23 PST of August 27, 1987 gives the best results compared with the observations, the results close to the lateral boundaries are found to be less satisfactory than those from the gridded analysis due to the fixed boundary treatment associated with the single sounding initialization. Since the focus of this study is the aerosol effects, the simulation with the full initial fields at 6 GMT of August 27, 1987 is used as the control case. Several fields are shown in Figures 6-12 to 6-14.

6.3 Single Column Simulations

Before presenting the three-dimensional simulations with aerosols, I will discuss some results of the single column simulations. These results can be used to compare with both previous RCM results and later three-dimensional results.

The single column mode is achieved by running the model without the horizontal equations of motion, lateral boundary conditions, or the horizontal derivatives. It is computationally and physically attractive for long-term integrations and module testing. The SCAQS sounding at EMUA for the boundary layer and the ECMWF vertical profile for the upper layers are combined for the initial condition. The resulting temperature and wind profiles are shown in Figure 6-11.

The radiation schemes developed by Chou [26, 27] (GSFC) and by Fu and Liou [51] (QFU) (cf. Chapter 4) have been modified to account for the aerosol radiative forcing in the mesoscale model. Figure 6-15 shows the short-wave and long-wave surface radiative flux and atmospheric heating rate using the QFU scheme for CCONT aerosol type. The changes of both the surface net flux and the heating rate in the short-wave range are about a factor of five larger than those in the long-wave range. This is also true for other aerosol types considered here.

Although the alternative radiation schemes (i.e., GSFC and QFU) are more suitable for studying aerosol-induced radiative forcing, their computational costs are much greater than the original radiation scheme (UKMO). These three methods have been timed for a one day simulation with a 60 second time step in the single column mode. The integration takes about 10 seconds using the original radiation scheme, compared with 100 seconds using Chou's scheme and 540 seconds using Fu and Liou's scheme. If the computational times in these one-dimensional simulations are scaled to a three-dimensional domain of 2400 columns, a one day integration will take about 7, 70, and 378 hours respectively⁴. Therefore the original UKMO short-wave radiation scheme will be modified to improve it without increasing too much its computational cost for all the three-dimensional simulations with aerosols. The long-wave effect will be neglected.

In the modification of the UKMO radiation scheme, the scattering and absorption within the boundary layer are treated using the delta-four-stream discrete-ordinate approximation [87]. The interaction between the aerosol layer and the underlying surface is dealt with

⁴The radiation subroutine is called every time step for short-wave and every five time steps for long-wave.

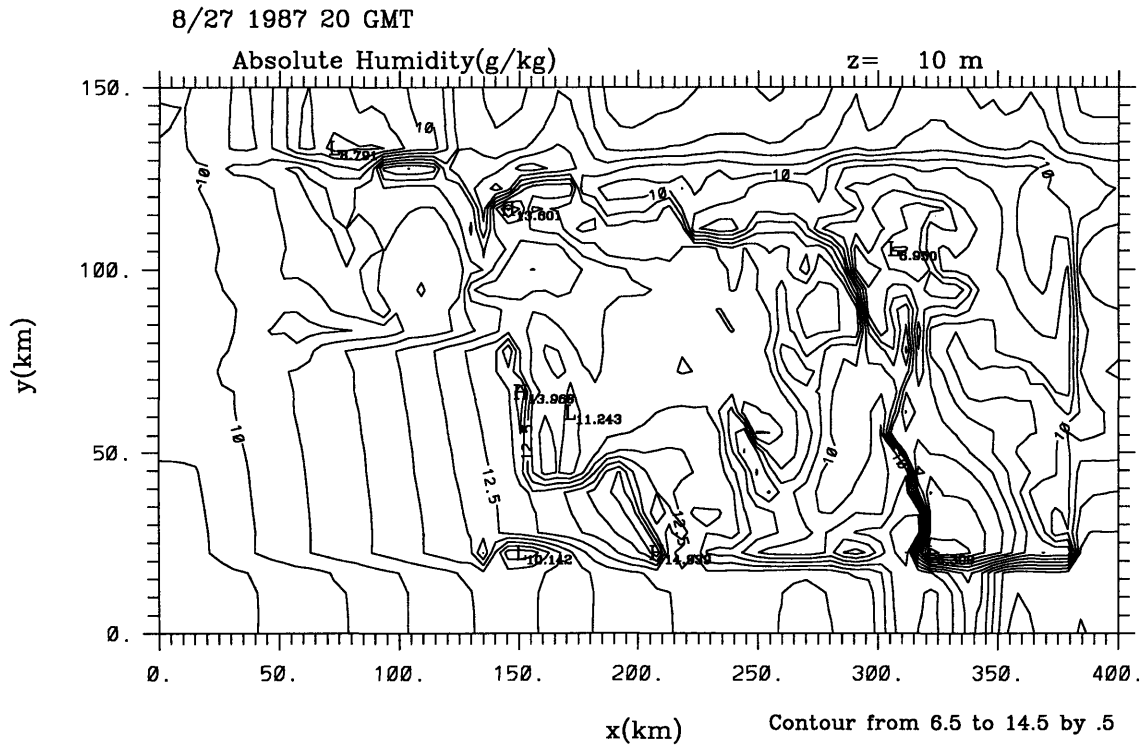
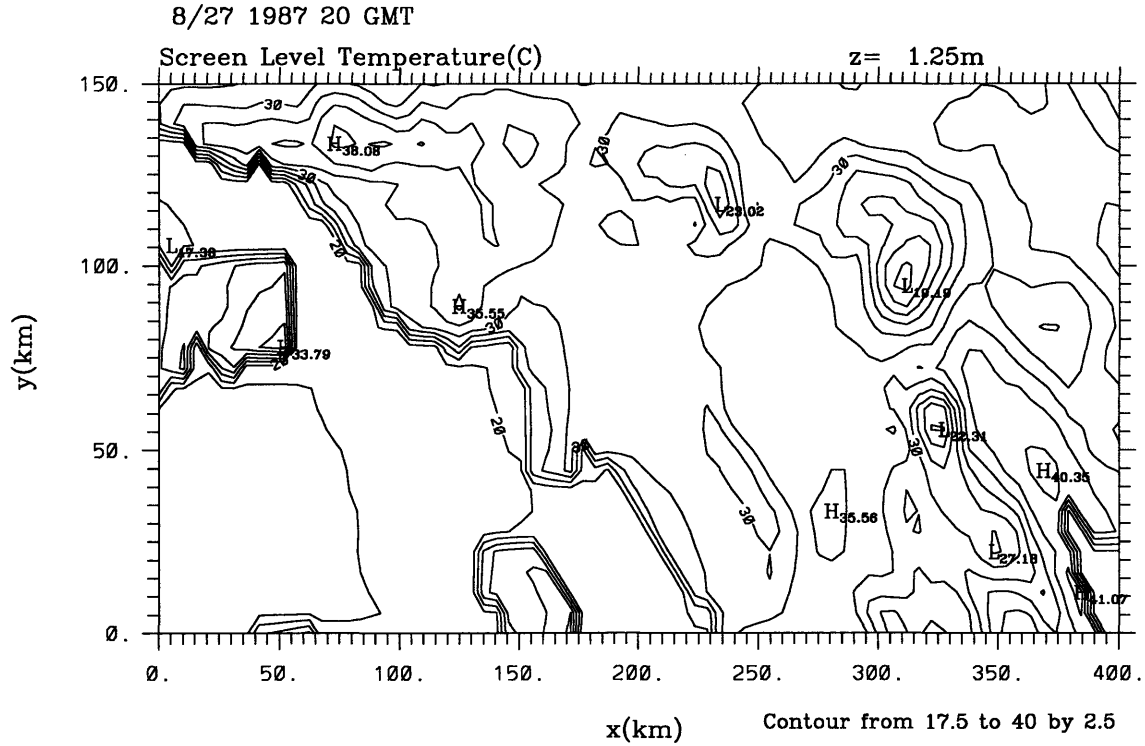


Figure 6-12: Simulated screen level temperature and first level absolute humidity for 12 PST of August 27, 1987.

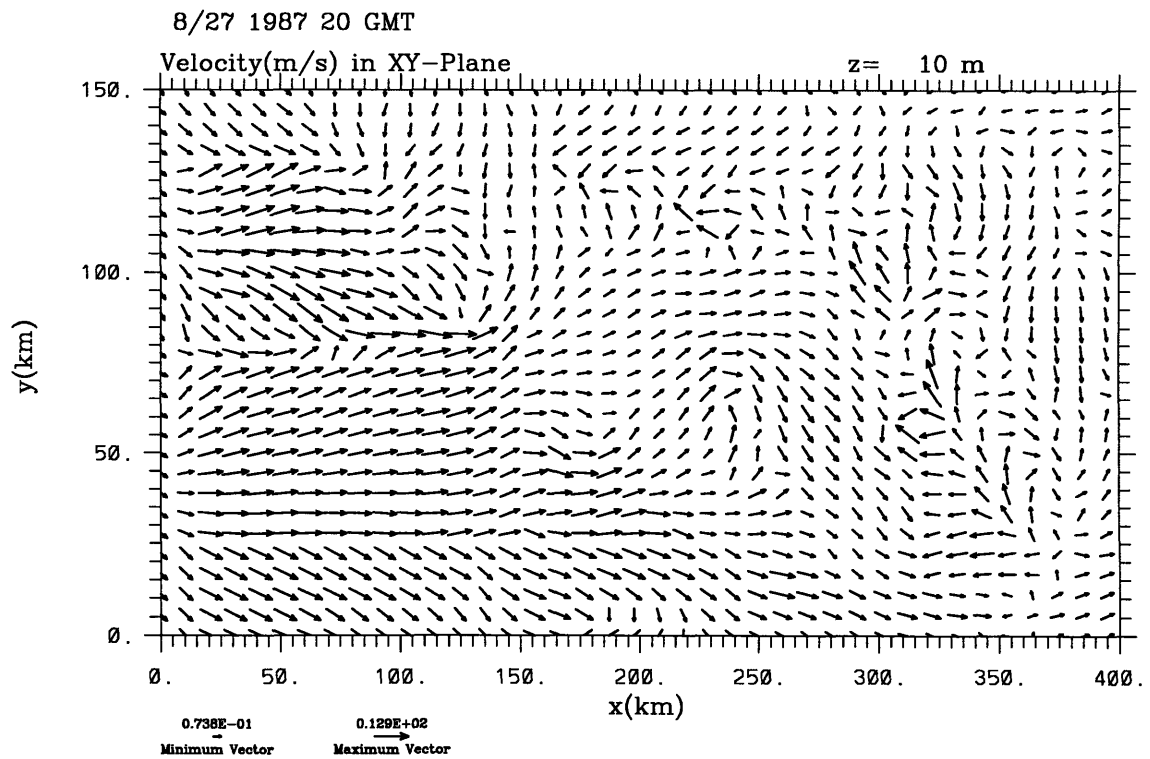
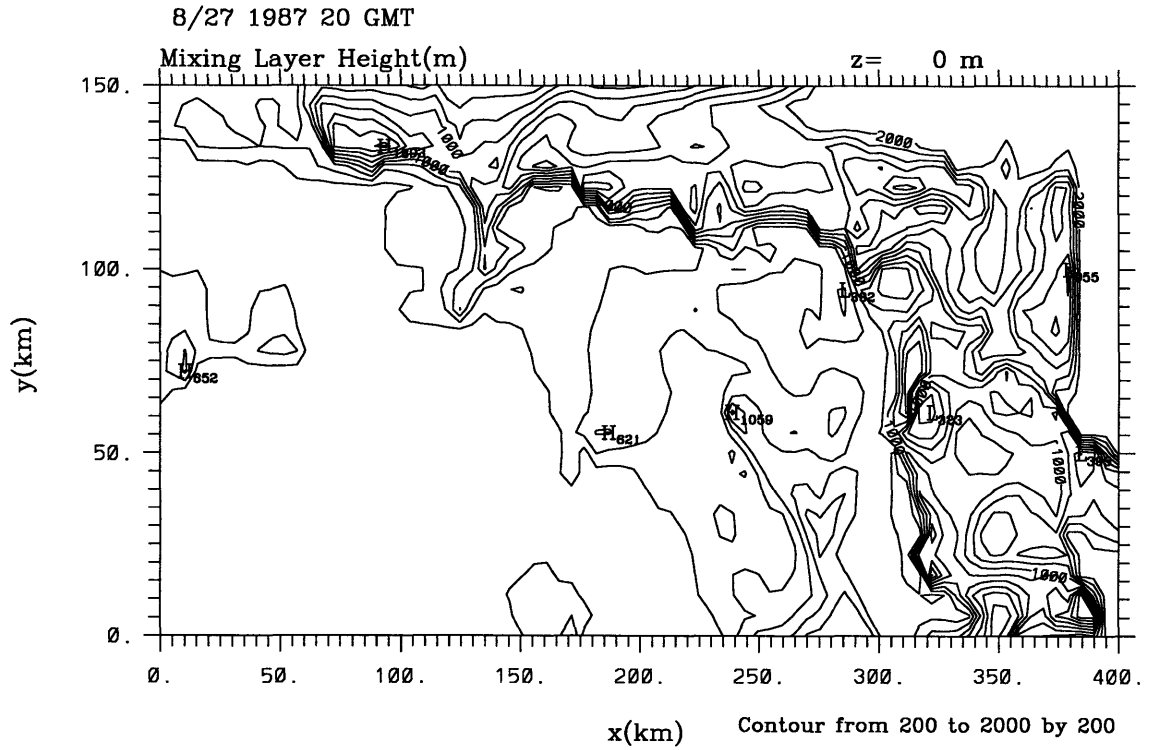


Figure 6-13: Simulated boundary layer height and first level wind for 12 PST of August 27, 1987.

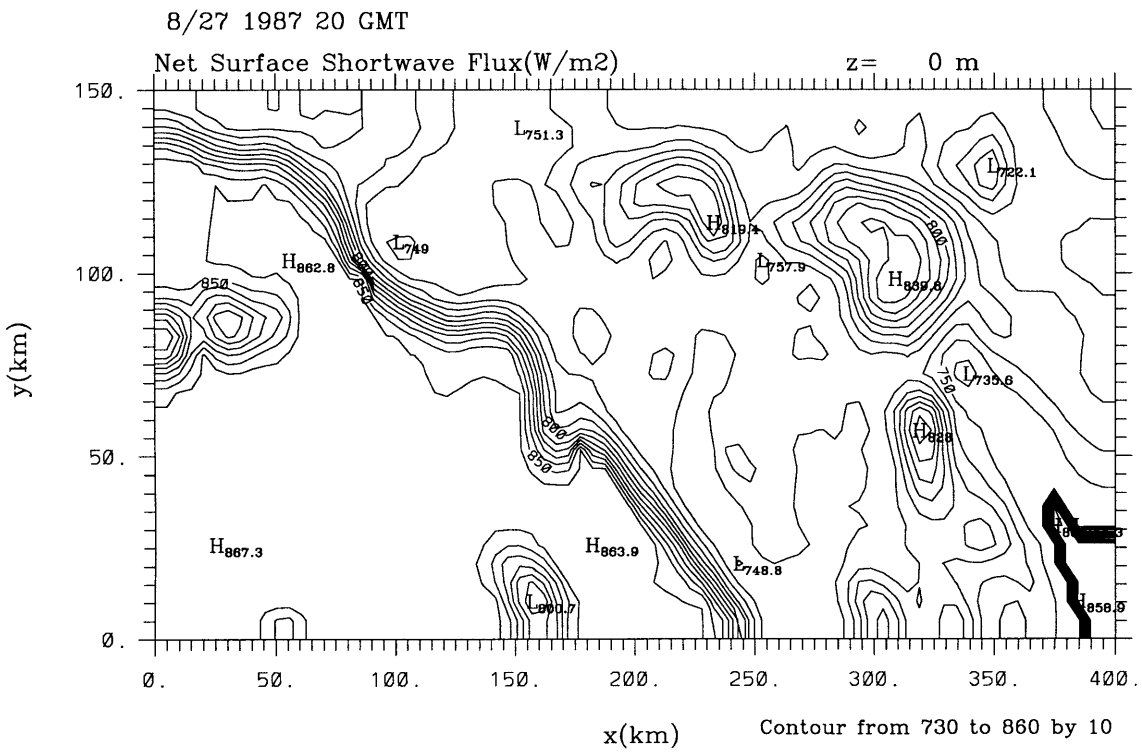


Figure 6-14: Simulated surface net downward solar radiation flux for 12 PST of August 27, 1987.

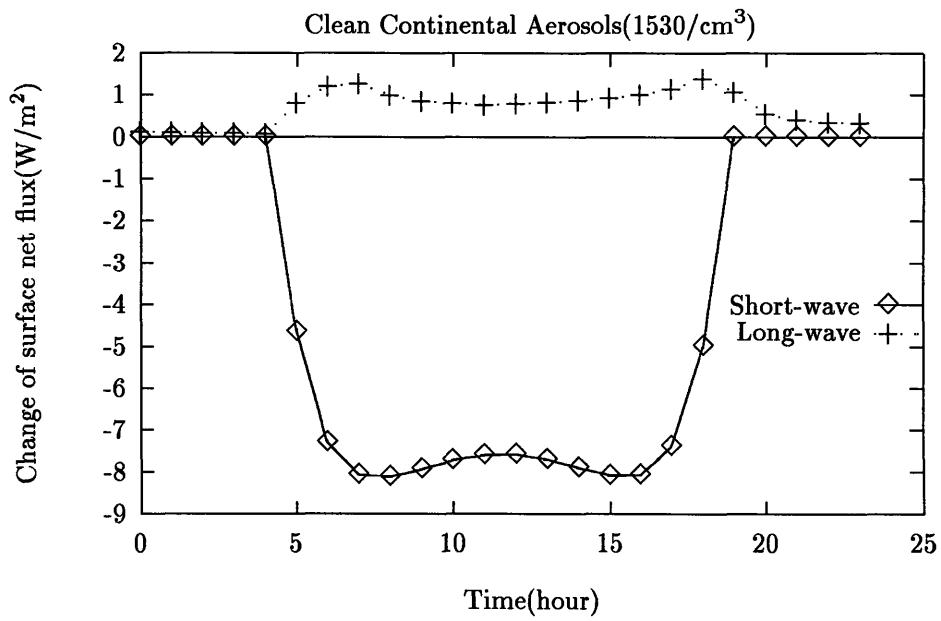
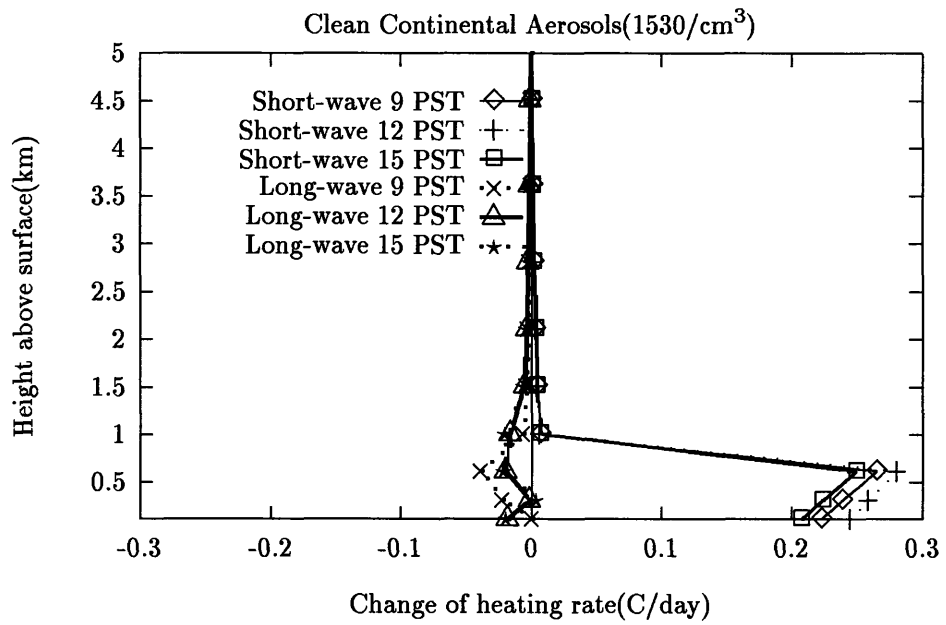


Figure 6-15: Comparisons of short-wave and long-wave surface radiative flux and mid-day atmospheric heating rate using QFU scheme for CCONT aerosol type.

using the two-stream adding method. After the flux changes at the top and bottom of the boundary layer are obtained, the heating rate is computed assuming the flux divergence is linear with height (cf. Equation 4.4).

The short-wave surface radiative flux and atmospheric heating rates using different radiation schemes for the CCONT aerosol type are shown in Figure 6-16. The modified UKMO scheme tends to overestimate the heating rate and surface flux change. Since the purpose of this study is not to define the exact changes due to aerosols but to study the model response to these changes, the modified UKMO scheme is accepted to efficiently handle aerosols in three-dimensional simulations.

In simulating the aerosol effects in single columns, four columns are assigned with different land use categories, i.e., No. 16, 9, 1, and 19 in Table 6.2. They contain aerosol types of CCONT, ACONT, URBAN, and CLMAR, respectively. Eight different simulations have been carried out using the QFU radiation scheme for the four different columns with the lower and the upper attenuation coefficients.

Figure 6-17 shows the diurnal variations of the surface energy budget components and the boundary layer height in the absence of aerosols. At the surface the temperature change depends on the balance among the incoming short-wave, the outgoing long-wave radiation, and the sensible, latent, and ground heat fluxes. During the day, sensible heat flux dominates the latent and ground heat fluxes. These three components all carry heat away from the surface. During the night, ground heat flux carries heat up to the surface. For the CLMAR case, small heat flux changes are due to the neutral condition near the surface. After sunrise, the boundary layer grows as turbulence develops and reaches a maximum in mid-day,

Figure 6-18 shows the vertical distributions of temperature, water vapor mixing ratio, turbulent kinetic energy, vertical diffusion coefficient for heat, and short-wave and long-wave heating rates in the lowest 5 km in mid-day. In the atmosphere the long-wave cooling competes with the heating due to solar radiation and vertical diffusion. A temperature inversion is well formed above the model boundary layer. Large radiative cooling is also observed at the top of boundary layer. The boundary layer is characterized by large turbulent kinetic energy and high vertical diffusion coefficient. As a result, the water vapor mixing ratio is close to be uniform within the boundary layer, supporting the assumption of uniform aerosol optical properties in the boundary layer.

Figure 6-19 shows the change of diurnal cycles for the surface energy budget and boundary layer height due to aerosols. Aerosols decrease the incoming solar radiation by 5% to 50%, depending on aerosol type and concentration. The downward terrestrial radiation increases by 1% to 15%. The reduced incoming solar flux is compensated by reduced fluxes of sensible heat, latent heat and ground heat. The boundary layer height decreases occur in the morning and range up to 50% before noon except in the case of urban aerosols, where the early collapse of an unstable boundary layer in the late afternoon is also observed.

The change of vertical profiles in mid-day is shown in Figure 6-20. Aerosols increase the short-wave heating rate and decrease the long-wave cooling rate as a result of aerosol short-wave absorption and long-wave emission. The change of the short-wave heating is about a factor of 10 larger than that of the long-wave cooling. The overall increase in the radiative forcing is compensated by the decrease in the diffusive heating, which is manifested by the decreases in the turbulent kinetic energy and the vertical diffusivity. Weaker turbulent mixing results in smaller heat flux into the atmosphere and therefore decreases the temperature and water vapor near the surface. For higher concentration urban aerosols, since the decrease in the vertical heat flux is not sufficient to compensate

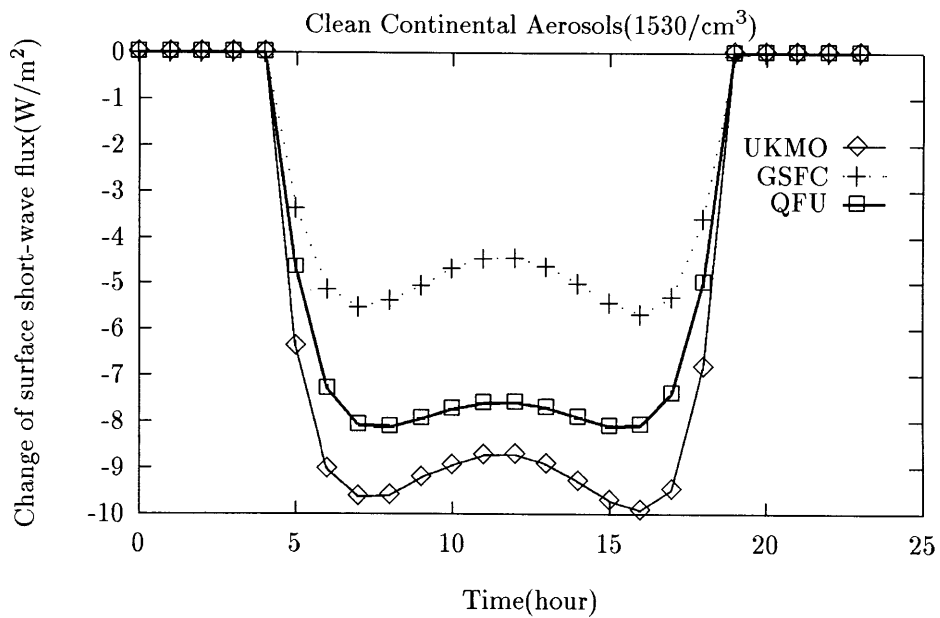
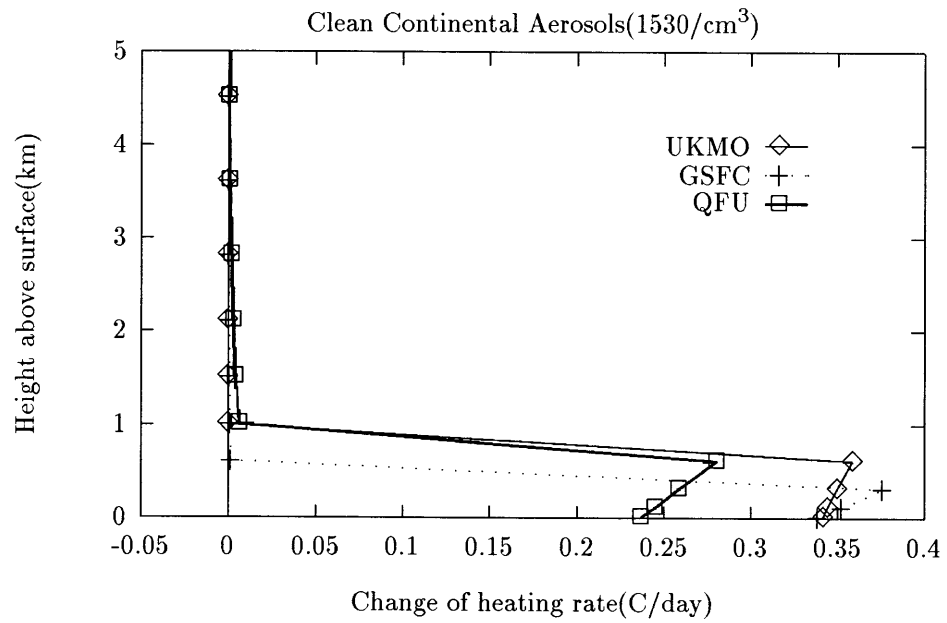


Figure 6-16: Comparisons of short-wave surface radiative flux and atmospheric heating rate using different radiation schemes for CCONT aerosol type.

Table 6.3: Radiative forcing and corresponding changes in the surface sensible/latent/ground heat fluxes and temperature at 12 PST of August 27, 1987. f_- is the positive feedback coefficient as defined in the previous chapter.

Aerosol Type Loading	CCONT		ACONT		URBAN		Sulfate	Double CO ₂
	low	high	low	high	low	high		
$\Delta F_{SW}(\frac{W}{m^2})$	-7.60	-97.35	-87.03	-110.12	-81.08	-233.26	-8.89	-5×10^{-3}
$\Delta F_{LW}(\frac{W}{m^2})$	0.79	10.03	10.72	13.90	4.67	16.27	0.93	0.487
$\Delta SH(\frac{W}{m^2})$	-5.24	-69.05	-56.84	-72.78	-57.36	-150.36	-5.36	0.16
$\Delta LH(\frac{W}{m^2})$	-1.10	-11.99	-13.76	-17.40	-5.99	-18.78	-1.72	0.22
$\Delta GH(\frac{W}{m^2})$	-0.34	-4.83	-5.05	-6.98	-9.97	-41.65	-0.62	0.07
f_-	-6.68	-7.90	-6.27	-6.27	-12.48	-10.81	-4.9	-2.4
$\Delta T_s(K)$	-0.16	-1.74	-1.93	-2.48	-0.97	-3.12	-0.25	0.03
$\frac{\Delta T_s}{\Delta F}(\frac{K}{W/m^2})$	0.023	0.020	0.025	0.026	0.013	0.014	0.03	0.06

the radiative heating, a large temperature increase is maintained near the top of boundary layer.

To relate the results obtained here to those in the 1-D RCM simulations, I have listed in Table 6.3 the changes in the surface sensible/latent/ground heat fluxes and temperature at 12 PST of August 27, 1987 under the radiative forcing of different aerosol types. Despite the different heat flux formulation in the mesoscale model, namely the Richardson number dependence of drag coefficient and the non-zero ground heat flux and surface resistance to evaporation, the initial sensitivity of surface temperature to surface radiative forcing is similar to that in the 1-D RCM, indicating the transient nature of temperature change in the mesoscale model.

In addition, the negative feedback factor increases as aerosols become more absorptive. For example, f_- for the sulfate aerosol, which is almost non-absorptive, is the smallest among those for all the aerosol types considered here. The sensitivity of the model response to the surface radiative forcing by doubling CO₂ is about a factor of 2 larger than that by sulfate aerosols. This is in contrast to the sensitivity of the model responses to the tropopause radiative forcing in the previous chapter. This is determined by the different characteristics of radiative forcings by sulfate aerosols and CO₂. The increased CO₂ causes both the tropospheric and the surface heating. For a doubling of CO₂, the tropospheric and surface heatings are 3 and 1.2 W/m² respectively [115]. For aerosols, however, the sign of the tropospheric radiative forcing is opposite to that of the surface radiative forcing. Therefore for the same radiative forcing at the surface, the response of the surface temperature is larger for CO₂ than for aerosols. On the other hand, if the sensitivity to the tropopause radiative forcing is compared (cf. Table 5.2), it should be larger for sulfate aerosols than for CO₂ since for nonabsorptive aerosols the radiative forcing at the tropopause is the same as at the surface. This analysis contradicts with the findings in Taylor and Penner [145]. For equal magnitudes of the radiative forcing, they found that the temperature response is markedly greater for CO₂ than for sulfate aerosol forcing.

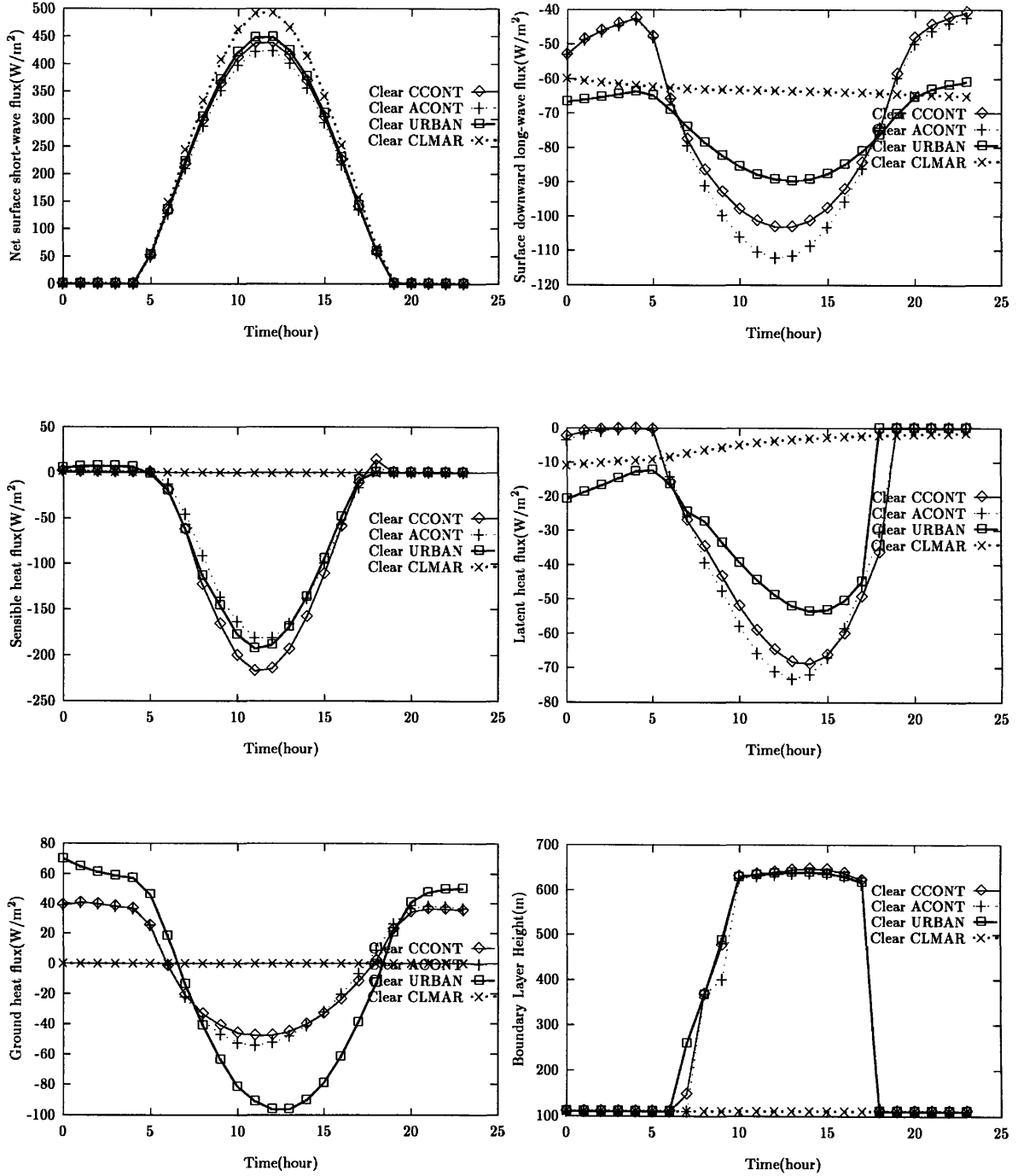


Figure 6-17: Diurnal variations of model variable in single column simulations without aerosols at 12 PST of August 27, 1987.

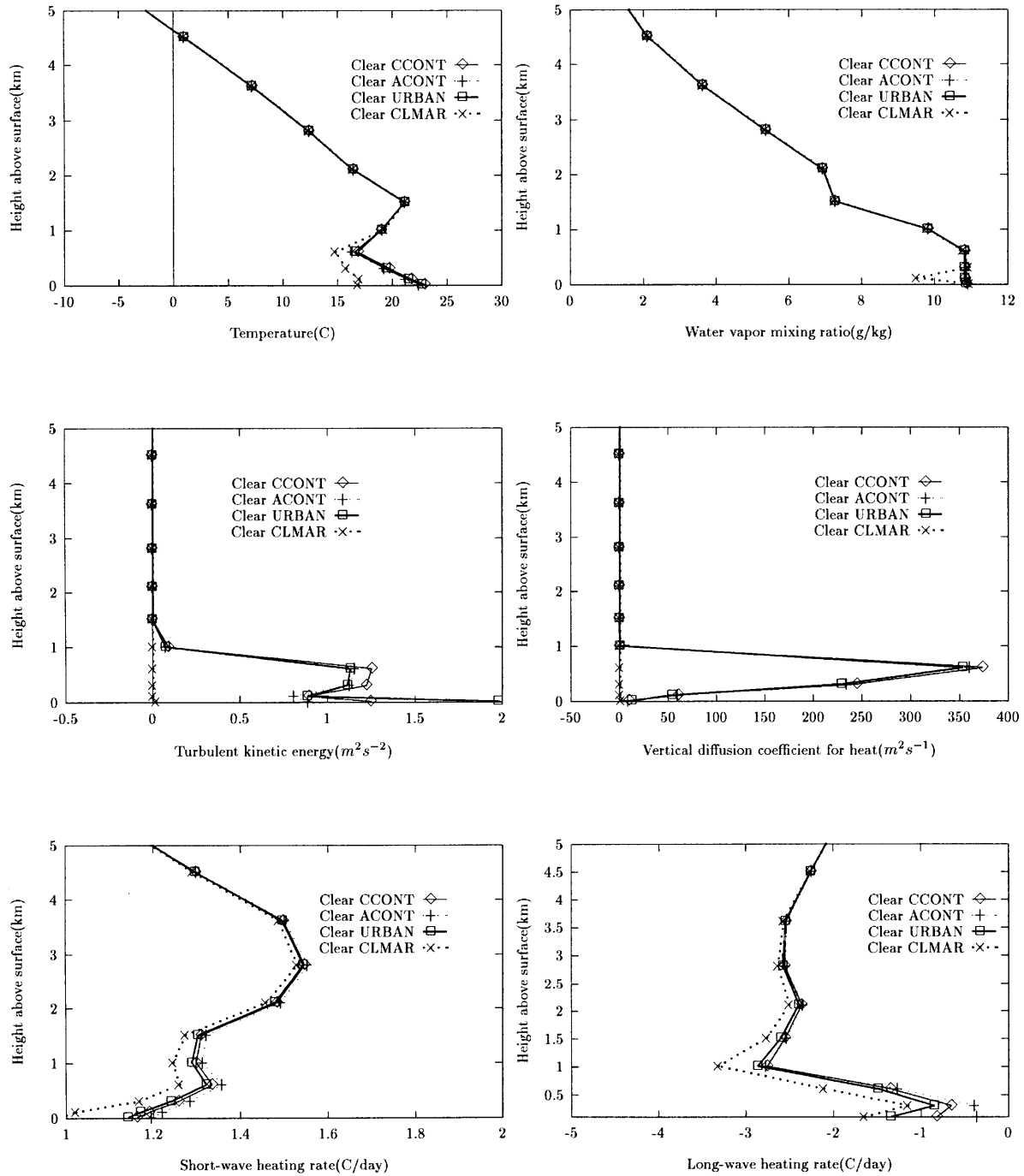


Figure 6-18: Vertical profiles of model variables in single column simulations without aerosols at 12 PST of August 27, 1987.

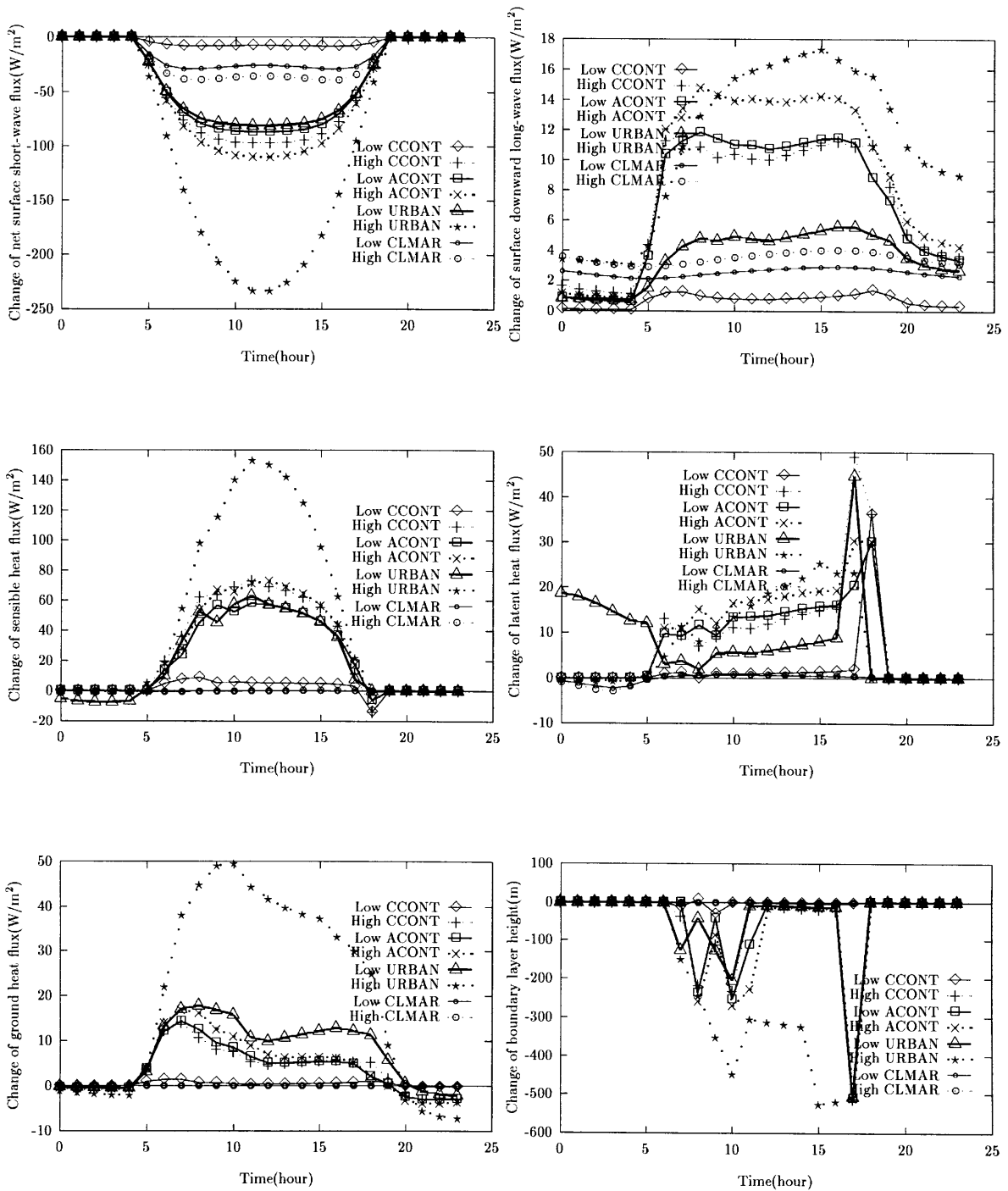


Figure 6-19: Change of diurnal variations due to aerosol radiative forcing in single column simulations of 12 PST of August 27, 1987.

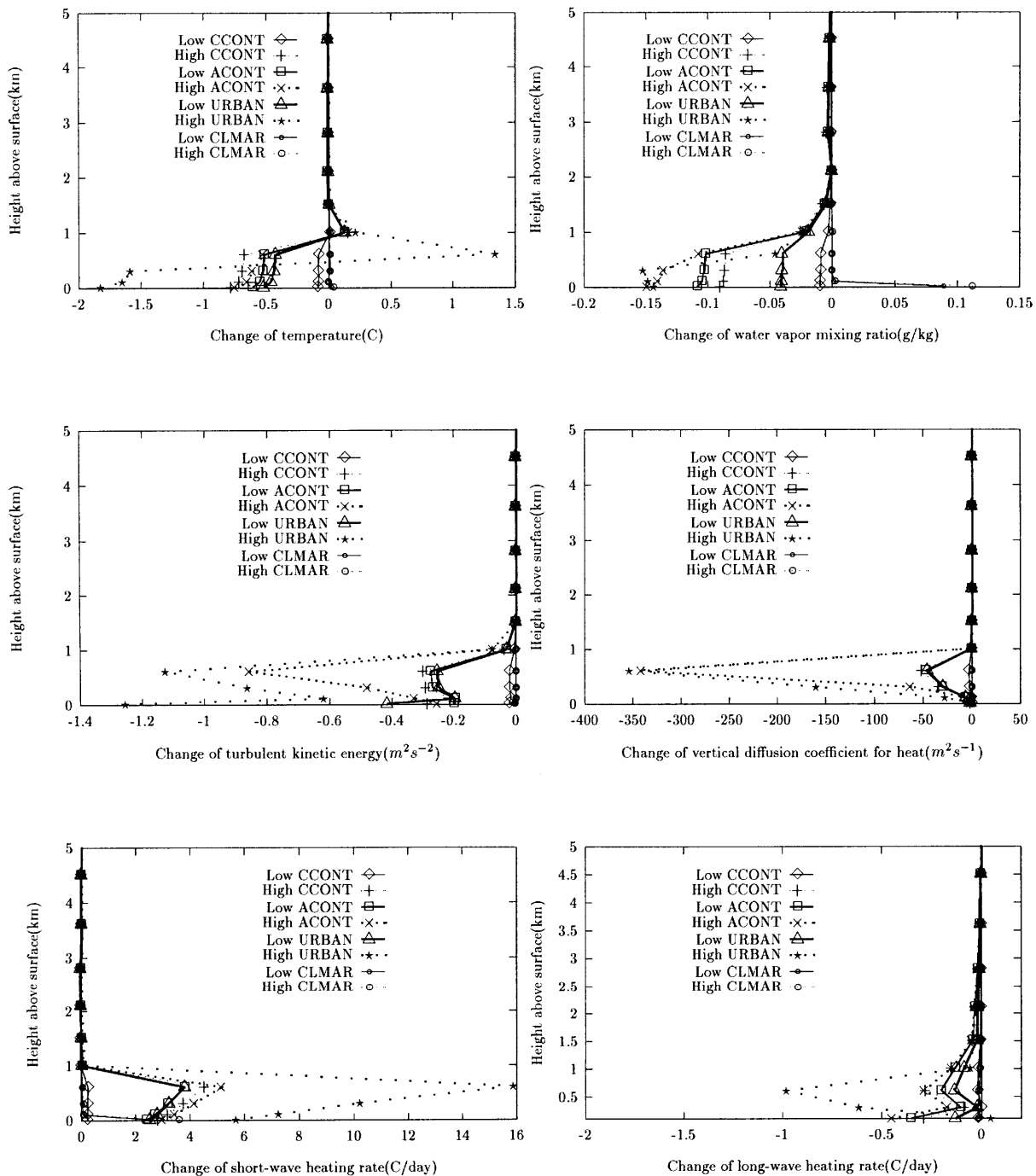


Figure 6-20: Change of vertical profiles due to aerosol radiative forcing in single column simulations of 12 PST of August 27, 1987.

6.4 Three-dimensional Simulations

The purposes of carrying out three-dimensional simulations are two-fold. First the results from these simulations can be used to examine the consequences of inhomogeneous aerosol forcing and to compare with those from single-column simulations. Second the resulting three-dimensional meteorological fields will be used to drive the photochemical air quality model in the next chapter.

Two experiments with different aerosol loading scenarios as listed in Table 6.2 have been carried out. Figures 6-21 to 6-26 show the relative changes in percentage of net downward surface solar radiative flux, surface air temperature, first level water vapor mixing ratio, boundary layer height, and first level wind speed and direction in the mid-day. The net downward surface solar radiative flux decreases by 5 to 10% for low aerosol loading and by 10 to 30% for high aerosol loading. Surface air temperature decreases as much as 10% throughout the modeling domain with the largest change occurring in the urban area. The absolute humidity increases or decreases, depending the location. The decreases in the boundary layer height varies between 10 to 30% and are not very sensitive to the shifting of aerosol loading. Aerosols in general weaken the wind by up to 30% and perturb the wind direction by 10 degrees or less.

Shifting aerosol loading from the lower level to the higher level appears to double the percentage change in all the meteorological fields except the boundary layer height, presumably due to the fact that the latter is controlled by both the surface heat flux and atmospheric heating.

Figures 6-27 and 6-28 show the diurnal variations of meteorological variables for the control and the aerosol cases. The center corresponds to the urban area where the aerosol effect reaches its maximum. The variables shown here are those important to air quality simulations, which will be discussed in the following chapter.

The surface solar radiation reductions lie between 50 to 250 W/m² as in the one-dimensional simulations. The changes in temperature and water vapor mixing ratio are slightly higher than those in the one dimensional simulations mainly because of the higher values in the control case. Surface temperature decreases range from 1 to 4.5°C and water vapor mixing ratio fluctuates by 1 g/kg or less. Boundary layer depth is lowered by 50 to 300 m as in the single column case. However, the diurnal cycles of the boundary layer changes are very different. The wind speed decreases during the day and increases during the night. The wind direction change is within 20 degrees with sporadic changes reaching up to 100 degrees.

Figures 6-29 and 6-30 show the vertical distributions of meteorological fields at mid-day. The small difference in both the turbulent kinetic energy and the vertical diffusion coefficient is consistent with that in the boundary layer height at this time.

The mean and standard deviation of changes in surface meteorological fields due to aerosol radiative forcing are listed in Table 6.4. Large changes occur in wind and boundary layer height and small changes occur in absolute humidity and temperature. Shifting the aerosol loading from low-level to high-level results in about a factor of 2 increase in the magnitude of temperature and net downward SW radiation.

From the perspective of conducting air quality simulations, the aerosol-induced changes in meteorological fields would result in changes in temporal and spatial distributions of chemical species. In the following chapter, a photochemical model will be driven with meteorological fields under different aerosol loading scenarios to evaluate the possible changes in the chemical fields.

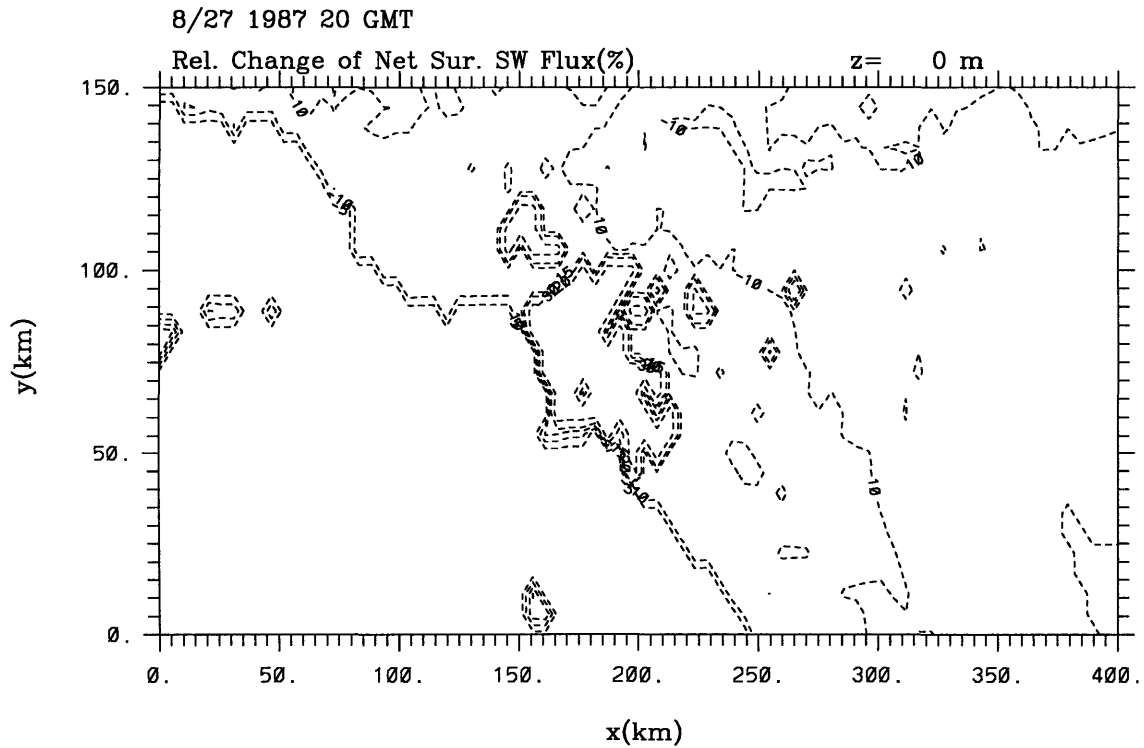
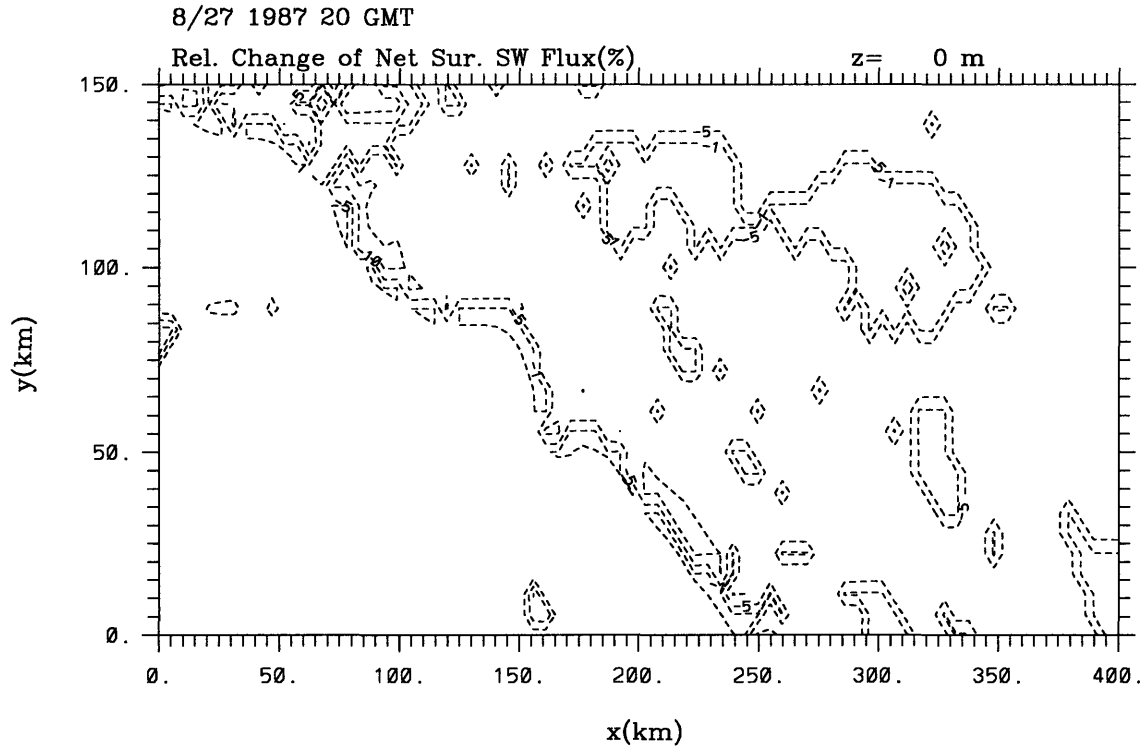


Figure 6-21: Relative change of net surface shortwave flux due to aerosols at 12 PST of August 27, 1987: top—low number density; bottom—high number density.

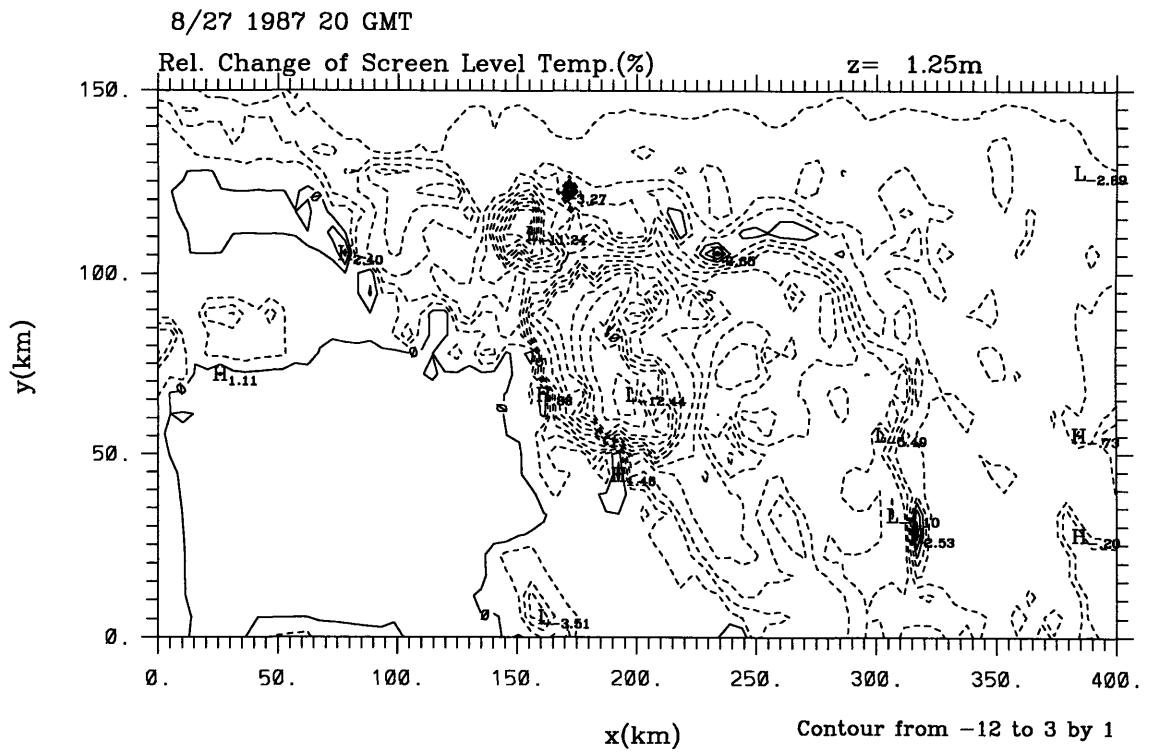
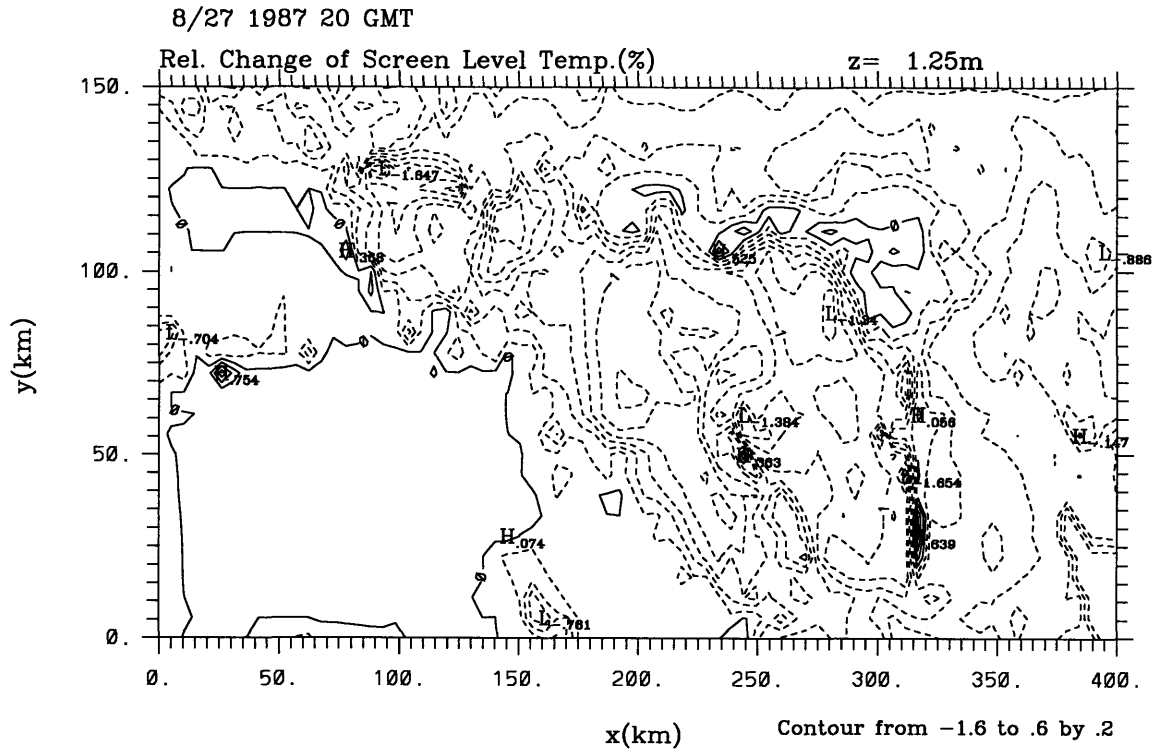


Figure 6-22: Relative change of surface temperature due to aerosols at 12 PST of August 27, 1987: top—low number density; bottom—high number density.

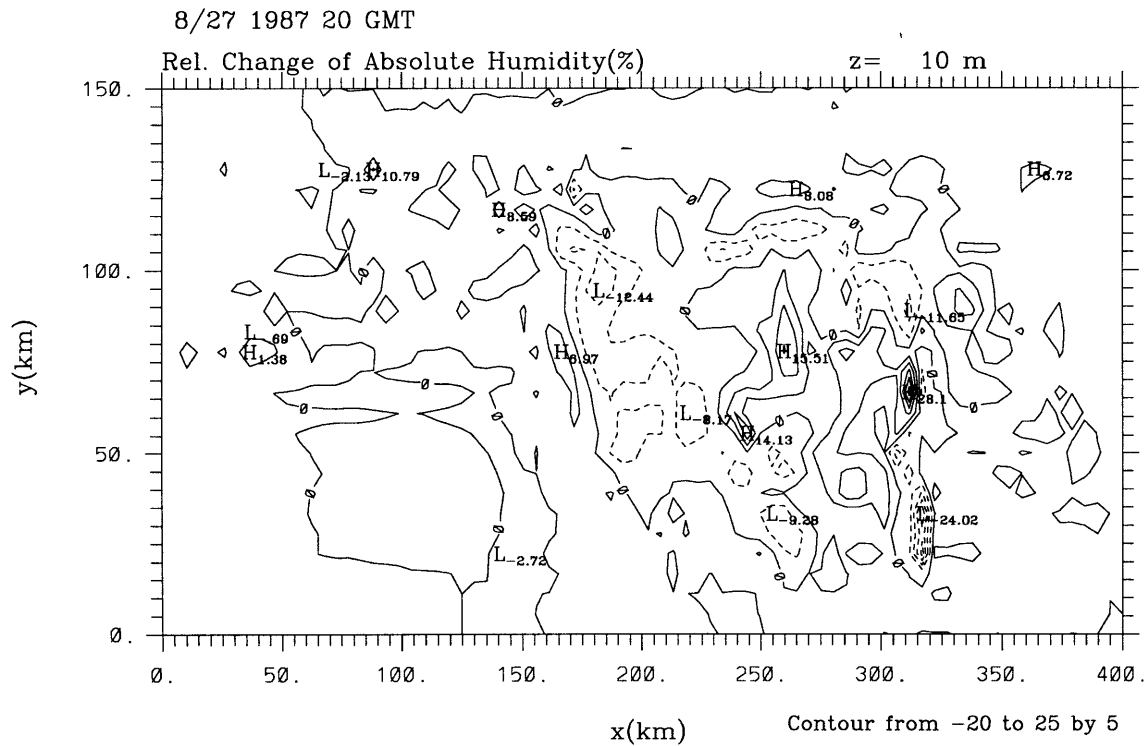
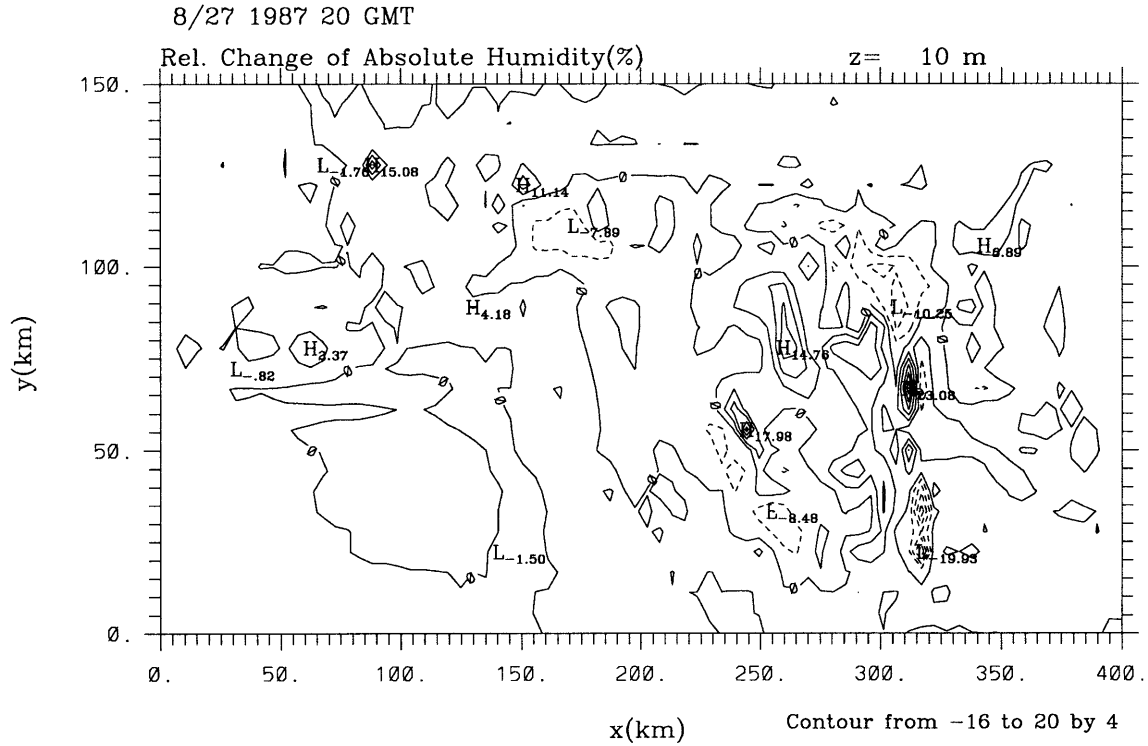


Figure 6-23: Relative change of water vapor mixing ratio at 10 m due to aerosols at 12 PST of August 27, 1987: top-low number density; bottom-high number density.

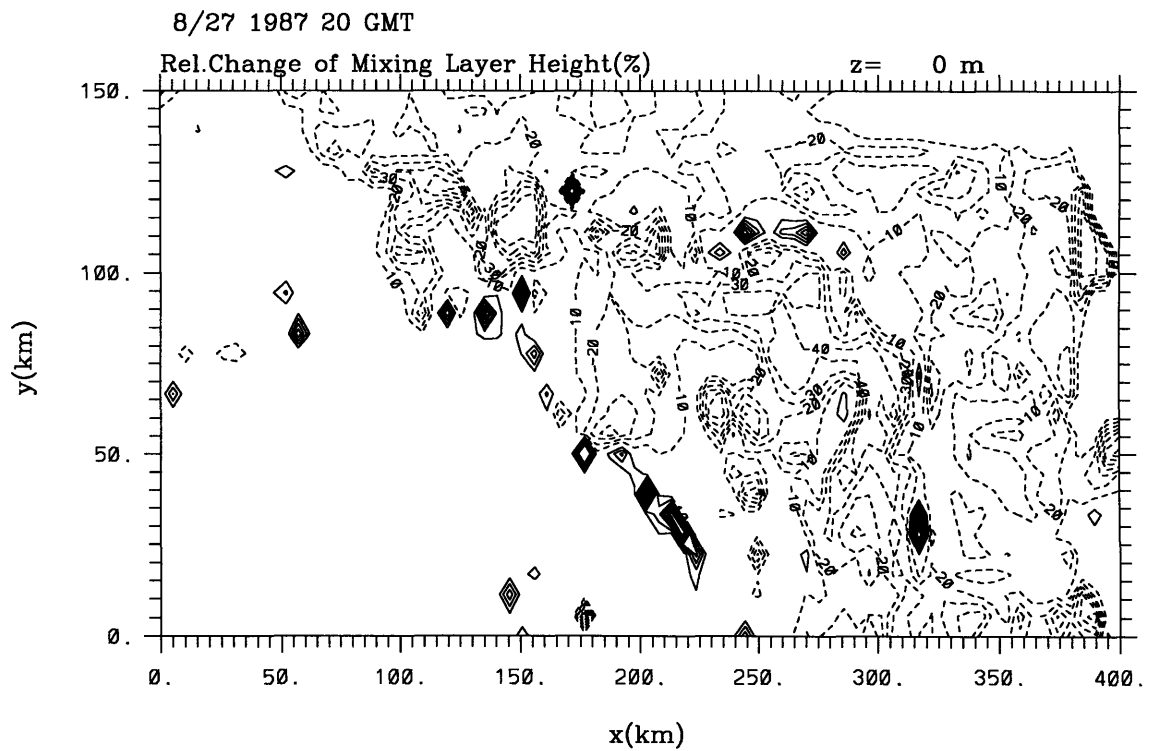
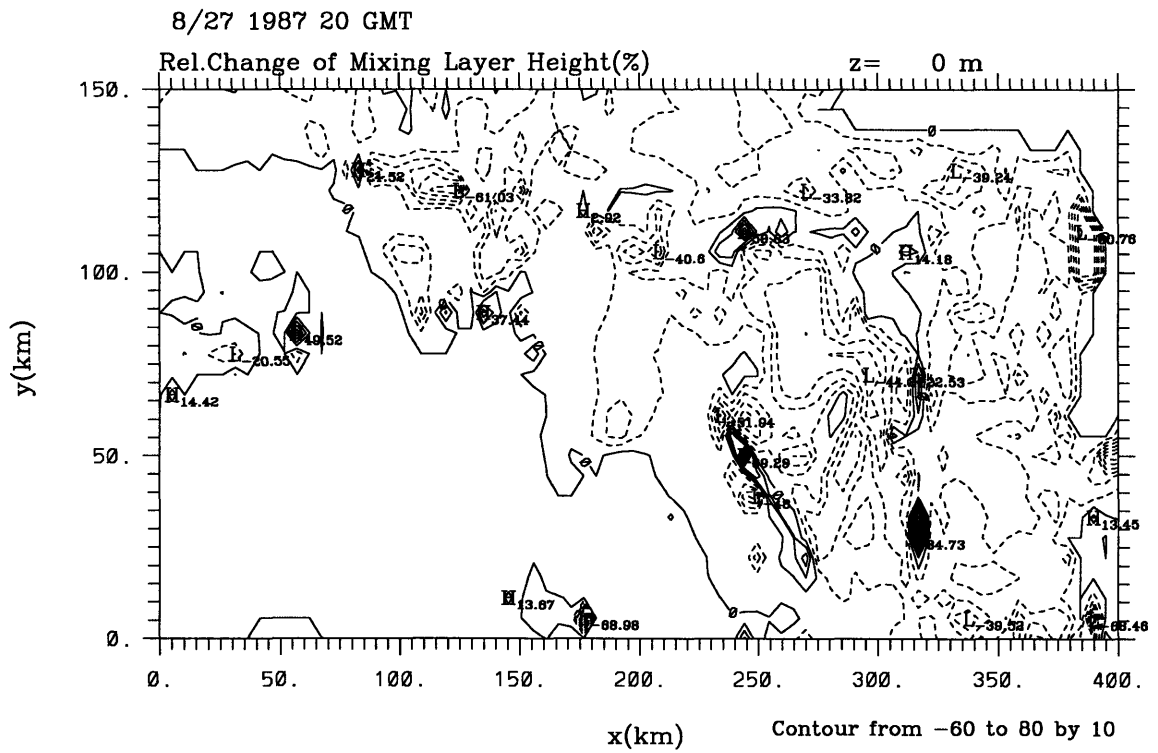


Figure 6-24: Relative change of mixing layer height due to aerosols at 12 PST of August 27, 1987: top—low number density; bottom—high number density.

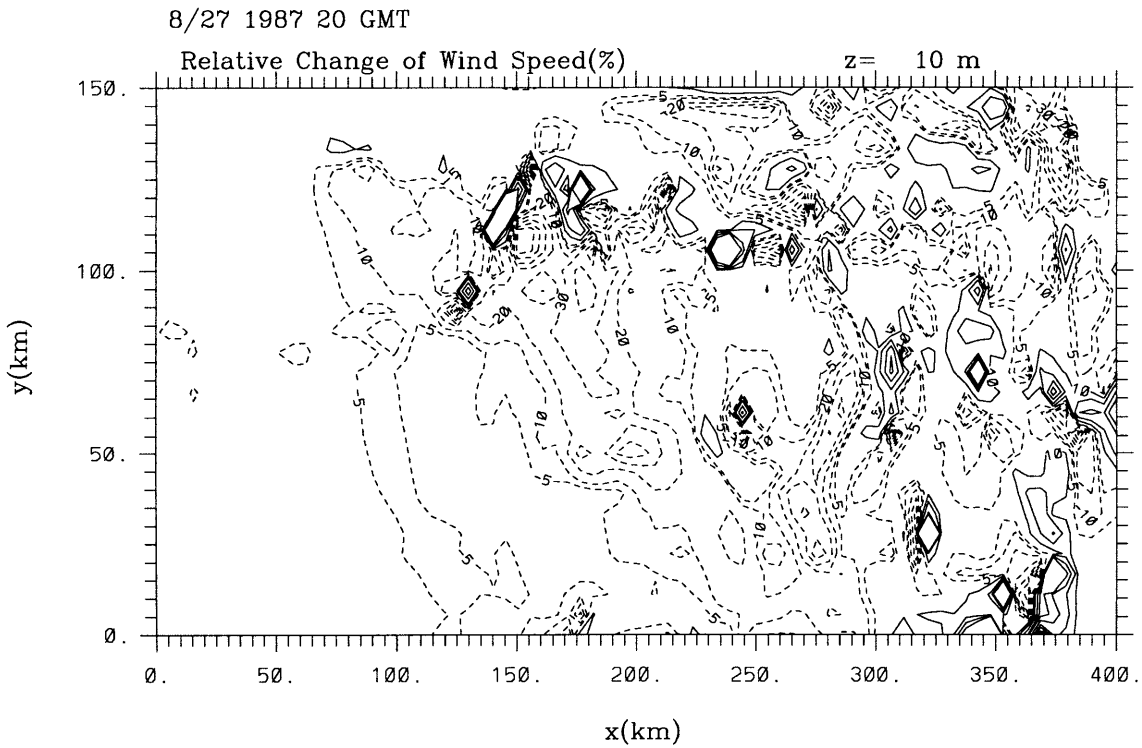
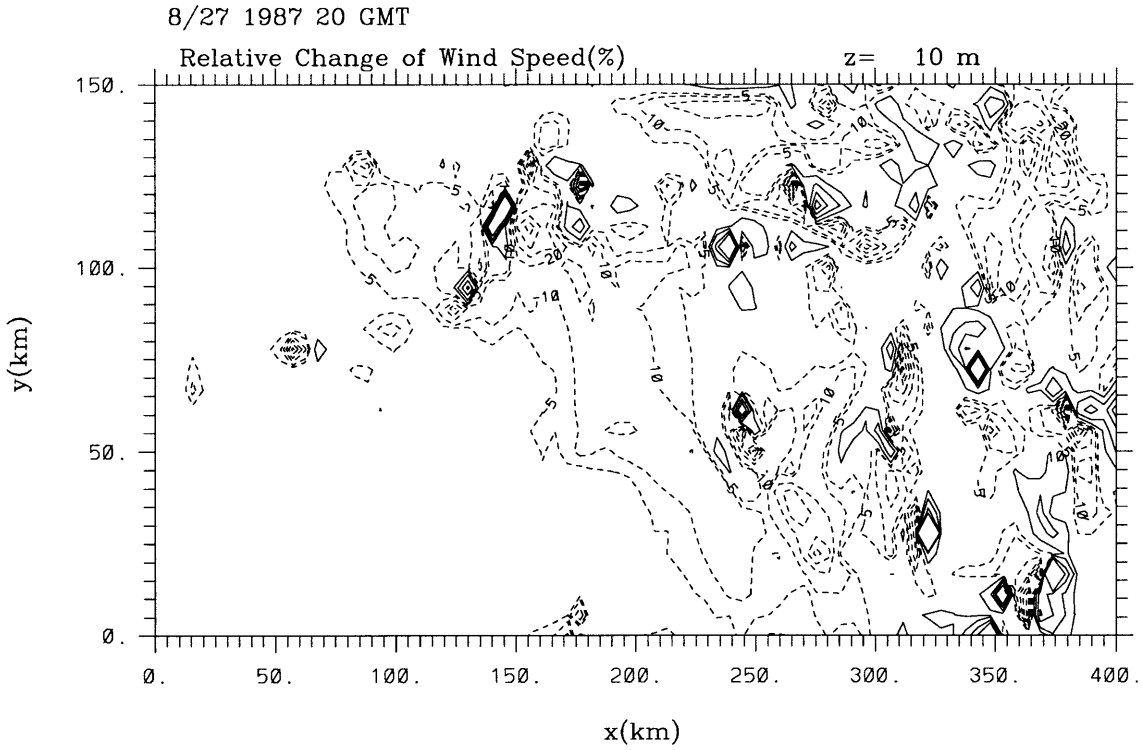


Figure 6-25: Relative change of horizontal wind speed at 10 m due to aerosols at 12 PST of August 27, 1987: top–low number density; bottom–high number density.

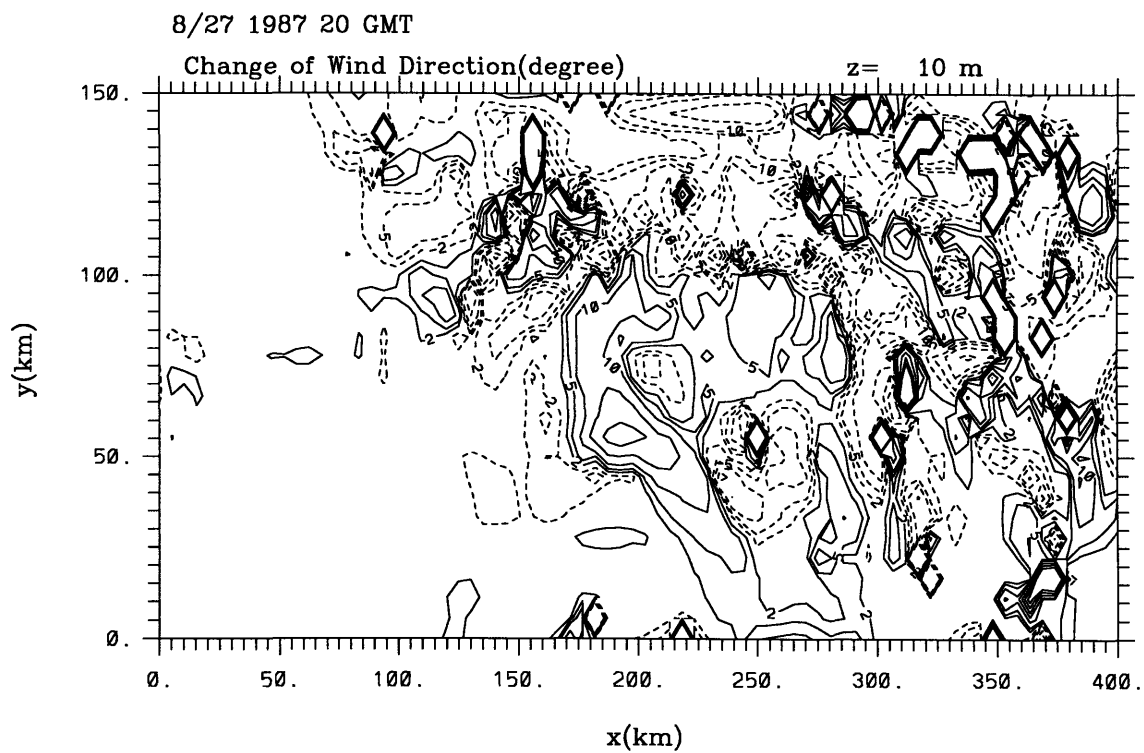
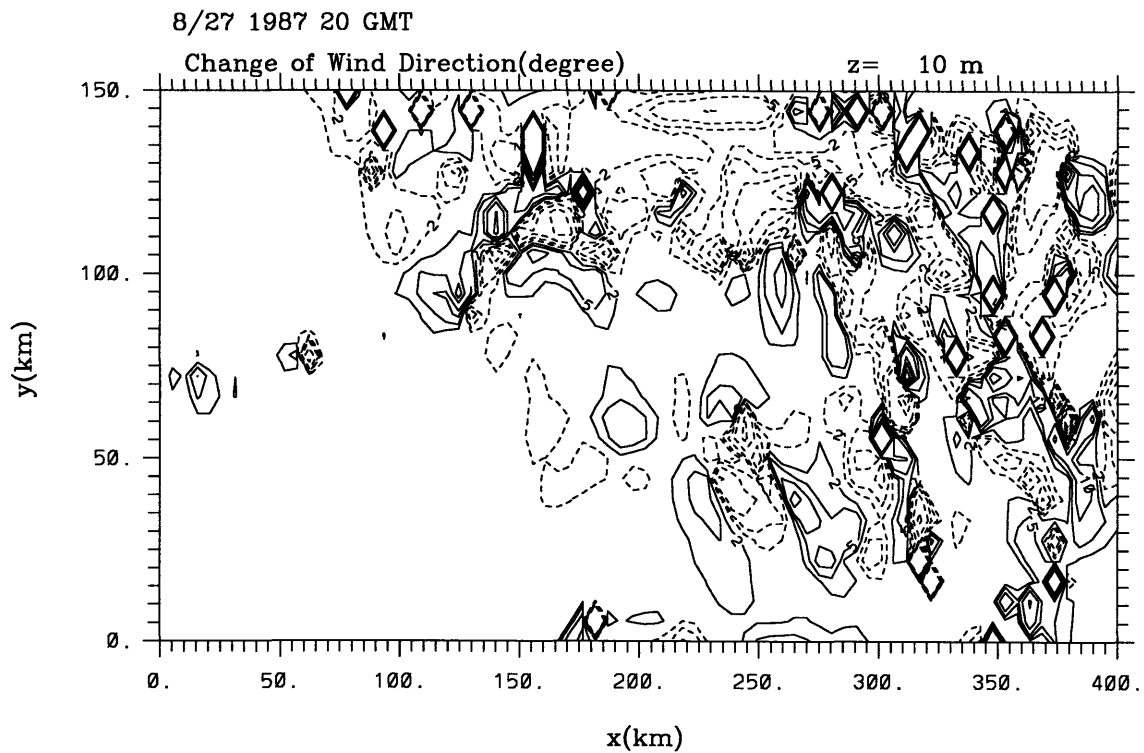


Figure 6-26: Relative change of horizontal wind direction at 10 m due to aerosols at 12 PST of August 27, 1987: top-low number density; bottom-high number density.

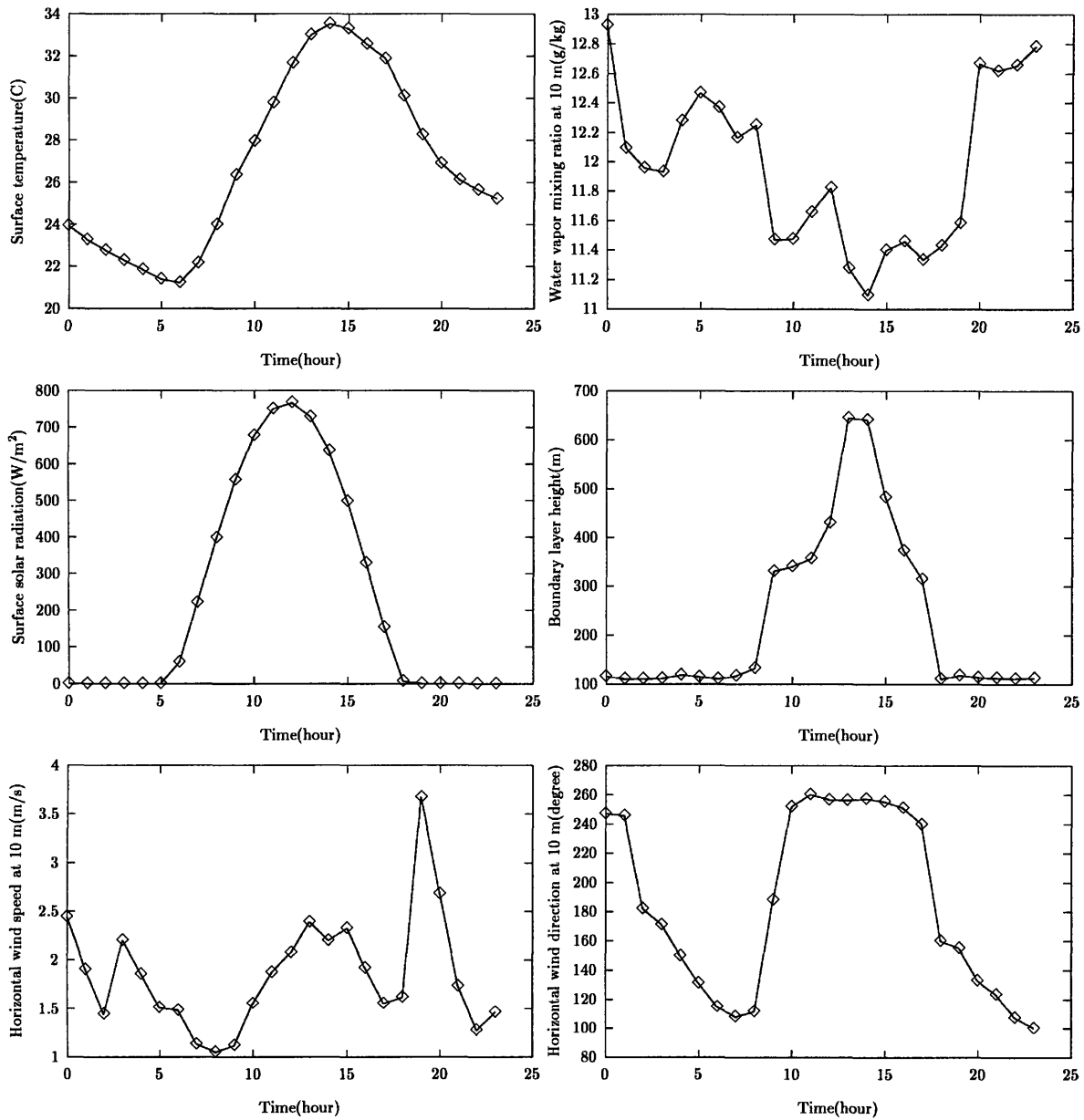


Figure 6-27: Diurnal variation of temperature, absolute humidity and solar radiation at surface, 10 m wind, and boundary layer height on August 27, 1987 at the center of the modeling domain.

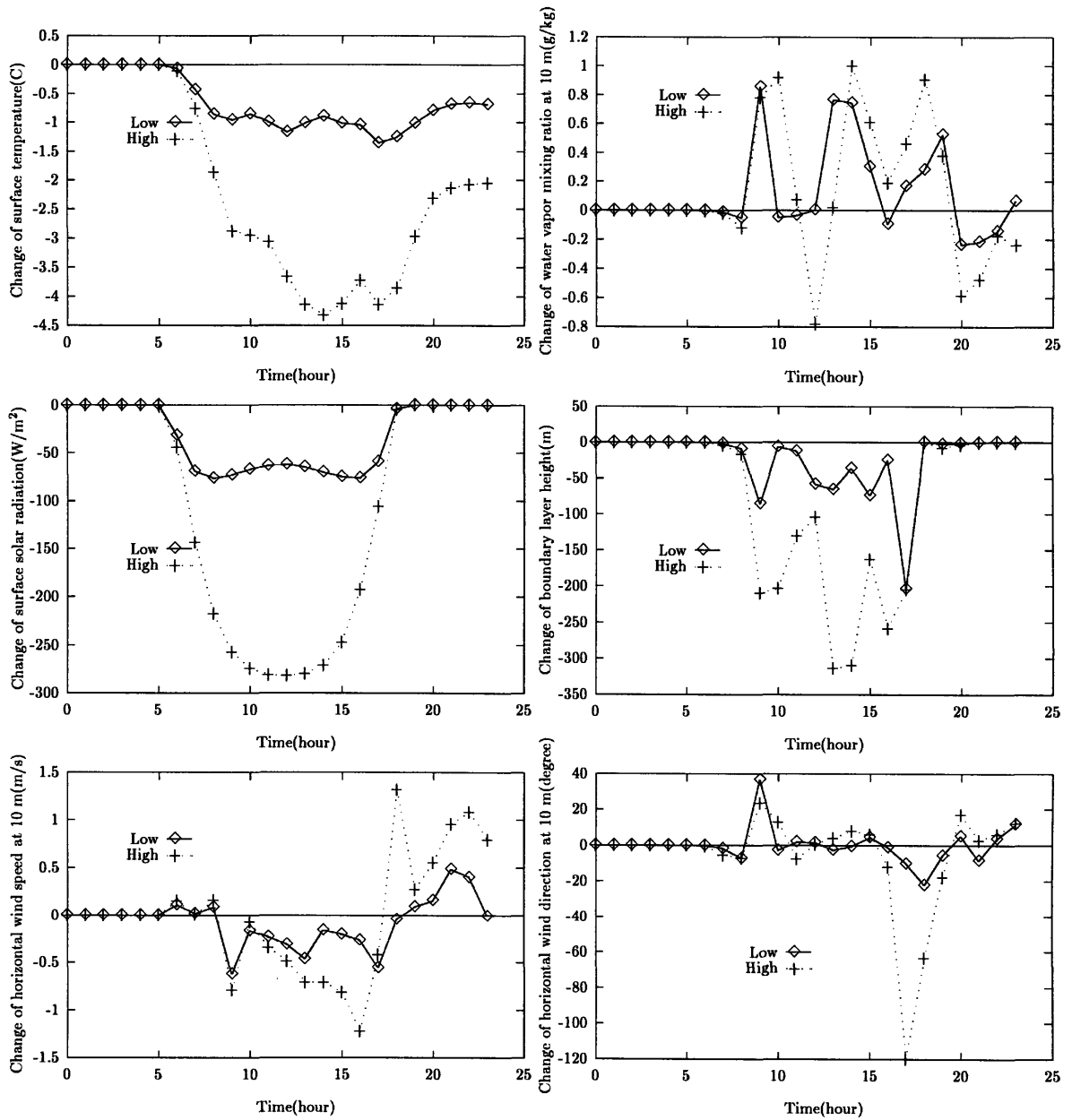


Figure 6-28: Aerosol-induced changes of diurnal variation of temperature, absolute humidity and solar radiation at surface, 10 m wind, and boundary layer height on August 27, 1987 at the center of the modeling domain.

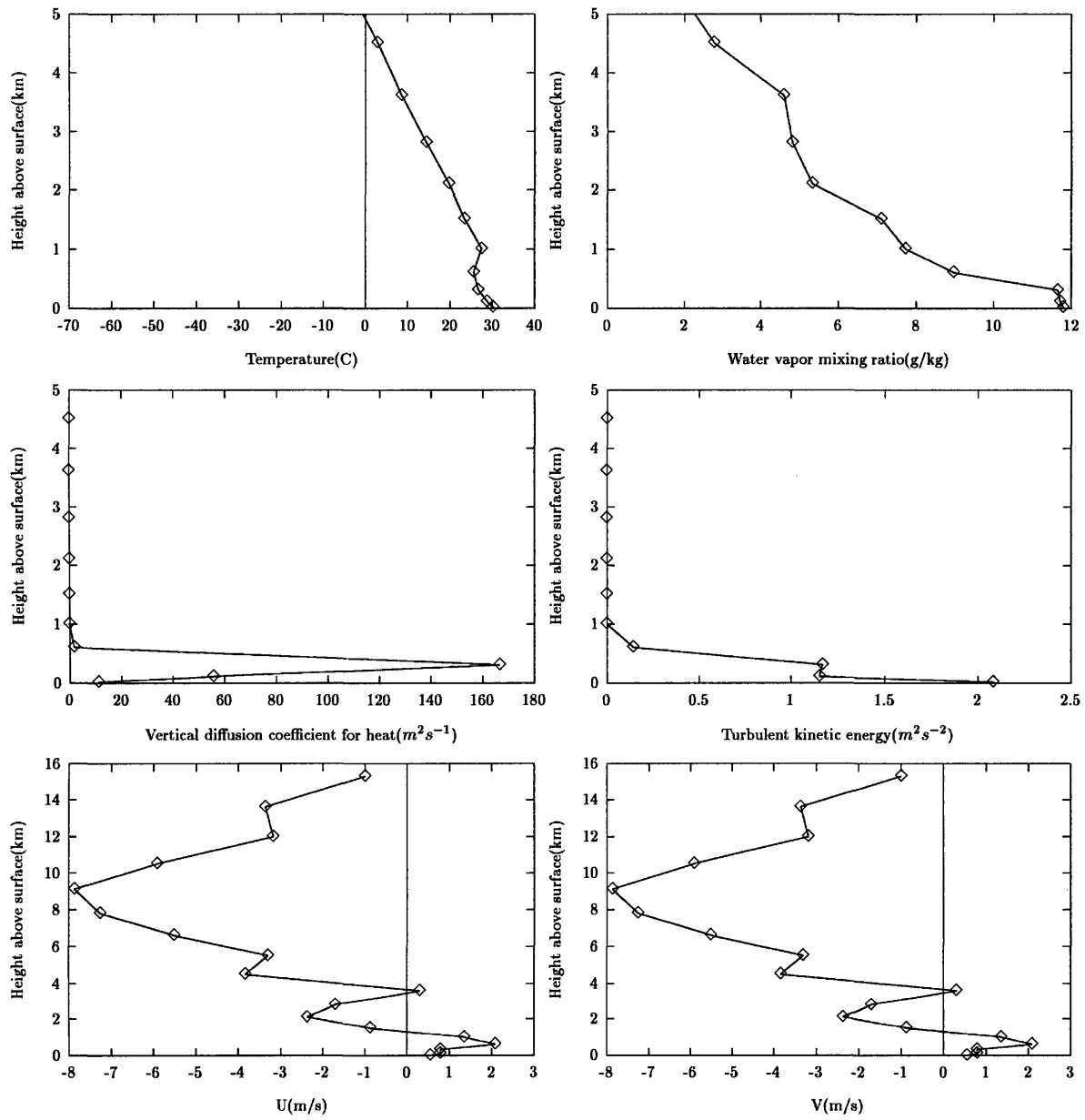


Figure 6-29: Vertical profiles of temperature, absolute humidity, turbulent kinetic energy, vertical diffusivity, and wind at 12 PST of August 27, 1987 at the center of the modeling domain.

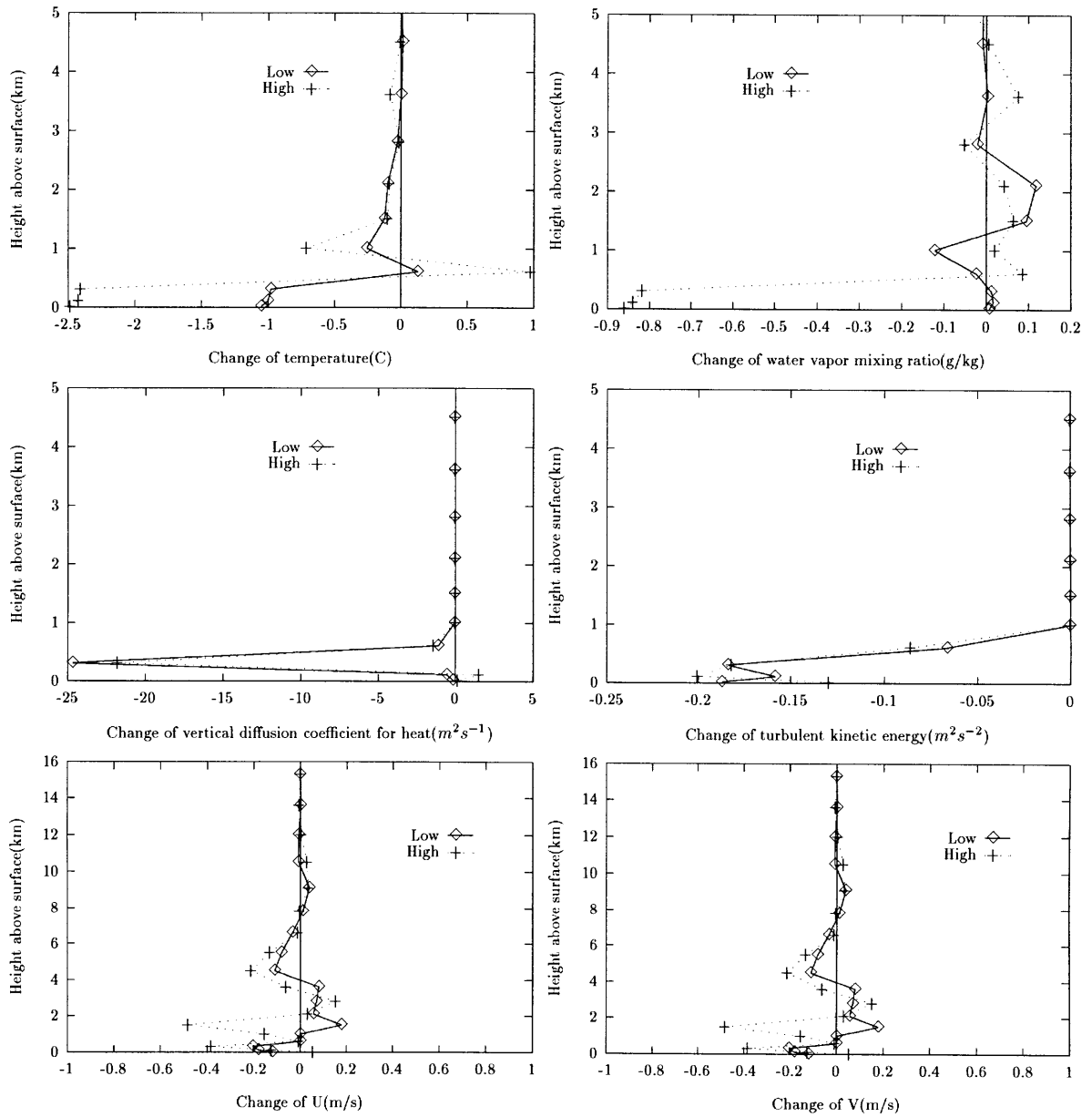


Figure 6-30: Aerosol-induced changes of vertical profiles of temperature, absolute humidity, turbulent kinetic energy, vertical diffusivity, and wind at 12 PST of August 27, 1987 at the center of the modeling domain.

Table 6.4: The mean and standard deviation of changes in meteorological fields due to aerosol radiative forcing on August 27, 1987. Temperature and radiation are at the surface; wind and humidity are at the first level (10m).

Absolute Change(degree)			Relative Change(%)		
Temperature	Wind direction	Absolute humidity	Boundary layer height	Net downward SW flux	Wind speed
-0.3±0.5	±45	±1	-5±13	-5±6	±25
-0.6±0.9	±50	±2	-10±18	-8±10	5±37

6.5 Conclusions

A mesoscale model has been applied to simulate the meteorological fields in the SCAQS region. Model sensitivity to both surface parameters and initial conditions is analyzed by using the observations of surface temperature and wind. Four different aerosol types from a climatological data set are introduced into the model based on the surface land use. Two different aerosol concentrations, both assumed well-mixed in the model boundary layer, are used to simulate the lower and higher level aerosol loading in the atmosphere. Humidity effects on aerosol optical properties are calculated using the initial and surface relative humidity. During the simulation, aerosol optical properties and number concentrations are fixed.

Aerosol effects are defined as the differences between meteorological fields with aerosols and those without aerosols in both one dimensional and three-dimensional model configurations. These effects are significant for the surface solar radiation, the boundary layer height, and the vertical diffusivity. For a large perturbation in the incoming solar radiation, the surface temperature change is limited by compensation of sensible, latent heat, and ground heat fluxes. The response in the dynamical processes as manifested in the changes of wind speed and wind direction is less significant. Therefore, results obtained in one dimensional simulations are generally good approximations to those in three-dimensional simulations.

Chapter 7

Model Responses to Aerosol Radiative Forcing: 3. Photochemical Air Quality

The temporal and spatial distribution of gas-phase chemistry is closely related to the ambient meteorology. As discussed in the previous chapter, aerosol radiative forcing modifies meteorological fields, especially the surface solar radiation, boundary layer height, and vertical diffusivity. Therefore changes in the concentration of chemical species due to aerosol radiative forcing may be expected. In this chapter, a three-dimensional photochemical air quality model will be used to quantify these changes. Two specific tasks include the model sensitivity to meteorological fields and the model responses to meteorological fields under different aerosol loading scenarios as simulated in the previous chapter.

7.1 Model Description

The model used here is the CIT photochemical air quality model¹, which has been described in detail previously [93]. The model equations take the form of Equation 2.8 and the model solves the species continuity equations using the operator splitting method. Diffusion is handled with explicit second-order finite differences. Advection is treated using implicit fourth-order finite element integration with spatial filtering in the horizontal and explicit first-order upstream finite difference in the vertical. Turbulent mixing is parameterized using the k -theory, where the diffusion coefficients are functions of Monin-Obukhov length and surface roughness height. Dry deposition is modeled through pollutant deposition velocities, which are also functions of Monin-Obukhov length and surface roughness height. The photochemical reaction mechanism employed in the CIT air quality model is based on the work of Lurmann *et al.* [89]. Thirty-five species and 106 reactions are included with 9 species specified in the initial conditions and 16 species specified in the emission inventory.

The emission inventory is from the California Air Resources Board [157]. Mobile source emission estimates are based on a travel demand model and the EMFAC 7E emission factor model [172]. Stationary source emission estimates, including day-specific power plant, air-

¹The acronym CIT is derived from the initials of the two organizations responsible for developing the air quality model, the California Institute of Technology and the Carnegie Institute of Technology at Carnegie Mellon University.

craft, and refinery emissions, are from the South Coast Air Quality Management District. In addition to the anthropogenic emissions, emissions of rural and urban vegetation and of ammonia from decomposition of livestock waste and from farm-related fertilizer use are also included.

Meteorological fields are estimated for each grid cell from measurements at nearby monitoring sites, using a weighted interpolation scheme [58, 59]. In this scheme, the weighting functions vary inversely with distance squared between the monitor and interpolation point. Mixing heights are inferred from the vertical profile of potential temperature derived from the upper air soundings.

The model has been used to study photochemical smog formation in the Los Angeles area [95, 123], formation and control of nitrogen-containing pollutants [123, 124], spatial patterns in pollutant responses to emission controls [98], effect of methanol fuel use in motor vehicles [126], modeling and control of deposition of nitrogen-containing air pollutants [125], and the effect of organic gas emissions on ozone concentration underpredictions in SCAQS [64].

7.2 Model Sensitivity to Meteorological Fields

Meteorological fields are necessary components of a photochemical model. They traditionally are obtained based on the objective analysis of *in situ* measurements in the modeling domain [95, 123, 64, 80]. Recently, three-dimensional mesoscale models have been used to generate the required meteorological data for photochemical modeling [140]. At this moment, no study has been carried out to quantitatively compare the model performance using a mesoscale model with that using observed winds with objective analysis.

Compared to the approach using with objective analysis of observations, mesoscale meteorological models offer the opportunity for reducing measurement cost, adding flexibility of generating meteorological fields under different weather conditions, and ensuring consistency by treating atmospheric processes which are important from both meteorological and chemical perspectives. These processes include in-cloud aqueous phase chemistry, cumulus convection, radiation, cloud nucleation, and boundary layer turbulence.

The meteorological fields required by the CIT photochemical air quality model are temperature, absolute humidity, solar radiation, cloud cover, mixing layer height, and three-dimensional winds. The original model has been modified to use mesoscale model outputs for all the above fields except ultraviolet radiation due to the single band treatment of radiative transfer. In addition, the vertical diffusion coefficient has been obtained from the mesoscale model, compared with the original formulations based on the roughness height, the Monin-Obukhov length, the convective velocity, and the friction velocity [95].

The modeling region and period are the same as those for the mesoscale modeling discussed earlier, i.e., SCAQS region in August of 1987. The horizontal resolution is 5 km and the vertical levels above the topography are set at 0, 38.5, 154, 308, 671, and 1100 m respectively.

Before simulating the aerosol radiative effect on gas-phase chemistry, I will test the model sensitivity to five meteorological fields: temperature, absolute humidity, boundary layer height, solar radiation, and wind. Combined with the aerosol-induced changes in meteorological fields as obtained in the previous chapter, the sensitivity results can be used to gain a qualitative sense of the aerosol radiative effect on gas-phase chemistry.

One control experiment and five sensitivity experiments are carried out with the mete-

orological fields of August 27 from the objective analysis. In each sensitivity experiment a specific meteorological field is perturbed by a certain percentage with all of the other fields fixed to the control. Therefore the model sensitivity to a given meteorological field can be inferred from the difference of model outputs relative to the control. Of the 35 species being modeled, particular attention is paid to eight species: NO, NO₂, HO₂, O₃, CO, SO₂, SO₃, and NIT (ammonium nitrate). The first four species are selected since they are the main components in forming photochemical smog. SO₂, SO₃, and ammonium nitrate are directly related to aerosol concentration. The concentration of CO can be viewed as a tracer due to its typical reaction time scale of a week.

Figures 7-1 and 7-2 show the simulated ground level concentrations of eight species at 12 and 23 PST of August 27, 1987 using analyzed meteorological fields. The concentration of CO follows the emission pattern and shows no significant diurnal variation. This is consistent with its characteristic of resembling a passive tracer. HO₂ is formed mainly through photolysis or reaction with OH of oxidation products of hydrocarbons such as formaldehyde HCHO and consumed in the reaction of converting NO to NO₂. Its distribution of concentration appears mirroring that of NO. O₃ is produced as a result of photolysis of NO₂ and conversion of NO to NO₂ in the presence of HO₂ radical. Therefore its distribution is highly related to that of NO₂ and HO₂ and displays large diurnal variation. The concentration of SO₂ is governed by its emission with higher values during the evening, suggesting higher night-time emission. SO₃ is produced as SO₂ reacts with OH radical and its distribution and diurnal variation resemble those of SO₂. In the current CIT model, ammonium nitrate comes from the reaction of NH₃ and HNO₃, the latter of which is formed from NO₂ oxidation with OH radical. Therefore its concentration depends on both NH₃ emission and the concentration of nitric acid. Results show large diurnal variation of spatial pattern, although the magnitude of concentration shows little change.

Figure 7-3 shows the change of ground level concentrations corresponding to 50% decrease in the surface temperature at 12 PST of August 27, 1987. Both SO₂ and CO fields are insensitive to temperature change. A 20% to 40% decrease in SO₃ and a 10% to 200% increase in ammonium nitrate are observed. HO₂ decreases by about 10% to 40%, corresponding to a 10 to 70% increase in NO and a similar percentage decrease in NO₂. As a result, 10% to 30% decrease in O₃ is observed.

The model sensitivity to a 50% decrease in the surface absolute humidity is shown in Figure 7-4. In contrast to the results in Figure 7-3, the ammonium nitrate decreases by 10 to 30% and NO₂ increases by 10 to 30%.

Figure 7-5 shows the model sensitivity to 50% decrease in solar radiation. Species which are not related to photolytic reactions, namely NO, SO₂, ammonium nitrate, and CO, appear insensitive to the change in the radiation field. On the other hand, species which are related to photolytic reactions show high sensitivity. For example, NO₂ gains about 10 to 30% increase in its concentration, resulting in a similar percentage decrease in O₃ concentration. A 10% to 30% decrease in the concentration of HO₂ is also observed, mainly due to the slowdown of photolysis of oxidation products of hydrocarbons and decrease in OH concentration. The decrease in OH concentration also leads to a 20 to 30% decrease of SO₃.

Figure 7-6 shows the change of ground level concentrations to 50% reduction in boundary layer height. Large positive changes of up to 100% are observed in NO_x and NIT. The changes in SO₂, SO₃, and CO ranges up to 50%, with both positive and negative variations. Smaller changes of around 10% are seen in the concentration fields of HO₂ and O₃.

Finally Figure 7-7 shows the change of ground level concentrations to 50% reduction in

Table 7.1: The mean and standard deviation of relative changes(%) of chemical fields due to uniform perturbation or aerosol-induced changes in meteorological fields on August 27, 1987.

Pert. Case	-50%					Aerosol Loading	
	Temp.	Humid.	Rad.	H _{BL}	Wind	Low	High
NO	15±40	7±12	±10	13±35	5±20	1±9	7.5±17.5
NO ₂	-5±15	-5±15	10±12	10±25	2±19	2±6	8±15
SO ₂	4±5	1.5±2.2	5±8	-5±20	7±25	±8	5±15
SO ₃	-20±25	-10±10	-20±25	-15±30	15±30	2±10	5±15
HO ₂	-20±35	-6±12	-14±22	±10	2±10	-3±6	-3±9
O ₃	-15±25	-1±7	-13±15	-5±10	2±10	±8	±10
NIT	100±250	-5±10	±5	20±60	40±150	25±200	100±600
CO	-0.6±1	0.06±0.5	1±3	22±35	5±15	2.5±7.5	5±15

wind field. Changes of up to 50% are observed in NO, NO₂, SO, SO₂, and HO₂. Smaller changes (10-20%) occur for CO and O₃; whereas a larger change of up to 80% occur for the ammonium nitrate.

Overall, the CIT model shows higher sensitivity to the boundary layer height and temperature and lower sensitivity to the wind, radiation and absolute humidity fields for spatially uniform perturbations in meteorological fields. A summary of the mean and standard deviation of relative changes of chemical fields is given in Table 7.1.

7.3 Model Responses to Aerosol-induced Meteorological Changes

To investigate the aerosol effects on air quality simulation, the CIT airshed model is driven by the mesoscale outputs with or without aerosols. Figures 7-8 and 7-9 show the relative change of the predicted spatial distributions of chemical species for two different loadings of aerosols at 12 PST of August 27, 1987.

The ground level concentrations of NO, NO₂, SO₂, and CO increases by 10% to 30% for low level aerosol loading, mostly in the coastal urban area where high emissions occur. Changes in SO₃, HO₂, and O₃ are within 10% with increases in the coastal region and decreases toward in-land areas. Higher sensitivity is observed for the ammonium nitrate.

The patterns of chemical field changes due to high-level aerosol loading are similar to those due to low-level aerosol loading. The magnitudes of response increase by up to a factor of 2.

As shown in Table 7.1, SO₂ and CO are insensitive to meteorological fields of temperature, humidity, and solar radiation. Therefore their changes to aerosol radiative forcing must have resulted from changes in the boundary layer height and wind. For other species, the resulted changes are results of combined effects of all the five meteorological fields considered here. Since the responses of chemical fields to different meteorological fields are not necessarily correlated, the the spatial pattern in the response of chemical fields bears little or no resemblance to that in any single meteorological perturbation.

The mean and standard deviation of relative changes(%) of chemical fields due to aerosol-

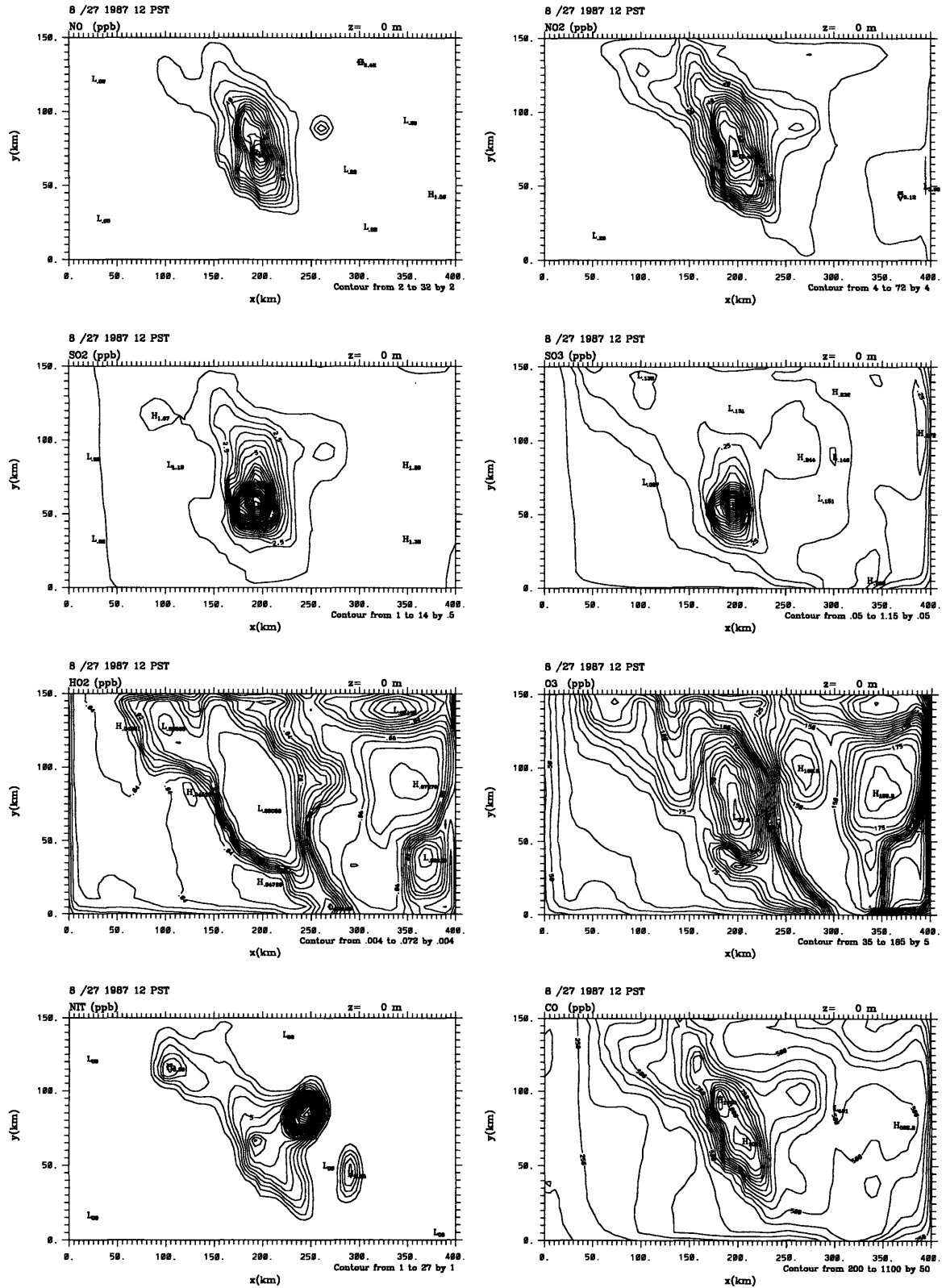


Figure 7-1: Simulated ground level concentrations of NO, NO₂, SO₂, SO₃, HO₂, O₃, NIT, and CO at 12 PST of August 27, 1987 using analyzed meteorological fields.

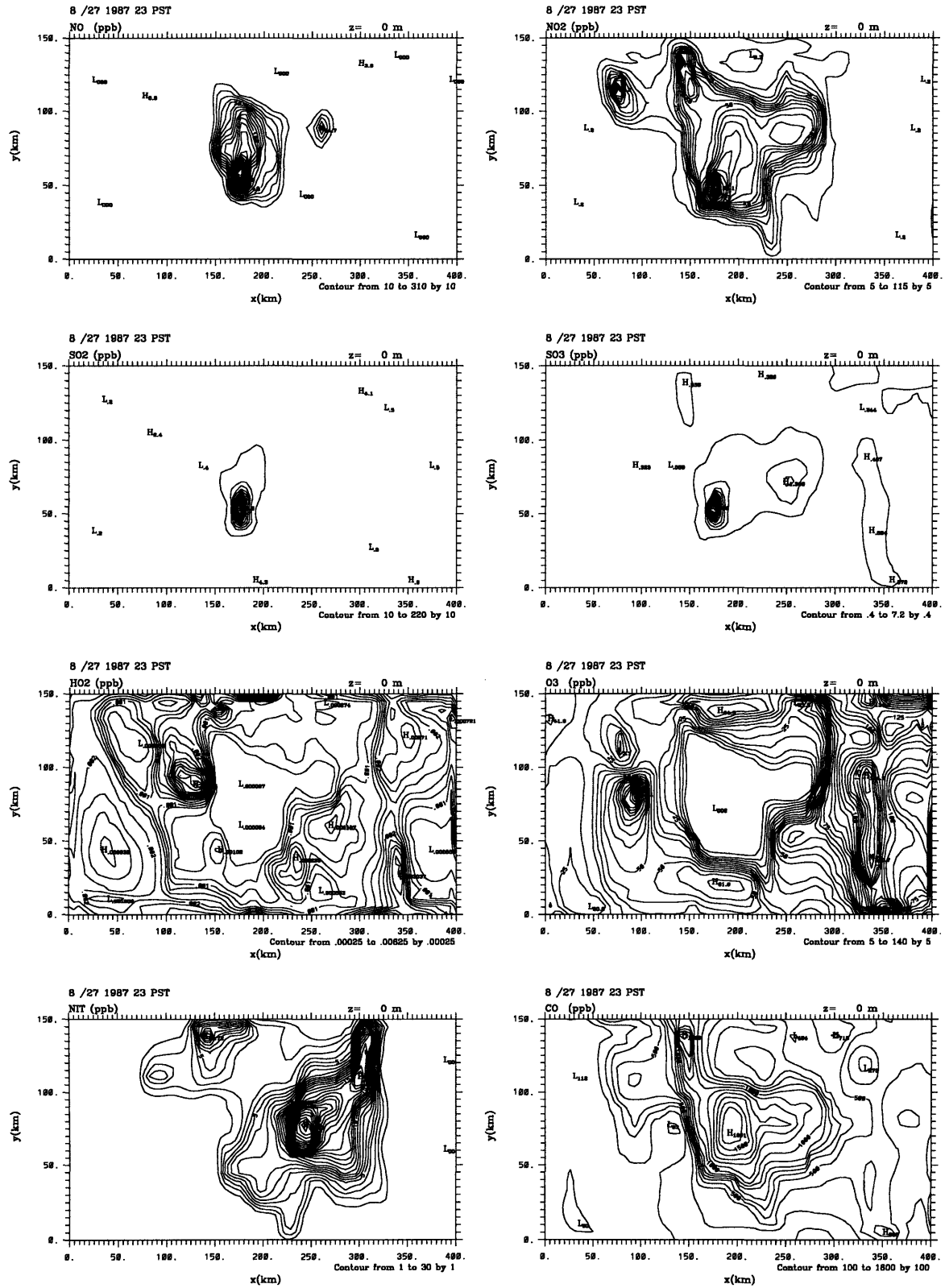


Figure 7-2: Simulated ground level concentrations of NO, NO₂, SO₂, SO₃, HO₂, O₃, NIT, and CO at 23 PST of August 27, 1987 using analyzed meteorological fields.

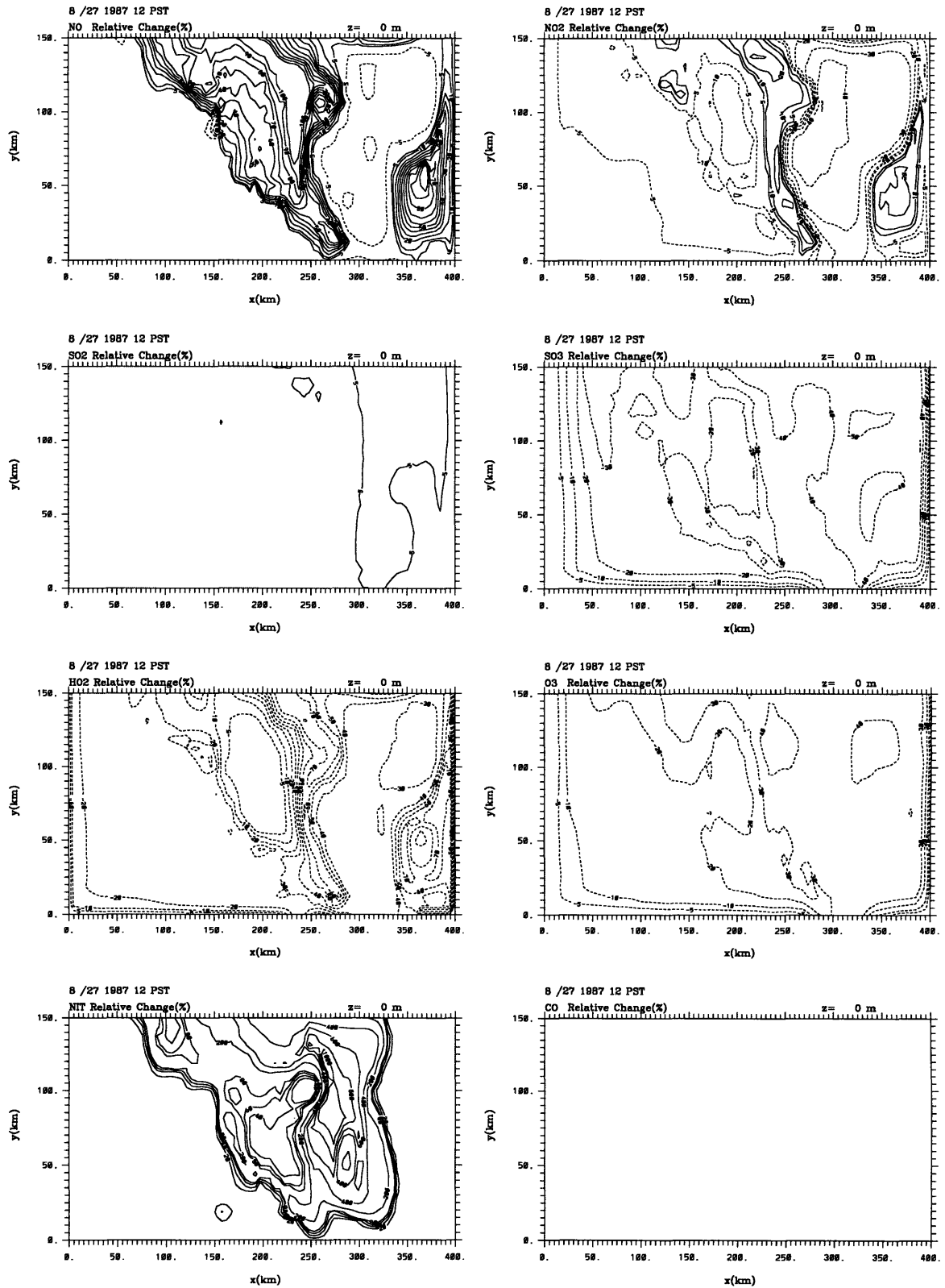


Figure 7-3: Relative change of ground level concentrations of NO, NO₂, SO₂, SO₃, HO₂, O₃, NIT, and CO corresponding to 50% change in surface temperature at 12 PST of August 27, 1987.

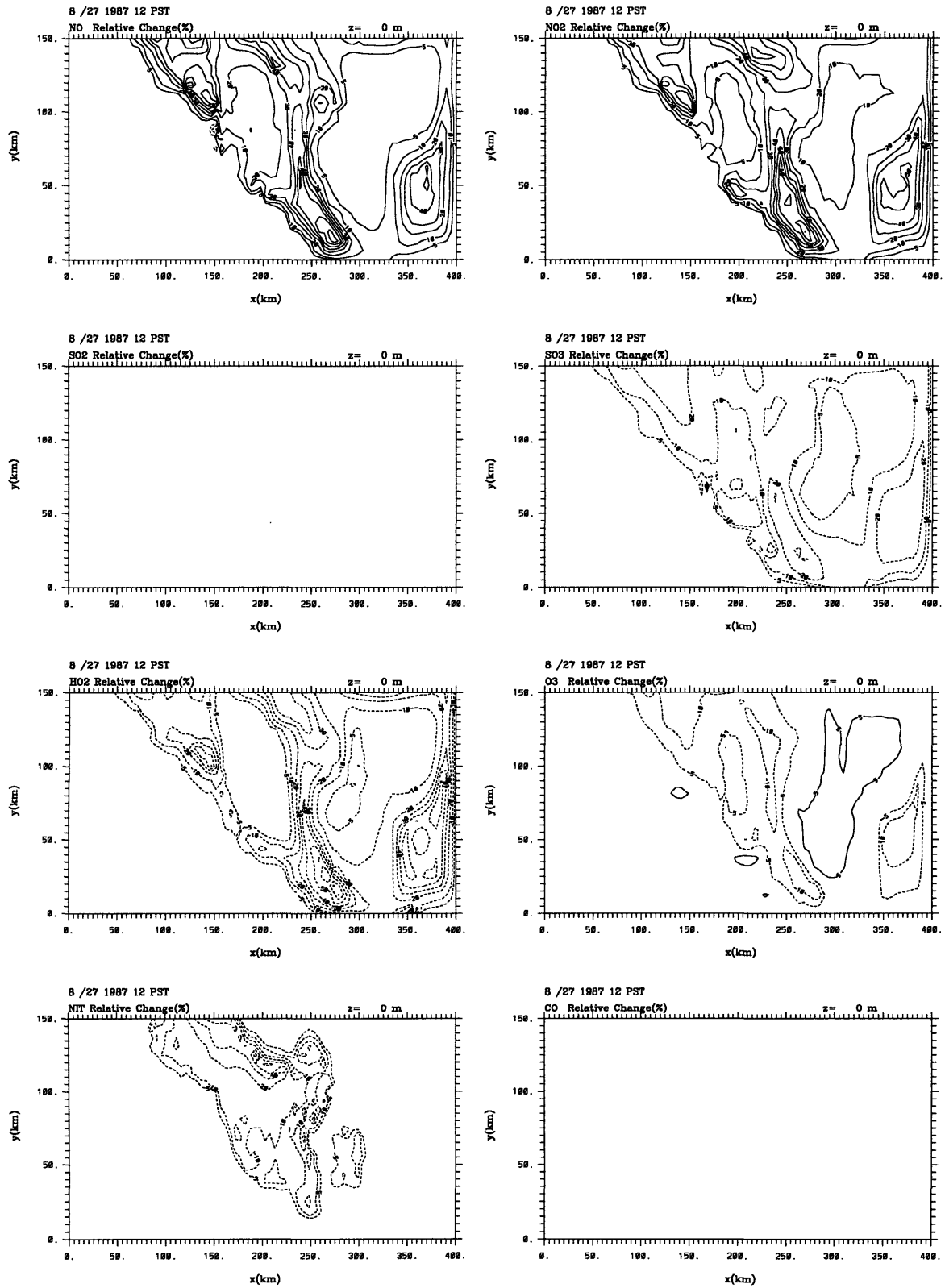


Figure 7-4: Relative change of ground level concentrations of NO, NO₂, SO₂, SO₃, HO₂, O₃, NIT, and CO corresponding to 50% change in surface absolute humidity at 12 PST of August 27, 1987.

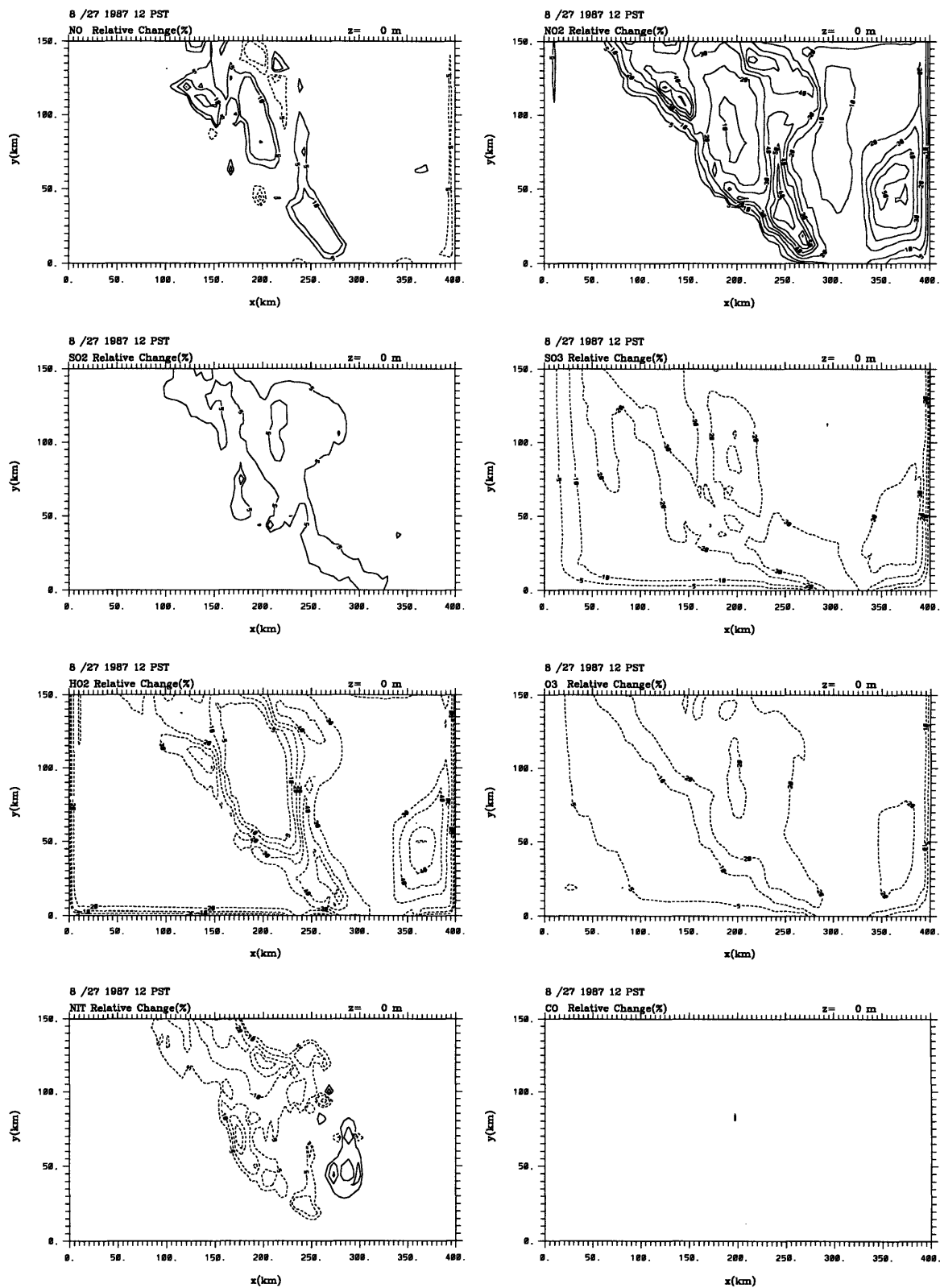


Figure 7-5: Relative change of ground level concentrations of NO, NO₂, SO₂, SO₃, HO₂, O₃, NIT, and CO corresponding to 50% change in surface solar radiation at 12 PST of August 27, 1987.

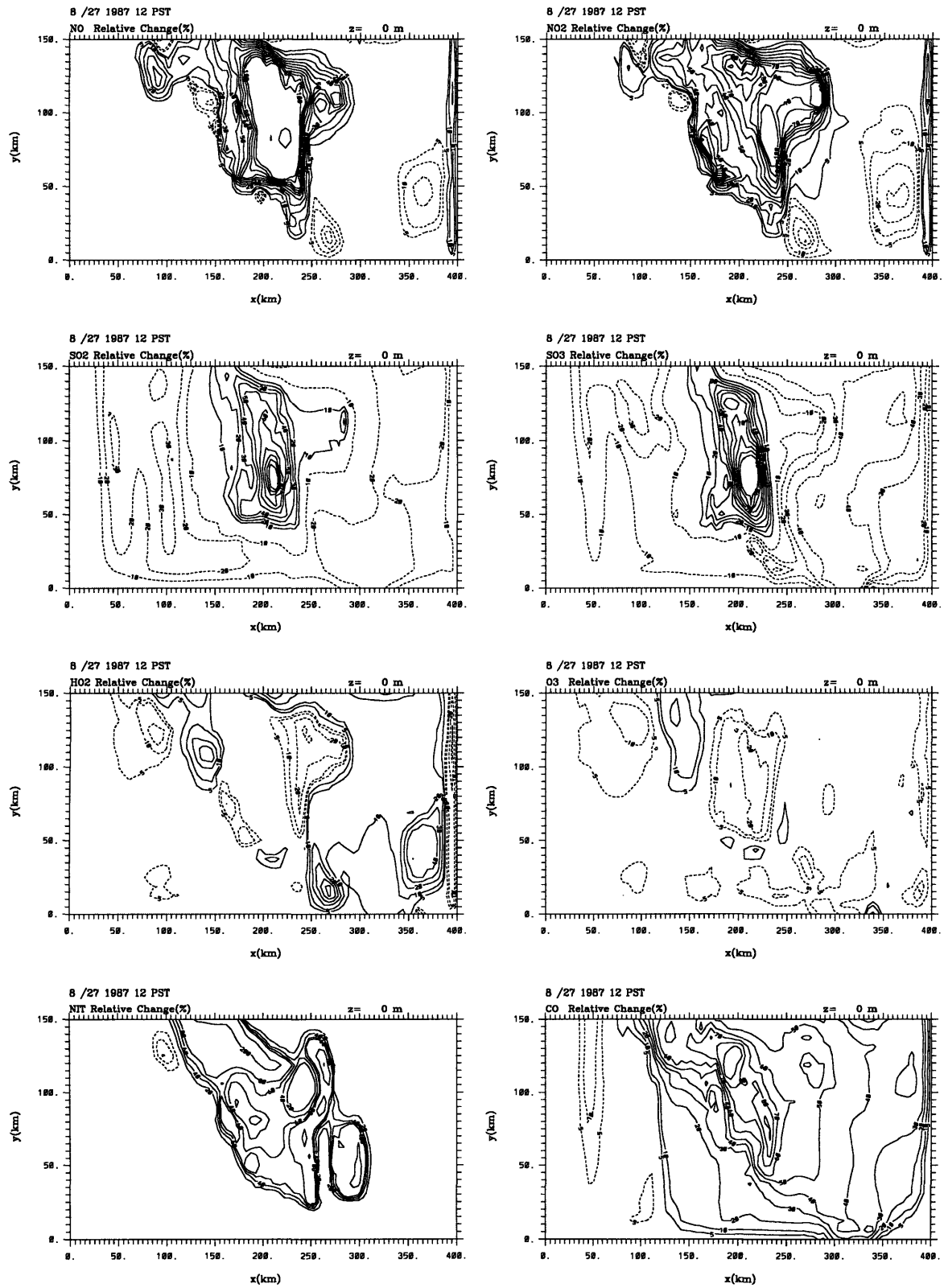


Figure 7-6: Relative change of ground level concentrations of NO, NO₂, SO₂, SO₃, HO₂, O₃, NIT, and CO according to 50% change in boundary layer height at 12 PST of August 27, 1987.

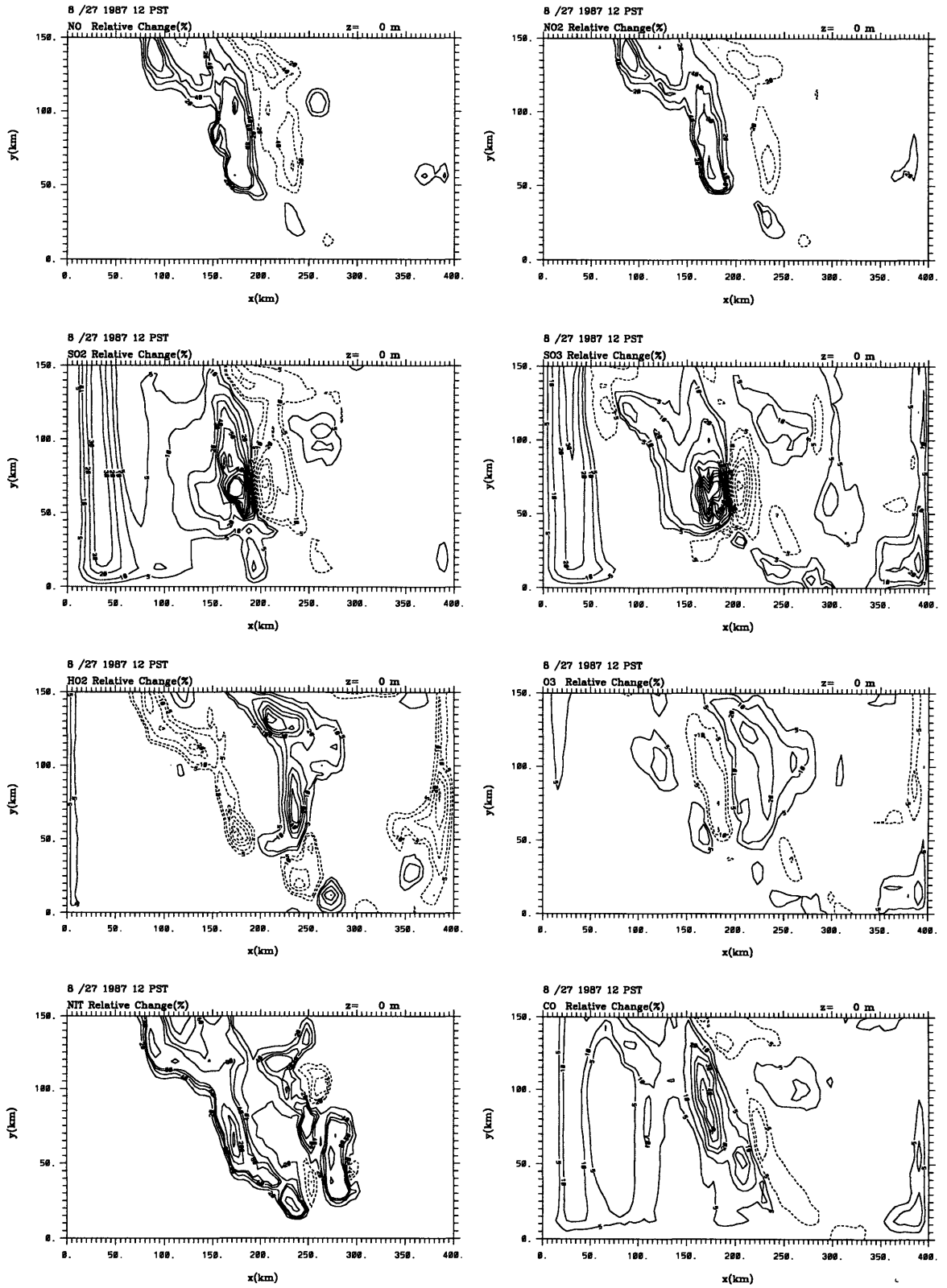


Figure 7-7: Relative change of ground level concentrations of NO, NO₂, SO₂, SO₃, HO₂, O₃, NIT, and CO corresponding to 50% change in wind field at 12 PST of August 27, 1987.

induced changes in meteorological fields are listed in Table 7.1.

Figure 7-10 shows the relative change of ground-level O₃ concentration at two selected sites with low and high aerosol loadings on August 27, 1987. Large diurnal variations are clear and changes at several time periods are much larger than the domain-averaged changes in Table 7.1.

Since in the above calculations the aerosol-induced radiative effect on chemical species is only accounted for in the visible range, the aerosol effect on photolysis needs to be addressed. Although in general a multi-band radiative transfer scheme is required to accurately calculate the actinic flux change due to aerosols and thus to determine this effect, it can be simply estimated from results in Tables 6.4 and 7.1 as follows. As in Tables 6.4, the net downward short-radiative flux decreases by less than 30% due to aerosols. Therefore, if the change of ultraviolet radiation is assumed the same as the visible radiation, it will cause changes of chemical fields about half of those in the sensitivity experiment of 50% decrease in solar radiation in Table 7.1. This implies that our results would underestimate the aerosol effect on chemical fields by less than 10%.

7.4 Conclusions

In this chapter, the CIT photochemical air quality model has been used to study the aerosol radiative forcing on gas-phase chemistry. The model sensitivity to meteorological fields is carried out with a uniform perturbation of five meteorological variables.

Aerosol effects on the prediction of species concentration are investigated using meteorological fields with or without aerosol radiative forcing. The domain-averaged relative changes of ground level concentrations of chemical species due to low-level aerosol loading range up to 10%. Shifting aerosol loading from the low-level to high-level appears to almost double the concentration response of species during the day. Changes at specific sites can be much larger than the domain-averaged changes. The spatial patterns of the aerosol-induced changes in the chemical fields bear little or no resemblance to those in the meteorological fields.

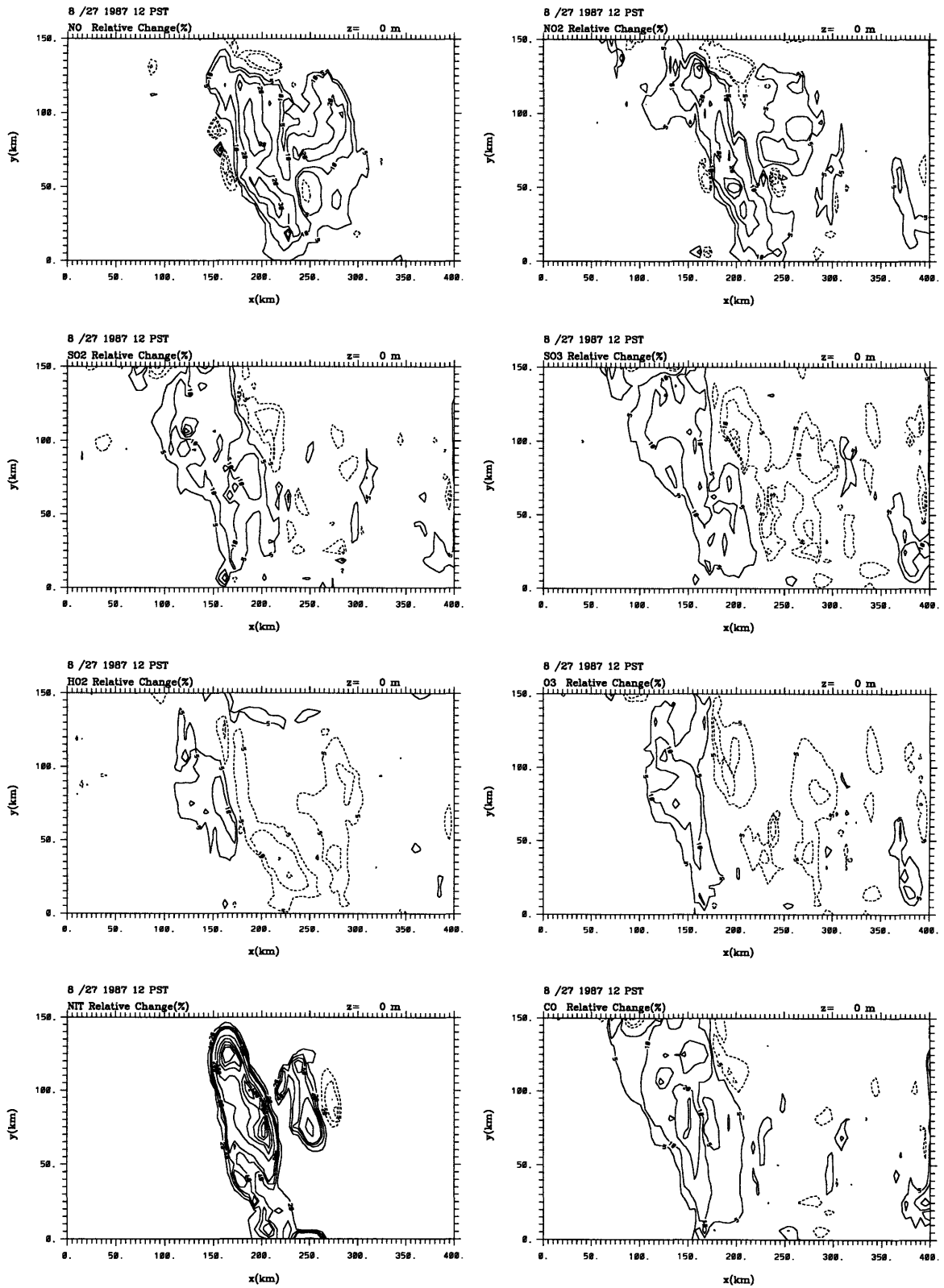


Figure 7-8: Relative change of spatial distribution of simulated ground level concentrations of NO, NO₂, SO₂, SO₃, HO₂, O₃, NIT, and CO at 12 PST of August 27, 1987 with low level aerosol loading.

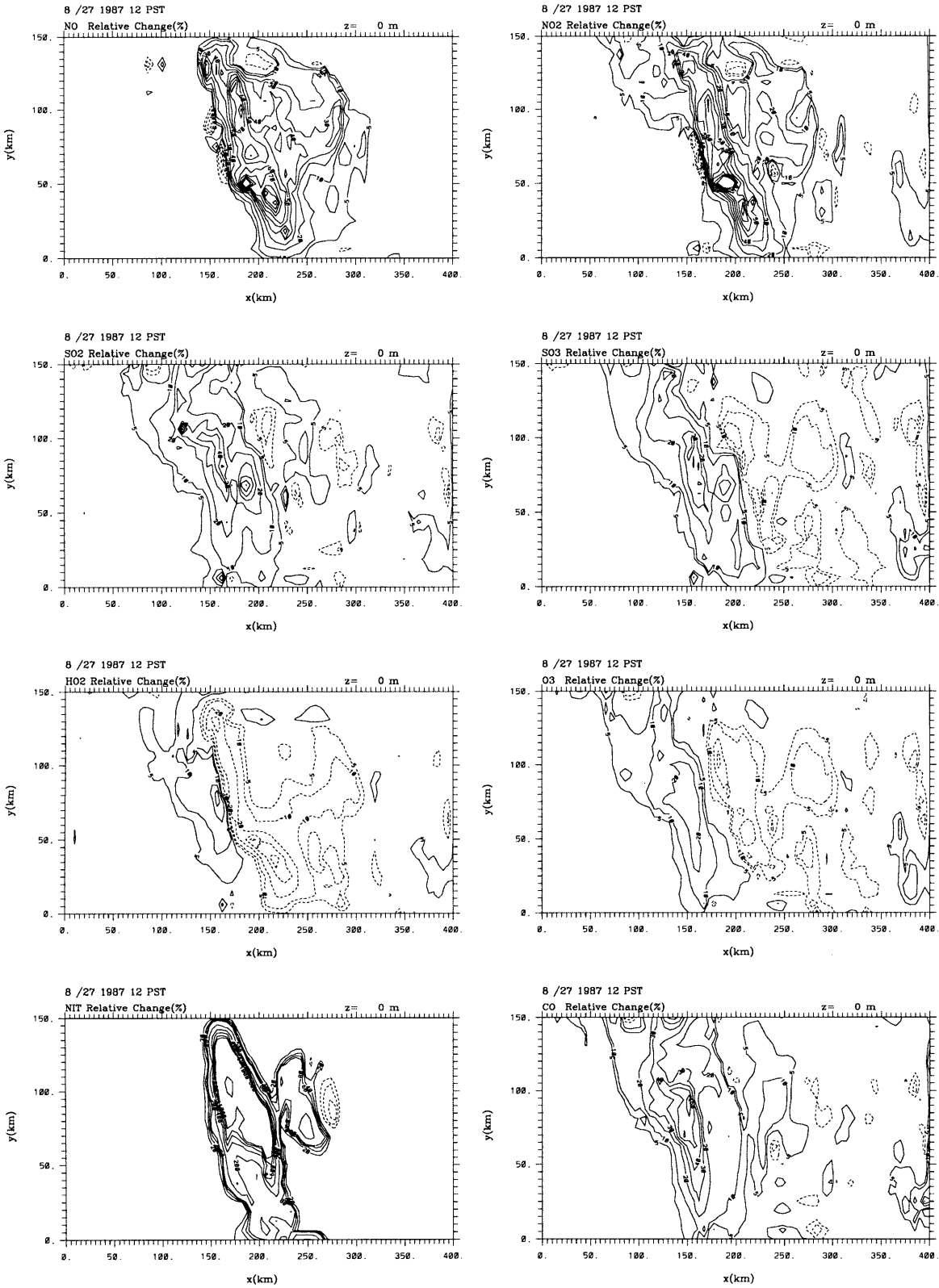


Figure 7-9: Relative change of spatial distribution of simulated ground level concentrations of NO, NO₂, SO₂, SO₃, HO₂, O₃, NIT, and CO at 12 PST of August 27, 1987 with high level aerosol loading.

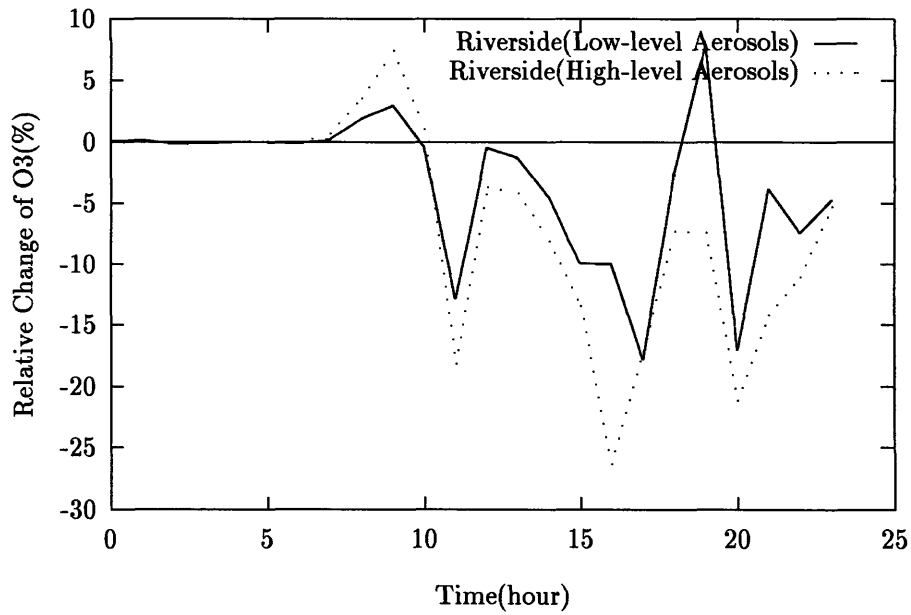
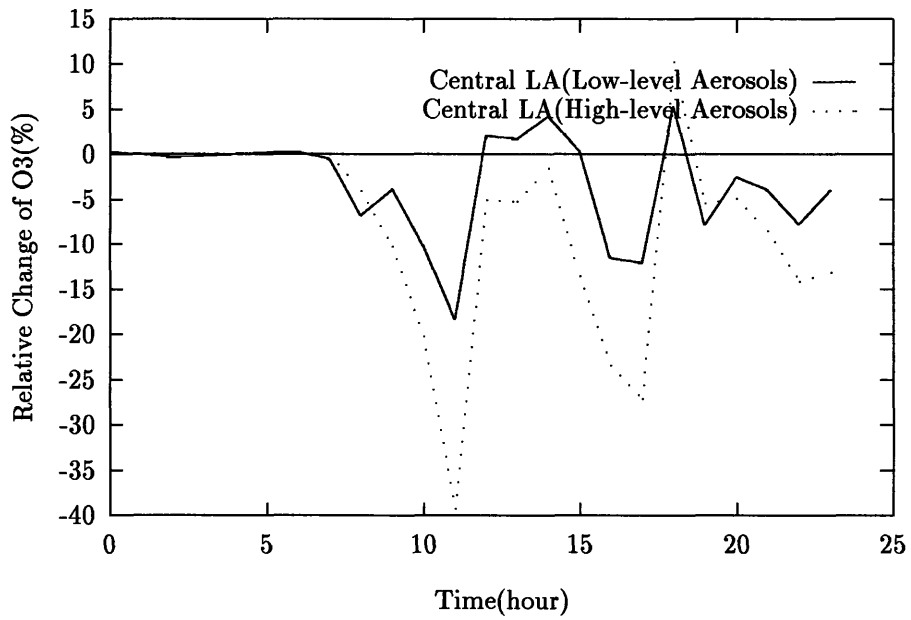


Figure 7-10: Relative change of ground-level O₃ concentration at two selected sites on August 27, 1987.

Chapter 8

Uncertainty Analysis in Large Implicit Models

Although uncertainty always exists in models of atmospheric systems, it has not received enough attention in the modeling community, due in part to a lack of appropriate analysis tools. Before proceeding to quantify the uncertainty of the radiative forcing by anthropogenic sulfate aerosols in the next chapter, some concepts and available methods for performing uncertainty analysis will be reviewed in the following sections.

8.1 Sources of Uncertainty in Atmospheric Modeling

Two main types of uncertainty affect our confidence in the results from atmospheric or most other models: parametric uncertainty and structural uncertainty. Parametric uncertainty arises because of incomplete knowledge of model parameters such as empirical quantities, defined constants, initial conditions, and boundary conditions. Structural uncertainty arises because of inaccurate treatment of model processes such as model dynamics, physical and chemical processes, numerical schemes, and model resolutions.

The importance of uncertainty analysis to atmospheric modeling is illustrated in Figure 8-1. Since both observations and model predictions may carry uncertainty, a meaningful comparison requires not only the mean but also the probability density function (PDF).

Although both uncertainties impair a model's output, they have not regularly received similar attention. A significant amount of effort has been made to reduce the structural uncertainty by increasing model resolution, improving parameterization schemes, refining model dynamics, and implementing state of the art numerical methods in atmospheric models. Some examples include the Atmospheric Model Intercomparison Project [52], the intercomparison and interpretation of climate feedback processes in 19 atmospheric general circulation models [20], the Project for Intercomparison of Land-surface Parameterization Schemes [67], and the proposal for intercomparison of the dynamical cores of atmospheric general circulation models [66].

However, studies on parametric uncertainty propagation in atmospheric models are only limited. Stolarski and Douglass [139] apply a full Monte Carlo analysis to evaluate ozone impacts of varied CFC emissions in the presence of key model inputs (i.e., rate coefficients, cross sections, solar fluxes, and boundary conditions). An another example is the concept of ensemble forecasting, in which an ensemble of forecasts is produced from different but appropriately chosen initial conditions [99, 148].

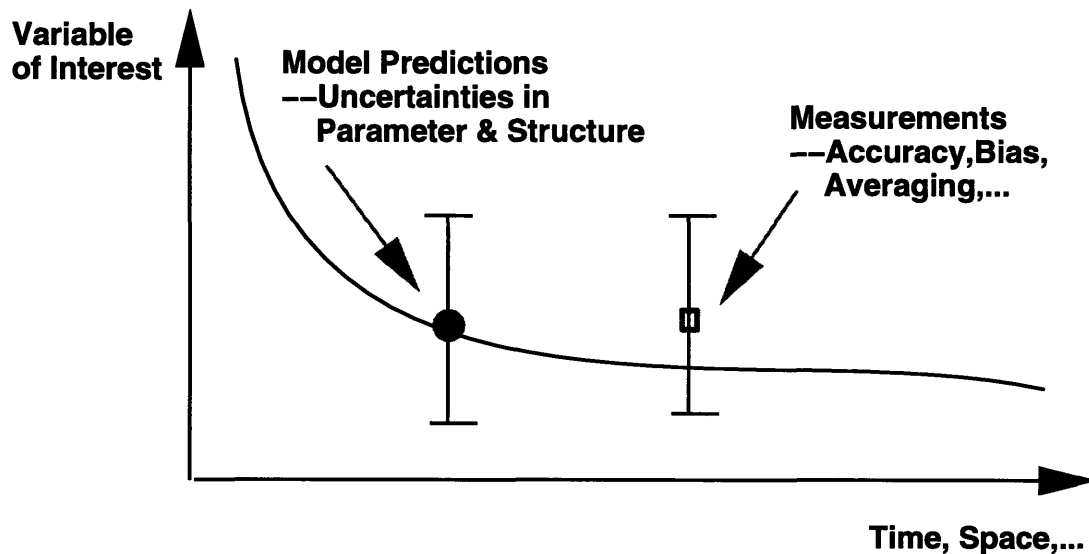


Figure 8-1: A schematic diagram for comparing measurements and model prediction in the presence of uncertainty.

The advantage of reducing parametric uncertainty is illustrated in Figure 8-2. The difference between the PDF of two model predictions may originate from both parametric uncertainty (ΔP) and structural uncertainty (ΔS). To achieve reasonably good performance, both uncertainties have to be reduced so that ΔS approaches zero and ΔP falls within the range of observation. Therefore, the goal of applying uncertainty analysis is to reduce both parametric and structural uncertainty of models so that not only the mean but also the PDFs from different models agree with each other.

In a parametric uncertainty analysis, we are interested in how the uncertainty in model parameters propagate through model systems and result in the uncertainty in model outputs. It is worthwhile to note the difference between sensitivity analysis and uncertainty analysis. In a sensitivity analysis we are interested in how the model outputs respond to changes in a given uncertainty parameter with all of the other parameters fixed. Therefore sensitivity analysis only reveals the local behavior of a model's response around a given parameter; whereas uncertainty analysis shows the global behavior of a model's response to a collective uncertainty in all the model parameters under consideration.

The main question addressed by parametric uncertainty analysis is as follows: given the PDFs of parameters, how can we obtain the PDFs of response variables? To answer this question, three issues are important. First, a representative estimate of the PDFs of uncertain parameters ultimately determines the accuracy of the PDFs of response variables. The Bayesian approach [138] or the minimum cross-entropy method [81, 134] are good techniques for estimating and improving the PDFs of uncertain parameters. Second, a consistent and general representation of random variables is necessary for dealing with different model structures. Finally, a major problem when performing uncertainty analysis in atmospheric models is the large dimensionality of uncertain parameters, which occur

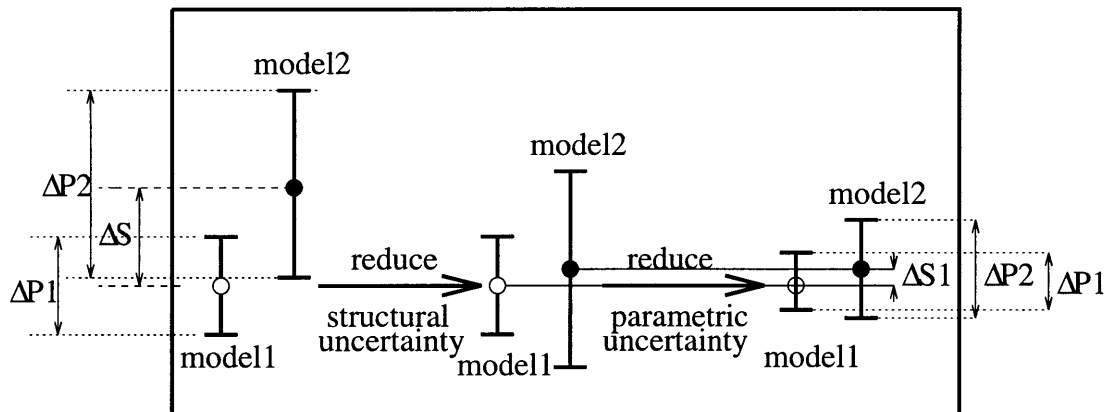


Figure 8-2: A schematic diagram for improving model comparison through reducing parametric uncertainty (ΔP) and structural uncertainty (ΔS).

either in large models or as random fields.

8.2 Parametric Uncertainty Analysis

There are several existing methods for performing parametric uncertainty analysis, such as the perturbation method [85, 79], moments method [101, 48], Neumann expansion method [5, 56], hierarchy method [85], semi-group operator method [128, 129], and spectral-based finite element method [56]. One major problem arising from these methods is the need to access and restructure model equations directly. Therefore, for given implicit type models, such as big subroutines or programs, one will find difficulties in applying these methods. Nevertheless, there is a class of methods called Monte Carlo methods (MCMs), which can be used for dealing with implicit type models.

Unfortunately, these methods can be prohibitively expensive, especially when the computational cost for solving those implicit type models is already high. Clearly, alternative approaches to MCMs are of interest in performing parametric uncertainty analysis to large implicit type models. The alternative method should be able to produce results as accurate as that of the MCM but require less computational cost. The goal of this chapter is to introduce a new approach called the deterministic equivalent modeling method (DEMM) and verify this method against the analytical and Monte Carlo results.

8.2.1 Monte Carlo Method

For an ideal model with one output variable x and p input parameters, k_1, \dots, k_p , the calculation of the n th moment of x involves a multi-dimensional integration as follows

$$E(x^n) = \int \dots \int x^n(k_1, \dots, k_p) f(k_1, \dots, k_p) dk_1 \dots dk_p, \quad (8.1)$$

Table 8.1: Number of sampling points required to achieve some error bounds with different methods.

Error bound	Dimension	Number of nodes		
		Trapezoidal	Ideal Monte Carlo	Quasi-Monte Carlo
0.01	2	100	10000	215
	4	10000	10000	989
	6	10^6	10000	4552
	10	10^{10}	10000	96518
0.0001	2	10000	10^8	30349
	4	10^8	10^8	279520
	6	10^{12}	10^8	$2.57448 \cdot 10^6$
	10	10^{20}	10^8	$2.18394 \cdot 10^8$
10^{-6}	2	10^6	10^{12}	$3.71692 \cdot 10^6$
	4	10^{12}	10^{12}	$5.13512 \cdot 10^7$
	6	10^{18}	10^{12}	$7.09443 \cdot 10^8$
	10	10^{30}	10^{12}	$1.3541 \cdot 10^{11}$

where f is the joint density function of input parameters.

To obtain the stable estimate of the model statistics, the number of sampling points depends on the response surface of the model, the specific statistics and the sampling method used.

For a p -dimension problem, the number of nodes required with the trapezoidal rule is $O\left(\left(\frac{1}{\epsilon}\right)^{\frac{p}{2}}\right)$ for an error bound of ϵ [104]. For an ideal MCM, the number of sampling points is $O\left(\left(\frac{1}{\epsilon}\right)^2\right)$, independent of the dimension. Quasi-Monte Carlo methods, such as the Hammersley-Wozniakowski sampling method [168], require only $O\left(\frac{1}{\epsilon} \left(\log \frac{1}{\epsilon}\right)^{\frac{p-1}{2}}\right)$ sampling points. For pseudo-Monte Carlo methods (e.g., RANDOM, a shift register method used in this study), the number of sampling points required falls between the ideal and the quasi-Monte Carlo method.

Table 8.1 [144] shows the comparison of the number of nodes needed for the three different methods. Clearly, in the case that model evaluation is expensive, both Monte Carlo methods and quasi-Monte Carlo methods are intractable for a reasonable accuracy.

8.2.2 Deterministic Equivalent Modeling Method with Collocation

As an example, let us consider a simple “black-box” type model with two independent random variables, $x(\omega)$ and $y(\omega)$, and one dependent random variable¹, $z(\omega)$,

$$z(\omega) = f(x(\omega), y(\omega)), \quad (8.2)$$

¹A real-valued random variable, $x(\omega)$, is a function, which maps the probability space Ω into the real line, such that the set $\omega \in \Omega \mid x(\omega) \leq x$ is an event for any real number x and the probabilities of the events $x(\omega) = \infty$ and $x(\omega) = -\infty$ equal to zero.

where ω stands for elements of probability space Ω .

The essence of DEMM with collocation [144] is to approximate the response surface, $z(\omega)$, with the orthogonal polynomials $P_k^x(x)$ and $P_k^y(y)$ whose weighting functions are the PDFs of random variables, $x(\omega)$ and $y(\omega)$.

These orthogonal polynomials can be obtained from the following recurrence relations

$$P_{k+1}^x(x) = (\alpha_k^x - x)P_k^x(x) - \beta_k^x P_{k-1}^x(x); k = 0, 1, \dots \quad (8.3)$$

$$P_{k+1}^y(y) = (\alpha_k^y - y)P_k^y(y) - \beta_k^y P_{k-1}^y(y); k = 0, 1, \dots \quad (8.4)$$

where the coefficients, α_{1k} , β_{1k} , α_{2k} and β_{2k} , can be generated from ORTHPOL [53].

Using the above recurrence relations, one can obtain two sets of orthogonal polynomials,

$$P_1^x(x), P_2^x(x), \dots, P_n^x(x),$$

$$P_1^y(y), P_2^y(y), \dots, P_n^y(y).$$

Then the independent random variables, $x(\omega)$ and $y(\omega)$, can be written as

$$x(\omega) = x_0 + x_1 P_1^x(x), \quad (8.5)$$

$$y(\omega) = y_0 + y_1 P_1^y(y), \quad (8.6)$$

and the dependent random variable, $z(\omega)$, can be approximated as

$$z(\omega) = \sum_{i=0}^{N_x} \sum_{j=0}^{N_y} z_{ij} P_i^x(x) P_j^y(y), \quad (8.7)$$

where N_x and N_y are orders of the expansion in P^x and P^y , respectively.

The residual random variable for this model, $R_N(\mathbf{z}, \omega)$, can be written as follows:

$$R_N(\mathbf{z}, x, y) = \sum_{i=1}^{N_x} \sum_{j=1}^{N_y} z_{ij} P_i^x(x) P_j^y(y) - f(x_0 + x_1 P_1^x(x), y_0 + y_1 P_1^y(y)), \quad (8.8)$$

where \mathbf{z} represents the vector of $N_x N_y$ unknown coefficients in the polynomial expansion of Equation 8.7.

Following the notion of the probabilistic variational process, the collocation method forces the residual random variable to be deterministically zero at $N_x N_y$ pairs of specifically chosen points,

$$\int_x \int_y f_x(x) f_y(y) R_N(\mathbf{z}, x, y) \delta(\{x, y\} - \{p_i^x, p_j^y\}) dx dy = 0; i = 1, \dots, N_x, j = 1, \dots, N_y \quad (8.9)$$

where δ denotes the delta function and $\{p_i^x, p_j^y\}$ is the set of $N_x N_y$ collocation points.

To choose these collocation points, we may use the $N_x N_y$ pairs of roots of the $(N_x + 1)th$ and $(N_y + 1)th$ orthogonal polynomials, $P_{N_x+1}^x(x)$ and $P_{N_y+1}^y(y)$, with high probabilities [154]. The solution of Equation 8.8 can then be solved at $N_x N_y$ pair of points to generate the coefficients \mathbf{z} in Equation 8.7.

The relative error of the approximation can be further estimated using the roots of

$(N_x + 2)$ th orthogonal polynomials, $P_{N_x+2}(x)$ and $P_{N_y+2}(y)$ as following,

$$\epsilon = \frac{\sqrt{\sum_{i=1}^{N_x+2} \sum_{j=1}^{N_y+2} f_x(x) f_y(y) (z(p_i^x, p_j^y) - \hat{z}(p_i^x, p_j^y))}}{\hat{z}(p_i^x, p_j^y)}, \quad (8.10)$$

where $z(p_i^x, p_j^y)$ and $\hat{z}(p_i^x, p_j^y)$ are the true and the approximated model results at collocation points, $\{p_i^x, p_j^y\}$, and $\hat{z}(p_i^x, p_j^y)$ is the mean of the approximation.

Therefore the model result, $z(\omega)$, can be iteratively approximated with increasing orders of polynomial expansions until the relative error is smaller than the tolerance.

After Equation 8.7 is obtained, its PDF can be simulated using certain sampling methods. The simplest way is to simulate the PDF with MCM. Since the response surface is reduced to a polynomial form, the required simulation time decreases tremendously compared to using the original model, provided that the original model is computational very expensive.

8.2.3 Verification: Comparison to Analytic Solution

Charlson et al.'s model [24] gives the direct radiative forcing by sulfate aerosols in a simple analytical form of

$$\Delta F = -\frac{1}{2} S_0^2 (1 - A_c) T^2 (1 - R_s)^2 \bar{\beta} \Psi_e f_{\Psi_e}(RH) \frac{3QYL}{A}, \quad (8.11)$$

where S_0 is the solar constant, T is the transmittance of the atmospheric layer above the aerosol layer, A_c is the fractional cloud cover, R_s is the mean albedo of the underlying surface, $\bar{\beta}$ is the backscattered fraction, Ψ_e is the specific scattering cross section, $f_{\Psi_e}(RH)$ is the scaling factor for the dependence of particle size on relative humidity (RH), Q is the source strength of anthropogenic sulfur, Y is the fraction of SO_2 oxidized to SO_4^{2-} aerosol, L is the sulfate lifetime in the atmosphere, and A is the area of the Earth.

The purpose of a parametric uncertainty analysis in this case is to find the PDF of $\overline{\Delta F_R}$, given the uncertainty of the parameters in Equation 8.11. To do this, we must assign the PDFs of all the uncertain parameters, which ultimately determine the PDF of the model result. Given the limited information, in this thesis all of the uncertain parameters are assumed log-normally distributed as in Penner et al. [107] with the central values and uncertainty factors² listed in Table 8.2.

Since the model is in a multiplicative form of

$$y_N = \prod_{i=1}^N y_i, \quad (8.12)$$

where y_i is log-normally distributed with central value of $c(y_i)$ and uncertainty factor of $u(y_i)$, the PDF of y_N is log-normal with the central value and uncertainty factor given by

$$c(y_N) = \exp\left(\sum_{i=1}^N \ln(c(y_i))\right), \quad (8.13)$$

²For lognormal distributed random variables, central values (c) and uncertainty factors (u) are the same as the geometric mean (i.e., median) and geometric standard deviation (i.e., 84% of all variables are smaller than $c \times u$)

Table 8.2: Central values, uncertainty factors for log-normally distributed parameters used in the Monte Carlo and the DEMM simulations.

Quantity	Central value	Uncertainty factor
Q(10^{12} g/yr)	71	1.15
Y	0.5	1.5
L(days)	5.5	1.5
Ψ_e (m^2/g)	5.0	1.4
β	0.3	1.3
$f\Psi_e$	1.7	1.2
T	0.76	1.2
1- A_c	0.39	1.1
1- R_s	0.85	1.1

$$u(y_N) = \exp \left(\sqrt{\sum_{i=1}^N \ln^2(u(y_i))} \right). \quad (8.14)$$

From Table 8.2 and Equations 8.13 and 8.14, the analytical central value and uncertainty factor of $\overline{\Delta F_R}$ is -0.9 W/m^2 and 2.3 respectively. The corresponding mean, standard deviation, and range of 95% confidence level are -1.3 W/m^2 , 1.3 W/m^2 , and -0.2 W/m^2 to -4.8 W/m^2 respectively. The analytical PDF is shown in Figure 8-3.

In order to compare the performance of DEMM with MCM, Equation 8.11 is simulated using MCM with up to 10000 sampling points. Figure 8-3 shows the PDFs from MCM using different sampling points. In Figure 8-4, the L_2 -norm error between simulated PDFs and analytical PDF is plotted with respect to the number of sampling points. The L_2 -norm error slowly decreases as number of sampling points increases. To obtain an error less than 1%, up to 9000 sampling points are required. The spurious increase of error at 5000 sampling points is a manifestation of probabilistic error.

Figure 8-5 shows the comparison of PDFs from DEMM with the analytical PDF. In Figure 8-6 the L_2 -norm error between simulated PDFs and analytical PDF is plotted with respect to the order and collocation points in DEMM. Here the PDFs from DEMM are empirically generated using 10000 sampling points MCM. Although the PDF of linear order approximation differs much from the analytical PDF, the difference decreases very fast as the order of approximation increases. It is noticed that the speed-up factor, which is defined as the ratio of computational time required by MCM and by DEMM, varies from 13 to 29, depending on the specific L_2 -norm error. This factor doubles if the variance contribution by each uncertainty parameter is required since the model has to be run with respect to each parameter while fixing others.

Of course, this estimation assumes that the time required for generating the PDF of Equation 8.7 is negligible compared to multiple runs of Equation 8.7. Although this is not true for this model, it is a reasonable assumption for a computationally expensive model.

The convergence of DEMM can be seen from Figure 8-7, which shows the relative error ϵ with the approximation order. The logarithm of ϵ decreases linearly, indicating the method

is fast converging. This is in contrast to the exponential decay of error in Figure 8-4 for MCM.

Besides obtaining the PDF of $\overline{\Delta F_R}$, we can also carry out variance analysis so that uncertain parameters can be ranked according to their contribution to the total variance.

The contribution of the normalized variance by each uncertain parameter using DEMM is listed in Table 8.3 with that estimated using the sensitivity and standard deviation. The results agree well for all parameters except for T and R_s , which are square terms in Equation 4.13. It can be easily shown using Taylor series expansion that the estimated variance, VAR_e , from the product of sensitivity and standard deviation, is not necessarily the same as the true variance VAR_t for nonlinear systems³. In Table 8.3 the variance contributions by T and R_s are 47% and 75% smaller than those made by DEMM respectively. The ranking will be Y/L , T , Ψ_0 , and so on. This ranking information may help us identify the key uncertain parameters in the model and allocate our efforts and resources if we are required to further reduce the uncertainty in the results.

8.3 Random Field Representation

The previous section illustrates DEMM is much more efficient than the traditional MCM in performing uncertainty analysis to random variables (i.e., uncertain parameters). However, in practice, uncertainty is also presented as random fields. A random field can be considered as a random variable with several parameters and can be written as $f(\mathbf{x}, \omega)$, where $\bar{\mathbf{x}}$ represents a vector of parameters. For example, emission fields in air quality modeling and initial conditions for meteorological modeling can be considered as random fields with both spatial and temporal parameter vectors.

A random field, $f(\mathbf{x}, \omega)$, corresponds to real functions of \mathbf{x} if ω is fixed; a random variable if \mathbf{x} is fixed; a real number if both \mathbf{x} and ω are fixed.

To perform uncertainty analysis for a random field with large dimensionality, one needs to represent it using a small number of independent⁴ random variables. This can be achieved by using a Karhunen-Loève expansion [74, 88].

³Consider a system $y = f(x)$, we define

$$VAR_t \equiv E[(y - \bar{y})^2],$$

$$VAR_e \equiv \left(\frac{dy}{dx}\right)_x^2 E[(x - \bar{x})^2],$$

and Taylor series expansion implies

$$y = \bar{y} + \frac{df}{dx}\bigg|_x (x - \bar{x}) + \frac{1}{2} \frac{d^2f}{dx^2}\bigg|_x (x - \bar{x})^2 + \dots,$$

If we put the expansion into Var_t , we have

$$\begin{aligned} VAR_t &= E\left[\left(\bar{y} + \frac{df}{dx}\bigg|_x (x - \bar{x}) + \frac{1}{2} \frac{d^2f}{dx^2}\bigg|_x (x - \bar{x})^2 + \dots - \bar{y}\right)^2\right] \\ &= VAR_e + \frac{df}{dx}\bigg|_x \frac{d^2f}{dx^2}\bigg|_x E[(x - \bar{x})^3] + \frac{1}{4} \left(\frac{d^2f}{dx^2}\bigg|_x\right)^2 E[(x - \bar{x})^4] + \dots \end{aligned} \quad (8.15)$$

⁴A set of random variables \mathbf{x}_n is independent if the joint PDF equals to the product of individual PDFs, i.e.,

$$f(x_1, x_2, \dots, x_n) = f(x_1)f(x_2)\dots f(x_n)$$

Table 8.3: Normalized variance contribution by each uncertain parameter estimated by DEMM and the sensitivity and standard deviation for Charlson et al.'s model [24].

Quantity	Normalized variance contribution(%)	
	DEMM	Sensitivity $\times \sigma$
Q(Tg/yr)	2.63	2.50
Y	22.2	26.1
L(days)	22.2	26.1
$\Psi_e m^2/g$	15.3	16.7
f(RH=75%)	4.48	4.36
β	9.28	9.53
T	17.9	10.2
A_c	1.22	1.15
R_s	4.90	3.33

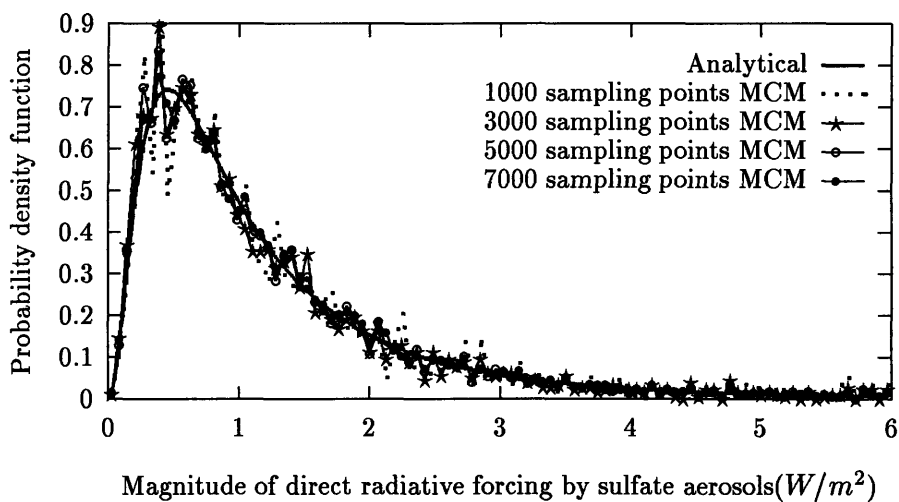


Figure 8-3: Comparison of the PDFs from MCM with different sampling points, with the analytical PDF.

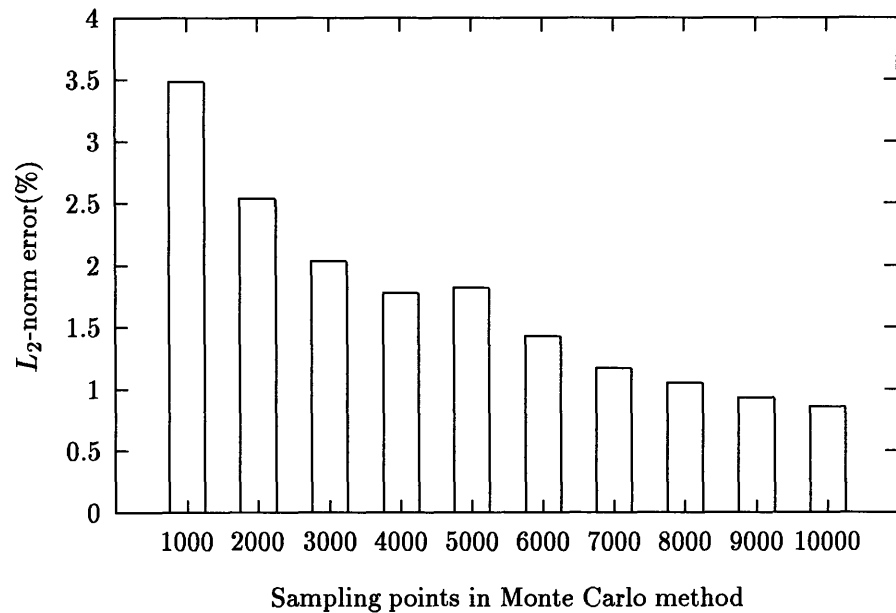


Figure 8-4: L_2 -norm error (%) between the PDFs from MCM and analytical PDF.

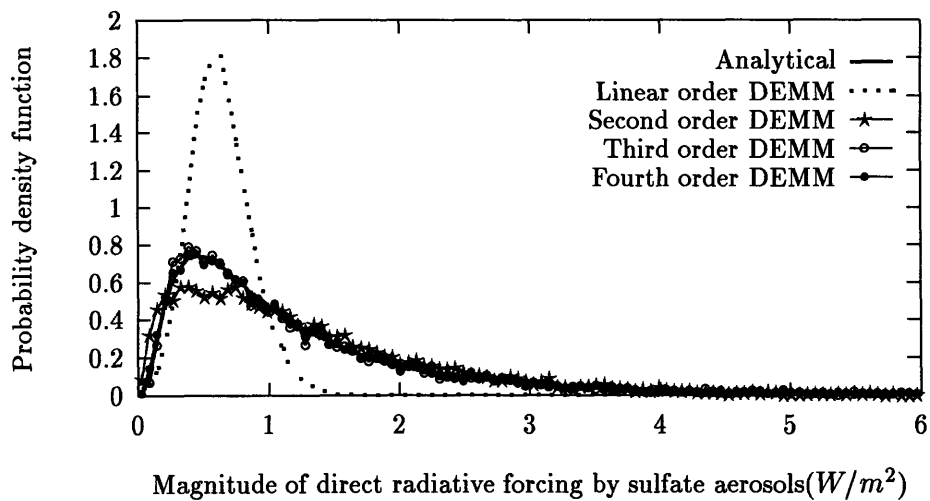


Figure 8-5: Comparison of the PDFs from DEMM with different approximation orders.

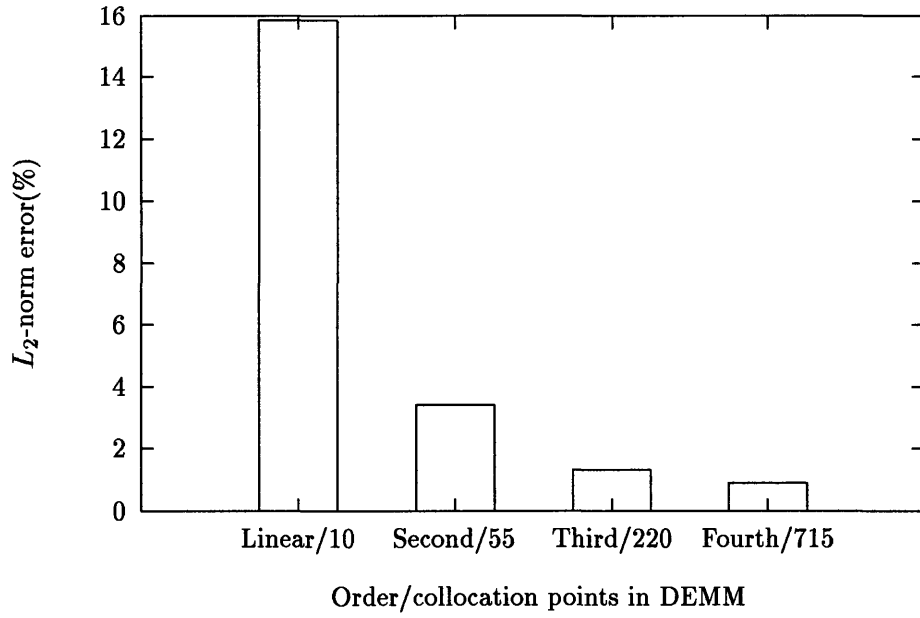


Figure 8-6: L_2 -norm error (%) between the PDFs from DEMM and the analytical PDF with different approximation orders.

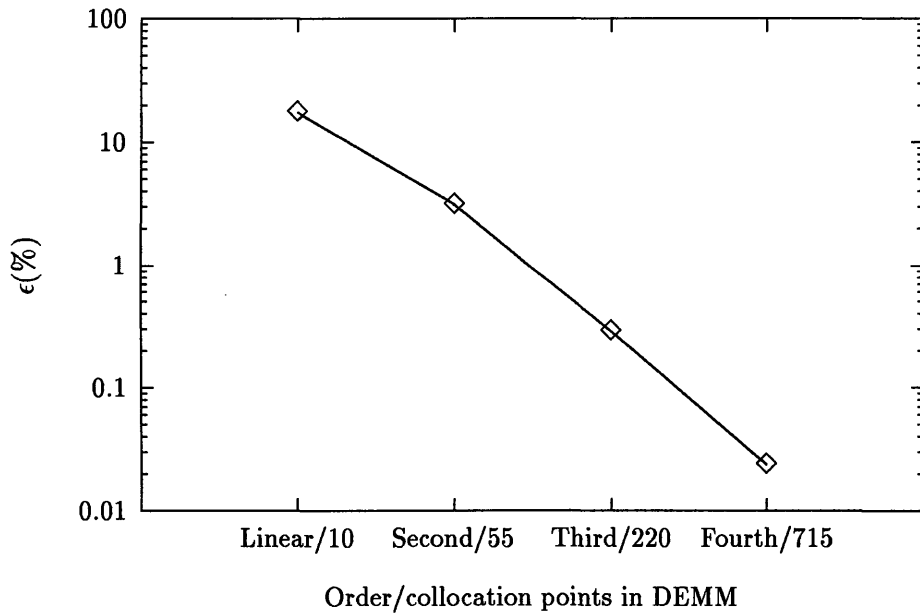


Figure 8-7: The relative error estimated using Equation (9) for different approximation orders in DEMM.

Mathematically, the Karhunen-Loeve expansion of a random variable, $f(\mathbf{x}, \omega)$, can be written as follows

$$f(\mathbf{x}, \omega) = \sum_{i=1}^N \sqrt{\lambda_i} \alpha_i(\mathbf{x}) \beta_i(\omega), \quad (8.16)$$

where λ_i and α_i is the i th eigenvalue and eigenfunction of covariance of $f(\mathbf{x}, \omega)$ and β_i are the resulting random variables.

Orthogonality requires

$$\int_{\mathbf{x}} f(\mathbf{x}, \omega) \alpha_i(\mathbf{x}) d\mathbf{x} = \sqrt{\lambda_i} \beta_i(\omega). \quad (8.17)$$

Multiplying Equation 8.17 by $f(\mathbf{y}, \omega)$ and taking the expected value of the resulting equation, we have

$$\int_{\mathbf{x}} C(\mathbf{x}, \mathbf{y}) \alpha_i(\mathbf{x}) d\mathbf{x} = \lambda_i \alpha_i(\mathbf{y}), \quad (8.18)$$

where $C(\mathbf{x}, \mathbf{y})$ is the covariance matrix of the random field.

The values of eigenvalue, λ_i , and eigenfunction, $\alpha_i(\mathbf{x})$ are the diagonal and orthogonal matrices of singular value decomposition (SVD) of the covariance matrix, $C(\mathbf{x}, \mathbf{y})$.

The random variable, $\beta_i(\omega)$, can be obtained as

$$\beta_i(\omega) = \frac{1}{\sqrt{\lambda_i}} \int_{\mathbf{x}} f(\mathbf{x}, \omega) \alpha_i(\mathbf{x}) d\mathbf{x}. \quad (8.19)$$

The level of the accuracy for M th-order approximation can be measured using the fractional variance,

$$\epsilon_M = \frac{\sum_{i=1}^M \lambda_i}{\sum_{i=1}^N \lambda_i}. \quad (8.20)$$

Therefore, instead of dealing with the original N -dimensional problem, DEMM can be applied to the resulting N -dimensional problem with $M \ll N$ for a given accuracy. Furthermore, since the random variables, $\beta_i(\omega)$, resulting from the K-L decomposition, are uncorrelated but not necessarily independent, the above method for treating random fields should be used with caution. Nevertheless, the K-L decomposition does provide us a powerful alternative for coping with uncertainty in random fields, especially when the random fields are highly correlated. This is to be illustrated in the following two examples.

The data were taken from a 5-year (March 1985 through February 1990) global, grid-ded 4-d assimilated atmospheric data set produced by the Laboratory for Atmospheric Data Assimilation Office (DAO) at Goddard Space Flight Center (GSFC). This data set assimilated rawinsonde reports, satellite retrievals of geopotential thickness, cloud-motion winds, aircraft, ship and rocketsonde reports with model forecasts employing version 1 of the Goddard Earth Observing System (GEOS-1) GCM. The data are archived at the GSFC Distributed Active Archive Center (DAAC), accessible through anonymous ftp.

Two fields are employed here: total cloud fraction and sea level pressure, both for 1989. The data originally have a resolution of 2 degree-latitude by 2.5 degree-longitude and were averaged to a coarse resolution of 10 degree-latitude by 10 degree-longitude, corresponding to 648 grid points in space. The total cloud fraction is a 3 hour average and corresponds to 2920 temporal points. And the sea level pressure is a 6 hour average and corresponds to 1460 temporal points.

To illustrate how the empirical K-L series expansion can help us reduce the dimension-

ality of a given problem, the annual means of the above two fields were approximated as follows

$$\bar{f}(\mathbf{x}, \mathbf{y}) = \sum_{i=1}^N \sqrt{\lambda_i} \alpha_i(\mathbf{x}) \beta_i(\mathbf{y}). \quad (8.21)$$

Figure 8-8 and Figure 8-9 show the global distribution of the original fields and their corresponding first five eigenfunctions. The eigenvalue spectrums explaining 95% of variance are shown in Figure 8-10. Since the cloud fields tend to be more spatially uncorrelated than the sea level pressure, the decay rates of the two eigenvalue spectrums differ significantly, with M -values of 9 and 5 respectively, which are much smaller than the N -value of 648.

Similarly, if we treat the temporal variation as a random process, the empirical K-L series expansion can be used to convert the random field into some random variables. Figure 8-11 shows the eigenvalue spectrums for sea level pressure and total cloud fraction. Consistent with the annual mean case, the eigenvalue spectrums have quite different decay rates. To be sure, to capture 95% of the variance or energy, 88 terms are required for sea level pressure whereas 317 terms are required for total cloud cover.

We can further obtain the probability density functions for the corresponding uncorrelated random variables. Figure 8-12 and Figure 8-13 show the probability density functions for the first five leading random variables. The first random variables show clear bimodal distributions, and the distributions appear to be converging for those random variables associated with lower eigenvalues. The PDFs for the resulting random variables can be applied to DEMM as discussed before and hence uncertainty analysis can be performed to on models with large dimensional random fields.

To further reduce the number of terms for the random field decomposition, we need to apply an empirical K-L series expansion to the two dimensional random field, $f(\mathbf{x}, \mathbf{y}, \omega)$. The corresponding Fredholm integral equation of Equation 8.18 becomes

$$\int_X \int_Y C(\mathbf{x}_1, \mathbf{x}_2; \mathbf{y}_1, \mathbf{y}_2) \alpha_n(\mathbf{x}_2, \mathbf{y}_2) d\mathbf{x}_2 d\mathbf{y}_2 = \lambda_n \alpha_n(\mathbf{x}_1, \mathbf{y}_1), \quad (8.22)$$

and similiary the uncorrelated random variables can be obtained from the following equation:

$$\beta_n(\omega) = \frac{1}{\lambda_n} \int_X \int_Y f(\mathbf{x}, \mathbf{y}, \omega) \alpha_n(\mathbf{x}, \mathbf{y}) d\mathbf{x} d\mathbf{y}. \quad (8.23)$$

Consequently, the random field can be expanded as follows

$$f(\mathbf{x}, \mathbf{y}, \omega) = \sum_{n=1}^N \sqrt{\lambda_n} \alpha_n(\mathbf{x}, \mathbf{y}) \beta_n(\omega). \quad (8.24)$$

To solve the above Fredholm integral equation, the Galerkin type procedure [56] can be used to approximate the eigenfunctions by a complete set of functions in the Hilbert space. In other words, each eigenfunction of the covariance kernel may be written as

$$\alpha_n(\mathbf{x}, \mathbf{y}) = \sum_{i=1}^M d_{i,n} h_i(\mathbf{x}, \mathbf{y}). \quad (8.25)$$

Since the above representation for eigenfunctions contains an error resulting from truncating the summation after the M th term, the induced error to the Fredholm integral equation

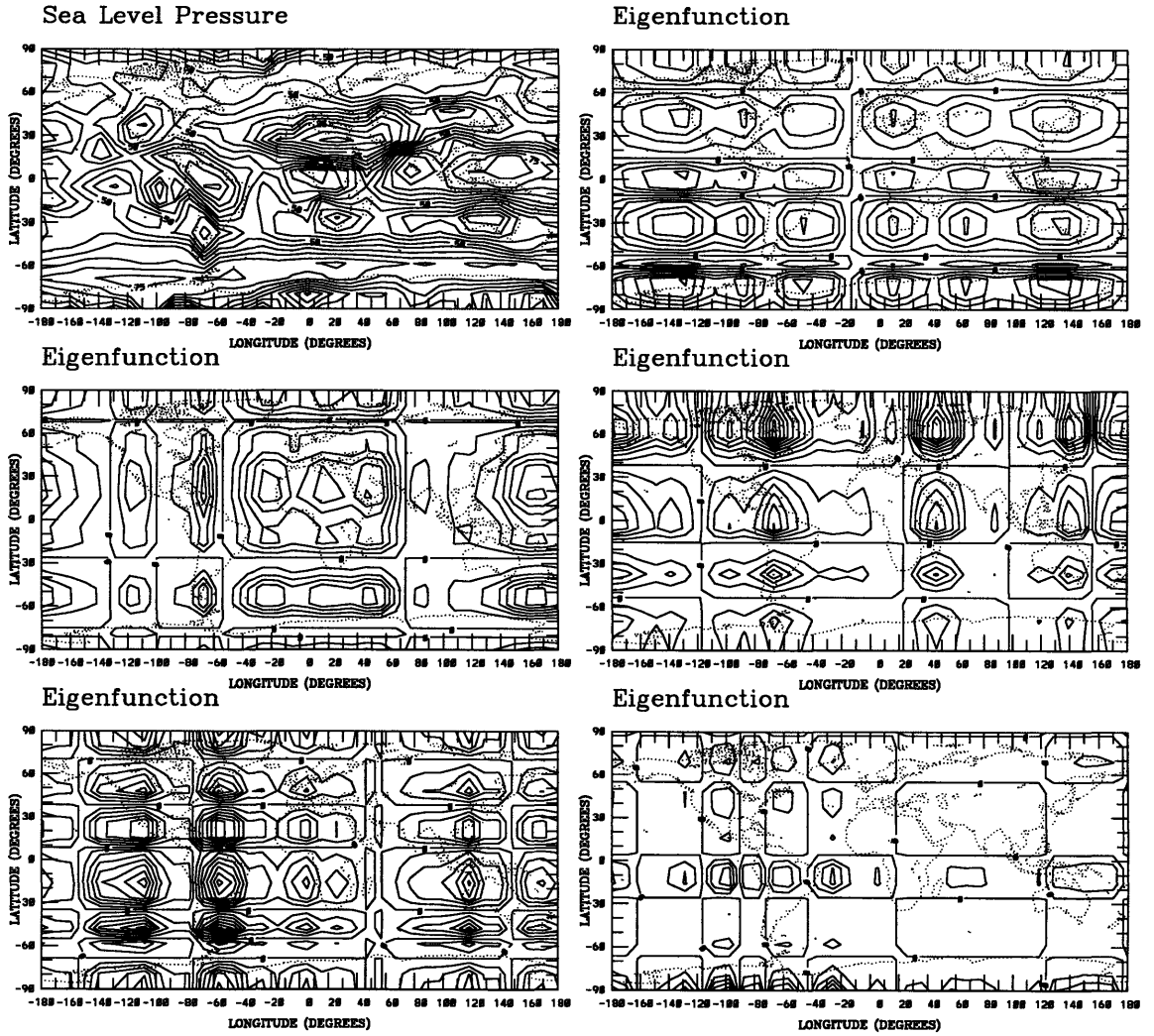


Figure 8-8: Annual mean of total cloud fraction and its first five associated eigenfunctions.

becomes

$$\epsilon_M = \sum_{i=1}^M d_{i,n} \left[\int_{\mathbf{X}} \int_{\mathbf{Y}} C(\mathbf{x}_1, \mathbf{x}_2; \mathbf{y}_1, \mathbf{y}_2) h_i(\mathbf{x}_2, \mathbf{y}_2) d\mathbf{x}_2 d\mathbf{y}_2 - \lambda_n h_i(\mathbf{x}_1, \mathbf{y}_1) \right]. \quad (8.26)$$

In the spirit of the Galerkin approach, this error should be made orthogonal to the approximation space. Such an orthogonalization process yields the following generalized algebraic eigenvalue problem,

$$\mathbf{C} \mathbf{D} = \Lambda \mathbf{B} \mathbf{D}, \quad (8.27)$$

where \mathbf{C} , \mathbf{B} , Λ , and \mathbf{D} are four M dimensional matrices whose elements are given as follows

$$C_{i,j} = \int_{\mathbf{X}} \int_{\mathbf{X}} \int_{\mathbf{Y}} \int_{\mathbf{Y}} C(\mathbf{x}_1, \mathbf{x}_2, \mathbf{y}_1, \mathbf{y}_2) h_i(\mathbf{x}_2, \mathbf{y}_2) h_j(\mathbf{x}_1, \mathbf{y}_1) d\mathbf{x}_1 d\mathbf{x}_2 d\mathbf{y}_2 d\mathbf{y}_2. \quad (8.28)$$

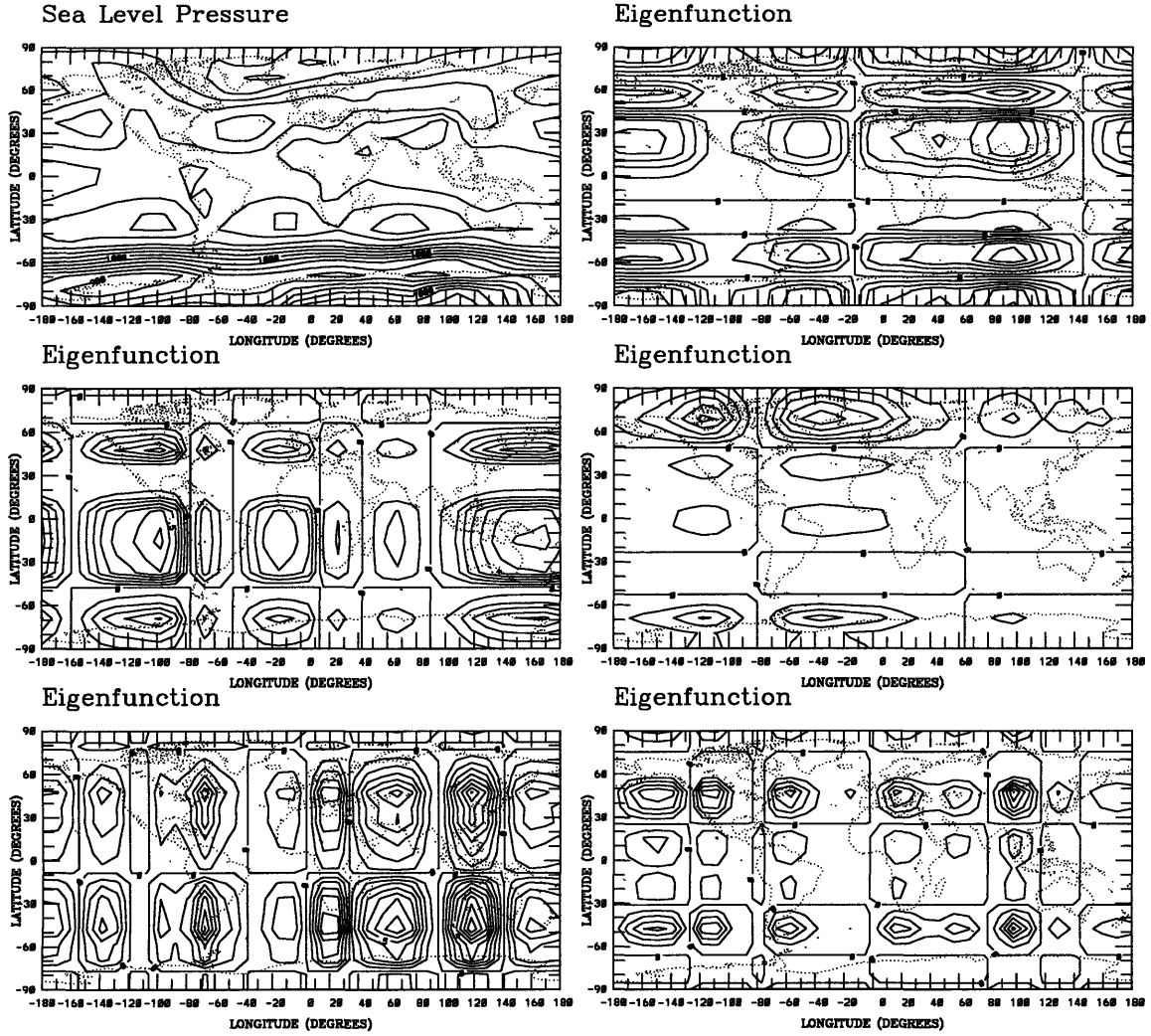


Figure 8-9: Annual mean of sea level pressure and its first five associated eigenfunctions.

$$\mathbf{B}_{i,j} = \int_{\mathbf{X}} \int_{\mathbf{Y}} h_i(\mathbf{x}, \mathbf{y}) h_j(\mathbf{x}, \mathbf{y}) d\mathbf{x}d\mathbf{y}, \quad (8.29)$$

$$\mathbf{D}_{i,j} = d_{i,j}, \quad (8.30)$$

$$\Lambda_{i,j} = \delta_{ij} \lambda_i. \quad (8.31)$$

In certain conditions, we may actually transform the above multi-dimensional problem into several one-dimensional problems. If the covariance function is separable

$$C(x_1, x_2; y_1, y_2) = C_x(x_1, x_2) C_y(y_1, y_2), \quad (8.32)$$

the eigenfunction can have the following form

$$\alpha_n(x, y) = \alpha_{x,n}(x) \alpha_{y,n}(y), \quad (8.33)$$

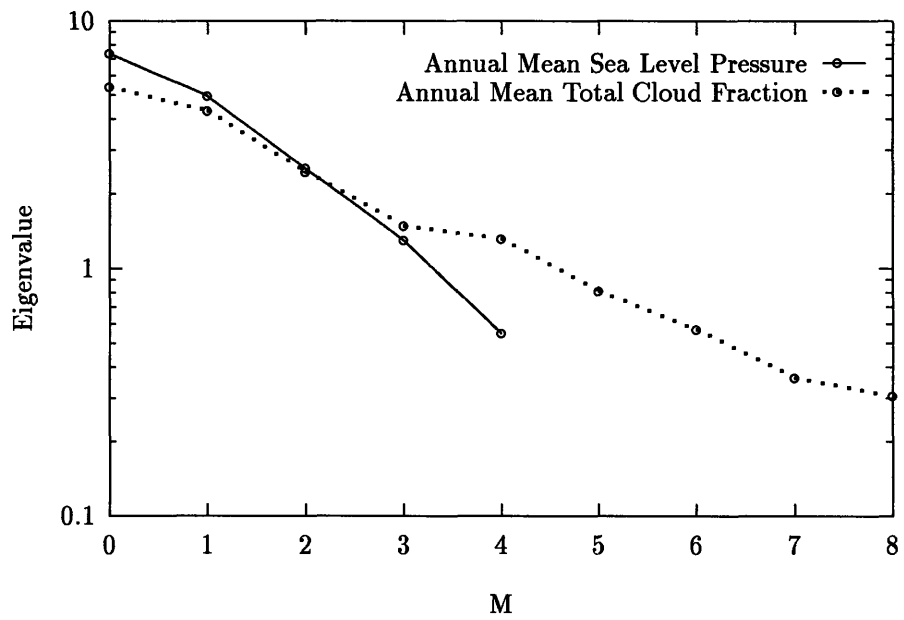


Figure 8-10: Eigenvalue spectrum for annual mean sea level pressure and total cloud fraction for the number of M values needed to explain 95% of the variance.

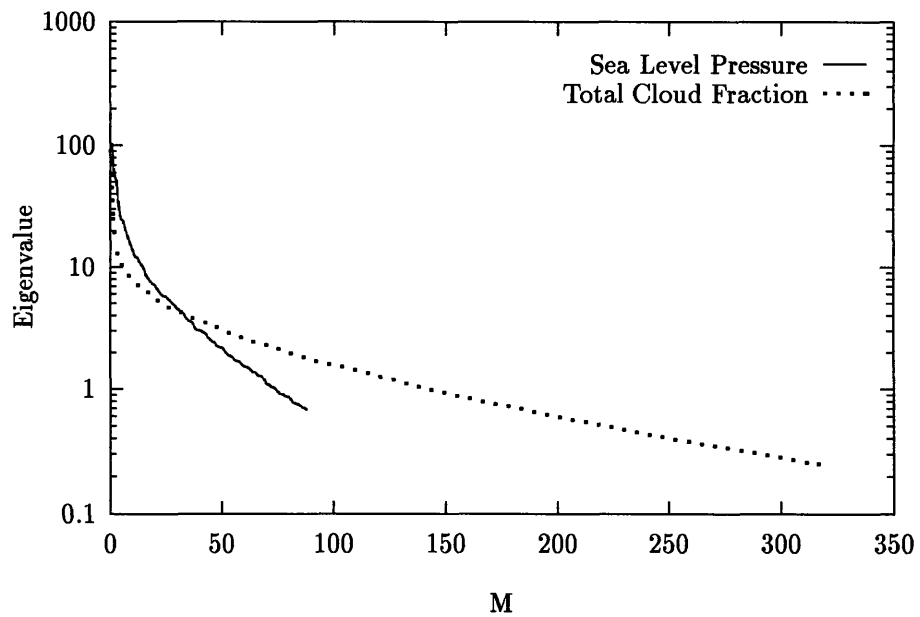


Figure 8-11: Eigenvalue spectrum for sea level pressure and total cloud fraction for the number of M values needed to explain 95% of the variance.

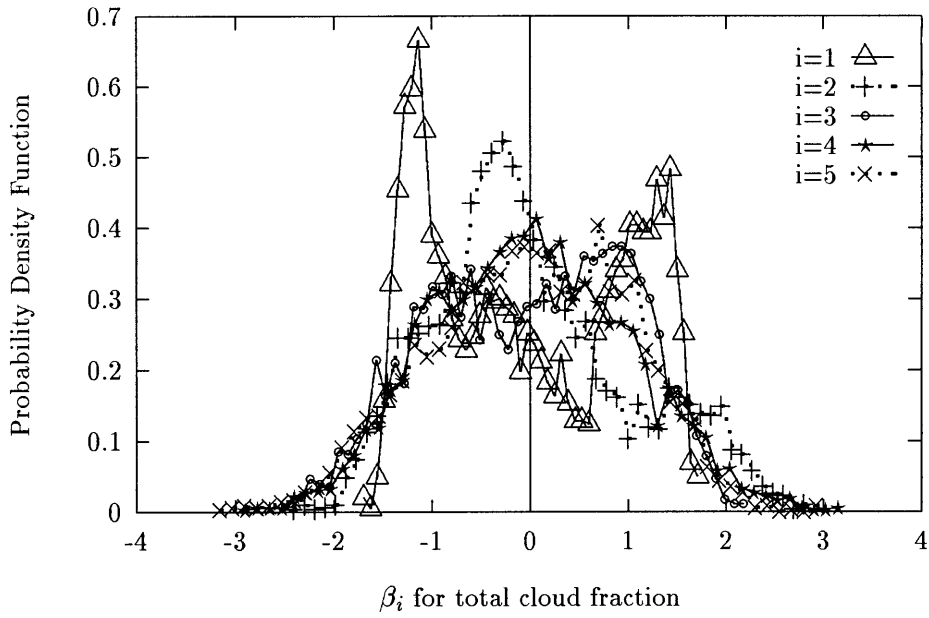


Figure 8-12: Probability density functions for the first five random variables of total cloud fraction.

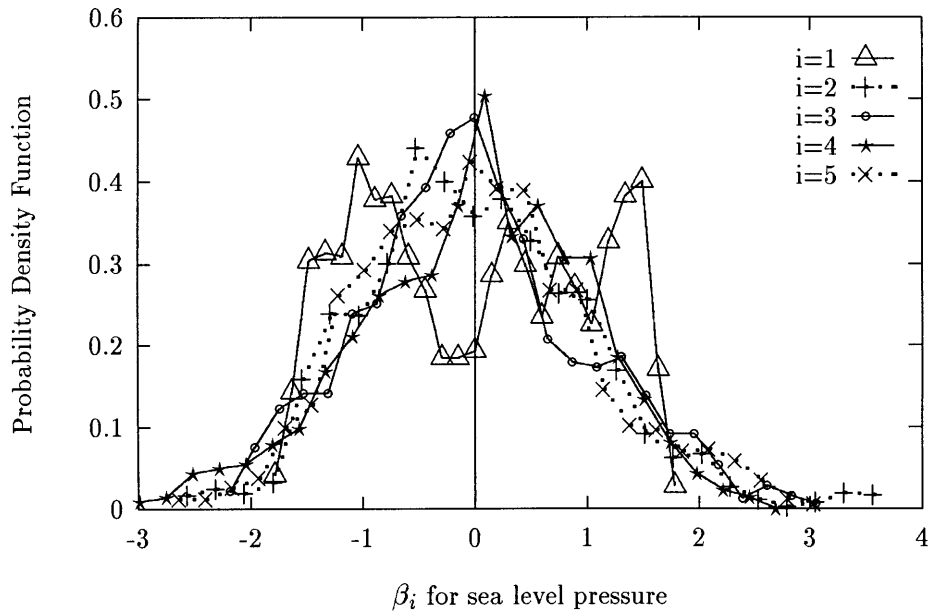


Figure 8-13: Probability density functions for the first five random variables of sea level pressure.

and similarly, the eigenvalue can be written as

$$\lambda_n = \lambda_{x,n} \lambda_{y,n}. \quad (8.34)$$

As a result, the original equation becomes two separate eigenvalue problems

$$\int_X C_x(x_1, x_2) \alpha_{x,n}(x_2) dx_2 = \lambda_{x,n} \alpha_{x,n}(x_1), \quad (8.35)$$

$$\int_Y C_y(y_1, y_2) \alpha_{y,n}(y_2) dy_2 = \lambda_{y,n} \alpha_{y,n}(y_1). \quad (8.36)$$

These two eigenvalue problems then can be solved separately using standard numerical subroutines or techniques described previously.

8.4 The Cascading Scheme

In large modeling systems, such as GCMs, which may have a very large number of uncertain parameters, another method called the cascading scheme can be applied to further overcome the “curse of dimensionality”. The essence of this method is to decompose the original model into several levels of submodels and carry uncertainty analysis sequentially downstream, feeding the next submodel with the output PDF of its preceding submodel. In the following this idea will be illustrated with Charlson et al.’s model [24].

Figure 8-14 shows the decomposition of an analytical radiative transfer model for sulfate aerosols into three levels of cascading (c.f., Equation 4.13). In the first level cascade, we have nine input variables and one output variable. This level can be decomposed into three second level units (three shaded boxes in Figure 8-14), which can be further decomposed into eight third level units (eight white boxes in Figure 8-14). For a given model, the decomposition depends on the separability of model units and requires that the intermediate outputs (e.g., Z_1, Z_2, \dots) should be independent of the other inputs for the next unit in the same cascading level (e.g., Z_1 should be independent of L).

As a result, the dimensionality of model units with respect to the number of inputs will become smaller as we move to the next higher level. For example, all inputs of model units in the third cascading level of Figure 8-14 have two dimensions (one for each input). Such a reduction of dimensionality will result in fewer sampling points required for uncertainty analysis.

An important issue of such a cascading or decomposing scheme is the trade-off between the reduction of dimensionality (or complexity) and the accuracy of approximating response variables of interest. This issue arises because we have to approximate the PDF of intermediate variables (e.g., Z_1, Z_2, \dots) in order to calculate the PDF for the next model unit.

The error involved in reducing the dimensionality from a two-dimensional polynomial chaos expansion into a one-dimensional polynomial chaos expansion can be evaluated as an L_2 -norm error in distribution:

$$\epsilon_{L_2}^d = \sqrt{\int (f_r(r) - \hat{f}_r(r))^2 dr}, \quad (8.37)$$

where $f_r(r)$ and $\hat{f}_r(r)$ are the density functions of output variable r from the two-dimensional polynomial chaos expansion and the regenerated one-dimensional polynomial chaos expansion.

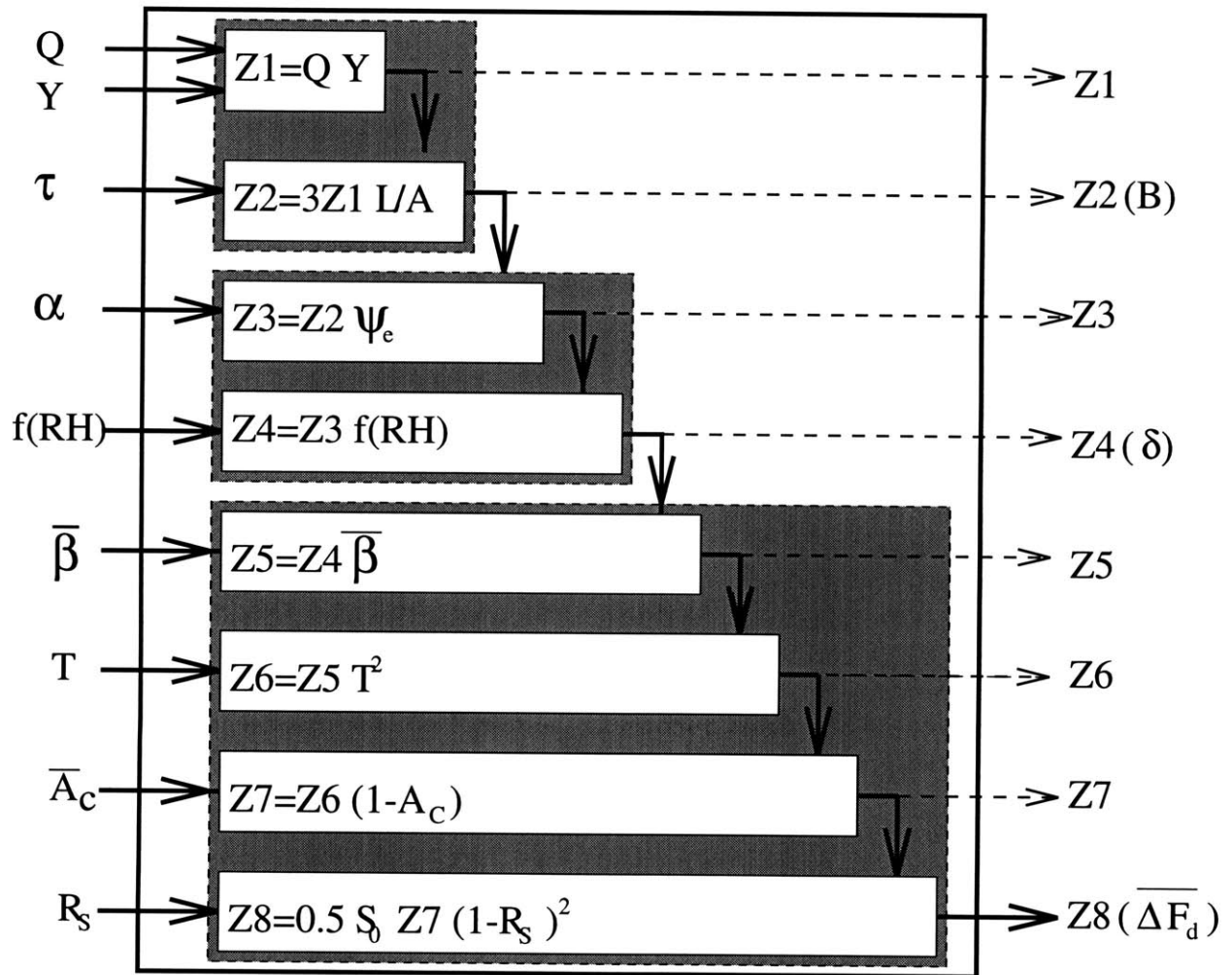


Figure 8-14: Illustration of cascading schemes: three cascading levels for Charlson et al.'s model [24].

sion respectively. This error definitely adds to the error of propagating the distribution of the inputs to the outputs of the corresponding model. Therefore in general, we will have two different kinds of errors: one is from the use of the MCM or DEMM approach to propagate the distribution through the corresponding model, and the other is from the reduction of dimensionality. It should be pointed out that these two errors may not be combined together because of different norms used. Specifically, the error from the collocation approach involves the L_2 -norm *in response surface*:

$$\epsilon_{L_2}^s = \sqrt{\int f_r(r)(r(p) - \hat{r}(p))^2 dr}, \quad (8.38)$$

where $r(p)$ and $\hat{r}(p)$ are the true and the approximated response surfaces of output variable r as functions of uncertain inputs or parameters respectively.

For an error bound of 0.01, a speed-up factor could vary between 8 and 200 for a 9-dimensional model, provided that it can be ideally decomposed into 2-dimensional units.

The success of using this method requires that the model can be decomposed into submodels such that no strong feedback processes cross them.

8.5 Conclusions

This chapter reviews a relatively new and computationally attractive approach (DEMM) for performing uncertainty analysis in large implicit modeling systems. The basic idea behind DEMM is to approximate the response surface of a random variable of interest with some form of orthogonal polynomials. The specific form of the polynomial depends on the PDFs of the uncertain parameters to be considered. For example, a Gaussian random variable corresponds to Hermite polynomials. To obtain the coefficients of these base functions, one can evaluate a model at the so-called collocation points, which are the roots of the orthogonal polynomials, according to their corresponding PDF. Therefore the model response surface can be iteratively approximated using different order polynomials until the error is tolerant. Although the resulting response surface is only an approximation to the actual response surface, its polynomial form greatly reduces the amount of time required to generate statistical information, such as expected value, PDF, and variance.

The performance of DEMM is illustrated with a nonlinear analytical model with nine uncertain parameters. The logarithm of the relative error decreases linearly with the order of approximation, indicating a fast convergence rate. The L_2 -norm error between the simulated and the analytical PDFs falls below 2% for a third order approximation. Comparison of DEMM with the MCM shows that DEMM is a factor of 25 to 60 faster.

For a large implicit model, DEMM can be used together with the K-L expansion technique and cascading scheme. The K-L expansion reduces the dimensionality of the original random field by decomposing a random field into some uncorrelated random variables. The global distributions of total cloud cover and sea level pressure are used as examples for the illustration of the idea. The cascading scheme on the other hand overcomes the ‘‘curse’’ of dimensionality by cascading the original model into several levels of submodels with fewer uncertain parameters. The uncertainty analysis for these submodels can be sped up by a factor of 8 to 200 for a 9-dimensional model at an error bound of 0.01, provided that the model can be ideally broken into 2-dimensional units.

In the following chapter, DEMM will be applied to the uncertainty analysis of direct and indirect radiative forcing by anthropogenic sulfate aerosols.

Chapter 9

Applications of Uncertainty Analysis: 1. Direct Radiative Forcing by Anthropogenic Sulfate Aerosols

In this and the following chapters, the technique discussed in the previous chapter will be applied to quantify the uncertainty of the radiative forcing by anthropogenic sulfate aerosols and to identify the key uncertain parameters.

9.1 Introduction

As discussed in Chapter 4, the DRF by anthropogenic sulfate aerosols estimated in the literature has a large variation, as shown in Figure 4-3. This is caused presumably by uncertainty in both model structures (structural uncertainty) and model parameters (parametric uncertainty). Tables 9.1 and 9.2 listed the known difference in model structures (i.e., model physical assumptions) and model parameters.

Table 9.1 shows that aerosol optical properties (AOPs), i.e., specific extinction, single scattering albedo, and asymmetry factor or backscattered fraction, used in C91, C92, P, and TP, are the observed values at a visible wavelength of $0.55 \mu m$. However, in KB and BT, AOPs are computed from standard Mie theory using observed aerosol size distribution and refractive index data. The DRF is evaluated in the solar spectrum using different radiative transfer schemes. In C91, C92 and P, Beer's law is used to compute the radiative forcing. In KB and TP, a δ -Eddington model with different spectral intervals is used; whereas in BT, a radiative perturbation technique [149] is applied at 23 wavelengths ranging from 0.3 to $4 \mu m$. It is claimed in KB that half of the difference between their result and that in C91 is that the latter doesn't account for the spectral dependence of AOPs.

As for the humidity effect on aerosol extinction, all studies except BT use an observed scaling function at $0.55 \mu m$ to give aerosol specific extinction at ambient relative humidity of 75%-80%. In BT, this scaling function is instead computed at different wavelengths for $(NH_4)_2SO_4$ using the method of [63]. As we see from Table 9.2, the calculated specific extinction differs the observed one by a factor of 1.7 and 1.4 at relative humidity of 0% and 75% respectively. Nevertheless, it is concluded in BT that one can resolve the factor-of-2 difference between C91 and KB by taking into account the spectral dependence of this

Table 9.1: A summary of treatment of model structures in different studies for computing the direct radiative forcing by anthropogenic sulfate aerosols, where LR stands for Langner and Rodhe [83], and other symbols are defined in the text.

Quantity	C91	C92	P	KB	TP	BT
Dimensionality	2	1	1	2	2	1
Y	LR	C92	C92	LR	TP	C92
Column burden	„	Q,Y,L	Q,Y,L	„	„	Q,Y,L
AOP		obs.		r_g, σ_g	obs.	r_g, σ_g
Humidity effect			obs.			r_g, σ_g, RH
Spectrum(μm)	0.55	0.55	0.55	0.2-5.0	0.3-1.5	0.3-4.0
Radiative transfer		Beer's Law		δ -Eddington		Perturbation
$\Delta F(W/m^2)$	-0.60	-1.30	-0.90	-0.28	-0.90	-0.60

scaling function.

In addition, model dimensions and column burden calculation in these studies are not all the same. In C92, P, and BT, radiative forcing is computed in a column with the estimated column burden; whereas in C91, KB, and TP column burden is explicitly calculated using a chemical transport model [83, 145].

In Table 9.2, key parameters used in the calculation of radiative forcing are listed for different studies. We see major differences in AOPs (e.g., optical depth and backscattered fraction), atmospheric properties (e.g., cloud cover fraction, surface albedo, and atmospheric transmittance above the aerosol layer), and column burden of sulfate. The difference in the radiative forcing among C91, C92, and P is mainly due to different optical depths. In addition, the backscattered fractions used in these studies are not consistent. As stated in KB, the radiative forcing will increase by 25% if the same backscattered fraction used in C91 is used in their calculation. It is also worthwhile to point out that the global calculation in C91 is obtained using constant surface albedo, atmospheric transmittance, and humidity scaling factor; whereas in KB these parameters are spatial dependent. Finally there is a difference in sulfate column burden data between C91/KB and TP. C91 and KB use the data from Langner and Rodhe [83], and TP uses the data computed from their climate-chemistry-ocean mixed layer model.

The point of listing so much uncertainty in evaluating the DRF by anthropogenic sulfate aerosols is to emphasize that the differences among various estimates may come from the differences in choosing both model assumptions and parameters. To quantify the uncertainty, one needs to carry out parametric uncertainty analysis using different models. If the parametric uncertainty is much larger than the structural uncertainty, one may stop further developing models and instead focus on improving our knowledge of uncertain parameters.

Table 9.2: A summary of specification of model parameters in different studies for computing the direct radiative forcing by anthropogenic sulfate aerosols, where symbols are defined in the text. All parameters are column value, except those indicated by (x, y) are two-dimensional. “/” indicates an item either not available or not applicable.

Quantity	C91	C92	P	KB	TP	BT
$Q(10^{12}gS/yr)$	72.5	90	71	72.5	78	71
Y	(x,y)	0.4	0.5	(x,y)	(x,y)	0.5
$L(days)$	(x,y)	7.3	5.5	(x,y)	(x,y)	6.0
$B(mg/m^2)$	(x,y)	4.6	3.2	(x,y)	(x,y)	3.3
$r_g(\mu m)$	/	/	/	0.05	/	0.0695
σ_g	/	/	/	2.0	/	2.0
$\Psi_e^{0.55\mu m}(m^2/g)$	5.0	5.0	5.0	5.0	5	3.0
$f_1^{0.55\mu m}(RH = 75\%)$	1.7	1.7	1.7	1.7	1.7	2.0
$\beta^{0.55\mu m}$	0.29	0.29	0.30	0.22	0.22	0.20
$\tau^{0.55\mu m}$	0.017	0.039	0.027	/	/	0.02
T	0.76	0.76	0.76	(x,y)	(x,y)	0.76
R_s	0.15	0.15	0.15	(x,y)	(x,y)	0.15
A_c	(x,y)	0.60	0.61	(x,y)	(x,y)	0.61
$\Delta F(W/m^2)$	-0.60	-1.30	-0.90	-0.28	-0.90	-0.60

9.2 Model Structures

In order to study the relative importance of parametric uncertainty vs. structural uncertainty, I will use four different model structures.

The first model (D1) (cf. Equation 4.13) is the same as in Charlson et al. [24].

The second model (D2) governed by Equation 4.12 evaluates AOPs at 24 wavelengths ranging from 0.3 to 4 μm with the solar irradiance data given by Labs and Neckel [82]. The refractive index of the sulfate aerosols is from d’Almeida et al. [36]. In the calculation of the refractive index change due to relative humidity change as discussed in Chapter 3, the refractive index of water is from Hale and Querry [61].

The third model (D3) employs the radiative transfer scheme developed at NASA Goddard Space Flight Center [27, 26]. This scheme (referred as the GSFC scheme in the following) solves the radiance separately for the long-wave and short-wave spectral ranges.

For short-wave radiation, the GSFC scheme includes the Rayleigh scattering and the absorption and scattering due to ozone, oxygen, carbon dioxide, water vapor, aerosols, and clouds. The spectral dependence of absorption and scattering is approximated by 7 water vapor bands in the near infrared region and 4 bands in the UV-visible region. The multiple scattering for each vertical layer is computed analytically using the delta-four-stream discrete-ordinate approximation [87], and the two-stream adding method is used to compute upward and downward fluxes for a composite of layers. The required aerosol optical properties for the scheme are optical depth, single-scattering albedo, and asymmetry factor. Fluxes and heating rates computed using this scheme are accurate to within a few percent compared to the calculations from high spectral resolution and detailed multiple-scattering methods [26].

For long-wave radiation, the GSFC scheme includes the absorption due to ozone, carbon dioxide, water vapor, aerosols, and clouds. It uses a so-called “medium-sized band” model for water vapor and CO_2 absorption with the infrared spectrum divided into 10 bands. Clouds and aerosols are assumed to be “gray bodies” with the diffuse transmission computed to be $\exp -1.66\tau$, where τ represents the optical depth for clouds and aerosols. This scheme introduces an error of $< 1.5W/m^2$ in computing the fluxes and $< 0.15^\circ C/day$ in computing the cooling rates in the troposphere and lower stratosphere [27]. Previous study [60] and our own calculation indicate that the multiple scattering can be negligible if $\tau(10\mu m) \leq 0.1$, which is satisfied even for an urban/industrial aerosol model in high relative humidity. Therefore we think the treatment for aerosols in the long-wave radiation calculation is accurate enough for this study.

The last model (D4) employs the radiative transfer scheme developed by Fu and Liou [51] and will be referred as the QFU scheme in the following. It has been described in Chapter 4.

The GSFC and QFU schemes both input AOPs of optical depth, single-scattering albedo, and asymmetry factor for each vertical layer. The main difference lies in their treatment of the vertical nonhomogeneity of the atmosphere. The QFU scheme assumes a simple correlation of absorption coefficient distributions at different temperatures and pressures; whereas the GSFC scheme extrapolates the absorption coefficient from that at a reference temperature and pressure. In addition, in the QFU scheme the multiple-scattering involving cloud and aerosol particles can be easily incorporated without introducing further assumptions and the treatment of short- and long-wave radiative transfer is more consistent. However, in the GSFC scheme, clouds and aerosols are assumed to be “gray bodies”.

In D3 and D4, the atmospheric profiles for subarctic summer as defined in McClatchey

Table 9.3: Central values, uncertainty factors for log-normally distributed parameters used in the Monte Carlo and the probabilistic collocation simulations.

Quantity	Models	Central value	Uncertainty factor	Reference
$Q(Tg/yr)$	D1,D2,D3,D4	71	1.15	Penner et al.(1994)
Y	„	0.5	1.5	„
$L(days)$	„	5.5	1.5	„
$r_g(\mu m)$	„	0.0488	1.26	Whitby(1978)
σ_g	„	2.00	1.16	Whitby & Sverdrup(1980)
$1 - R_s$	„	0.85	1.1	Robock(1980)
$1 - A_c$	„	0.39	1.1	Warren et al.(1986)
RH	D2,D3,D4			β distribution mean=0.75, σ =0.13
T	D1,D2	0.76	1.2	Charlson et al.(1992)
$H(km)$	D3,D4	1.42	1.4	mean=1.5, σ =0.5
f(RH)	D1	1.7	1.2	Charlson et al.(1992)

et al. [91] are used in the radiative calculation. with an average solar zenith angle of 60° .

9.3 Uncertainty Analysis

As discussed in the previous sections, the estimated radiative forcing by sulfate aerosols depends on both model structures and parameters. Therefore it is necessary to study the PDFs from different model structures given the same input parameters so that one may determine which uncertainty source is more important.

To do that, one has to know the PDFs for uncertain parameters under consideration. As in P, we assume most of the uncertain parameters are log-normally distributed with the same central values and uncertainty factors given there. Since AOPs depend on the size distribution and are highly correlated with each other, we will compute the AOPs from r_g and σ_g according to Whitby (1978) [163] and Whitby and Sverdrup (1980) [164]. We give the central values and uncertainty factors for those log-normally distributed parameters in Table 9.3, where H is the mixed layer height.

The mixed layer height is the parameter used only in D3 and D4. The central value and uncertainty factor of H is chosen such that the mean and standard deviation are 1.5 km and 0.5 km, respectively.

Since the relative humidity is bounded between zero and unity, we approximate its PDF with a beta distribution with mean of 75% and standard deviation of 13%. This distribution is plotted in Figure 9-1.

In Figure 9-2, the PDFs of the resultant radiative forcing with 10000 sampling points for D2, D3, and D4 are plotted, along with the analytically obtained PDF for D1. The corresponding means and ranges for 95% confidence of the PDFs are shown in Figure 9-8. The PDF for D1 is log-normally distributed with central value (c) of 0.9 and uncertainty

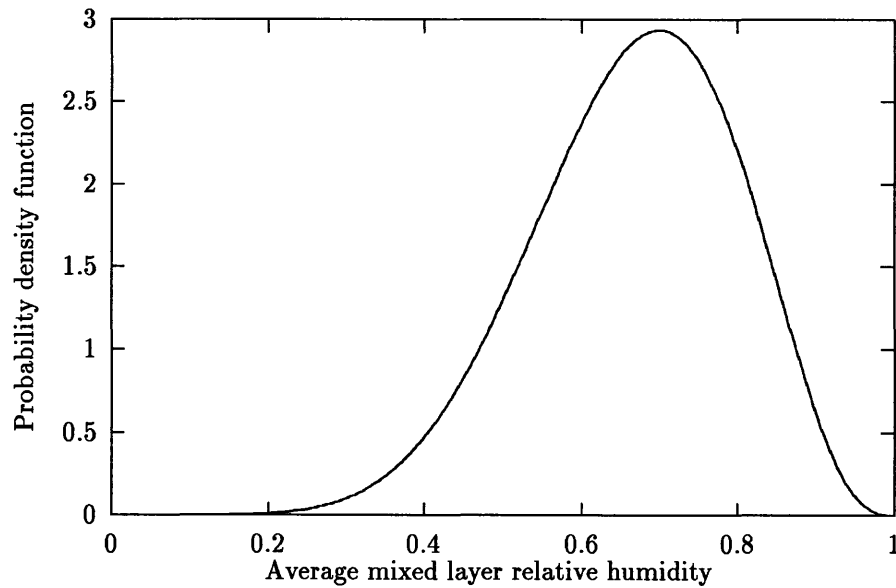


Figure 9-1: The PDF of mixed layer relative humidity used in this paper. It is assumed to be a beta distribution with mean of 0.75 and standard deviation of 0.13.

Table 9.4: Comparison of mean (μ), standard deviation (σ), and 95% confidence range ($R_{95\%}$) for D1.

Quantity	Analytical	Second order DEMM	MCM(1000)
$\mu(W/m^2)$	1.3	1.3	1.2
σ	1.3	1.0	1.0
$R_{95\%}$	0.2-4.8	0.1-4.0	0.2-4.2

factor (u) of 2.3, which are the same as in P. The mean and standard deviation are about 1.3. Since the standard deviation is quite large, the range for 95% confidence is between 0.2 and 4.8 (cf. Table 9.4). The main reason for this wide range is that some of the uncertainty parameters (i.e., Ψ_e , $\bar{\beta}$, and f_{Ψ_e}) used in the calculation are highly correlated.

The PDFs for D2, D3, and D4 are close to each other, suggesting that D2 is a much better approximation than D1. The mean, standard deviation and ranges for 95% confidence are listed in Tables 9.4 to 9.7. The structural uncertainty, defined as the magnitude of the difference between the means of different outputs, is within 0.13. However the parametric uncertainty is at least a factor of 5 times larger. Therefore, it is clear that much efforts should be focused on reducing the parametric uncertainty instead of structural uncertainty.

Figure 9-3 shows the PDF from second order DEMM along with that using 1000 sampling points MCM and the analytical PDF. It is seen that the second order DEMM, which solves the model at only 55 points, can give as accurate PDF as using a 1000 sampling point MCM. Table 6 shows the corresponding means, standard deviations, and the ranges of 95% confidence.

In Figure 9-4, the PDF using DEMM with second order terms is compared to those using

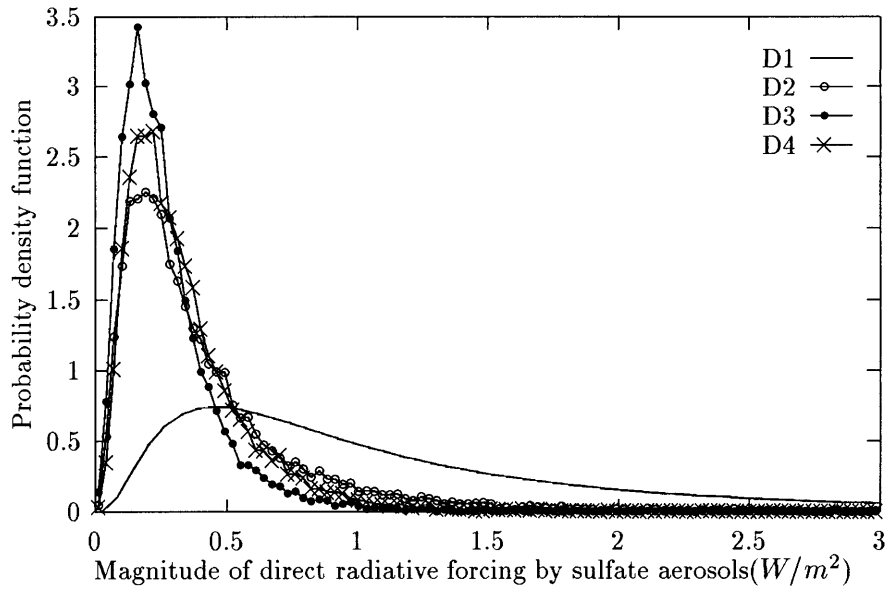


Figure 9-2: The PDFs of global-mean DRF by anthropogenic sulfate aerosols using 10000 sampling points MCM for D2, D3, and D4. The PDF for D1 is analytically obtained.

Table 9.5: Comparison of mean (μ), standard deviation (σ), and 95% confidence range ($R_{95\%}$) for D2.

Quantity	MCM(10000)	Second order DEMM	MCM(1000)
$\mu(W/m^2)$	0.41	0.43	0.42
σ	0.35	0.33	0.36
$R_{95\%}$	0.1-1.4	0.1-1.3	0.1-1.4

Table 9.6: Comparison of mean (μ), standard deviation (σ), and 95% confidence range ($R_{95\%}$) for D3.

Quantity	MCM(10000)	Second order DEMM	MCM(2200)
$\mu(W/m^2)$	0.28	0.28	0.28
σ	0.20	0.18	0.20
$R_{95\%}$	0.1-0.78	0.1-0.71	0.1-0.78

Table 9.7: Comparison of mean (μ), standard deviation (σ), and 95% confidence range ($R_{95\%}$) for D4.

Quantity	MCM(10000)	Second order DEMM	MCM(1100)
$\mu(W/m^2)$	0.35	0.37	0.35
σ	0.25	0.25	0.25
$R_{95\%}$	0.1-0.99	0.1-1.0	0.1-0.99

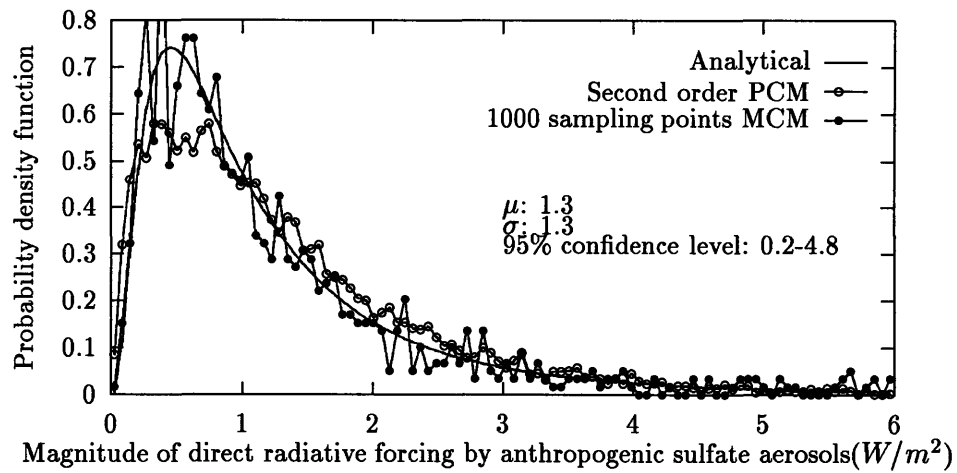


Figure 9-3: Comparison of PDFs from 10000 sampling points MCM, second order DEMM and 1000 samplings points MCM for D1.

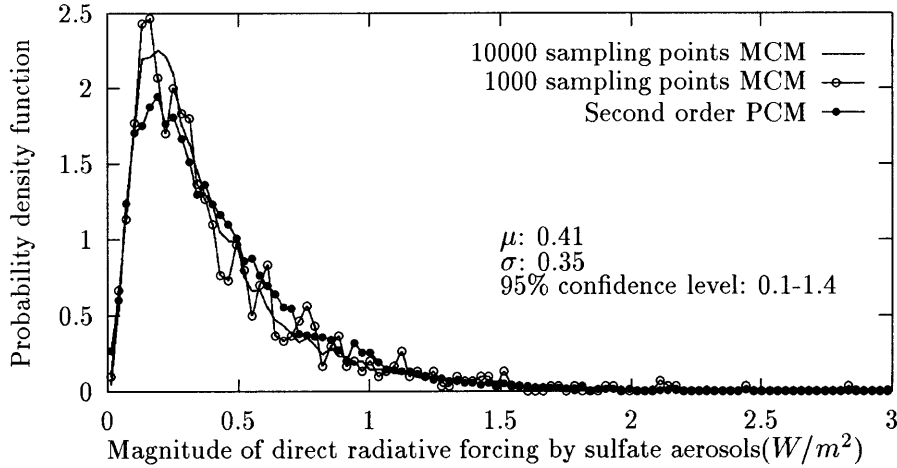


Figure 9-4: Comparison of PDFs from a 10000 sampling point MCM, a second order DEMM and a 1000 sampling point MCM for D2.

1000 and 10000 sampling point MCMs. By checking the L_2 -norm error of the resulting PDF with respect to that from the 10000 sampling point MCM, we find that the PDF from DEMM is comparable to that from the 1000 sampling point MCM. Table 6 shows the corresponding means, standard deviations, and the ranges of 95% confidence.

Similar results are shown in Figure 9-5 for D3 and in Figure 9-6 for D4. The means, standard deviations, and the ranges of 95% confidence are close to 2200 and 1100 sampling point Monte Carlo simulations respectively.

Figure 9-7 shows the PDFs from DEMM for D1, D2, D3, and D4. Figure 9-8 compares the means and ranges of 95% confidence for D1, D2, D3, and D4 using MCM and DEMM. It seems that the second order approximation of DEMM is able to capture as much information regarding the PDFs as the computationally expensive MCM.

The normalized variance contributions by each uncertain parameter using DEMM for D2, D3, and D4 are shown in Table 9.8. The agreement is quite good except that the contribution by R_s in D3 is much larger than in D2 and D4. When making comparisons, one thing should be kept in mind. Uncertainty resulting from atmospheric composition is embedded in T for D2, whereas it is not taken into account in D3 and D4. Nevertheless, the ranking in terms of variance contributions is straightforward. Y and L make the largest contribution, followed by relative humidity in D3 and D4. In D2, T contributes more than RH . Surprisingly, the variance contributions from r_g and σ_g are relatively low comparing with those from most of the other parameters, with r_g being the lowest of all. This can be explained from Figure 10, which shows that the sensitivity of radiative forcing to r_g and σ_g is very small around of the mean (i.e., $r_g = 0.05\mu m$, $\sigma_g = 2.0$).

The speed-up factor, which is defined as the ratio of computational time required by MCM and by DEMM, depends on the specific L_2 -norm error. It should double since variance contributions by each uncertain parameter using MCM requires running the model with respect to each parameter while fixing others. Of course, this assumes that the time required for generating the PDF of Equation 8.7 is negligible. Although this is not true for D1, it

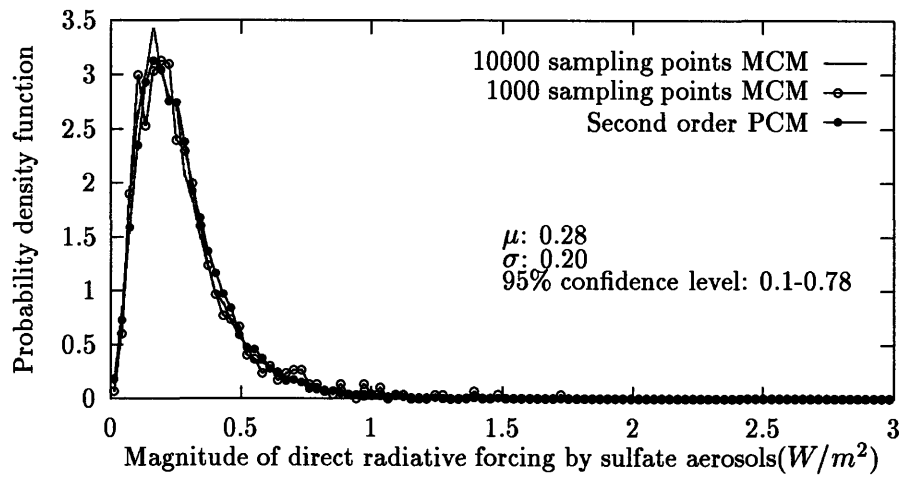


Figure 9-5: Comparison of PDFs from a 10000 sampling point MCM, a second order DEMM and a 1000 sampling point MCM for D3.

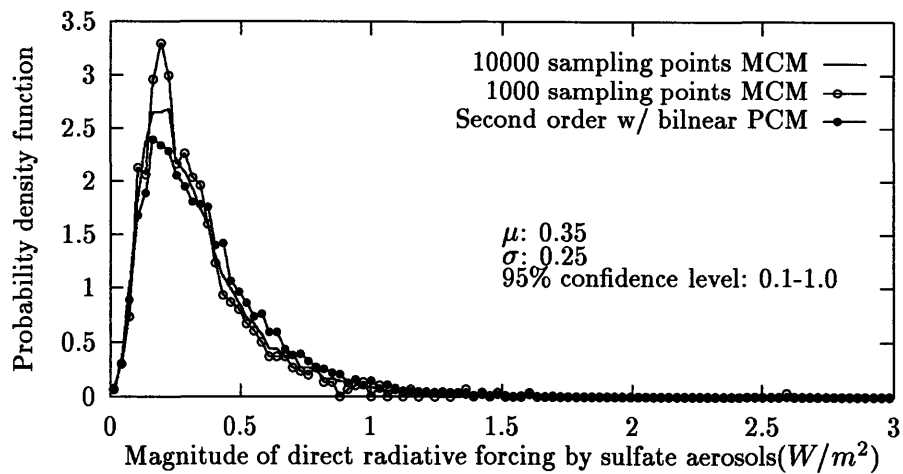


Figure 9-6: Comparison of PDFs from a 10000 sampling point MCM, a second order DEMM and a 1000 sampling point MCM for D4.

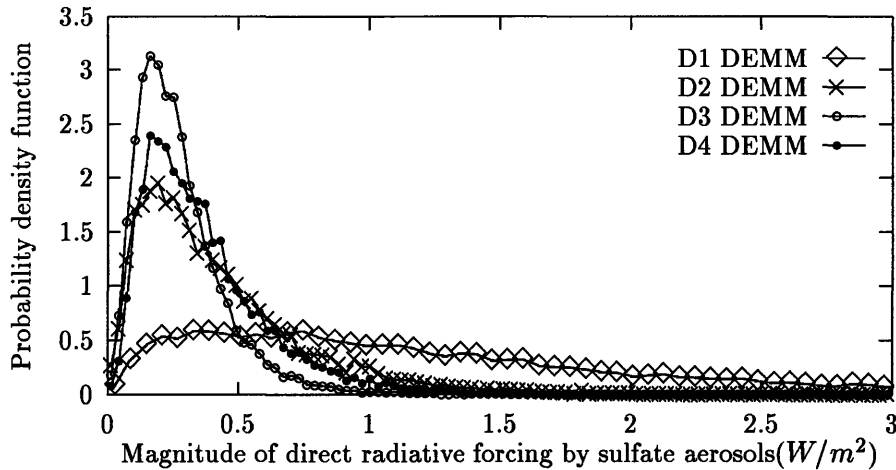


Figure 9-7: Comparison of PDFs from DEMM for D1, D2, D3, and D4.

is a reasonable assumption for the computationally expensive models (D2, D3, and D4). From Tables 9.4 to 9.7, the speed-up factor ranges from 40 to 80 if a second order DEMM is used.

The normalized variance contribution by each uncertain parameters is plotted in Figure 9-9.

Figure 9-9 shows the key uncertain parameters are Y , τ , T , and $f(RH)$.

Also the size parameters make little contribution to the model variance. This can be understood from Figure 9-10, which contours the direct aerosol radiative forcing with respect to r_g and σ_g .

One limitation for the uncertainty analysis in the previous section is that uncertainty parameters are only scalar variables. However, in practice uncertainty may exist as random fields. For example, uncertainty in the direct radiative forcing by aerosols may come from inaccurate knowledge of aerosol refractive index, which is a function of wavelength and therefore is a random process. Also if the radiative forcing is calculated on the globe, one may treat some parameters including surface albedo, cloud fraction and sulfate burden as random fields. Although the treatment of random fields has been discussed in Chapter 8, in this thesis we will only focus the uncertainty analysis for random parameters.

9.4 Conclusions

In this chapter, the DRF by anthropogenic sulfate aerosols has been evaluated using the uncertainty analysis technique discussed in Chapter 8.

Four different model structures have been used to obtain the probability density function of the direct radiative forcing of anthropogenic sulfate aerosols in the presence of nine uncertain parameters, whose probability density functions are specified as in the literature. The mean values vary from 0.3 to 1.3 W/m^2 and the 95% confidence range is 0.1 to 4.2 W/m^2 (Figure 9-8). The structural uncertainty is about 1.0 W/m^2 and is much smaller than the parametric uncertainty of 4.1 W/m^2 . This implies that it is relatively more important

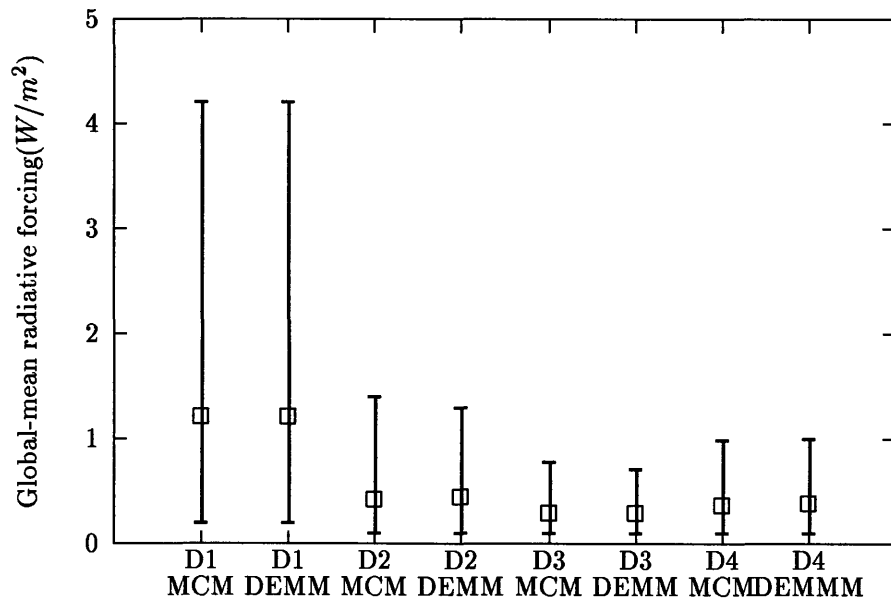


Figure 9-8: The mean and 95% confidence range of global-mean direct radiative forcing by anthropogenic sulfate aerosols estimated by MCM and DEMM for D1, D2, D3, and D4.

Table 9.8: Normalized variance contribution by each uncertain parameter estimated by DEMM for D2, D3, and D4.

Quantity	Normalized variance contribution(%)		
	D2	D3	D4
$Q(Tg/yr)$	2.78	3.29	3.58
Y	33.7	39.6	40.8
$\tau(days)$	33.7	39.6	40.8
$r_g(\mu m)$	0.010	0.073	0.093
σ_g	0.44	1.60	1.20
RH	11.4	9.84	11.0
T	16.5	/	/
H	/	0.40	0.77
A_c	1.30	1.80	1.55
R_s	0.18	3.69	0.14

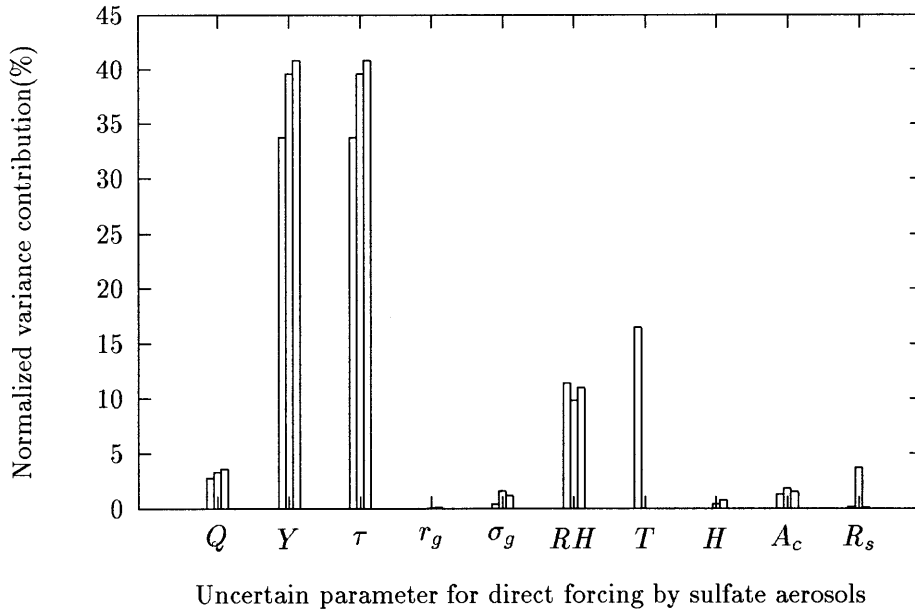


Figure 9-9: Normalized variance contribution by each uncertain parameter to direct radiative forcing by sulfate aerosols.

to reduce the uncertainties in model parameters than to improve models. Variance analysis indicates that the sulfate yield and lifetime are the top two contributors to the model output variance, followed by the dependence function of aerosol optical properties on the relative humidity of ambient air. Therefore, much effort should be focused on understanding chemical transformations of sulfate aerosols in the atmosphere, at least based on the models and parameters applied here.

It should be noted that the conclusions reached here are subject to the choice of both model structures and parameter distributions. The focus is not to determine what exactly the mean and range of confidence are, but to present a rational attempt of coping with uncertainty in climate issues.

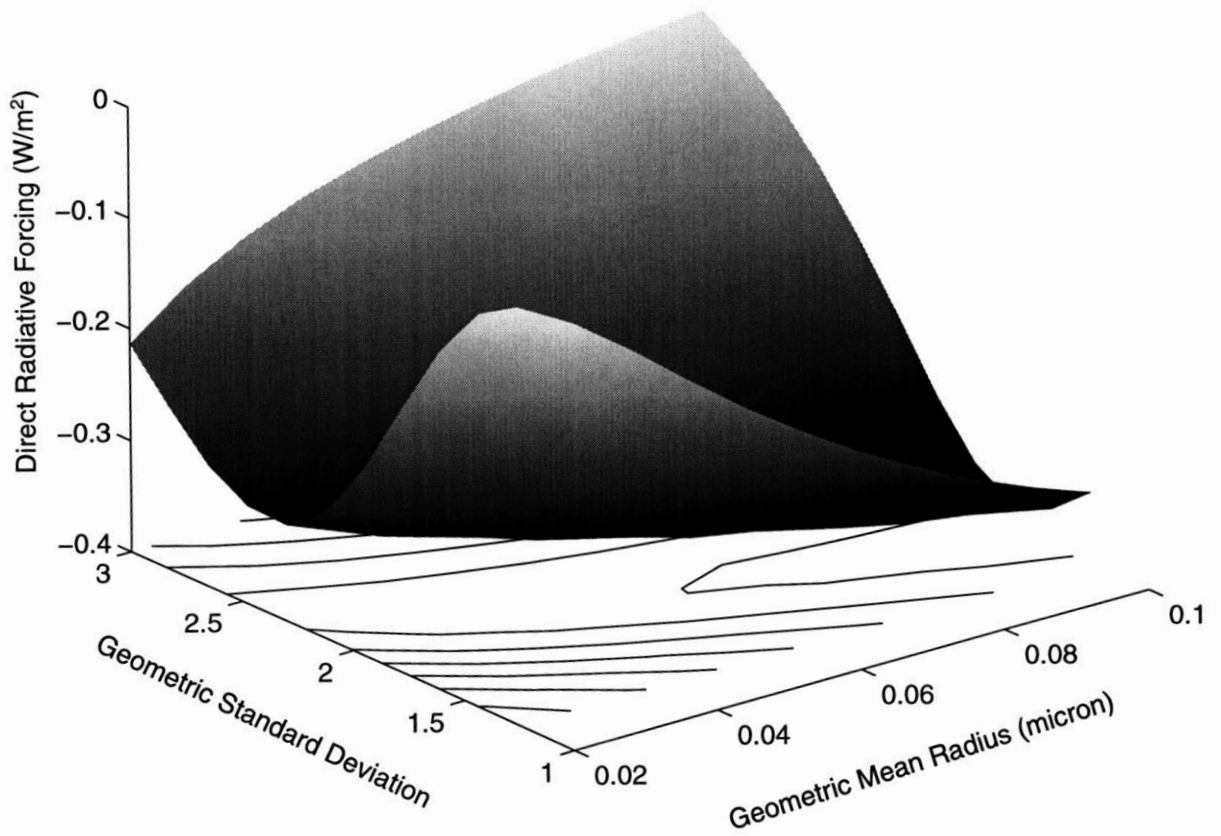


Figure 9-10: Direct radiative forcing by anthropogenic sulfate aerosols with respect to geometric mean radius and standard deviation of the size distribution.

Chapter 10

Applications of Uncertainty Analysis: 2. Indirect Radiative Forcing by Anthropogenic Sulfate Aerosols

10.1 Introduction

The indirect radiative forcing (IRF) by aerosols represents the perturbation of cloud-top albedo due to an increase in cloud droplet number concentration resulting from an increase of atmospheric aerosols. As for the DRF, the IRF by anthropogenic sulfate aerosols has also caught much attention over recent years due to the studies by Charlson et al. (1992) [24], Kaufman and Chou (1993) [76], Boucher and Rodhe (1994) [15], Jones et al. (1994) [70], and Chuang and Penner (1995) [28]. These studies will be identified hereafter by C92, KC, BR, JRS, and CP, respectively. A summary of these results is shown in Figure 10-1, along with the radiative forcing by carbon dioxide and total greenhouse gases from preindustrial time to 1990 [133]. To facilitate the comparison, only the magnitude of the radiative forcing is shown. Although the indirect radiative forcing is believed to have larger uncertainty than the direct radiative forcing, surprisingly, the various estimates of median value on Figure 10-1 tend to agree with each other. As we have done for the DRF, in the following sections we will evaluate the uncertainty of the IRF caused by model structures and model parameters.

10.2 Model Structures

Five different models are used to simulate the structural uncertainty. As in the previous chapter, anthropogenic sulfate aerosols are assumed vertically well-mixed in the boundary layer with a log-normal size distribution.

The first model structure (I1) takes the form of Twomey's model [151]. The governing equations for computing the global mean indirect radiative forcing, $\overline{\Delta F_i}$, can be summarized as follows:

$$\overline{\Delta F_i} = -\frac{1}{4}F_T T^2 A_{st} \Delta R_{ct}, \quad (10.1)$$

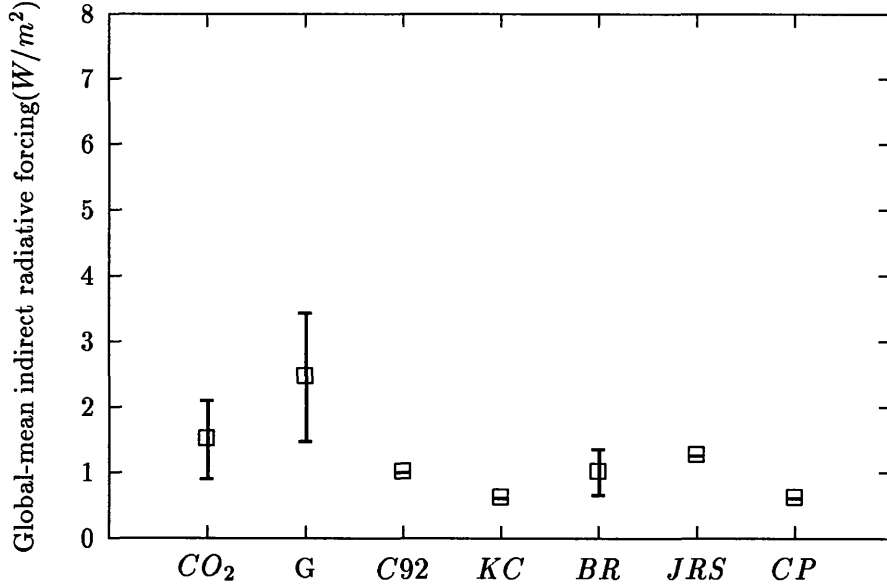


Figure 10-1: Comparison of global-mean IRF by anthropogenic sulfate aerosols estimated by various studies, along with the radiative forcing change by carbon dioxide (CO_2) and total greenhouse gases (G) from preindustrial time to 1990. C92, KC, BR, JRS, and CP are defined in the text, and error bars indicate the ranges of the forcing for 95% confidence where they apply. Only the magnitudes of the forcings are shown here.

$$\Delta R_{ct} = R_{ct}(1 - R_{ct}) \frac{\Delta N_d}{3N_d}, \quad (10.2)$$

$$N_d = cS_{max}^k, \quad (10.3)$$

$$\Delta N_d = f_{ac} \Delta N_a, \quad (10.4)$$

$$f_{ac} = \frac{1}{2}[1 - \text{erf}(x_c)], \quad (10.5)$$

$$x_c = \frac{\ln(r_{min}/r_g)}{\sqrt{2} \ln \sigma_g}, \quad (10.6)$$

$$r_{min} = 0.0145 S_{max}^{-2/3}, \quad (10.7)$$

$$\Delta N_a = \frac{9QYL}{4H\pi\rho \int r^3 n(r) dr}, \quad (10.8)$$

where F_T is the solar constant, T the atmospheric transmittance above the aerosol layer, A_{st} the fraction of stratiform cloud cover, R_{ct} the cloud top albedo, N_d the cloud droplet number density, S_{max} the maximum supersaturation in the cloud, c and k the slope and y-offset for the cloud condensation nuclei (CCN) activation spectrum, f_{ac} the aerosol activation fraction, r_{min} the radius of the smallest aerosol activated, and r_g and σ_g are the size parameters of the aerosol distribution. The rest of the symbols follow the definitions in Chapter 9.

Under the two-stream approximation in radiative transfer, the reflectance of a nonabsorbing, horizontally homogeneous cloud can be expressed as [32]

$$R_{ct} = \frac{\beta(\mu_0)\tau_c/\mu_0}{1 + \beta(\mu_0)\tau_c/\mu_0}, \quad (10.9)$$

where τ_c is the optical depth of the cloud,

$$\tau_c = \pi r_e^2 Q_e N \Delta z. \quad (10.10)$$

Here Δz is the thickness of the cloud, r_e is the effective drop radius, and Q_e is the average extinction efficiency. Since the radius of cloud droplets is much larger than the wavelength of visible light, Q_e may be approximated as a constant of 2, N is the cloud droplet number concentration and is related to the cloud liquid water content W as

$$W = \frac{4}{3} \pi r_e^3 N. \quad (10.11)$$

Under the assumption of constant liquid water content [152] and cloud thickness by the perturbation in N , R_{ct} may be written as

$$R_{ct} = \frac{C N^{1/3}}{1 + C N^{1/3}}, \quad (10.12)$$

with the constant $C = 2\pi\beta\Delta z(\frac{3W}{4\pi})^{2/3}/\mu_0$. Taking the logarithm of Equation 10.12 and then differentiating, one can obtain Equation 10.2.

The logarithmic form of the CCN activation spectrum of Equation 10.3 is obtained based on observations [151]. The perturbation of the cloud droplet concentration, ΔN_d , is the same as the number of aerosols activated, which is the number of aerosols larger than the size of the smallest activated aerosols, r_{min} :

$$\Delta N_d = \int_{r_{min}}^{\infty} n(r) dr. \quad (10.13)$$

Substitution of Equation 3.3 in Equation 10.13 yields Equations 10.4 to 10.6. Based on a closed adiabatic parcel model, r_{min} can be related to the in-cloud maximum supersaturation S_{max} as in Equation 10.7.

The second model (I2) is the same as I1 except that the empirical relation between ΔN_d and ΔN_a [90] replaces Equation 10.4. The resulting equations are

$$\overline{\Delta F_i} = -\frac{1}{4} F_T T^2 A_{st} \Delta R_{ct}, \quad (10.14)$$

$$\Delta R_{ct} = R_{ct} (1 - R_{ct}) \frac{\Delta N_d}{3 N_{d0}}, \quad (10.15)$$

$$\Delta N_d = 375 (1 - \exp[-2.5 \times 10^{-3} \Delta N_a]), \quad (10.16)$$

$$\Delta N_a = \frac{9 Q Y L}{4 H \pi \rho \int r^3 n(r) dr}. \quad (10.17)$$

The third model structure (I3) is the same as I1 except that Ghan's nucleation parameterization for f_{ac} [55] is used for aerosol activation fraction, f_{ac} . This model is governed by

$$\overline{\Delta F_i} = -\frac{1}{4} F_T T^2 A_{st} \Delta R_{ct}, \quad (10.18)$$

$$\Delta R_{ct} = R_{ct}(1 - R_{ct}) \frac{\Delta N_d}{3N_d}, \quad (10.19)$$

$$N_d = cS_{max}^k, \quad (10.20)$$

$$\Delta N_d = f_{ac}\Delta N_a, \quad (10.21)$$

$$f_{ac} = \frac{1}{1 + d\Delta N_a/w^*}, \quad (10.22)$$

$$d = d_0(T, P, \sigma_g) f_d(\epsilon, r_g), \quad (10.23)$$

$$w^* = 0.24 \left(ckB \left(\frac{k}{2}, \frac{3}{2} \right) S_{max}^{k+2} \right)^{2/3}, \quad (10.24)$$

$$\Delta N_a = \frac{9QYL}{4H\pi\rho \int r^3 n(r) dr}, \quad (10.25)$$

where the coefficient d depends on d_0 (a function of σ_g and ambient temperature and pressure) and the scaling factor, f_d (a function of the mass fraction of water-soluble substance in the aerosol, ϵ , and r_g), w^* is the effective vertical velocity in cloud, which is in general the sum of vertical velocity and the upward motion driven by radiative cooling and turbulent processes [55].

Since the effective vertical velocity depends on the specific cloud processes, for simplicity it is approximated as in Equation 10.24, using a closed adiabatic parcel model assuming the logarithmic form of the activation spectrum [151], where B is the Beta function.

The fourth model (I4) replaces the radiation calculation in I1 with the NASA/GSFC radiation scheme [27, 26]:

$$\frac{\Delta\tau_c}{\tau_c} = \frac{1}{3} \frac{\Delta N_d}{N_d}, \quad (10.26)$$

$$\Delta N_d = f_{ac}\Delta N_a, \quad (10.27)$$

$$N_d = cS_{max}^k, \quad (10.28)$$

$$f_{ac} = \frac{1}{2}[1 - erf(x_c)], \quad (10.29)$$

$$x_c = \frac{\ln(0.0145S_{max}^{-2/3}/r_g)}{\sqrt{2} \ln \sigma_g}, \quad (10.30)$$

$$\Delta N_a = \frac{9QYL}{4H\pi\rho \int r^3 n(r) dr}, \quad (10.31)$$

$$\tau_c(z) = \begin{cases} 0 & z > z_{top} \\ \frac{z_{bot} + \Delta z - z}{\Delta z} \tau_{c0} & z_{bot} \leq z \leq z_{top}, \\ 0 & z < z_{bot} \end{cases} \quad (10.32)$$

where τ_c is the cloud optical depth, and z_{bot} , z_{top} and Δz the cloud base, cloud top and cloud thickness respectively. The cloud optical depth is assumed to be linear with respect to height.

The last model (I5) is similar to the approach used in Jones et al. [70]. It uses the radiation scheme of Fu and Liou [51] to compute the radiative transfer in the cloud and is based on the cloud liquid water content. The model is:

$$r_e(z) = \left(\frac{3W(z)}{4\pi\rho\kappa N_{d0}} \right)^{1/3}, \quad (10.33)$$

$$\Delta N_d = 375(1 - \exp[-2.5 \times 10^{-3} \Delta N_a]), \quad (10.34)$$

$$\Delta N_a = \frac{9QYL}{4H\pi\rho \int r^3 n(r) dr}, \quad (10.35)$$

$$W(z) = \begin{cases} 0 & z > z_{top} \\ \frac{z - z_{bot}}{\Delta z} W_0 & z_{bot} \leq z \leq z_{top}, \\ 0 & z < z_{bot} \end{cases} \quad (10.36)$$

where L_0 is the liquid water content at cloud top and κ is a constant depending whether the cloud is maritime or continental. The cloud droplet effective radius (r_e) is parameterized using liquid water content and total droplet number density [90].

10.3 Uncertainty Analysis

Table 10.1 lists all the uncertain parameters used in the estimate of indirect radiative forcing by anthropogenic sulfate aerosols. All the parameters are assumed log-normal except κ , which is assumed to have uniform probability density between 0.67 and 0.80.

Figures 10-2 to 10-6 show the resulting PDFs, means, and standard deviations of the IRF using a third-order DEMM for the five model structures considered here. The mean for the first model has the largest mean, standard deviation, and 95% confidence range. The use of more rigorous radiative transfer models in I4 and I5 decreases the mean, standard deviation, and 95% confidence by more than 30%. Introducing more rigorous nucleation parameterization as in I3 results in a mean of 1.51 W/m² with standard deviation of 1.04 W/m² and 95% confidence range between 0.20 to 4.09 W/m². The use of the empirical relation ΔN_d and ΔN_a results in a mean of 1.18 W/m² with standard deviation of 0.84 W/m² and 95% confidence range between 0.12 to 3.23 W/m².

The comparison of the PDFs from the five models is shown in Figure 10-7. The comparison of the corresponding mean and 95% confidence ranges are shown in Figure 10-8. The mean values vary from 1.2 to 1.7 W/m² and the 95% confidence range is 0.1 to 5.2 W/m². Therefore the structural uncertainty is 0.5 W/m² and the parametric uncertainty is 5.1 W/m². It appears that the the parametric uncertainty is about a factor of 10 larger than the structural uncertainty.

Results from the variance analysis are shown in Figure 10-9. The parameters which contribute most to the model variance are the size parameters of the aerosol distribution and atmospheric transmittance, followed by the sulfate yield and lifetime. This variance spectrum with respect to parameters shows little variation among different models. To understand the higher contribution from the aerosol size distribution, Figure 10-10 illustrates the response surface of indirect radiative to r_g and σ_g and clearly shows the steep response surface around the mean value of r_g and σ_g , compared to the flat surface in Figure 9-10.

10.4 Conclusions

In this chapter, the IRF by anthropogenic sulfate aerosols has been evaluated using the uncertainty analysis technique discussed in Chapter 8.

Table 10.1: Uncertain parameters used in the estimate of indirect radiative forcing by anthropogenic sulfate aerosols.

Quantity	Models	Central value	Uncertainty factor	Reference
$Q(10^{12}g/yr)$	I1,I2,I3,I4,I5	71	1.15	Penner et al. [107]
Y	„	0.5	1.5	„
$L(days)$	„	5.5	1.5	„
$r_g(\mu m)$	„	0.0488	1.26	Whitby [163]
σ_g	„	2.0	1.16	Whitby & Sverdrup [164]
$H(km)$	„	1.0	1.4	Kaufman & Chou [75]
A_{mst}	„	0.25	1.1	„
R_{ct}	I1,I2,I3,I4	0.5	1.2	Charlson et al. [24]
T	I1,I2,I3	0.76	1.2	Penner et al. [107]
$c(/cm^3)$	I1,I3,I4	350	1.5	Twomey [151]
k	I1,I3,I4	0.50	1.3	„
$S_{max}(\%)$	I1,I3	0.35	1.3	Martin & Johnson [90]
N_{d0}	I2,I5	300	1.1	„
$z_{bot}(m)$	I4,I5	400	1.1	Nicholls [103]
$\Delta z(m)$	I4,I5	500	1.05	„
R_s	I4,I5	0.15	1.1	Robock [122]
d_0	I3	0.005	1.15	Ghan et al. [55]
τ_{c0}	I4	12	1.1	Peng et al. [106]
$W_0(g/m^3)$	I5	0.5	1.1	„
κ	I5	0.67-0.80	uniform	Jones et al. [70]

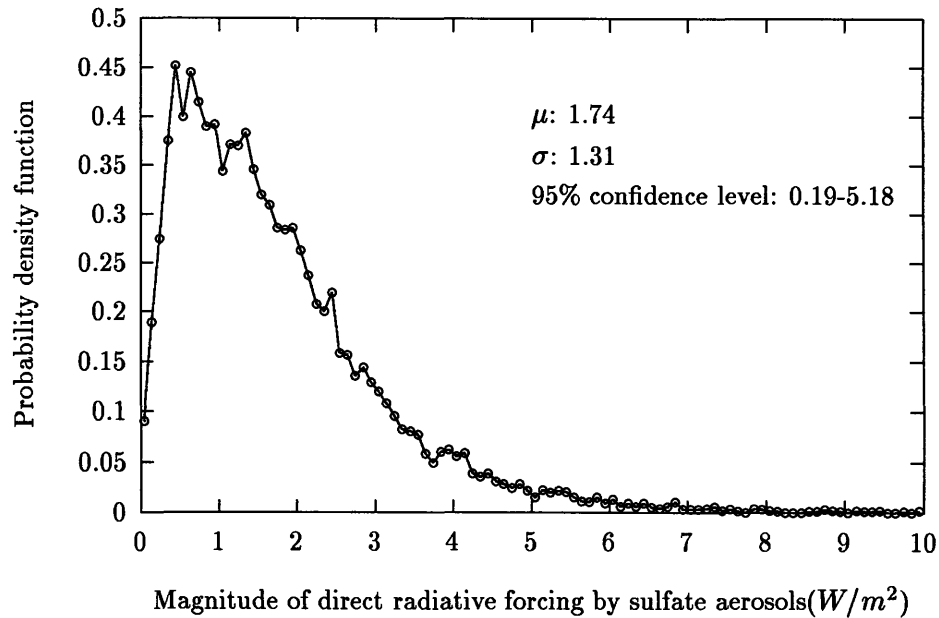


Figure 10-2: Probability density function of the indirect radiative forcing by anthropogenic sulfate aerosols: I1.

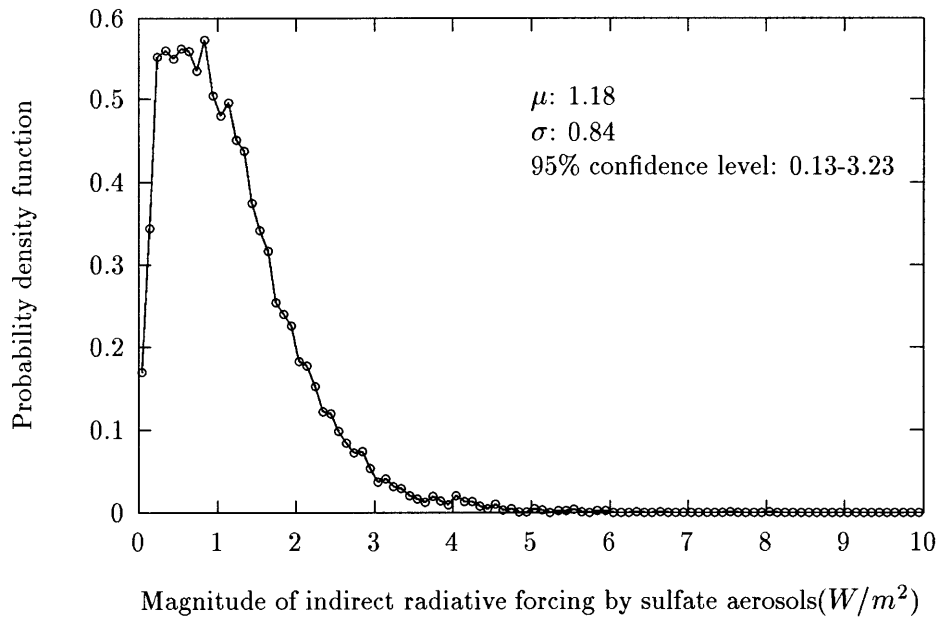


Figure 10-3: Probability density function of the indirect radiative forcing by anthropogenic sulfate aerosols: I2.

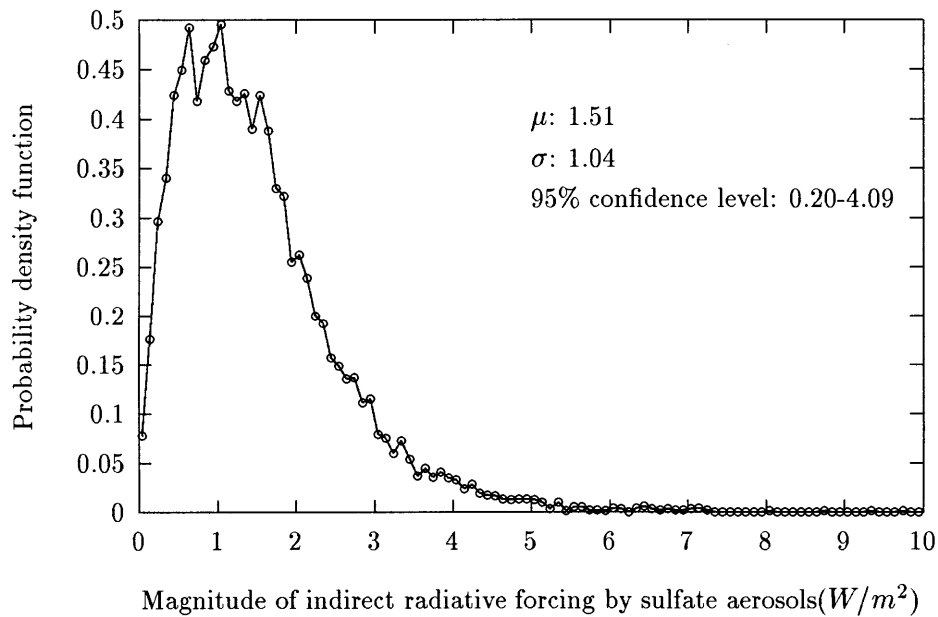


Figure 10-4: Probability density function of the indirect radiative forcing by anthropogenic sulfate aerosols: I3.

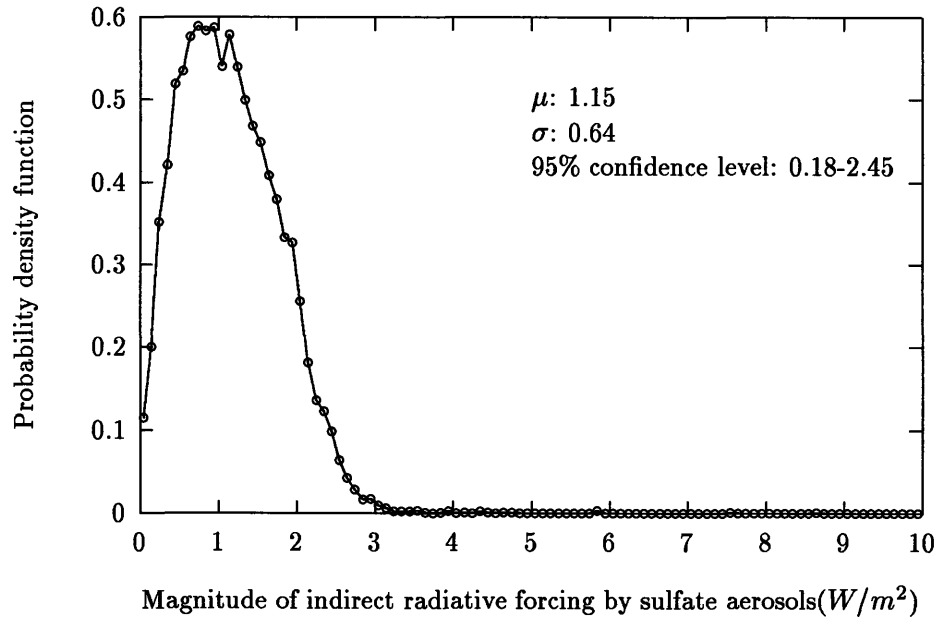


Figure 10-5: Probability density function of the indirect radiative forcing by anthropogenic sulfate aerosols: I4.

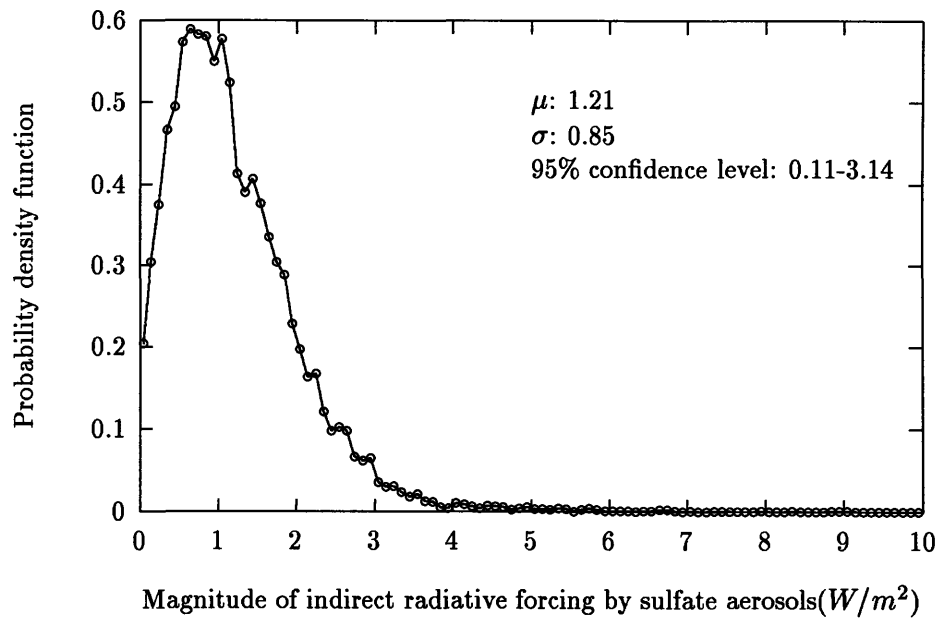


Figure 10-6: Probability density function of the indirect radiative forcing by anthropogenic sulfate aerosols: I5.

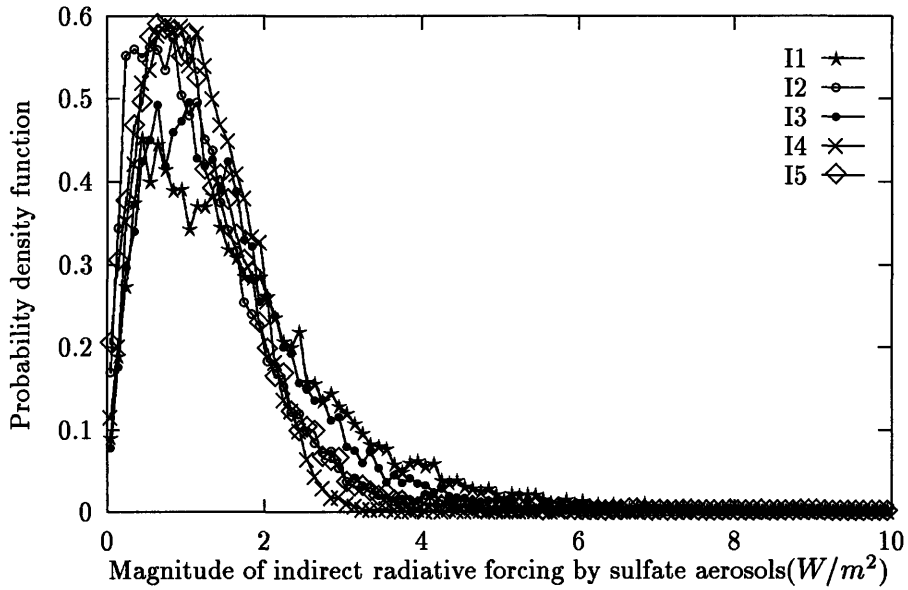


Figure 10-7: Probability density functions of the indirect radiative forcing by anthropogenic sulfate aerosols for five model structures.

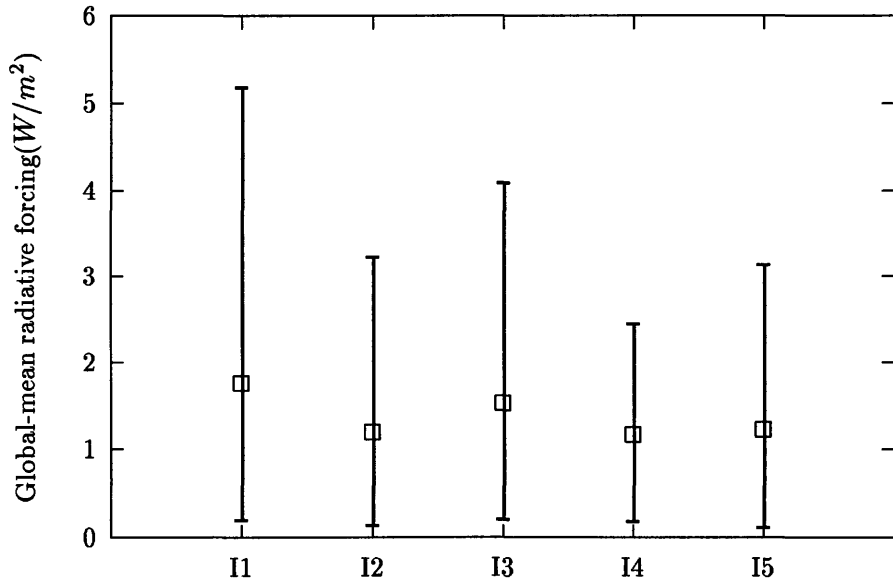


Figure 10-8: Mean and 95% confidence range of the indirect radiative forcing by anthropogenic sulfate aerosols for five model structures.

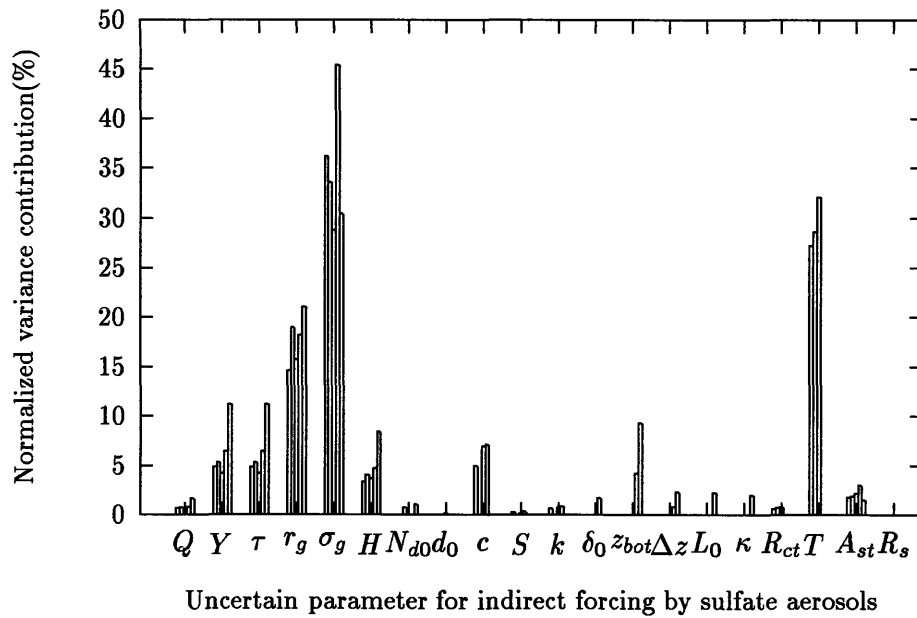


Figure 10-9: Normalized variance contribution to the indirect radiative forcing by uncertain parameters.

For the indirect radiative forcing by anthropogenic sulfate aerosols, five different models have been selected to evaluate the probability density function with 20 uncertain parameters. The mean values vary from 1.2 to 1.7 W/m^2 and the 95% confidence range is 0.1 to 5.2 W/m^2 (Figure 10-8). The structural uncertainty of 0.5 W/m^2 is also much smaller than the parametric uncertainty of 5.1 W/m^2 . Variance analysis ranks the size parameters as the leading contributor to the total model uncertainty, suggesting that aerosol size distributions should be the main focus for improvement.

As in the previous chapter, the conclusions reached here are subject to the choice of both model structures and parameter distributions. Although the results obtained so far are quite preliminary, the underlined approach can be readily extended to more comprehensive studies.

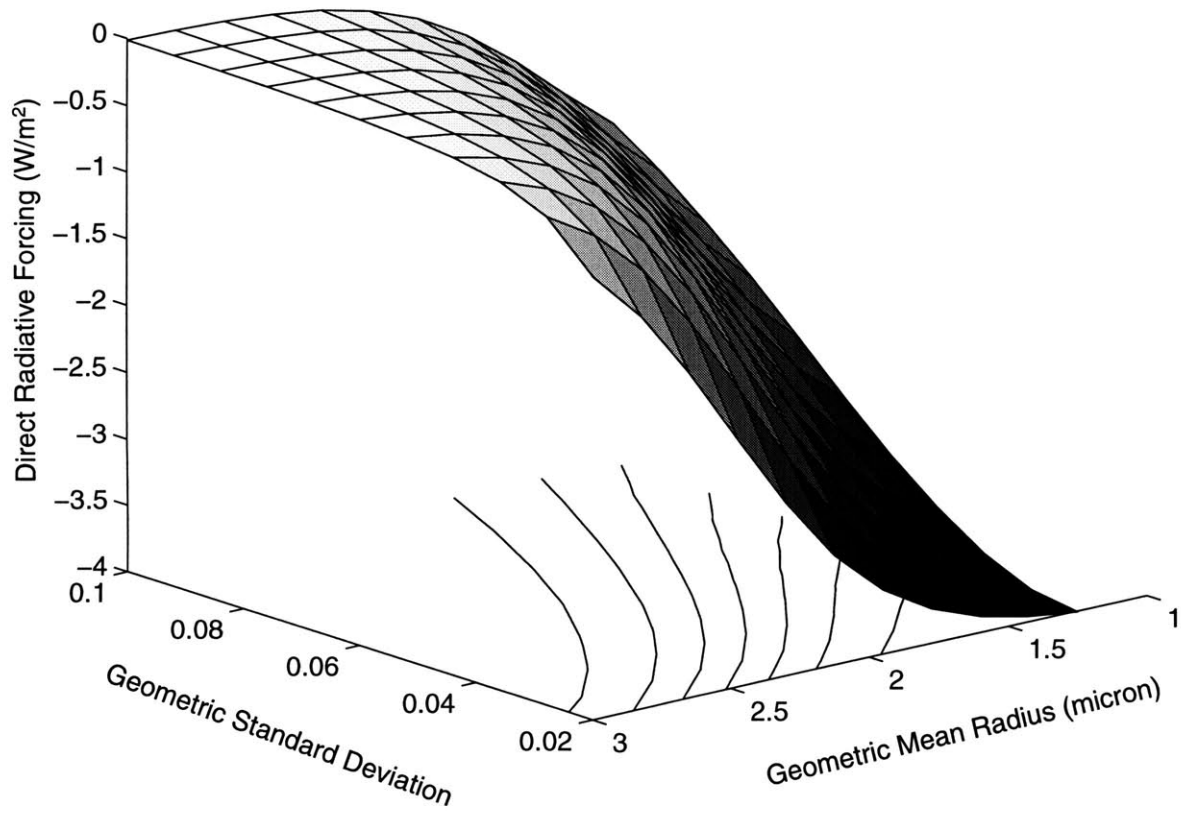


Figure 10-10: Indirect radiative forcing as function of geometric mean and standard deviation of size distribution for I1.

Chapter 11

Conclusions

11.1 Summary

The objective of this thesis is to improve our understanding of aerosol effects in the troposphere. Three specific topics have been selected: (1) the radiative forcing by aerosols; (2) responses of meteorological and chemical fields to the aerosol radiative forcing; (3) uncertainty analysis of the radiative forcing by anthropogenic sulfate aerosols.

In Chapter 4, the radiative forcing by both anthropogenic sulfate aerosols and climatological aerosols has been evaluated with appropriate radiative transfer schemes and available aerosol data.

The sensitivity of the direct radiative forcing by anthropogenic sulfate aerosols to their optical properties, concentrations, and the ambient humidity indicate that that aerosol concentrations and optical properties contribute about equally to the factor-of-three difference in the current estimates of this forcing. The spectral dependence of aerosol optical properties on ambient humidity can be approximated by observed scaling factors in the visible wavelength. The humidity effect on aerosol single-scattering albedo and asymmetry factor accounts for only 10% of the difference.

The global distribution of radiative flux changes at the top of the atmosphere and the surface due to total aerosols, including natural and anthropogenic aerosols, is calculated based on the climatological aerosol data set by d'Almeida et al. [36] and the radiative transfer scheme by Fu and Liou [51]. At the top of the atmosphere aerosols decrease the net downward short-wave radiation except in the Saharian desert region, its downwind equatorial east Atlantic, and part of the Australia, where high absorptive mineral aerosols occur. The decrease of the net downward short-wave radiation at the surface more than doubles that at the top of the atmosphere. Decreases in the net outgoing long-wave radiation are about an order of magnitude smaller than that in the short-wave radiation. Changes in both the short- and long-wave radiation show large spatial variations and gradients, indicating inhomogeneous sources and short lifetime of aerosols. The annual global mean radiative forcing increases by about a factor of 2 when the humidity effect on aerosol optical properties is included. Replacing the boundary layer heights as prescribed in the aerosol data set by the actual values decreases the result by a similar factor.

In Chapters 5 to 7, the mechanism and magnitude of meteorological and chemical responses to aerosol radiative forcing are studied in three different models: a one-dimensional radiative-convective equilibrium model, a mesoscale model, and a photochemical air quality model. The simulations in the one-dimensional radiative-convective model show that

introducing aerosols in the lower troposphere causes a decrease of the convective heating throughout the troposphere and an increase in the long-wave heating in the upper troposphere, resulting in a cooler and drier atmosphere at the new equilibrium. Analysis of the surface energy balance shows that for a given external radiative forcing the equilibrium temperature change is controlled by two internal feedbacks: a negative feedback between the surface temperature and the sensible and latent heat fluxes and a positive feedback between the surface temperature and the water vapor content in the atmosphere. The negative feedback coefficient increases by a factor of 4 to 5 when the equilibrium is reached. In the meantime, the positive feedback coefficient also increases to its equilibrium value, which is comparable to the magnitude of the negative feedback. As a result, the initial sensitivity of surface temperature change to aerosol radiative forcing is about a factor of 4 to 5 smaller than the equilibrium sensitivity. The transient surface temperature change approaches the equilibrium one with a characteristic time scale, which depends on both feedback factors and surface properties. For an equal magnitude forcing at the tropopause, aerosols with higher absorption lead to smaller surface temperature changes. Results also indicate that the surface temperature change is greater for sulfate aerosols than for carbon dioxide.

The mesoscale model is set up in the SCAQS region. The model sensitivity to surface parameters and initial conditions is carried out. The model prediction without aerosols is validated against the SCAQS observations. Four aerosol types with low- and high-level concentrations from the climatological aerosol data set in d'Almeida et al. [36] are then introduced into the mesoscale model. The sensitivity of the surface temperature change to prescribed aerosol radiative forcing in the 1-D mesoscale model is much smaller than that in the 1-D RCM. This attributes to the difference between initial and equilibrium sensitivity of surface temperature change to aerosol radiative forcing. Results also indicate that the surface temperature response is greater/smaller for sulfate than for carbon dioxide radiative forcing at the tropopause/surface. The three-dimensional mesoscale simulations indicate that the domain averaged relative changes are -30 to 10% for boundary layer height, -30 to 40% from wind speed, and -20 to 0% for net downward SW radiation. Temperature changes vary from -1.5 to 0.5°C, and wind direction changes vary within 50 degrees.

The simulations with either uniformly perturbed or aerosol-induced meteorological fields in the photochemical air quality model show the chemical fields are more sensitive to changes in temperature, wind, and boundary layer height. The domain-averaged relative changes of ground level concentrations of chemical species range up to 10% due to the prescribed low-level aerosol loading. Shifting aerosol loading from the low-level to high-level appears to almost double the concentration response of species during the day. Changes at specific sites can be much larger than the domain-averaged changes. Since the responses of chemical fields to different meteorological fields are quite different, the spatial pattern in the response of chemical fields bears little or no resemblance to that in any single meteorological perturbation.

In Chapters 8 to 10, the uncertainty of the direct and indirect radiative forcing by anthropogenic sulfate aerosols has been addressed with a new uncertainty analysis technique. The probability density function of the direct radiative forcing under the influence of 9 uncertain parameters is calculated for 4 different models. The mean value of the direct forcing varies from 0.3 to 1.3 W/m² with a 95% confidence range of 0.1 to 4.2 W/m². Variance analysis identifies the sulfate yield and lifetime as the two primary uncertain parameters. The probability density function of the indirect radiative forcing has been evaluated in 5 different models with respect to 20 uncertain parameters. The mean value of the indirect forcing varies from 1.2 to 1.7 W/m² with a 95% confidence range of 0.1 to 5.2 W/m². Vari-

ance analysis ranks aerosol size distribution as the leading contributor to the total model uncertainty.

11.2 Implications and Future Work

Based on the results from this work, I will outline several implications and related future work as follows:

- Aerosol processes cannot be decoupled from mesoscale meteorology in air pollution modeling. An aerosol model can be incorporated into a mesoscale model so that the temporal and spatial distribution of aerosols can be used for the radiative calculations. Initial efforts should be focused on modeling bulk aerosol properties such as concentration. However, aerosol size distributions need to be modeled to understand the interaction between aerosol and cloud processes.
- Aerosol radiative forcing needs to be incorporated into global circulation models (GCMs) for climate studies. One straightforward future task is to incorporate the aerosol-induced radiative forcing calculated in Chapters 4 into a global climate model and thus to evaluate the global climate impact of aerosols. Special attention should be placed on the humidity effect on aerosol optical properties and boundary layer variation. Results with these static aerosol models will serve as a guide for further studies with dynamical aerosol models. Aerosol models and data need to be size-resolved to understand the indirect effect.
- There is a critical need to quantify structural and parametric uncertainty in atmospheric modeling. Efficient tools such as DEMM can be used together with Karhunen-Loève expansion and cascading schemes in large and complex models.

Appendix A

Subroutine for Calculating Aerosol Optical Properties

This routine computes the aerosol optical properties of attenuation coefficients, single-scattering albedo, and asymmetry factor at a given wavelength for aerosols with a lognormal distribution. The required input variables include the geometric mean and standard deviation of the distribution, wavelength, and refractive index.

It uses subroutine LSODE, an ODE solver developed at LLNL, to compute the integrals in Equations 3.4, 3.5, and 3.7, with attenuation efficiencies and Mie intensity parameter calculated from subroutine BHMIE, which was modified from the original code by Bohren and Huffman [14].

```
CLL Routine: aerlopt.f-----
CLL Purpose: Computes the aerosol optical properties of
CLL           attenuation coefficients, single-scattering albedo, and
CLL           asymmetry factor at a given wavelength given the size
CLL           parameters of lognormal distribution and refractive index.
CLL
CLL Author: Wenwei Pan
CLL           Department of Earth, Atmospheric and Planetary Sciences
CLL           Massachusetts Institute of Technology
CLL
CLL Version: 1.0
CLL Date: March 5, 1995
CLL
CLL Tested under
CLL machines:
CLL   DEC 3000 AXP/SGI Indigo2
CLL operating systems:
CLL   OSF1 V2.0/IRIX 5.2
CLL
CLL Code modification history:
CLL Version Date
CLL 1.1   03/06/95 Scattering angle range of 0-Pi is nonlinearly
CLL           divided into 180 intervals to account the
CLL           strong forward peak of Mie scattering.
CLL           Set mf to 23 to reflect the stiffness of
CLL           the coupling integrations.
CLL           To make use of relative tolerance, set atol,
CLL           absolute tolerance, as small as possible,
CLL           e.g., 10**(-50), to avoid the case when the
CLL           result itself is too small.
```

CLL 1.2 03/10/95 The calculation of three integrals are
 CLL separated to make the code more robust.
 CLL 1.3 03/10/95 To make the code more robust, r1 and r2 should be
 CLL dependent on rg and sg. We set r1=rg/sg**3 and
 CLL r2=rg*sg**3 so that 99.7% of all particles lie
 CLL in the range of [r1,r2].
 CLL 1.4 03/13/95 To reduce the error, r1/r2 reset to
 CLL rg/sg**5 and rg*sg**5.
 CLL 1.4 05/07/95 Backscattered fraction is added using
 CLL Equation (15b) of Wiscombe and Grams
 CLL (1976, JAS, Vol.33, 2440-2451).
 CLL-----

```

      subroutine aerlopt(rg,sg,wavl,refre,refim,error,
&      ext,sca,omg,asy,bac)

```

C Input variables.

```

      real
&      rg,sg,          !geometric mean(micron) and standard deviation
&      wavl,          !wavelength(micron)
&      refre,refim,  !real and imaginary part of refractive index
&      error          !relative error for ODE solver

```

C Output variables.

```

      real
&      ext,          !extinction coefficient(1/km)
&      sca,          !scattering coefficient(1/km)
&      omg,          !single-scattering albedo
&      asy,          !asymmetry factor
&      bac           !backscattered fraction

```

C Constants.

```

      integer neq,lrw,liw
      real pi
      parameter (
&      neq=1,
&      lrw=20+16*neq,
&      liw=20,
&      pi=3.141592654)

```

C Local variables.

```

      integer itol,itask,iopt,istate,mf,iwork(liw)
      real
&      r1,r2,
&      y(neq),
&      atol,rtol,rwork(lrw),
&      wavnum

```

C Common blocks.

```

      common //wavl1,rg1,sg1,refre1,refim1

```

C Externals.

```

      external
&      lsode,        !ODE solver
&      jac,          !subroutine for Jacobian matrix
&      fext,         !subroutine for extinction coeff.
&      fsca,         !subroutine for scattering coeff.
&      fasy,         !subroutine for asymmetry factor
&      fbac          !subroutine for backscattered fraction

```

C*-----

C Assign values to common block variables

```
wavl1=wavl
rg1=rg
sg1=sg
refre1=refre
refim1=refim
wavnum=2*pi/wavl
```

CL-----

CL 1.0 Compute extinction coefficient.

CL

```
r1=rg/(sg*sg*sg*sg*sg)
r2=rg*(sg*sg*sg*sg*sg)
itol=1
rtol=error
atol=1.d-50
itask=1
istate=1
iopt=0
mf=10

do i=1,neq
  y(i)=0.0
enddo

call lsode(fext,neq,y,r1,r2,itol,rtol,atol,itask,
&         istate,iopt,rwork,lrw,iwork,liw,jac,mf)

if(istate.lt.0)then
  write(9999,'(a)')'Error in aerlopt() Step 1'
  write(9999,'(a,i5)')'istate=',istate
  write(9999,'(a,i5)')'no. steps = ',iwork(11)
  stop
endif
ext=y(neq)
```

CL-----

CL 2.0 Compute scattering coefficient.

CL

```
r1=rg/(sg*sg*sg*sg*sg)
r2=rg*(sg*sg*sg*sg*sg)
itol=1
rtol=error
atol=1.d-50
itask=1
istate=1
iopt=0
mf=10

do i=1,neq
  y(i)=0.0
enddo

call lsode(fsca,neq,y,r1,r2,itol,rtol,atol,itask,
&         istate,iopt,rwork,lrw,iwork,liw,jac,mf)

if(istate.lt.0)then
```

```

        write(9999,'(a)')'Error in aerlopt() Step 2'
        write(9999,'(a,i5)')'istate=',istate
        write(9999,'(a,i5)')'no. steps = ',iwork(11)
        stop
    endif
    sca=y(neq)

```

CL-----

CL 3.0 Compute asymmetry factor.

CL

```

    r1=rg/(sg*sg*sg*sg*sg)
    r2=rg*(sg*sg*sg*sg*sg)
    itol=1
    rtol=error
    atol=1.d-50
    itask=1
    istate=1
    iopt=0
    mf=10

    do i=1,neq
        y(i)=0.0
    enddo

    call lsode(fasy,neq,y,r1,r2,itol,rtol,atol,itask,
&         istate,iopt,rwork,lrw,iwork,liw,jac,mf)

    if(istate.lt.0)then
        write(9999,'(a)')'Error in aerlopt() Step 1'
        write(9999,'(a,i5)')'istate=',istate
        write(9999,'(a,i5)')'no. steps = ',iwork(11)
        stop
    endif
    asy=0.5*y(neq)*wavl*wavl/(pi*sca)

```

CL-----

CL 4.0 Compute backscattered fraction from isotropically incident radiation.

CL

```

    r1=rg/(sg*sg*sg*sg*sg)
    r2=rg*(sg*sg*sg*sg*sg)
    itol=1
    rtol=error
    atol=1.d-50
    itask=1
    istate=1
    iopt=0
    mf=10

    do i=1,neq
        y(i)=0.0
    enddo

    call lsode(fbac,neq,y,r1,r2,itol,rtol,atol,itask,
&         istate,iopt,rwork,lrw,iwork,liw,jac,mf)

    if(istate.lt.0)then
        write(9999,'(a)')'Error in aerlopt() Step 1'
        write(9999,'(a,i5)')'istate=',istate
        write(9999,'(a,i5)')'no. steps = ',iwork(11)
    endif

```



```

    stop
  endif
  bac=y(neq)*wavl*wavl/(2*pi*pi*sca)

```

```

CL-----
CL 5.0 Convert ext and sca to unit of 1/km; adjust single-scattering albedo;
CL   check if asymmetry factor is reasonable.

```

```

  ext=ext*1.e-3
  sca=sca*1.e-3
  if((sca/ext).gt.1.)then
    omg=1.
    sca=omg*ext
  else
    omg=sca/ext
  endif
  if(abs(asy).gt.1.)then
    write(9999,'(a)')
    & 'Abs(asymmetry factor) > 1 in aerlopt() Step 4'
    write(9999,'(a,e12.3)')'Asy=',asy
    stop
  endif

  return
end

```

```

CLL Routine: fext-----
CLL Purpose: Integrand for the extinction coefficient integral.
CLL-----

```

```

  subroutine fext(neq,r,y,ydot)

  integer neq
  real r,y(neq),ydot(neq)

  integer nang
  real pi
  parameter (nang=181,pi=3.141592654)
  real wavl,refre,refim,rg,sg,
&   theta(nang),x
  real qext,q sca
  complex refcp,s1(nang),s2(nang)
  common //wavl,rg,sg,refre,refim

  external bhmie,sized

```

```

C*-----

  x=2*pi*r/wavl
  refcp=cplx(refre,refim)
  call bhmie(x,refcp,nang,theta,s1,s2,qext,q sca)
  call sized(rg,sg,r,dnr)
  ydot(neq)=pi*r*r*qext*dnr

  return
end

```

```

CLL Routine: fsca-----
CLL Purpose: Integrand for the scattering coefficient integral.

```

CLL-----

```
subroutine fsca(neq,r,y,ydot)

integer neq
real r,y(neq),ydot(neq)

integer nang
real pi
parameter (nang=181,pi=3.141592654)
real wavl,refre,refim,rg,sg,
&   theta(nang),x
real qext,qzca
complex refcp,s1(nang),s2(nang)
common //wavl,rg,sg,refre,refim

external bhmie,sized
```

C*-----

```
x=2*pi*r/wavl
refcp=cplx(refre,refim)
call bhmie(x,refcp,nang,theta,s1,s2,qext,qzca)
call sized(rg,sg,r,dnr)
ydot(neq)=pi*r*r*qzca*dnr
return
end
```

CLL Routine: fasy-----

CLL Purpose: Integrand for the asymmetry factor integral.

CLL-----

```
subroutine fasy(neq,r,y,ydot)

integer neq
real r,y(neq),ydot(neq)

integer j,nang
real pi,theta0
parameter (nang=181,pi=3.141592654,theta0=1.e-9)
real wavl,refre,refim,rg,sg,
&   theta(nang),i(nang),si,x

real qext,qzca
complex refcp,s1(nang),s2(nang)
common //wavl,rg,sg,refre,refim

external bhmie,sized
```

C*-----

```
x=2*pi*r/wavl
refcp=cplx(refre,refim)
do j=1,nang
  theta(j)=exp(log(theta0)+
&   (log(pi)-log(theta0))*(j-1)/(nang-1))
enddo
call bhmie(x,refcp,nang,theta,s1,s2,qext,qzca)
call sized(rg,sg,r,dnr)
```

```

do j=1,nang
  i(j)=0.5*(cabs(s1(j))*cabs(s1(j))+
&      cabs(s2(j))*cabs(s2(j)))
  i(j)=cos(theta(j))*sin(theta(j))*i(j)
enddo
si=0.
do j=2,nang
  si=si+.5*(i(j)+i(j-1))*(theta(j)-theta(j-1))
enddo
ydot(neq)=si*dnr
return
end

```

CLL Routine: fbac-----
 CLL Purpose: Integrand for the backscattered fraction integral.
 CLL-----

```

subroutine fbac(neq,r,y,ydot)

integer neq
real r,y(neq),ydot(neq)

integer j,nang
parameter (nang=181)
real wavl,refre,refim,rg,sg,
&      theta(nang),i(nang),si,x

real qext,qscs
complex refcp,s1(nang),s2(nang)
common //wavl,rg,sg,refre,refim

external bhmie,sized

pi=3.141592654
C      theta0=0.
      theta0=1.e-9
      si=0.

x=2*pi*r/wavl
refcp=cplx(refre,refim)

C      print*, 'r=',r, 'x=',x
do j=1,nang
C      theta(j)=theta0+(pi-theta0)*(j-1)/(nang-1)
      theta(j)=exp(log(theta0)+
&      (log(pi)-log(theta0))*(j-1)/(nang-1))
enddo

call bhmie(x,refcp,nang,theta,s1,s2,qext,qscs)
call sized(rg,sg,r,dnr)
do j=1,nang
  i(j)=0.5*(cabs(s1(j))*cabs(s1(j))+
&      cabs(s2(j))*cabs(s2(j)))
  i(j)=theta(j)*sin(theta(j))*i(j)
enddo
do j=2,nang
  si=si+.5*(i(j)+i(j-1))*(theta(j)-theta(j-1))
enddo
ydot(neq)=si*dnr

```

```

return
end

CLL Routine: sized-----
CLL Purpose: Compute the number density at a given particle radius
CLL           for a lognormal distribution.
CLL-----

      subroutine sized(rg,sg,r,dnr)

      implicit none

C Global variables
      real rg,sg,r,dnr

C Local constants
      real pi
      parameter (pi=3.141592654)

C*-----

C log(x)----- natural logarithm of x
C dN/dr=dN/dlog10(r)/(rln10)
C
      dnr=exp(-(log10(r)-log10(rg))**2/(2*log10(sg)*log10(sg)))/
&   (sqrt(2*pi)*log10(sg)*r*log(10.))

      return
      end

CLL ROUTINE: BHMIE-----
CLL PURPOSE: CALCULATES AMPLITUDE SCATTERING MATRIX ELEMENTS AND
CLL           EFFICIENCIES FOR EXTINCTION, TOTAL SCATTERING AND
CLL           BACKSCATTERING FOR A GIVEN SIZE PARAMETER AND RELATIVE
CLL           REFRACTIVE INDEX.
CLL SOURCE: MODIFIED FROM THE ORIGINAL CODE IN ‘‘ ABSORPTION AND
CLL           SCATTERING OF LIGHT BY SMALL PARTICLES’’ BY C.F. BOHREN
CLL           AND D.R. HUFFMAN(JOHN WILLEY & SONS, INC., 1983).
CLL-----

      SUBROUTINE BHMIE(X,REFREL,NANG,THETA,S1,S2,QEXT,QSCA)

      PARAMETER (NL=2000,ML=20000)
      DIMENSION AMU(NL),THETA(NANG),PI(NL),TAU(NL),PIO(NL),PI1(NL)
      COMPLEX D(ML),Y,REFREL,XI,XIO,XI1,AN,BN,S1(NANG),S2(NANG)
      DOUBLE PRECISION PSIO,PSI1,PSI,DN,DX

      DX=X
      Y=X*REFREL

C SERIES TERMINATED AFTER NSTOP TERMS
      XSTOP=X+4.*X**.3333+2.
      NSTOP=XSTOP
      YMOD=CABS(Y)
      NMX=AMAX1(XSTOP,YMOD)+15
      IF((NMX-1).GT.ML.OR.NANG.GT.NL)THEN
        PRINT*,'(NMX-1)=',NMX-1

```

```

        PRINT*, 'NANG=', NANG
        PAUSE 'INCREASE ML OR NL IN BHMIE !'
    ENDIF
    DO 555 J=1, NANG
        AMU(J)=COS(THETA(J))
555  CONTINUE

C LOGARITHMIC DERIVATIVE D(J) CALCULATED BY DOWNWARD RECURRENCE
C BEGINNING WITH INITIAL VALUE 0.0+I*0.0 AT J=NMX
    D(NMX)=CMPLX(0.0,0.0)
    NN=NMX-1
    DO 120 N=1, NN
        RN=NMX-N+1
        D(NMX-N)=(RN/Y)-(1./(D(NMX-N+1)+RN/Y))
120  CONTINUE

    DO 666 J=1, NANG
        PIO(J)=0.0
        PI1(J)=1.0
666  CONTINUE

    DO 777 J=1, NANG
        S1(J)=CMPLX(0.0,0.0)
        S2(J)=CMPLX(0.0,0.0)
777  CONTINUE

C RECCATI-BESSEL FUNCTIONS WITH REAL ARGUMENT X CALCULATED BY UPWARD
C RECURRENCE.
    PSIO=DCOS(DX)
    PSI1=DSIN(DX)
    CHIO=-SIN(X)
    CHI1=COS(X)
    APSIO=PSIO
    APSI1=PSI1
    XI0=CMPLX(APSIO, -CHIO)
    XI1=CMPLX(APSI1, -CHI1)
    QSCA=0.0
    QEXT=0.0
    N=1
200  DN=N
    RN=N
    FN=(2.*RN+1.)/(RN*(RN+1.))
    PSI=(2.*DN-1.)*PSI1/DX-PSIO
    APSI=PSI
    CHI=(2.*RN-1.)*CHI1/X-CHIO
    XI=CMPLX(APSI, -CHI)
    AN=(D(N)/REFREL+RN/X)*APSI-APSI1
    AN=AN/((D(N)/REFREL+RN/X)*XI-XI1)
    BN=(REFREL*D(N)+RN/X)*APSI-APSI1
    BN=BN/((REFREL*D(N)+RN/X)*XI-XI1)
    QSCA=QSCA+(2.*RN+1.)*(CABS(AN)*CABS(AN)+CABS(BN)*CABS(BN))
    QEXT=QEXT+(2.*RN+1.)*REAL(AN+BN)

    DO 789 J=1, NANG
        PI(J)=PI1(J)
        TAU(J)=RN*AMU(J)*PI(J)-(RN+1.)*PIO(J)
        P=(-1.)**(N-1)
        S1(J)=S1(J)+FN*(AN*PI(J)+BN*TAU(J))
        T=(-1.)**N

```

```

      S2(J)=S2(J)+FN*(AN*TAU(J)+BN*PI(J))
789  CONTINUE

      PSIO=PSI1
      PSI1=PSI
      APSI1=PSI1
      CHIO=CHI1
      CHI1=CHI
      XI1=CMPLX(APSI1,-CHI1)
      N=N+1
      RN=N
      DO 999 J=1,NANG
        PI1(J)=((2.*RN-1.)/(RN-1.))*AMU(J)*PI(J)
        PI1(J)=PI1(J)-RN*PIO(J)/(RN-1.)
        PIO(J)=PI(J)
999  CONTINUE
      IF(N-1-NSTOP)200,300,300
300  QSCA=(2./(X*X))*QSCA
      QEXT=(2./(X*X))*QEXT
      RETURN
      END

```

Appendix B

A Climatological Aerosol Data Set

The climatological aerosol data set used here is from d’Almeida et al. [36]. It consists of 11 aerosol types with a spatial resolution of 5° latitude by 5° longitude on the globe and 3 or 4 layers in the vertical and a temporal resolution of one month. These aerosol types are constructed from 20 aerosol components, weighted by their number density fractions. Each component is characterized by a specific log-normal size distribution and a wavelength-dependent refractive index ranging from $0.3 \mu m$ to $40 \mu m$.

Table B.1 lists the geometric mean radius and standard deviation for the size distributions of aerosol components. The corresponding size distributions are shown in Figure B-1. The distributions have been normalized to a number density of 1 cm^{-3} to facilitate the comparison between different size distributions. The wavelength-dependent refractive index of some of these components are shown in Figure B-2.

Table B.2 summarizes the formation and geographical location and time for each aerosol type. The variation of some aerosol types in space and time follows the seasonal migration of the meteorological regimes (e.g., polar fronts and inter-tropical convergence zone), which dynamically control the meridional mixing and determine the trajectories of different air masses. The size distributions of 10 aerosol types are shown in Figure B-3. Since the maritime mineral aerosol is the same as the clean maritime aerosol in the first layer its size distribution is not shown.

Based on Equations 3.4 to 3.7, optical properties of aerosol components are obtained at 40 wavelengths. The results are shown in Figures B-4. The dust-like, mineral, and sea-salt components have smaller variations of attenuation coefficients in the visible range than other components due to their larger particle size. Large spectral variations of single-scattering albedo are clear especially in the infrared range. Weaker absorption is observed in water-soluble, sea-salt, and sulfate components, which have relatively higher water contents than other components. Soot has the strongest absorption due to its high content of elemental carbon. Asymmetry factors of components with fine particle size, including sulfate, soot, and water-soluble, decay with increasing wavelength much faster than those of other components.

The spectral variations of optical properties of aerosol types are shown in Figure B-5. At a given wavelength, attenuation coefficients differ by two orders of magnitude on a unit number density basis, indicating the high variability of aerosol optical properties in the atmosphere. Small variations of attenuation coefficient are observed in aerosol types consisting of large size particles. The single-scattering albedo and asymmetry factor of aerosol types depend not only on their components but also the attenuation coefficients of

Table B.1: Parameters characterizing the size distributions for different aerosol components for an assumed relative humidity of 0%.

Aerosol component	$r_{g_i}(\mu m)$	σ_{g_i}	Reference
dust-like	0.471	2.512	[131]
water-soluble	0.0285	2.239	„
soot	0.0118	2.00	[167]
sea-salt			
SRA-oceanic	0.30	2.51	[131]
nucleation mode	0.05	2.03	[39]
accumulation mode	0.40	2.03	„
coarse mode	3.3	2.03	„
background mineral			
nucleation mode	0.07	1.95	[35]
accumulation mode	0.39	2.00	„
coarse mode	1.90	2.15	„
wind-carry. dust			
nucleation mode	0.05	1.65	„
accumulation mode	0.27	2.67	„
coarse mode	4.00	2.40	„
mineral(transport.to mar.env.)	0.5	2.2	[127]
mineral(poleward)	0.4	1.6	[130]
H ₂ SO ₄ droplets	0.0695	1.86	[39]
non-sea-salt sulfate	0.0695	2.03	[130]
biogenic			
nucleation mode	0.04	2.03	[96]
coarse mode	2.50	2.03	[10, 41, 42, 110]
volcanic	0.217	1.77	[39, 65]

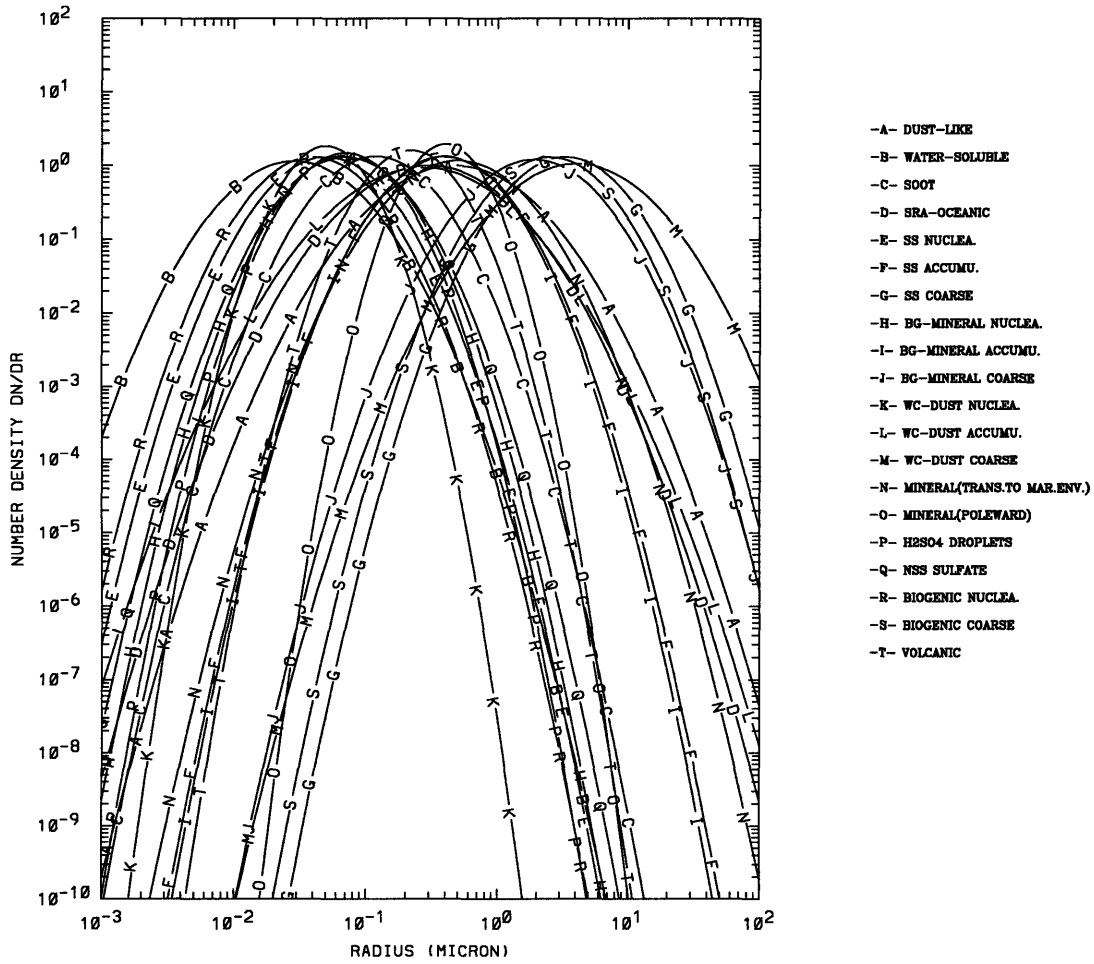


Figure B-1: Size distributions of the components and of the modes of the multimodal components normalized to number density of 1 cm^{-3} .

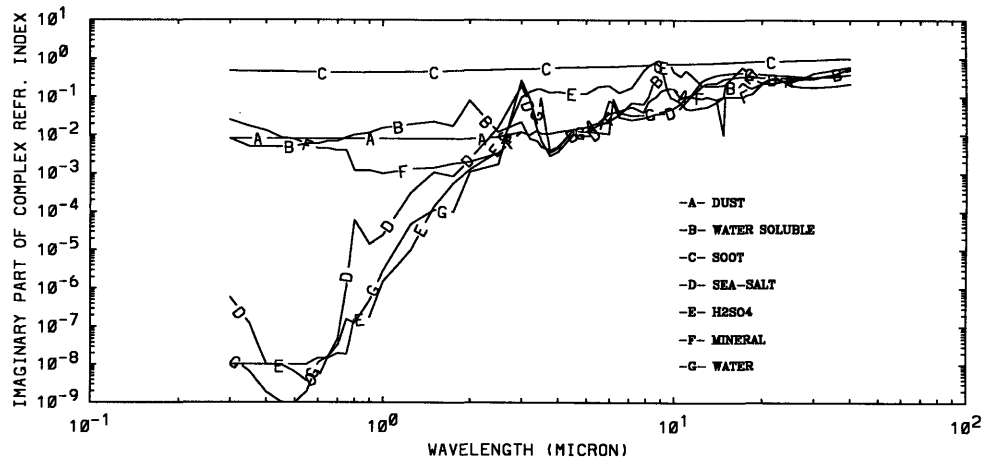
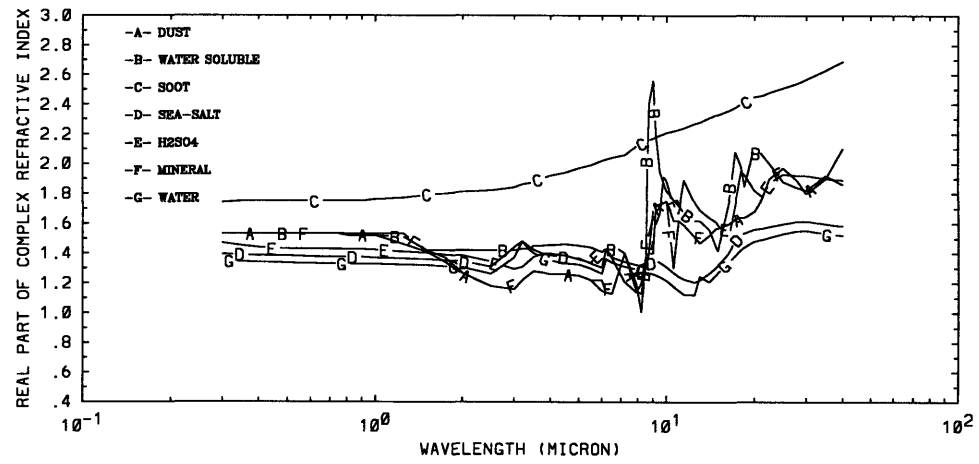


Figure B-2: Real and imaginary parts of the wavelength-dependent refractive index of several aerosol components.

Table B.2: Aerosol components, their number density fraction, and geographical locations for different aerosol types. “Bg.” and “wc.” stand for background and wind-carrying respectively.

Aerosol type	Aerosol component(<i>i</i>)	Number density fraction(N_i/N)	Location and time
Clean continental	dust-like	0.0001	rural environment
	water-soluble	0.9999	
Average continental	dust-like	2.27×10^{-6}	continental environ. slightly influenced by pollution
	water-soluble	0.93877	
	soot	0.06123	
Urban/Industrial	dust-like	1.67×10^{-7}	highly polluted continental environ.
	water-soluble	0.5945	
	soot	0.4055	
Desert(wintertime)	bg. mineral(nuclea.)	0.9274	arid/semi-arid regions in winter
	bg. mineral(accum.)	0.07246	
	bg. mineral(coarse)	9.661×10^{-5}	
Desert(summertime)	wc. mineral(nuclea.)	0.8542	arid/semi-arid regions in summer
	wc. mineral(accum.)	0.14568	
	wc. mineral(coarse)	7.2842×10^{-5}	
Clean maritime	sea-salt(nuclea.)	0.512	undisturbed maritime environ.: southeast Pacific, s. equatorial Atlantic, Indian Ocean
	sea-salt(accum.)	0.030	
	sea-salt(coarse)	0.001	
	NSS-sulfate	0.457	
Maritime mineral	sea-salt(nuclea.)	0.512	maritime environ. influenced by desert airmasses
	sea-salt(accum.)	0.030	
	sea-salt(coarse)	0.001	
	sulfate	0.457	
	mineral in maritime	1.000	
Maritime polluted	water-soluble	0.5939	polluted maritime environ: North Atlantic,Mediterran.
	soot	0.4051	
	sea-salt(SRA-oceanic)	9.6×10^{-4}	
Arctic(wintertime)	soot	.3274	Arctic in wintertime
	sea-salt(accum.)	.1100	
	mineral(poleward)	.0003	
	NSS-sulfate	.5624	
Arctic(summertime)	sea-salt(accum.)	.7361	Arctic in summertime
	mineral(poleward)	.0749	
	H_2SO_4 droplets	.1890	
Antarctic	sea-salt(accum.)	5.0×10^{-3}	Antarctic
	mineral(poleward)	5.0×10^{-3}	
	H_2SO_4 droplets	0.9900	

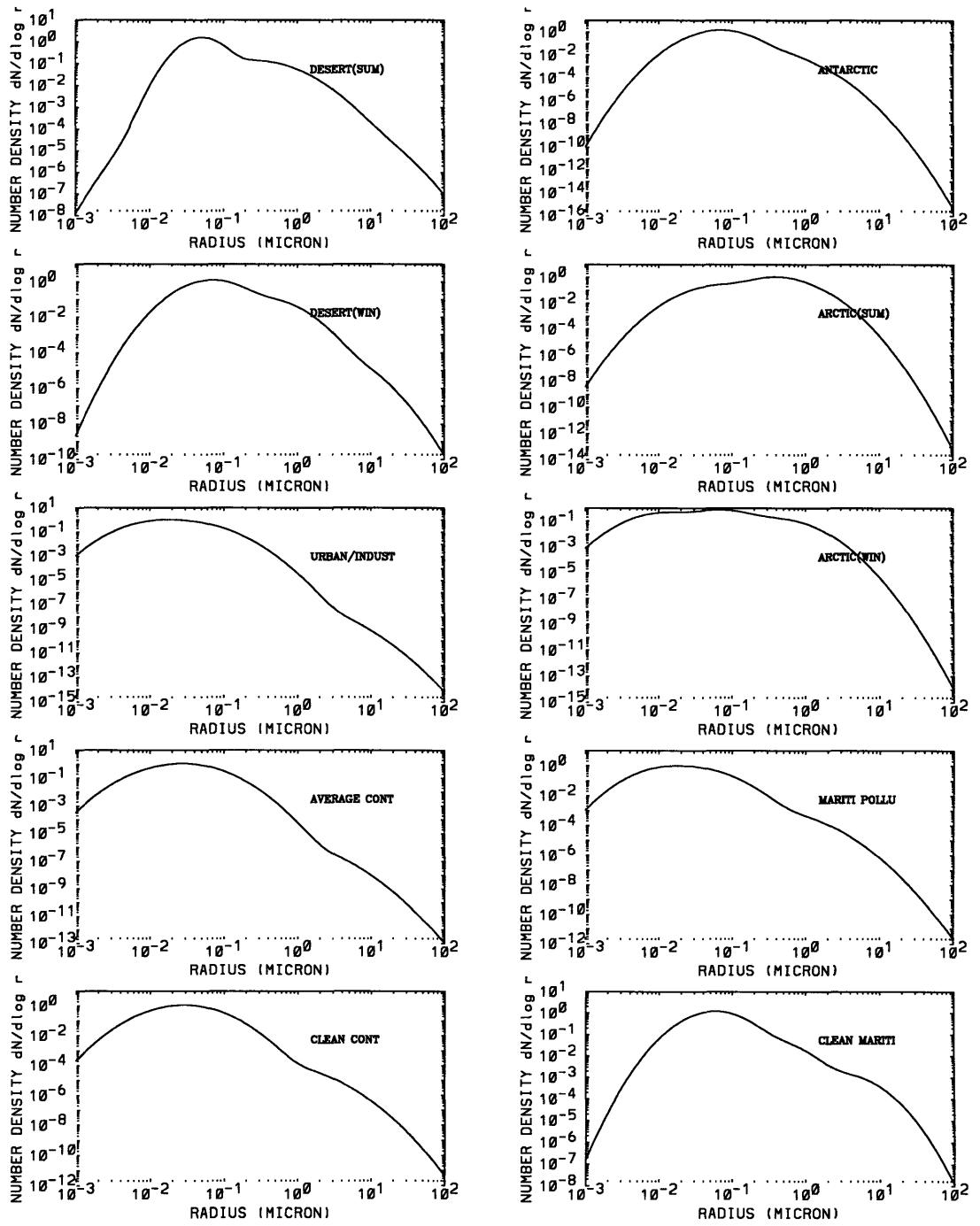
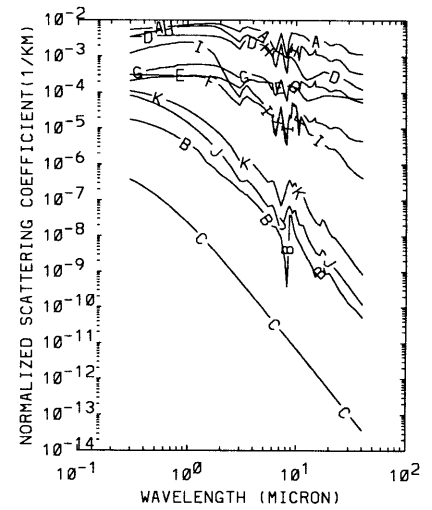
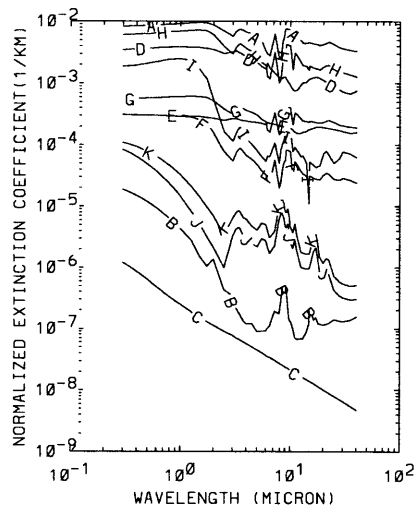


Figure B-3: Size distributions of 10 aerosol types.

these components (cf. Equations 3.11 and 3.12).

Using Equations 3.19, 3.21 and 3.22, we can obtain the size distributions and refractive indices of aerosol components at a given relative humidity. The optical properties of aerosol types at this relative humidity can be computed as before. As an example, Figure B-6 shows the optical properties of clean-continental aerosols at 8 different relative humidities. Results for other aerosol types can be found in d'Almeida et al.[36]. Since clean-continental aerosols contain substantial water-soluble substances (i.e., about 99% by number, cf. Table B.2), the attenuation coefficients are sensitive to relative humidities larger than 70%. Due to the very weak absorptivity in the visible and near-infrared spectral range, the single scattering albedo is almost invariable to relative humidity change and becomes sensitive only at longer wavelengths. The discontinuities observed near $3 \mu m$ and $10 \mu m$ reflect the liquid water absorption features for water-soluble components, as captured in the refractive index plot of Figure B-2.

Although most aerosol particles are produced in the low atmosphere, vertical dynamical processes such as advection, convection, and diffusion may render vertically inhomogeneous profiles of aerosol size distributions and compositions. These profiles are needed for computing the radiative transfer. However, in a static model it is difficult to resolve these variations in detail. The model considered here consists of 3 to 4 vertical layers (e.g., boundary layer, free troposphere, and stratosphere). Within each layer the single-scattering albedo and asymmetry factor are constant and the attenuation coefficients are functions of height as determined by the profile of aerosol number density. Table B.3 summarizes the vertical distributions of different aerosol types. The first and second layers encompass tropospheric aerosols with geographical signatures and the third and fourth layers encompass spatially invariable background aerosols in the free troposphere and stratosphere. The first five aerosol types are assumed homogeneous in a boundary layer which has a constant height; the remaining aerosol types are assumed exponentially distributed characterized by the scale heights. The maritime mineral aerosol type consists of an additional layer representing the mineral dust transported over long distances. In the free troposphere above the boundary layer, a constant extinction coefficient of 0.002 km^{-1} is assumed for all the aerosol types to represent the tropospheric background aerosol radiative effects.



- A- DUST-LIKE
- B- WATER-SOLUBLE
- C- SOOT
- D- SRA-OCEANIC
- E- SEA-SALT
- F- MINERAL(BACKGROUND)
- G- MINERAL(WIND-CARRYING)
- H- MINERAL(MAR.ENV.)
- I- MINERAL(POLEWARDS)
- J- H2SO4 DROPLETS
- K- NSS-SULFATE

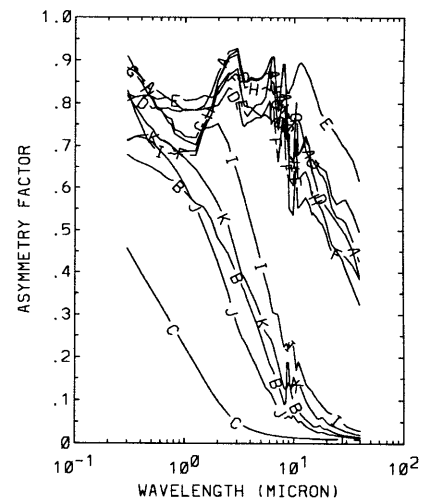
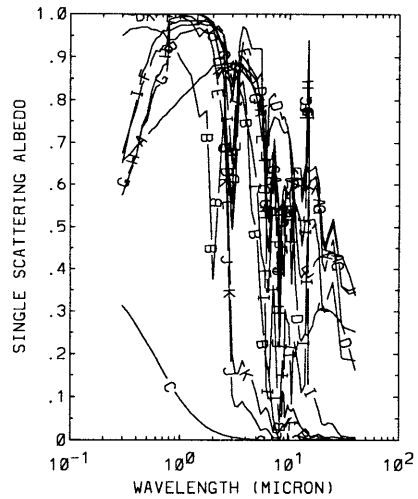
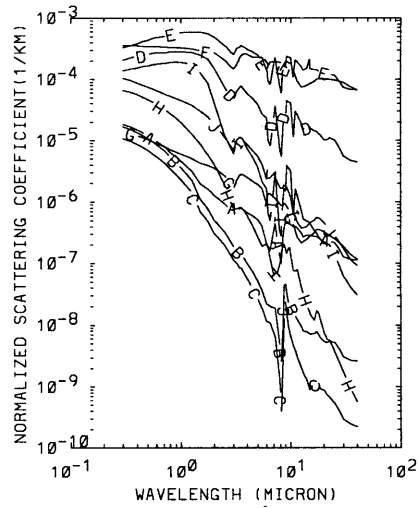
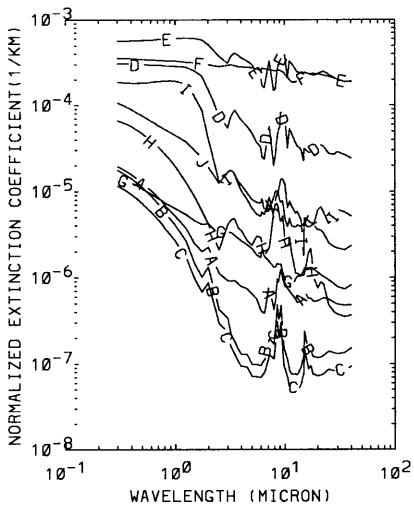


Figure B-4: Wavelength dependence of optical properties of aerosol components.



- A- CL. CONT.
- B- AV. CONT.
- C- URBAN
- D- DESERT(WIN.)
- E- DESERT(SUM.)
- F- CL. MARITIME
- G- MARITIME POLL.
- H- ACRTIC(WIN.)
- I- ACRTIC(SUM.)
- J- ANTARCTIC

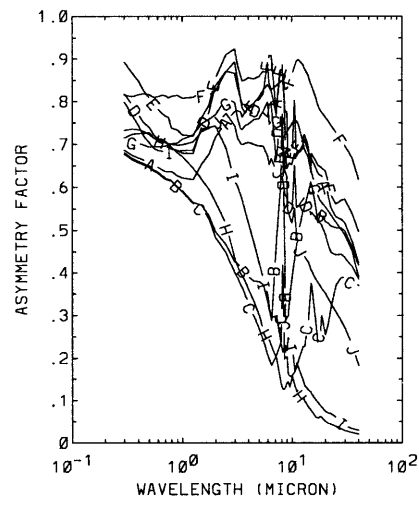
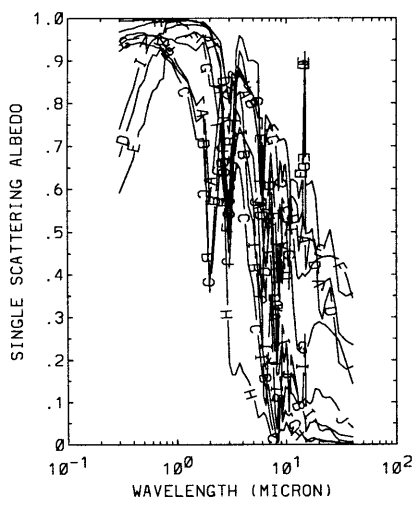


Figure B-5: Wavelength dependence of optical properties of aerosol types.

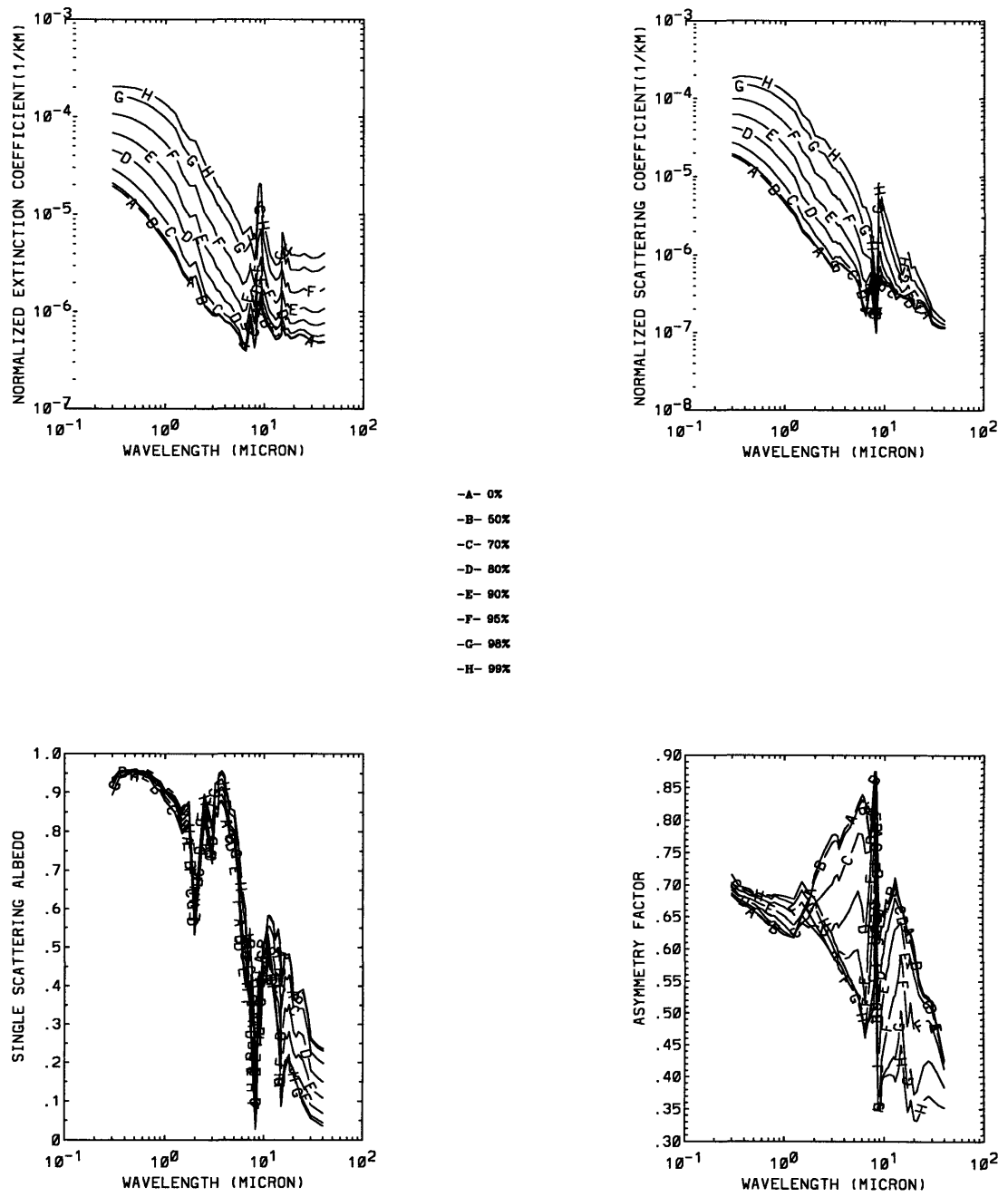


Figure B-6: Wavelength dependence of optical properties of clean continental aerosols at different relative humidities.

Table B.3: Vertical distribution of atmospheric aerosols. The extinction coefficient values refer to dry particles. The underlined values represent normalized extinction coefficients with respect to number density of 1 cm^{-3} and z is in unit of km.

Aerosol type	Vertical layer <i>km</i>	$\sigma_e(z)(0.5\mu m)$ <i>km</i> ⁻¹
Clean continental	0-2	<u>1.263×10^{-5}</u>
	2-12	0.002
	12-35	2.174×10^{-4}
Average continental	0-2	<u>1.113×10^{-5}</u>
	2-12	0.002
	12-35	2.174×10^{-4}
Desert(wintertime)	0-3	<u>3.032×10^{-4}</u>
	3-12	0.002
	12-35	2.174×10^{-4}
Desert(summertime)	0-3	<u>4.904×10^{-4}</u>
	3-12	0.002
	12-35	2.174×10^{-4}
Urban/Industrial	0-2	<u>7.277×10^{-6}</u>
	2-12	0.002
	12-35	2.174×10^{-4}
Clean maritime	0-3	<u>$2.054 \times 10^{-4} e^{-h}$</u>
	3-12	0.002
	12-35	2.174×10^{-4}
Maritime mineral	0-3	<u>$2.054 \times 10^{-4} e^{-h}$</u>
	3-4.5	<u>5.71×10^{-4}</u>
	4.5-12	0.002
	12-35	2.174×10^{-4}
Maritime polluted	0-3	<u>$4.334 \times 10^{-6} e^{-h}$</u>
	3-12	0.002
	12-35	2.174×10^{-4}
Arctic	0-3.5	<u>$3.963 \times 10^{-4} e^{-h/1.4}$</u>
	3.5-12	0.002
	12-35	2.174×10^{-4}
Antarctic	0-10	<u>$8.809 \times 10^{-5} e^{-h/3.5}$</u>
	10-12	0.002
	12-35	2.174×10^{-4}

Appendix C

Shell Scripts of Generating Initial Data for Mesoscale Model

Two shell scripts of generating the initial fields for the UKMO/nonhydrostatic mesoscale model are presented in the following.

The first script was written to retrieve through the network by ftp the real-time and high-resolution analysis or forecast fields from the NMC Eta Model and its associated four-dimensional Eta Data Assimilation System (EDAS). The Eta forecast model generates forecast fields out to 36 hours from initial states at 00Z and 12Z, and the EDAS generates eight 3-hourly initial states or analyses during each 24-hour period. The model grid is defined on a Lambert Conformal projection with nominal 40-km resolution and grid dimensions of 185x129, covering most of North America and the surrounding oceans. Three-dimensional output is provided on 39 constant pressure surface spanning from 1000 mb to 50 mb at intervals of 25 mb.

The second script was written to prepare the initial fields of August 26-31, 1987 for the UKMO/nonhydrostatic mesoscale model from ECMWF analysis datasets ds111.0 and ds111.1, which are archived in the Data Support Section of NCAR. The data are originally in spherical harmonic representation. They are first converted to a 320×160 grid on 14 pressure levels with about 1.125 degree in longitude and 160 Gaussian latitudes and then interpolated to fine resolution UTM grid and vertical η -levels.

```
#!/bin/sh
#LL-----
#LL Script: getdata.eta.sh
#LL Purpose: Auto-ftp NMC ETA model analysis/forecast fields and
#LL           prepare them for the use of UKMO/nonhydrostatic
#LL           mesoscale model.
#LL
#LL Author: Wenwei Pan
#LL           Department of Earth, Atmospheric and Planetary Sciences
#LL           Massachusetts Institute of Technology
#LL
#LL Version: 1.0
#LL Date: August 23, 1995
#LL
#LL Tested under
#LL Machines:
#LL   DEC 3000 AXP/SGI Indigo2
#LL Operating systems:
#LL   OSF1 V2.0/IRIX 5.2
```

```

#LL
#LL Code modification history:
#LL Version Date
#LL 1.1      08/25/95  User-defined UTM projection option added.
#LL                               Header added to binary output file.
#LL 1.2      09/30/95  Bug fixed in Section 1.1.3 where lon_0 and ellps
#LL                               are determined by GDS #6(00001000): Earth
#LL                               assumed spherical w/ a=6367.47km and
#LL                               #7(-95): y-axis parallels to 95W meridian.
#LL-----

#L-----
#L 1. Environment variables set-up and prepare for the ftp.
#L
set -ax
DIR=/data/wpan/ETA
TMP=$DIR/tmp
FILE_TYPE=AWIP3D

#L 1.1 Generate x/y positions on Lamber Conformal Conic projection
#L   for UTM grid.

#L 1.1.1 User-defined constants for grid on UTM projection.
UTMX0=410      #x position of UTM center grid(40,15)
UTMY0=3755
LON0=-117.97  #longitude of UTM center grid
LAT0=33.93
UTMNX=80
UTMNY=30
NP=39
UTMDX=5000
UTMDY=5000
UTMZONE=11

#L 1.1.2 Generate lon/lat for UTM grid.
make utmgrid
if test $? -ne 0
then
echo 'Fail to compile utmgrid.f'
exit 1.1.2
fi
cat > input_utmgrid << EOF
  &input_utmgrid x0=$UTMX0,y0=$UTMY0,nx=$UTMNX,ny=$UTMNY,dx=$UTMDX,dy=$UTMDY, &end
EOF
ln -f -s input_utmgrid fort.1
$DIR/utmgrid > utmgrid.out
FLAG="+proj=utm -I +ellps=WGS84 +zone=$UTMZONE -f %.8f"
proj $FLAG utmgrid.out > utm2ll.out
if test $? -ne 0
then
echo 'Fail to generate lon/lat for UTM grid'
exit 1.1.2
fi

#L 1.1.3 Generate x and y position for UTM grid on Lamber
#L   conformal conic projection.
FLAG="+proj=lcc +lat_1=25 +lat_2=25 +lon_0=-95.0 \
+a=6367470 -f %.8f"
proj $FLAG utm2ll.out > utm2lcc.out

```

```

if test $? -ne 0
then
echo 'Fail to generate x/y on LCC from lon/lat'
exit 1.1.3
fi

#L 1.2 Update unpk--unpack program for GRIB file.
#L
make unpk
if test $? -ne 0
then
echo 'Fail to compile unpkgrb1.f'
exit 1.2
fi

#L 1.3 Update interp--read unpacked data and do the horizontal
#L interpolation.
#L
make interp
if test $? -ne 0
then
echo 'Fail to compile interp.f'
exit 1.3
fi

#L 1.4 Update header--create header for the output data.
make header
if test $? -ne 0
then
echo 'Fail to compile header.f'
exit 1.4
fi

#L-----
#L 2. Loop over all the forecast times.
#L

for i in 00 03 06 09 12 15 18 21 24 27 30 33;do
#L Go to working directory: tmp
#L
cd $TMP
if test -f *
then
rm -r * #empty tmp
fi

FORECAST_TIME=$i
DATA_DIR=/pub/mso/meso.cur/$FILE_TYPE/f$FORECAST_TIME

#L 2.1 ftp data from nic.fb4.noaa.gov: 3d variables and surf. variables.
#L U(m/s),V(m/s),Temp(K),Q(specific humidity kg/kg),
#L Z(geopotential height gpm), surface pressure, gph,
#L specific humidity, and temperature.
#L

ftp nic.fb4.noaa.gov << EOF
cd $DATA_DIR
bin
prompt

```

```

mget datefile PRES_SFC_0 HGT_SFC_0 TMP_SFC_0 \
TMP_P_* SPFH_P_* HGT_P_* UGRD_P_* VGRD_P_*
quit
EOF
if test $? -eq 0
then
echo ftp succeeded
else
echo ftp failed
exit 2.1

fi

#L 2.2 Concatenate separate files together as f$date.
#L
date='cat datefile | sed 's/\(.....\)*/\1/'
if test $? -eq 0
then
rm datefile
cat * > f$i
if test ! -d $DIR/$date
then
mkdir $DIR/$date
fi
mv f$i $DIR/$date
rm *
else
echo 'Failed to extract date from datefile'
exit 2.2
fi

#L 2.3 Unpack files.
#L
cd $DIR/$date #go to directory

#L Prepare control card.
if test -f unpkgrb1.dat
then
rm unpkgrb1.dat
fi
echo 11003f$i > unpkgrb1.dat
echo f$i.out >> unpkgrb1.dat
echo 'Check contents of file unpkgrb1.dat'
cat unpkgrb1.dat

#L Unpack starts.
$DIR/unpk > f$i.log
if test $? -eq 0
then
echo 'unpk running OK'
rm f$i
else
echo 'unpk running failes'
exit 2.3
fi
echo 'Unpacking done successfully'

#L 2.4 Read specific variable from unpacked file(i.e., $i.out).
#L      Do the horizontal interpolation to the user-defined

```

```

#L      UTM projection.

#L 2.4.1 3d variables.
for var in U V TMP SPF HGT #unit:m/s,K,kg/kg.gpm,pa
do
for level in 50 75 100 125 150 175 200 225 250 275 300 325 \
350 375 400 425 450 475 500 525 550 575 600 625 650 \
675 700 725 750 775 800 825 850 875 900 925 950 975 1000
do
#total records
NREC1='fgrep 'NUMBER OF GRIB RECORDS IN FILE' f$i.log | sed 's/.* //'
#get the specific record
IREC1='fgrep " $var " f$i.log | fgrep " $level "'
#get record #
IREC2='echo $IREC1 | sed 's/.*N\(...\).*\/\1/'
#make record # an integer
IREC3='echo $IREC2 | awk '{print int($1)}'
infile1=f"$i"
outfile1=f"$i"_"$var"_"$level"
cat > input_interp << EOF
    &input_interp NREC=$NREC1,IREC=$IREC3,IOP0=1, &END
EOF
#L no space after EOF(stupid shell !!)
ln -f -s input_interp fort.2
ln -f -s $infile1.out fort.11          #Input of unpacked data
ln -f -s $DIR/utm2lcc.out fort.12     #Input UTM grid position on LCC
ln -f -s $outfile1 fort.13           #Output
$DIR/interp
if test $? -ne 0
then
echo 'Error running interp for 3d variables'
exit 2.4.1
fi
done
done

#L 2.4.2 Surface variables.
for var in TMP HGT PRES #unit:m/s,K,kg/kg.gpm,pa
do
level=SFC
NREC1='fgrep 'NUMBER OF GRIB RECORDS IN FILE' f$i.log | sed 's/.* //'
IREC1='fgrep " $var " f$i.log | fgrep " $level "'
IREC2='echo $IREC1 | sed 's/.*N\(...\).*\/\1/'
IREC3='echo $IREC2 | awk '{print int($1)}'
infile1=f"$i"
outfile1=f"$i"_"$var"_"$level"
cat > input_interp << EOF
    &input_interp NREC=$NREC1,IREC=$IREC3, IOP0=1, &END
EOF
#L no space after EOF(stupid shell !!)
ln -f -s input_interp fort.2
ln -f -s $infile1.out fort.11          #Input of unpacked data
ln -f -s $DIR/utm2lcc.out fort.12     #Input UTM grid position on LCC
ln -f -s $outfile1 fort.13           #Output
$DIR/interp
if test $? -ne 0
then
echo 'Error running interp for surface variables'
exit 2.4.2
fi
done
done

```

```
fi
done
```

```
#L 2.5 Concatenate all variable into one binary file.
#L
```

```
#L 2.5.1 Make sure no previous f$date exists
if test -f f$i
then
rm f$i
fi
```

```
#L 2.5.2 Start concatenating files with 3d variables.
```

```
#L      The structure of dump file f$date:
#L      DO 3DVAR=U,V,TMP SPF HGT
#L      DO K=1000,975,...,50
#L      (U(L),L=1,$UTMNX*$UTMNY)
#L      ENDDO
#L      ENDDO
#L
for var in U V TMP SPF HGT
do
for level in 1000 975 950 925 900 875 850 825 800 \
775 750 725 700 675 650 625 600 575 550 525 500 475 \
450 425 400 375 350 325 300 275 250 225 200 175 \
150 125 100 75 50
do
cat f"$i"_"$var"_"$level" >> f$i
#rm f"$i"_"$var"_"$level"      #remove separate files.
done
done
cat f"$i"_PRES_SFC >> f$i
cat f"$i"_HGT_SFC >> f$i
cat f"$i"_TMP_SFC >> f$i
#rm f"$i"*_SFC
```

```
#L 2.6 Generate header for the data file and place it on the
```

```
#L      top of the above obtained data field.
```

```
#L
year1='echo $date | sed 's/\(..\)*/\1/'
month1='echo $date | sed 's/..\(..\)*/\1/' | awk '{print int($1)}'
day1='echo $date | sed 's/....\(..\)*/\1/' | awk '{print int($1)}'
hour1='echo $date | sed 's/.....\(..\)*/\1/' | awk '{print int($1)}'
dt1='echo $FORECAST_TIME | awk '{print int($1)}'
cat > input_header << EOF
&input_header fixx=$UTMX0,fixy=$UTMY0,fixlon=$LONO,fixlat=$LATO, \
mx=$UTMNX,my=$UTMNY,mz=$NP,dx=$UTMDX,dy=$UTMDY,\
year=$year1,month=$month1,day=$day1,hour=$hour1,dt=$dt1, iopo=1, &end
EOF
ln -f -s input_header fort.3
ln -f -s header.out fort.22
$DIR/header
if test $? -ne 0
then
echo 'Error running header'
exit 2.6
fi
cat header.out f$i > dump
mv dump f$i
```

```
#L 2.7 Clean up garbage files.
rm fort.* unpkgrb1.* *_* f$i.* header.out input_*
done #Finish preparing data fields.
```

```
#!/bin/sh
#LL-----
#LL Script: getdata.ecmwf.sh
#LL Purpose: Prepare data for UKMO/nonhydrostatic mesoscale model from
#LL          ECMWF analysis datasets ds111.0 and ds111.1, which are
#LL          archived in the Data Support Section of NCAR.
#LL
#LL Author: Wenwei Pan
#LL          Department of Earth, Atmospheric and Planetary Sciences
#LL          Massachusetts Institute of Technology
#LL
#LL Version: 1.0
#LL Date: August 23, 1995
#LL
#LL Tested under
#LL Machines:
#LL   DEC 3000 AXP/SGI Indigo2
#LL Operating systems:
#LL   OSF1 V2.0/IRIX 5.2
#LL
#LL Code modification history:
#LL Version Date
#LL 1.1   08/25/95 User-defined UTM projection option added.
#LL          Header added to binary output file.
#LL 1.2   09/28/95 Modified to use ECMWF data.
#LL-----
```

```
#L-----
#L 1. Environment variables set-up.
#L
set -ax
DIR=/net/sleazy/data/wpan/data/NCAR
```

```
#L Initial time for the data.
YEAR0=87
MONTH0=8
DAY0=26
HOUR0=0
```

```
#L User-defined constants for grid on UTM projection.
#L
UTMX0=410          #x position of UTM center grid(40,15)
UTMY0=3755
LON0=-117.97      #longitude of UTM center grid
LAT0=33.93
UTMNX=80
UTMNY=30
NP=39
UTMDX=5000
UTMDY=5000
UTMZONE=11
```

```
#L Update header--create header for the output data.
```



```

#L
f77 -o header header.f
if test $? -ne 0
then
echo 'Fail to compile header.f'
exit 1
fi

#L-----
#L 2. Loop over all the valid times (8/26-31, every six hours).
#L

for i in 00 06 12 18 24 30 36 42 48 54 60 66 72 78 \
84 90 96 102 108 114 120 126 132 138;do
    if test -f $DIR/data/f$i;then
rm $DIR/data/f$i
    fi
    DT='echo $i | awk '{ print int ( $1 ) }'
    i1='echo $i | awk '{ print $1 - 24 * int ( $1 / 24 ) }'
    if test $i1 -lt 10;then
i1=0$i1
    fi
    DAY='echo $i | awk '{ print '$DAYO' + int ( $1 / 24 ) }'

#L 2.1 Concatenate all files into one file every six hour.
#L
    cd $DIR/ds111.0
    for j in 131 132 130 157 129;do
        cat "$YEARO"$MONTHO"$DAYO"$i1"_"$j" >> $DIR/data/f$i
    done
    cd $DIR/ds111.1
    for j in 134 129 139;do
        cat "$YEARO"$MONTHO"$DAYO"$i1"_"$j" >> $DIR/data/f$i
    done

#L 2.2 Generate header for the data file and place it on the
#L top of the above obtained data field.
#L
    cd $DIR
cat > input_header << EOF
    &input_header fixx=$UTMXO,fixy=$UTMYO,fixlon=$LONO,fixlat=$LATO, \
    mx=$UTMX,my=$UTMY,mz=$NP,dx=$UTMDX,dy=$UTMDY,\
    year=$YEARO,month=$MONTHO,day=$DAYO,hour=$HOURO,dt=$DT,iopo=1, &end
EOF
    ln -f -s input_header fort.3
    ln -f -s header.out fort.22
    $DIR/header
    if test $? -ne 0;then
echo 'Error running header'
exit 2.6
    fi
    cat header.out $DIR/data/f$i > $DIR/data/dump
    mv $DIR/data/dump $DIR/data/f$i
done #Finish preparing data fields.
rm header.out input_header fort.*

```

Appendix D

IMAQS Shell Scripts

The Integrated Meteorological and Air Quality System (IMAQS) is designed to facilitate the running of UKMO nonhydrostatic mesoscale model, the preparing of meteorological and other necessary data for CIT air quality model, and the running of CIT photochemical air quality model. IMAQS has been developed in collaboration with G. Adamkiewicz and Dr. J.C. Angrill and is not in its final stage.

The following codes contain a job script for SCAQS simulation, and four subshells: mesomet.sndng.sh, mesomet.ecmwf.sh, prepcit.sh, and airshed.sh.

```
#!/bin/sh
#LL#####
#LL Script: scaqs3d.sh
#LL Purpose: Job script to run Integrated Meteorological
#LL           (UKMO/nonhydrostatic mesoscale model) and Air
#LL           Quality(CIT airshed model) System(IMAQS).
#LL
#LL Authors: Wenwei Pan
#LL           Department of Earth, Atmospheric and Planetary Sciences
#LL           Massachusetts Institute of Technology
#LL
#LL           Gary Adamkiewicz
#LL           Department of Chemical Engineering
#LL           Massachusetts Institute of Technology
#LL
#LL           Josep C. Angrill, Ph.D.
#LL           Department of Earth, Atmospheric and Planetary Sciences
#LL           Massachusetts Institute of Technology
#LL
#LL Version: 1.0
#LL Date: January 31, 1996
#LL
#LL Tested under
#LL machines:
#LL DEC 3000 AXP/SGI Indigo2
#LL operating systems:
#LL OSF1 V2.0/IRIX 5.2
#LL
#LL Code modification history:
#LL Version Date
#LL 1.1 02/04/96 Added machtype check and put source files other
#LL           than airshed to $SRC.
#LL 1.2 02/05/96 More clean up. Group source files in /net/sleazy/
#LL           data/wpan/IMAQS to cit,ukmo,prep, and post.
```

```

#LL          Added JOBL and DAY1 to the namelist of files.f.
#LL          Added TZ.
#LL 1.3      02/07/96 Mesoscale output goes to MESO.
#LL 1.4      02/22/96 Added TSEA and DIFTSL; copied preprocessing and
#LL          airshed sources to user directories.--J.C.Angrill
#LL 1.5      02/22/96 Imaqs.sh splitted into subshells.
#LL
#LL Calls:
#LL          mesomet.sh
#LL          prepcit.sh
#LL          airshed.sh
#LL
#LL#####

set -x
SETOPT=x
MACHTYPE='uname -n'

#L-----
#L Define the user working directory, the job code and the date for
#L the air aquality modeling.
#L
SRC=/net/sleazy/data/wpan/IMAQS
TMP=/net/sleazy/data/wpan/airshed/SCAQS
YEAR=1987
MONTH=8
DAY=27
JOB=scaqs3d

#L-----
#L Define the parameters for the UTM zone 11 projection domain.
#L
LAT0=34      #latitude of grid origin(<0->S)
LON0=-118    #longitude(<0->W)
TZ=8         #time zone in hours difference from GMT(>0)
X0=0         #GTM coordinates of model origin
Y0=0
XSW=210000   #position of SW corner(m) to GTM origin
YSW=3680000

#L-----
#L Define the grid for meoscale and airshed modeling.
#L Horizontal grid same and vertical can be different.
#L Keep vertical levels same to avoid interpolation error.
#L
NX=80        #number of grid cells
NY=30
DX=5000      #grid size(m)

#L Define the total number and height(m) of airshed model
#L eta-levels, where U/V sit.
NZ_CHEM=5
cat > chemlevel << EOF
  &CHEMLEVEL ZUV=19.25,96.25,231,489.5,885.5, &END
EOF

#L-----
#L Define the landuse file.
#L Format: 50I2;

```

```

#L Origin: south-west corner;
#L Scan: west-to-east then south-to-north.
#L
LANDUSE=$TMP/global/lufield.data

#L-----
#L Define the topography file.
#L
TOPOGRAPHY=/net/cork/d0/wpan/UKMO/jobs/SCAQS/org.dat

#L-----
#L Define the time(GMT), total levels and file location
#L for the sounding.
#L TSEA:sea surface temperature(C); DIFTSL=Tsoil-Tsurf(C).
#L
YEAR_SND=1987
MONTH_SND=8
DAY_SND=27
HOUR_SND=7
MINUTE_SND=0
NZ_SND=56
SOUNDING=/net/cork/d0/wpan/UKMO/jobs/SCAQS/IC.82707Z/EMUascaqsLAXecmf.profile
TSEA=17
DIFTSL=3

#L-----
#L Define switches for running mesoscale meteorological model.
#L
I1D=0
I2D=0
I3D=1
IUKMO=1
IQFU=0
IGSFC=0
EXPID=1
MPBL=1          #Method for diagnosing PBLD(1:T;2:Richardson #;3:TKE)
PBLDMN=110      #Minimum PBLD(m)
PBLDMX=2500     #Maximum PBLD(m)
RIC=1.0         #Critical Richardson number
TEMIN=0.005     #Minimum TKE(m**2/s**2)
IARL=0          #Flag for treating aerosols
NCCONT=1530     #Clean continental average number concentration(1/cm**3)
NACONT=24300    #Average -----
NURBAN=28100    #Urban -----
NCLMAR=500      #Clean maritime -----

#L-----
#L Define the emission inventory. If only area or point source
#L is available, set AREA=1 or POIN=1.
#L
EMISSION=$TMP/area_inventory
AREA=1
POIN=1
UVS=0          #spatial resolution for surf. & top UV scaling factors.
UVC=1
YEST=1

#L-----
#L Set skip flags for each subshells.

```

```

#L
MESOMET=1
PREPCIT=0
AIRSHED=0

if test $MESOMET -eq 1;then
#L-----
#L Call script mesomet.sh to run mesoscale meteorological model.
#L
export SETOPT SRC TMP
export TOPOGRAPHY LANDUSE
export NX NY DX
export LATO LONO TZ XO YO XSW YSW
export I1D I2D I3D IUKMO IQFU IGSFC EXPID MPBL PBLDMN PBLDMX RIC TEMIN IARL \
      NCCONT NACONT NURBAN NCLMAR
cp $SRC/mesomet.ecmwf.sh .
./mesomet.ecmwf.sh
CC=$?
if test $CC -ne 0;then
    echo "$0: failed in mesomet.ecmwf.sh"
    exit $CC
fi

fi

if test $PREPCIT -eq 1;then
#L-----
#L Call script prepcit.sh to preprocess CIT airshed model.
#L
export SETOPT SRC TMP MACHTYPE
export YEAR MONTH DAY JOB EXPID
export LANDUSE EMISSION
export NX NY NZ_CHEM NZ_MESO DX
export LONO LATO XO YO XSW YSW
export AREA POIN UVC UVS TZ YEST
cp $SRC/prepcit.sh .
./prepcit.sh
CC=$?
if test $CC -ne 0;then
    echo "$0: failed in prepcit.sh"
    exit $CC
fi

fi

if test $AIRSHED -eq 1;then
#L-----
#L Call script airshed.sh to run CIT airshed model.
#L
export SETOPT SRC TMP NX NY NZ_CHEM MACHTYPE
cp $SRC/airshed.sh .
./airshed.sh
CC=$?
if test $CC -ne 0;then
    echo "$0: failed in airshed.sh"
    exit $CC
fi

fi

```

```
echo "$JOB.sh OK"
```

```
#!/bin/sh
#LL#####
#LL Script: mesomet.sndng.sh
#LL Purpose: Script to run mesoscale meteorological model using
#LL           a single sounding profile.
#LL
#LL Authors: Wenwei Pan
#LL           Department of Earth, Atmospheric and Planetary Sciences
#LL           Massachusetts Institute of Technology
#LL
#LL           Gary Adamkiewicz
#LL           Department of Chemical Engineering
#LL           Massachusetts Institute of Technology
#LL
#LL           Josep C. Angrill, Ph.D.
#LL           Department of Earth, Atmospheric and Planetary Sciences
#LL           Massachusetts Institute of Technology
#LL
#LL Version: 1.0
#LL Date: January 31, 1996
#LL
#LL Tested under compiler: f77 (?)
#LL Tested under OS version: IRIX 5.2 02282016 IP22 mips
#LL
#LL Code modification history:
#LL Version Date
#LL 1.1    02/04/96  Added machtype check and put source files other
#LL                    than airshed to $SRC.
#LL 1.2    02/05/96  More clean up. Group source files in /net/sleazy/
#LL                    data/wpan/IMAQS to cit,ukmo,prep, and post.
#LL                    Added JOBL and DAY1 to the namelist of files.f.
#LL                    Added TZ.
#LL 1.3    02/07/96  Mesoscale output goes to MESO.
#LL 1.4    02/22/96  Added TSEA and DIFTSL; copied preprocessing and
#LL                    airshed sources to user directories.--J.C.Angrill
#LL 1.5    02/22/96  Imaqs.sh splitted into subshells.
#LL
#LL Called by:
#LL           job.sh
#LL
#LL Imports:
#LL           SETOPT
#LL           SRC
#LL           TMP
#LL           TOPOGRAPHY
#LL           LANDUSE
#LL           NX
#LL           NY
#LL           DX
#LL           LATO
#LL           LONO
#LL           TZ
#LL           XO
#LL           YO
#LL           XSW
```

```

#LL      YSW
#LL      YEAR_SND
#LL      MONTH_SND
#LL      DAY_SND
#LL      HOUR_SND
#LL      MINUTE_SND
#LL      NZ_SND
#LL      SOUNDING
#LL      TSEA
#LL      DIFTSL
#LL      I1D
#LL      I2D
#LL      I3D
#LL      IUKMO
#LL      IQFU
#LL      IGSFC
#LL      EXPID
#LL
#LL#####

```

```
set -$SETOPT
```

```

if test ! -d meso;then
  mkdir meso
fi

```

```

UKMO=$SRC/ukmo
cd $TMP/meso
cp $SRC/prep/init.f .
cp $UKMO/prepro.f .
f77 -o prepro.x -static -O2 prepro.f

```

```

#L
#L Initialisation.
#L
#L Define the total number and height(m) of mesoscale model
#L eta-levels, where most variables sit except for vertical
#L velocity(mid-levels).

```

```

DY=$DX
NZ_MESO=18
cat > mesolevel << EOF
  &MESOLEVEL ILVL=10,110,310,610,1010,1510,2110,2810,3610,4510,5510,\
  6610,7810,9110,10510,12010,13610,15310,\
  TSEA=$TSEA, DIFTSL=$DIFTSL, &END
EOF

```

```

cat > cminit << EOF
*COMDECK INIT
  INTEGER NX,NY,NZ,NP,NXY,YEAR,MONTH,DAY,HOUR,MINUTE
  PARAMETER (NX=$NX,NY=$NY,NZ=$NZ_MESO,NP=$NZ_SND,NXY=NX*NY,
  ,YEAR=$YEAR_SND,MONTH=$MONTH_SND,DAY=$DAY_SND,HOUR=$HOUR_SND,
  ,MINUTE=$MINUTE_SND)
  REAL FIXLON, FIXLAT,XO,YO,XSW,YSW,DX,DY
  PARAMETER(FIXLON=$LONO, FIXLAT=$LATO,XO=$XO,YO=$YO,
  ,XSW=$XSW,YSW=$YSW,DX=$DX,DY=$DY)
*COMDECK MEM
  INTEGER MEMX,MEMY,MEMXY,MEMZ
  PARAMETER (MEMX=$NX,MEMY=$NY,MEMXY=MEMX*MEMY,MEMZ=$NZ_MESO)

```

```

EOF

cat $UKMO/cm >> cminit
ln -f -s init.f fort.10
ln -f -s cminit fort.11
ln -f -s int.f fort.12
ln -f -s mesolevel fort.1
./prepro.x << end
  &FT05IN IEXCL=1,IDIAG=1,IMEM=1, &END
end

f77 -o int.x -static -O2 int.f
CC=$?
if test $CC -ne 0;then
  echo "Fail to compile $TMP/meso/int.f"
  exit $CC
fi
ln -f -s ws0 fort.10
ln -f -s $SOUNDING fort.11
ln -f -s $TOPOGRAPHY fort.21
ln -f -s $LANDUSE fort.8
./int.x
CC=$?
if test $CC -ne 0;then
  echo "Fail to run $TMP/meso/int.x"
  exit $CC
fi

#L
#L Preprocessing.
#L

if test -f sl;then
  rm sl
fi

for i in \
  ma pt ad di dyn bd io chario ute cs tsurf cv precip aerlopt \
  rad \
  stdatm \
  swqfu lwqfu swrad_qfu lwrad_qfu qfu \
  swgsfc lwgsfc swrad_gsfc lwrad_gsfc
do
  cat $UKMO/$i >> sl
done
cat > cm << EOF
*COMDECK DIN
  INTEGER NX,NY,NXY,NZ,NCON,NRAD
  PARAMETER (NX=$NX,NY=$NY,NZ=$NZ_MESO,NXY=NX*NY,NCON=1,NRAD=NZ-1)
*COMDECK MEM
  INTEGER MEMX,MEY,MEMXY,MEMZ,MEMCON,MEMRAD,MEMSM
  PARAMETER (MEMX=$NX,MEY=$NY,MEMZ=$NZ_MESO,MEMSM=20,MEMXY=MEMX*MEY,
    ,MEMCON=1,MEMRAD=MEMZ-1)
*COMDECK INQFU
  INTEGER
  & NV,          !VERTICAL LAYERS.
  & NV1,         !VERTICAL LEVELS.
  & NDFS,
  & MDFS,

```



```

& NDFS4,
& NC,           !NUMBER OF CLOUD TYPES
& MB,           !NUMBER OF SPECTRAL BANDS.
& MBS,         !SPECTRAL BANDS FOR SW.
& MBIR,        !SPECTRAL BANDS FOR LW.
& ICOLN        !NUMBER OF COLUMNS=MEMXY
  PARAMETER (
& NV = 30, NV1 = NV + 1,
& NDFS = NV, MDFS = NV + 1, NDFS4 = 4 * NDFS,
& MB = 18, MBS = 6, MBIR = 12,
& NC = 8, ICOLN = 1 )
*COMDECK INGSFC
  INTEGER
& NV,           !VERTICAL LAYERS.
& NV1,         !VERTICAL LEVELS.
& NUVV,NNIR,NIR !NUMBER OF BANDS FOR UV/V,NIR AND IR.
  PARAMETER (
& NV = 30,NV1 = NV + 1,
& NUVV=4,NNIR=8,NIR=10)
EOF

cat $UKMO/cm >> cm
ln -f -s sl fort.10
ln -f -s cm fort.11
ln -f -s sl.f fort.12
./prepro.x << EOF
&FT05IN IMEM=1,IEXCL=1,IDIAG=0,ICV=0,IRAD=1,IPR=0,ISX=1,IGR=1,IDF=1,
IVIRT=1,I1D=$I1D,I2D=$I2D,I3D=$I3D,IWET=0,IMADJ=1,ICE=0,IPIO=1,
IUUKMO=$IUUKMO,IQFU=$IQFU,IGSFC=$IGSFC, IARL=$IARL, &END
EOF
CC=$?
if test $CC -ne 0;then
  echo "Preprocessing mesoscale model fails"
  exit $CC
fi

#L
#L Compile & load code.
#L

f77 -o sl.x -static -O2 -r8 sl.f
CC=$?
if test $CC -ne 0;then
  echo "Compiling mesoscale model fails"
  exit $CC
fi

cat > deltat << EOF
&DELTAT NTSWU=60,120,180,240,300,360,420,480,540,600,660,720,780,840,\
900,960,1020,1080,1140,1200,1260,1320,1380,1440,
DT=60,IOPI=1,IOPO=1,HORKM=0.1,HORKH=0.1,VNTN=1.,HNTN=1.,NSM=5,\
VERKMO=0.0,VERKHO=0.0,RHCRIT=0.3,IDX=1,IDY=1,WTSND=0.7,WTGRV=0.5,\
WTDIF=2.0,NFTBDY=0,NTSBDY=0,NVARA=10,NVARS=7,NTSPADJ=1,IDDG=0,NDDG=1,\
IML=$MPBL,PBLDMN=$PBLDMN,PBLDMX=$PBLDMX,RIC=$RIC,TEMIN=$TEMIN,\
NCCONT=$NCCONT,NACONT=$NACONT,NURBAN=$NURBAN,NCLMAR=$NCLMAR, &END
76 77 83 74 36 82 17 18 23 24
36 11 12 13 14 15 16
0 0 0 0 0 0 0
EOF

```

```

#L
#L Assign fortran unit numbers.
#L

ln -f -s deltat fort.1
ln -f -s ws0 fort.10
ln -f -s $UKMO/cdch fort.9

ln -f -s $UKMO/OPCCont.out fort.201
ln -f -s $UKMO/OPACont.out fort.202
ln -f -s $UKMO/OPUrban.out fort.203
ln -f -s $UKMO/OPCleanMar.out fort.204

n=10
for i in 1 2 3 4 5 6 7 8 9 a b c d e f g h i j k l m n o;do
n='expr $n + 1'
ln -f -s ws"$EXPID""$i" fort.$n
done

#L
#L Run mesoscale forecast model.
#L
time ./sl.x > meso"$EXPID".out
CC=$?
if test $CC -ne 0;then
    echo "Running mesoscale model fails"
    exit $CC
fi

#rm fort.* *.f *.x cm cminit deltat sl

#!/bin/sh
#LL#####
#LL Script: mesomet.ecmwf.sh
#LL Purpose: Script to run mesoscale meteorological model using
#LL          initial fields from ECMWF global analysis.
#LL
#LL Authors: Wenwei Pan
#LL          Department of Earth, Atmospheric and Planetary Sciences
#LL          Massachusetts Institute of Technology
#LL
#LL          Gary Adamkiewicz
#LL          Department of Chemical Engineering
#LL          Massachusetts Institute of Technology
#LL
#LL          Josep C. Angrill, Ph.D.
#LL          Department of Earth, Atmospheric and Planetary Sciences
#LL          Massachusetts Institute of Technology
#LL
#LL Version: 1.0
#LL Date: January 31, 1996
#LL
#LL Tested under compiler: f77 (?)
#LL Tested under OS version: IRIX 5.2 02282016 IP22 mips
#LL
#LL Code modification history:

```

```

#LL Version Date
#LL 1.1    02/04/96  Added machtype check and put source files other
#LL                    than airshed to $SRC.
#LL 1.2    02/05/96  More clean up. Group source files in /net/sleazy/
#LL                    data/wpan/IMAQS to cit,ukmo,prep, and post.
#LL                    Added JOBL and DAY1 to the namelist of files.f.
#LL                    Added TZ.
#LL 1.3    02/07/96  Mesoscale output goes to MESO.
#LL 1.4    02/22/96  Added TSEA and DIFTSL; copied preprocessing and
#LL                    airshed sources to user directories.--J.C.Angrill
#LL 1.5    02/22/96  Imaqs.sh splitted into subshells.
#LL
#LL Called by:
#LL         job.sh
#LL
#LL Imports:
#LL     SETOPT
#LL     SRC
#LL     TMP
#LL     TOPOGRAPHY
#LL     LANDUSE
#LL     NX
#LL     NY
#LL     DX
#LL     LATO
#LL     LONO
#LL     TZ
#LL     XO
#LL     YO
#LL     XSW
#LL     YSW
#LL     I1D
#LL     I2D
#LL     I3D
#LL     IUKMO
#LL     IQFU
#LL     IGSFC
#LL     EXPID
#LL
#LL#####

set -$SETOPT

if test ! -d meso;then
  mkdir meso
fi

UKMO=$SRC/ukmo
OPT=02
cd $TMP/meso
cp $SRC/prep/init.ecmwf .
cp $UKMO/prepro.f .
f77 -o prepro.x -static -$OPT prepro.f

#L
#L Initialisation.
#L
#L Define the total number and height(m) of mesoscale model
#L eta-levels, where most variables sit except for vertical

```

```

#L velocity(mid-levels).

NZ_MESO=18
XSW1='expr $XSW / 1000'
YSW1='expr $YSW / 1000'
DX1='expr $DX / 1000'
cat > cminit << EOF
*COMDECK INTDIM
    INTEGER NADI, LNHD2
    PARAMETER (NADI=5, LNHD2=1000)
*COMDECK INTDIN
C OUTPUT GRID DIMENSION, ORIGIN
    INTEGER NX, NY, NZ, NXY, NP, LREC
    PARAMETER(NX=$NX, NY=$NY, NXY=NX*NY, NZ=$NZ_MESO, LREC=NX*NY, NP=14)
    REAL DX, DY, XO, YO
    PARAMETER(XO=$XSW1, YO=$YSW1, DX=$DX1, DY=DX)
    REAL HT2(NZ)
    DATA HT2/10., 110., 310., 610., 1010., 1510., 2110., 2810., 3610.,
, 4510., 5510., 6610., 7810., 9110., 10510., 12010., 13610., 15310./
    REAL PL(NP)
    DATA PL/
    & 1000, 850, 700, 500, 400, 300, 250, 200, 150, 100, 70, 50, 30, 10/
*COMDECK MEM
    INTEGER MEMX, MEMY, MEMXY, MEMZ, MEMNP
    PARAMETER (MEMX=$NX, MEMY=$NY, MEMXY=MEMX*MEMY, MEMZ=$NZ_MESO, MEMNP=14)
EOF

cat $UKMO/cm >> cminit
ln -f -s init.ecmwf fort.10
ln -f -s cminit fort.11
ln -f -s int.f fort.12
./prepro.x << end
&FT05IN IEXCL=1, IDIAG=1, IMEM=1, &END
end

f77 -o int.x -static -$OPT int.f
CC=$?
if test $CC -ne 0; then
    echo "Fail to compile $TMP/meso/int.f"
    exit $CC
fi

#L Link input ECMWF data on pressure levels and UTM grid.
DATA=/net/cork/d0/wpan/UKMO/jobs/SCAQS
ln -f -s $DATA/ecmwf/f30 fort.10 #8/27/06 GMT
ln -f -s $DATA/ecmwf/f36 fort.11
ln -f -s $DATA/ecmwf/f42 fort.12
ln -f -s $DATA/ecmwf/f48 fort.13
ln -f -s $DATA/ecmwf/f54 fort.14
ln -f -s $DATA/ecmwf/f60 fort.15 #8/28/12 GMT

#L Link output data for mesoscale simulation.
ln -f -s ws0 fort.50
ln -f -s ms2 fort.51
ln -f -s ms3 fort.52
ln -f -s ms4 fort.53
ln -f -s ms5 fort.54
ln -f -s ms6 fort.55

```

```

#L Link SCAQS topography and roughness height.
ln -f -s $TOPOGRAPHY fort.21
ln -f -s $LANDUSE fort.8

./int.x << end
  &interpin iopi=1,iopo=1,ipois=1,ammhs1=20,nt=6,nft=10, &END
end

CC=$?
if test $CC -ne 0;then
  echo "Fail to run $TMP/meso/int.x"
  exit $CC
fi

#L
#L Create time depedent boundary conditions.
#L

cat > cmbd << EOF
*COMDECK BDY
  INTEGER NX,NY,NZ
  PARAMETER (NX=$NX,NY=$NY,NZ=$NZ_MESO)
EOF

cat $UKMO/cm >> cmbd

#L Preprocess code.
ln -f -s $UKMO/mefbdy fort.10
ln -f -s cmbd fort.11
ln -f -s bd.f fort.12
./prepro.x << end
  &FT05IN IEXCL=1,IDIAG=1,IMEM=1, &END
end

#L Compile & load code.
f77 -o bd.x -static -$OPT -r8 bd.f
CC=$?
if test $CC -ne 0
then
echo 'Error compiling bd.f'
exit $CC
fi
cat > nbdyin << end
  &nbdyin nbdy=6,iop=1,icloud=0,imtm=0, &END
end

#L Assign fortran input unit numbers.
ln -f -s nbdyin fort.1
ln -f -s ws0 fort.40
ln -f -s ms2 fort.41
ln -f -s ms3 fort.42
ln -f -s ms4 fort.43
ln -f -s ms5 fort.44
ln -f -s ms6 fort.45

#L Assign fortran output unit numbers.
ln -f -s mbd fort.70

#L Running the code.

```

```

./bd.x
CC=$?
if test $CC -ne 0;then
echo 'Error running bd.x'
exit $CC
fi

#L
#L Preprocessing.
#L

if test -f sl;then
  rm sl
fi

for i in \
  ma pt ad di dyn bd io chario ute cs tsurf cv precip aerlopt \
  rad \
  stdatm \
  swqfu lwqfu swrad_qfu lwrad_qfu qfu \
  swgsfc lwgsfc swrad_gsfc lwrad_gsfc
do
  cat $UKMO/$i >> sl
done
cat > cm << EOF
*COMDECK DIN
  INTEGER NX,NY,NXY,NZ,NCON,NRAD
  PARAMETER (NX=$NX,NY=$NY,NZ=$NZ_MESO,NXY=NX*NY,NCON=1,NRAD=NZ-1)
*COMDECK MEM
  INTEGER MEMX,MEY,MEMXY,MEMZ,MEMCON,MEMRAD,MEMSM
  PARAMETER (MEMX=$NX,MEY=$NY,MEMZ=$NZ_MESO,MEMSM=20,MEMXY=MEMX*MEY,
  MEMCON=1,MEMRAD=MEMZ-1)
*COMDECK INQFU
  INTEGER
  & NV,          !VERTICAL LAYERS.
  & NV1,         !VERTICAL LEVELS.
  & NDFS,
  & MDFS,
  & NDFS4,
  & NC,          !NUMBER OF CLOUD TYPES
  & MB,          !NUMBER OF SPECTRAL BANDS.
  & MBS,         !SPECTRAL BANDS FOR SW.
  & MBIR,        !SPECTRAL BANDS FOR LW.
  & ICOLN        !NUMBER OF COLUMNS=MEMXY
  PARAMETER (
  & NV = 30, NV1 = NV + 1,
  & NDFS = NV, MDFS = NV + 1, NDFS4 = 4 * NDFS,
  & MB = 18, MBS = 6, MBIR = 12,
  & NC = 8, ICOLN = 1 )
*COMDECK INGSFC
  INTEGER
  & NV,          !VERTICAL LAYERS.
  & NV1,         !VERTICAL LEVELS.
  & NUVV,NNIR,NIR !NUMBER OF BANDS FOR UV/V,NIR AND IR.
  PARAMETER (
  & NV = 30,NV1 = NV + 1,
  & NUVV=4,NNIR=8,NIR=10)
EOF

```

```

cat $UKMO/cm >> cm
ln -f -s sl fort.10
ln -f -s cm fort.11
ln -f -s sl.f fort.12
./prepro.x << EOF
&FT05IN IMEM=1, IEXCL=1, IDIAG=0, ICV=0, IRAD=1, IPR=0, ISX=1, IGR=1, IDF=1,
IVIRT=1, I1D=$I1D, I2D=$I2D, I3D=$I3D, IWET=0, IMADJ=1, ICE=0, IPIO=1,
IUUKMO=$IUUKMO, IQFU=$IQFU, IGSFC=$IGSFC, IARL=$IARL, &END
EOF
CC=$?
if test $CC -ne 0;then
echo "Preprocessing mesoscale model fails"
exit $CC
fi

#L
#L Compile & load code.
#L

f77 -o sl.x -static -$OPT -r8 sl.f
CC=$?
if test $CC -ne 0;then
echo "Compiling mesoscale model fails"
exit $CC
fi

cat > deltat << EOF
&DELTAT NTSWU=120,180,240,300,360,420,480,540,600,660,720,780,840,\
900,960,1020,1080,1140,1200,1260,1320,1380,1440,1500,
DT=60, IOPI=1, IOPD=1, HORKM=0.1, HORKH=0.1, VNTN=1., HNTN=1., NSM=5,\
VERKMO=0.0, VERKHO=0.0, RHCRIT=0.3, IDX=1, IDY=1, WTSND=0.7, WTGRV=0.5,\
WTDIF=2.0, NFTBDY=0, NTSBDY=0, NVARA=7, NVAR=3, NTSPADJ=1, IDDG=0, NDDG=1,\
IML=$MPBL, PBLDMN=$PBLDMN, PBLDMX=$PBLDMX, RIC=$RIC, TEMIN=$TEMIN,\
NCCONT=$NCCONT, NACONT=$NACONT, NURBAN=$NURBAN, NCLMAR=$NCLMAR, &END
76 77 83 74 36 82 23
36 11 12
0 0 0
EOF

#L
#L Assign fortran unit numbers.
#L

ln -f -s deltat fort.1
ln -f -s ws0 fort.10
ln -f -s mbd fort.71
ln -f -s $UKMO/cdch fort.9

ln -f -s $UKMO/OPCCont.out fort.201
ln -f -s $UKMO/OPACCont.out fort.202
ln -f -s $UKMO/OPUrban.out fort.203
ln -f -s $UKMO/OPCleanMar.out fort.204

MESO=/net/cork/d0/wpan/UKMO/jobs/SCAQS/IC.82706Z.cork
n=10
for i in 1 2 3 4 5 6 7 8 9 a b c d e f g h i j k l m n o;do
n='expr $n + 1'
ln -f -s $MESO/ws"$EXPID""$i" fort.$n

```

```

done

#L
#L Run mesoscale forecast model.
#L
time ./sl.x > meso"$EXPID".out
CC=$?
if test $CC -ne 0;then
    echo "Running mesoscale model fails"
    exit $CC
fi

rm fort.* *.f *.x cm cminit deltat

```

```

#!/bin/sh
#LL#####
#LL Script: prepcit.sh
#LL Purpose: Script to preprocess mesoscale meteorological model
#LL          output for CIT airshed model and prepare the following
#LL          data for running CIT airshed model:
#LL          meteorological data;
#LL          surface roughness height;
#LL          landuse fraction;
#LL          total hydrocarbon splitting factors;
#LL          ground level emission;
#LL          computational region;
#LL          IC and BC;
#LL          command file;
#LL          input file list.
#LL
#LL Authors: Wenwei Pan
#LL          Department of Earth, Atmospheric and Planetary Sciences
#LL          Massachusetts Institute of Technology
#LL
#LL          Gary Adamkiewicz
#LL          Department of Chemical Engineering
#LL          Massachusetts Institute of Technology
#LL
#LL          Josep C. Angrill, Ph.D.
#LL          Department of Earth, Atmospheric and Planetary Sciences
#LL          Massachusetts Institute of Technology
#LL
#LL Version: 1.0
#LL Date: January 31, 1996
#LL
#LL Tested under compiler: f77 (?)
#LL Tested under OS version: IRIX 5.2 02282016 IP22 mips
#LL
#LL Code modification history:
#LL Version Date
#LL 1.1    02/04/96  Added machtype check and put source files other
#LL                    than airshed to $SRC.
#LL 1.2    02/05/96  More clean up. Group source files in /net/sleazy/
#LL                    data/wpan/IMAQS to cit,ukmo,prep, and post.
#LL                    Added JOBL and DAY1 to the namelist of files.f.
#LL                    Added TZ.
#LL 1.3    02/07/96  Mesoscale output goes to MESO.

```



```

#LL 1.4      02/22/96  Added TSEA and DIFTSL; copied preprocessing and
#LL          airshed sources to user directories.--J.C.Angrill
#LL 1.5      02/22/96  Imaqs.sh splitted into subshells.
#LL
#LL Called by:
#LL          job.sh
#LL
#LL Imports:
#LL          SETOPT
#LL          SRC
#LL          TMP
#LL          YEAR
#LL          MONTH
#LL          DAY
#LL          JOB
#LL          MACHTYPE
#LL          EMISSION
#LL          LANDUSE
#LL          NX
#LL          NY
#LL          NZ_CHEM
#LL          NZ_MESO
#LL          DX
#LL          LATO
#LL          LONO
#LL          TZ
#LL          YEST
#LL          XO
#LL          YO
#LL          XSW
#LL          YSW
#LL          AREA
#LL          POIN
#LL          UVS
#LL          UVC
#LL          EXPID
#LL
#LL#####

```

```

set -$SETOPT

if test ! -d prep;then
  mkdir prep
else
  rm prep/*
fi
if test ! -d input;then
  mkdir input
else
  rm input/*
fi
if test ! -d global;then
  mkdir global
else
  rm global/*
fi

cd $TMP/prep
cp $SRC/prep/* .

```

```

#L
#L Generate the parameter file.
#L
case $MONTH in
1) MONTH1=jan;;
2) MONTH1=feb;;
3) MONTH1=mar;;
4) MONTH1=apr;;
5) MONTH1=may;;
6) MONTH1=jun;;
7) MONTH1=jul;;
8) MONTH1=aug;;
9) MONTH1=sep;;
10) MONTH1=oct;;
11) MONTH1=nov;;
12) MONTH1=dec;;
esac

DY=$DX
HEADER="AIR QUALITY SIMULATION FOR $JOB at $MONTH/$DAY/$YEAR"
YEAR1='expr $YEAR - 1900'
DATE=$YEAR1$MONTH1$DAY
cat > param_global.h << EOF
    INTEGER NX,NY,NXY,NC,YEAR,MONTH,DAY,NZ,NT
    INTEGER MEMX,MEY,MEZ
    REAL XO,YO,DX,DY
    PARAMETER (NX=$NX,NY=$NY,NXY=NX*NY,NC=$NZ_CHEM,
        , NZ=$NZ_MESO,NT=24,
        , YEAR=$YEAR1,MONTH=$MONTH,DAY=$DAY,
        , XO=$XSW,YO=$YSW,DX=$DX,DY=$DY,
        , MEMX=$NX,MEY=$NY,MEZ=$NZ_CHEM)
EOF

#L-----
#L Process mesoscale meteorological model output for CIT airshed model.
#L
#L
#L Link mesoscale model hourly output.
#L

nft=38
for i in 1 2 3 4 5 6 7 8 9 a b c d e f g h i j k l m n o;do
nft='expr $nft + 1'
ln -f -s $TMP/meso/ws"EXPID"$i" fort.$nft
done

#L
#L Link for the resulting CIT input files.
#L
ln -f -s $TMP/input/w3field.$DATE fort.3
ln -f -s $TMP/input/zifield.$DATE fort.4
ln -f -s $TMP/input/tmfield.$DATE fort.8
ln -f -s $TMP/input/hmfield.$DATE fort.9
ln -f -s $TMP/input/srfield.$DATE fort.10

#L
#L Run.
#L

```

```

if test $MACHTYPE = sleazy;then
cp Makefile.sleazy Makefile
fi
if test $MACHTYPE = cork;then
cp Makefile.cork Makefile
fi

make met2cit.x
CC=$?
if test $CC -ne 0;then
echo "Fail to make $TMP/prep/met2cit.x"
exit $CC
fi

ln -f -s chemlevel fort.1
./met2cit.x
CC=$?
if test $CC -ne 0;then
echo "Fail to run $TMP/prep/met2cit.x"
exit $CC
fi

#L-----
#L Create surface roughness height, landuse fraction, total
#L hydrocarbon splitting factors using landuse data.
#L
f77 -o lumap.x -static lumap.f
if test $? -ne 0;then
echo "Fail to compile $TMP/prep/lumap.f"
exit
fi
ln -f -s $LANDUSE fort.8
ln -f -s $TMP/global/lufield.data fort.9
ln -f -s $TMP/global/z0field.data fort.10
ln -f -s $TMP/global/thc_regions.$JOB fort.11
./lumap.x

#L-----
#L Create emission data file.
#L
cc -o gridemiss.x gridemiss.c
./gridemiss.x $EMISSION
ln -f -s airshed_gls $TMP/input/baseline_gls_lcc.$DATE

#L-----
#L Create the definition of computational region.
#L
f77 -o comp_region.x -static comp_region.f
ln -f -s $TMP/global/region.$JOB.full fort.9
./comp_region.x

#L-----
#L Create the background air quality data.
#L
f77 -o icbc_bg.x -static icbc_bg.f
ln -f -s $TMP/global/upper_$JOB.$MONTH1 fort.9
./icbc_bg.x

```

```

#L-----
#L Create the observed air quality data.
#L
f77 -o icbc_obs.x -static icbc_obs.f
ln -f -s $TMP/input/aqfield.$DATE fort.9
./icbc_obs.x

#L-----
#L Link look-up tables.
#L
ln -f -s /net/sleazy/data/wpan/airshed/global/resistance.drydep \
$TMP/global/resistance.drydep
ln -f -s /net/sleazy/data/wpan/airshed/global/landuse_z0.data \
$TMP/global/landuse_z0.data

#L-----
#L Create the command file.
#L
LON01='expr 0 - $LON0'
cat > command_input << EOF
&command_input
iarea=$AREA,ipoin=$POIN,
iatmo=1,irate=1,ichem=1,istep=1,idepo=1,
imeso=1,iziscal=1,ziscal=1.0,
iuvc=$UVC,iuvs=$UVS,
uvc=1.00,1.00,1.00,1.00,1.00,1.00,\
1.48,1.20,1.17,1.16,1.17,1.22,\
1.24,1.24,1.27,1.24,1.18,0.96,\
1.00,1.00,1.00,1.00,1.00,1.00, &END
EOF

cat > param_command.h << EOF
INTEGER IREGI,NX,NY,DX,DY,NC,
,IDATE,YEAR,MONTH,DAY,
,ITIME,BEGHR,BEGMN,ENDHR,ENDMN,INTPR,
,ILOCA
PARAMETER (IREGI=1,NX=$NX,NY=$NY,DX=$DX,DY=$DY,NC=$NZ_CHEM,
,IDATE=1,YEAR=$YEAR,MONTH=$MONTH,DAY=$DAY,
,ITIME=1,BEGHR=0,BEGMN=0,ENDHR=23,ENDMN=0,INTPR=60,
,ILOCA=1)
REAL DX,DY,SLA,SLO,TZ
PARAMETER (DX=$DX,DY=$DY,SLA=$LATO,SLO=$LON01,TZ=$TZ)
CHARACTER*80 HEADER
PARAMETER (HEADER=$HEADER)
EOF

f77 -o command.x -static command.f
ln -f -s command_input fort.101
./command.x > $TMP/command.$DATE

#L-----
#L Create the input file list.
#L
JOB1='echo $JOB | wc -c'
JOB1='expr $JOB1 - 1'
DAY1='expr $DAY - 1'
cat > param_files.h << EOF
INTEGER IAREA,IPOIN,IUVS,BCFIX,ICFIX

```

```

CHARACTER YEAR*2,MONTH*3,DAY*2,DAY1*2,INPUT*5,OUTPUT*6,GLOBAL*6,JOB*$JOBL
PARAMETER (IAREA=$AREA,IPOIN=$POIN,IUVS=$UVS,IYEST=$YEST,
, YEAR='$YEAR1',DAY='$DAY',DAY1='$DAY1',
, MONTH='$MONTH1',INPUT='input',
, OUTPUT='output',GLOBAL='global',JOB='$JOB')
EOF

```

```

f77 -o files.x -static files.f
./files.x > $TMP/files.$DATE

```

```

#!/bin/sh
#LL#####
#LL Script: airshed.sh
#LL Purpose: Script to compile and run CIT airshed model.
#LL
#LL Authors: Wenwei Pan
#LL      Department of Earth, Atmospheric and Planetary Sciences
#LL      Massachusetts Institute of Technology
#LL
#LL      Gary Adamkiewicz
#LL      Department of Chemical Engineering
#LL      Massachusetts Institute of Technology
#LL
#LL      Josep C. Angrill, Ph.D.
#LL      Department of Earth, Atmospheric and Planetary Sciences
#LL      Massachusetts Institute of Technology
#LL
#LL Version: 1.0
#LL Date: January 31, 1996
#LL
#LL Tested under compiler: f77 (?)
#LL Tested under OS version: IRIX 5.2 02282016 IP22 mips
#LL
#LL Code modification history:
#LL Version Date
#LL 1.1      02/04/96  Added machtype check and put source files other
#LL                    than airshed to $SRC.
#LL 1.2      02/05/96  More clean up. Group source files in /net/sleazy/
#LL                    data/wpan/IMAQS to cit,ukmo,prep, and post.
#LL                    Added JOBL and DAY1 to the namelist of files.f.
#LL                    Added TZ.
#LL 1.3      02/07/96  Mesoscale output goes to MESO.
#LL 1.4      02/22/96  Added TSEA and DIFTSL; copied preprocessing and
#LL                    airshed sources to user directories.--J.C.Angrill
#LL 1.5      02/22/96  Imaqs.sh splitted into subshells.
#LL
#LL Called by:
#LL      job.sh
#LL
#LL Imports:
#LL      SETOPT
#LL      SRC
#LL      TMP
#LL      MACHTYPE
#LL      YEAR
#LL      MONTH
#LL      DAY
#LL      JOB

```

```

#LL      LANDUSE
#LL      EMISSION
#LL      NX
#LL      NY
#LL      NZ_CHEM
#LL      NZ_MESO
#LL      DX
#LL      LONO
#LL      LATO
#LL      XO
#LL      YO
#LL      XSW
#LL      YSW
#LL      AREA
#LL      POIN
#LL      UVC
#LL      UVS
#LL      TZ
#LL      YEST
#LL
#LL#####

set -$SETOPT

if test ! -d output;then
  mkdir output
else
  rm output/*
fi
if test ! -d chem;then
  mkdir chem
else
  rm chem/*
fi

cd $TMP/chem
cp $SRC/cit/* .

#L
#L Compile the airshed model.
#L
cat > parameter.h << EOF
  PARAMETER (NGMX = $NX, NGMY = $NY, NGMZ = $NZ_CHEM)
  PARAMETER (LBIGRC = NGMX)

  PARAMETER (NSMAX = 35, NIMAX = 10, NEMAX = 20)
  PARAMETER (NHCMAX = 20, NLUMAX = 32, NRMAX = 125)
  PARAMETER (NPMAX = 900, NCMAX = 29)

  PARAMETER (LWORK = NGMX * NGMY * NEMAX)
  PARAMETER (LSCAL = NGMX * NGMY)
  PARAMETER (LWIND = NGMX * NGMY * (NGMZ+1))
  PARAMETER (LAREAS = NGMX * NGMY * NEMAX)
  PARAMETER (LC = NGMX * NGMY * NGMZ * NSMAX)
  PARAMETER (LIC = NGMX * NGMY * NGMZ * NIMAX)
  PARAMETER (LAVG = NGMX * NGMY * NSMAX)
  PARAMETER (LBR = NGMY * NGMZ * NSMAX)
  PARAMETER (LBRIC = NGMY * NGMZ * NIMAX)
  PARAMETER (LBC = NGMX * NGMZ * NSMAX)

```

```
PARAMETER (LBCIC = NGMX * NGMZ * NIMAX)
PARAMETER (LCOLSP = NSMAX * NGMZ)
PARAMETER (NRZ = NRMAX * NGMZ)
EOF
```

```
if test $MACHTYPE = sleazy;then
cp Makefile.sleazy Makefile
fi
if test $MACHTYPE = cork;then
cp Makefile.cork Makefile
fi
```

```
make airshed
if test $? -ne 0;then
echo "Fail to compile $TMP/airshed"
exit 6.3
fi
```

```
#L
#L Run airshed model.
#L
cd $TMP
time chem/airshed < files.$DATE
CC=$?
if test $CC -ne 0;then
echo "Fail to run $TMP/chem/airshed"
exit $CC
fi
```

Bibliography

- [1] S.A. Ackerman and Cox S.K. The saudi arabian heat low: Aerosol distributions and thermodynamic structure. *J. Geophys. Res.*, 87:8991–9002, 1982.
- [2] T.P. Ackerman. A model of the effect of aerosols on urban climates with particular applications to the Los Angeles basin. *J. Atmos. Sci.*, 34:531–547, 1977a.
- [3] T.P. Ackerman and M.B. Baker. Shortwave radiative effects of unactivated aerosol particles in clouds. *J. Appl. Met.*, 16:531–547, 1977b.
- [4] T.P. Ackerman and O.B. Toon. The absorption of visible radiation in atmospheres containing mixtures of absorbing and nonabsorbing particles. *Appl. Opt.*, 20:3661–3667, 1981.
- [5] G. Adomian. Stochastic system analysis. In G. Adomian, editor, *Applied Stochastic Processes*, pages 1–17, New York, 1980. Academic Press, Inc.
- [6] B.A. Albrecht. Aerosols, cloud microphysics, and fractional cloudiness. *Science*, 245:1227–1230, 1989.
- [7] J.C. Angrill. Personal communication. 1996.
- [8] A. Angstrom. On the atmospheric transmission of sun radiation and on dust in the air. *Geografiska Annaler*, 11:156–169, 1929.
- [9] R.J. Ball and Robinson G.D. The origin of haze in the central United States and its effect on solar radiation. *J. Appl. Met.*, 21:171–188, 1982.
- [10] L.A. Barrie, R.M. Hoff, and S.M. Daggupaty. The influence of mid-latitudinal pollution sources on haze in the Arctic. *Atmos. Environ.*, 15:1407–1419, 1981.
- [11] C.M. Benkovitz, C.M. Berkowitz, R.C. Easter, S. Nemesure, R. Wagener, and S.E. Schwartz. Sulfate over the North Atlantic and adjacent continental regions: Evaluation for October and November 1986 using a three-dimensional model driven by observation-derived meteorology. *J. Geophys. Res.*, 99:20725–20756, 1994.
- [12] R. W. Bergstrom and R. Viskanta. Modeling of the effects of gaseous and particulate pollutants in the urban atmosphere. Part II, Pollutant dispersion. *J. Appl. Met.*, 12:913–918, 1973.
- [13] F.S. Binkowski. Aerosol dynamics. In *The First Models-3 Science Design Workshop*, Research Triangle Park, Rayleigh, North Carolina, 1994. U.S. Environmental Protection Agency.

- [14] C.F. Bohren and D.R. Huffman. *Absorption and Scattering of Light by Small Particles*. John Willey & Sons, Inc., 1983.
- [15] O. Boucher and H. Rodhe. Department of meteorology report, Stockholm University, 1994.
- [16] M.A. Box and T. Trautmann. Computation of anthropogenic sulphate aerosol forcing using radiative perturbation theory. *Tellus*, 46B:33–39, 1994.
- [17] K. Bullrich. Streulichtmessungen in Dunst und Nebel. *Met. Rundschau*, 13:21–29, 1960.
- [18] T.N. Carlson and Benjamin S.G. Radiative heating rates for Saharan dust. *J. Atmos. Sci.*, 37:193–213, 1980.
- [19] K.M. Carpenter. An experimental forecast using a nonhydrostatic mesoscale model. *Q.J.R. Met. Soc.*, 105:629–655, 1979.
- [20] R.D. Cess and *et al.* Intercomparison and interpretation of climate feedback processes in 19 atmospheric general circulation models. *J. Geophys. Res.*, 95:16601–16615, 1990.
- [21] T.P. Charlock and W.D. Sellers. Aerosol, cloud reflectivity and climate. *J. Atmos. Sci.*, 37:1136–1137, 1980.
- [22] T.P. Charlock and W.D. Sellers. Aerosol effects on climate: Calculations with time-dependent and steady-state radiative convective models. *J. Atmos. Sci.*, 37:1327–1341, 1980.
- [23] R.J. Charlson, J. Langner, H. Rodhe, C.B. Leovy, and S.G. Warren. Perturbation of the northern hemisphere radiative balance by backscattering from anthropogenic sulfate aerosols. *Tellus*, 43AB:152–163, 1991.
- [24] R.J. Charlson, S.E. Schwartz, J.M. Hales, R.D. Cess, J.A. JR. Coakley, J.E. Hansen, and D.J. Hofmann. Climate forcing by anthropogenic aerosols. *Science*, 255:423–430, 1992.
- [25] H. Charnock. Wind stress on a water surface. *Q.J.R. Met. Soc.*, 81:639–640, 1955.
- [26] M.-D. Chou. A solar radiation model for use in climate studies. *J. Atmos. Sci.*, 49:762–772, 1992.
- [27] M.-D. Chou, D.P. Krats, and W. Ridgway. Infrared radiation parameterization in numerical climate models. *J. Climate*, 4:424–437, 1991.
- [28] C.C. Chuang and J.E. Penner. Effects of anthropogenic sulfate on cloud drop nucleation and optical properties. *Tellus*, 47B, 1995.
- [29] J.A. Coakley, R.L. Bernstein, and P.A. Durkee. Effect of ship-stack effluents on cloud reflectivity. *Science*, 237:1020–1022, 1987.
- [30] J.A. Coakley and R.D. Cess. Response of the NCAR community model to the radiative forcing by the naturally occurring tropospheric aerosol. *J. Atmos. Sci.*, 42:1677–1692, 1985.

- [31] J.A. Coakley, R.D. Cess, and F.B. Yurevich. The effect of tropospheric aerosols on the Earth's radiation budget: A parameterization for climate models. *J. Atmos. Sci.*, 116:137, 1983.
- [32] J.A. Coakley Jr. and P. Chýlek. The two-stream approximation in radiative transfer: including the angle of the incident radiation. *J. Atmos. Sci.*, 32:409–418, 1975.
- [33] G.P. Cox. Modeling precipitation in frontal rainbands. *Q.J.R. Met. Soc.*, 114:115–127, 1988.
- [34] M.J.P. Cullen. A test of a semi-implicit integration technique for a fully compressible non-hydrostatic model. *Q.J.R. Met. Soc.*, 116:1253–1258, 1990.
- [35] G.A. d'Almeida. On the variability of desert-dust radiative characteristics. *J. Geophys. Res.*, 92:3017–3026, 1987.
- [36] G.A. d'Almeida, P. Koepke, and E.P. Shettle. *Atmospheric Aerosols: Global Climatology and Radiative Characteristics*. A. Deepak Publishing, Hampton, Virginia, 1991.
- [37] C.N. Davies. Size distribution of atmospheric particles. *J. Aerosol Sci.*, 5:293–300, 1974.
- [38] A. Deepak and H.E. Gerber, editors. *Meeting of JSC Experts on Aerosols and Climate*. World Meteorological Organization, Geneva, 1980.
- [39] A. Deepak and H.E. Gerber, editors. *Report of the Experts Meeting on Aerosols and Their Climatic Effects*. World Meteorological Organization, Geneva, 1983.
- [40] D. Deirmendjian. *Electromagnetic Scattering on Spherical Polydispersions*. American Elsevier Pub. Co., New York, 1969.
- [41] F. Desalmand, J. Podzimek, and R. Serpolay. A continental well-aged aerosol in the Guinea savannah at the level of a through along the ITCZ. *J. Aerosol Sci.*, 16:19–28, 1985.
- [42] F. Desalmand, R. Serpolay, and J. Podzimek. Some specific features of the aerosol particle concentrations during the dry season and during a bush fire event in West Africa. *Atmos. Environ.*, 9:1535–1543, 1985.
- [43] A. Eliassen. The OCED study of long range transport of air pollutants: Long range transport modeling. *Atmos. Environ.*, 12:479–487, 1978.
- [44] A. Eliassen and J. Saltbones. Decay and transformation rates of SO_2 , as estimated from emission data, trajectories and measured air concentrations. *Atmos. Environ.*, 9:425–429, 1975.
- [45] L. Elterman. Rayleigh and extinction coefficients to 50 km for the region .27 μ to .55 μ . *Appl. Opt.*, 5:1139–1147, 1964.
- [46] K.A. Emanuel. A scheme for representing cumulus convection in large-scale models. *J. Atmos. Sci.*, 48:2313–2335, 1991.

- [47] W. Fett. Sichtweite und atmosphärisches aerosol in Berlin Dahlem. *Contrib. Atmos. Phys.*, 40:262–278, 1967.
- [48] R.J. Fleming. The dynamics of uncertainty: Application to parameterization constants in climate models. *Climate Dynamics*, 8:135–150, 1993.
- [49] E. Frankenberger. Beziehungen zwischen der Normsichtweite und der relativen Feuchte nach Messungen in Quickborn. *Contrib. Atmos. Phys.*, 37:183–196, 1964.
- [50] J.M. Fritsch and C.F. Chappell. Numerical prediction of convectively driven pressure systems. Part I: Convective parameterization. *J. Atmos. Sci.*, 37:1722–1733, 1980.
- [51] Q. Fu and K.N. Liou. On the correlated k -distribution method for radiative transfer in nonhomogeneous atmospheres. *J. Atmos. Sci.*, 49:2139–2156, 1992.
- [52] W.L. Gates. AMIP: The atmospheric model intercomparison project. *Bull. Am. Met. Soc.*, 73:1962–1970, 1992.
- [53] W. Gautschi. Algorithm 726: ORTHPOL - A package of routines for generating orthogonal polynomials and Gauss-type quadrature rules. *ACM Transactions on Mathematical Software*, 20(1):21–62, 1994.
- [54] F. Gelbard and J.H. Seinfeld. Simulation of multicomponent aerosol dynamics. *Journal of Colloid and Interface Science*, 78(2):485–501, 1980.
- [55] S.J. Ghan, C.C. Chuang, and J.E. Penner. A parameterization of cloud droplet nucleation part i: single aerosol type. *Atmos. Res.*, 30(4):197–221, 1993.
- [56] R.G. Ghanem and P.D. Spanos. *Stochastic Finite Elements: A Spectral Approach*. Springer-Verlag, New York, 1991.
- [57] B.W. Golding. An efficient non-hydrostatic forecast model. *Met. Atmos. Phys.*, 50:89–103, 1992.
- [58] W.R. Goodin, G.J. McRae, and J.H. Seinfeld. A comparison of interpolation methods for sparse data: application to wind and concentration fields. *J. Applied Meteorology*, 18:761–771, 1979.
- [59] W.R. Goodin, G.J. McRae, and J.H. Seinfeld. An objective analysis technique for constructing three-dimensional, urban-scale wind fields. *J. Applied Meteorology*, 19:98–108, 1980.
- [60] H. Grassl. Aerosol influence on radiative cooling. *Tellus*, 25:386–395, 1973.
- [61] G.M. Hale and M.R. Querry. Optical constants of water in the 200-nm to 200 μm wavelength region. *Appl. Opt.*, 12:555–563, 1973.
- [62] G. Hänel. The properties of atmospheric aerosol particles as functions of the relative humidity at thermodynamic equilibrium with the surrounding air. In R.E. Landsburg and J. Van Miegham, editors, *Advances in Geophysics*, volume 19, pages 73–188, 1976.
- [63] G. Hanel. Heating of the atmosphere due to absorption of shortwave radiation within particles. In H.E. Gerber and Deepak A., editors, *Aerosols and Their Climatic Effects*, pages 241–244. A. Deepak Publishing, 1984.

- [64] R.A. Harley, A.G. Russell, G.J. McRae, G.R. Cass, and J.H. Seinfeld. Photochemical modeling of the Southern California Air Quality Study. *Environ. Sci. Technol.*, 27:378–388, 1993.
- [65] Harshvardhan and Cess R.D. Effect of tropospheric aerosols upon atmospheric temperature and global climate. *J. Quant. Spectrosc. Rad. Transfer*, 19:621–632, 1978.
- [66] I.M. Held and M.J. Suarez. A proposal for the intercomparison of the dynamical cores of atmospheric general circulation models. *Bull. Am. Met. Soc.*, 75:1825–1830, 1994.
- [67] A. Henderson-Sellers, Z.-L. Yang, and R.E. Dickinson. The project for intercomparison of land-surface parameterization schemes. *Bull. Am. Met. Soc.*, 74:1335–1349, 1993.
- [68] P.V. Hobbs. *Aerosol-cloud-climate interaction*. Academic Press, New York, 1993.
- [69] R. Husar. Sulfur and nitrogen over eastern North America. EPA Contract R806548, Washington University, St. Louis, Missouri, 1983.
- [70] A. Jones, D.L. Roberts, and A. Slingo. A climate model study of indirect radiative forcing by anthropogenic sulphate aerosols. *Nature*, 370:450–453, 1994.
- [71] S. Joussaune. *Modelisation des cycles des especes isotopiques de l'eau et des aerosols d'origine desertique dans un modele de circulation generale de l'atmosphere*. PhD thesis, Universite de Paris VI, 1983.
- [72] C.E. Junge. Gesetzmäßigkeiten in der größenverteilung atmosphärischer aerosole über dem kontinent. *Ber. D. Wetterd. US-Zone*, 35:261–277, 1952.
- [73] C. G. Justus and B. B. Murphey. Temporal trends in surface irradiance at ultraviolet wavelengths. *J. Geophysical Res.*, 99:1389, 1994.
- [74] K. Karhunen. Zur spektraltheorie stochastischer prozesse. *Annales Academiae Scientiarum Fennicae*, Series A, 1:34, 1946.
- [75] Y.J. Kaufman and M.-D. Chou. Model simulations of the competing climatic effects of SO_2 and CO_2 . *J. Climate*, 6:1241–1252, 1993.
- [76] Y.J. Kaufman and Robert S. F. Fossil fuel and biomass burning effect on climate—heating or cooling? *J. Climate*, 4:578–588, 1991.
- [77] J.T. Kiehl and B.P. Briegleb. The relative roles of sulfate aerosols and greenhouse gases in climate forcing. *Science*, 260:311–314, 1993.
- [78] Y.P. Kim and J.H. Seinfeld. Simulation of multicomponent aerosol dynamics. *Journal of Colloid and Interface Science*, 149(2):425–449, 1992.
- [79] M. Kleiber and T.D. Hien. *The Stochastic Finite Element Method: Basic Perturbation Technique and Computer Implementation*. John Wiley & Sons, New York, 1992.
- [80] J. Kuebler, J.M. Giovannoni, and A.G. Russell. Eulerian modeling of photochemical pollutants over the Swiss plateau and control strategy analysis. *Atmos. Environ.*, 30:951–966, 1996.

- [81] S. Kullback. *Information Theory and Statistics*. Wiley, New York, 1959.
- [82] D. Labs and H. Neckel. Transformation of the absolute solar radiation data into the international practical temperature scale of 1968. *Solar Physics*, 15:79–87, 1970.
- [83] J. Langner and H. Rodhe. A global three-dimensional model of the tropospheric sulfur cycle. *J. Atmos. Chemistry*, 13:225–263, 1991.
- [84] D.R. Lawson. The Southern California Air Quality Study. *J. Air Waste Manage. Assoc.*, 40:156–165, 1990.
- [85] M.D. Lax. Approximate solution of random differential and integral equations. In G. Adomian, editor, *Applied Stochastic Processes*, pages 121–134, New York, 1980. Academic Press, Inc.
- [86] W.R. Leaitch, G.A. Isaac, J.W. Strapp, C.M. Banic, and H.A. Wiebe. The relationship between cloud droplet number concentrations and anthropogenic pollution: Observations and climatic implications. *J. Geophys. Res.*, 97:2463–2472, 1992.
- [87] K.N. Liou, Q. Fu, and T.P. Ackerman. A simple formulation of the delta-four-stream approximation for radiative transfer parameterization. *J. Atmos. Sci.*, 45:1940–1947, 1988.
- [88] M. Loève. Fonctions aléatoire de second ordre. *Comptes Rendus des Seances de l'Academie des Sciences*, 220, 1945.
- [89] F.W. Lurmann, W.P. Carter, and L.A. Coyner. A surrogate species chemical reaction mechanism for urban-scale air quality simulation models, Volume 1–Adaptation of the mechanism. Final report to the U.S. EPA under contract number 68-02-4104, ERT Inc. and Statewide Air Pollution Research Center, University of California, 1987.
- [90] G.M. Martin, D.W. Johnson, and A. Spice. The measurement and parameterization of effective radius of droplets in warm stratocumulus clouds. *J. Atmos. Sci.*, 51:1823–1842, 1994.
- [91] R.A. McClatchey, R.W. Fenn, J.E.A. Selby, F.E. Volz, and J.S. Garing. Optical properties of the atmosphere. Technical report, Air Force Geophysics Laboratory, Hanscom AFB, Massachusetts, 1972.
- [92] J.L. McGregor. Economical determination of the departure points for semi-Lagrangian models. *Mon. Wea. Rev.*, 121:221–230, 1993.
- [93] G.J. McRae, W.R. Goodin, and J.H. Seinfeld. Development of a second-generation mathematical model for urban air pollution–I. Model formulation. *Atmos. Environ.*, 16:679–696, 1982.
- [94] G.J. McRae, A.G. Russell, and R.A. Harley. CIT photochemical airshed model–data preparation manual. Final report to the coordinating research council under contract SCAQS-8, Carnegie Mellon University and California Institute of Technology, 1992.
- [95] G.J. McRae and J.H. Seinfeld. Development of a second-generation mathematical model for urban air pollution–II. Model performance evaluation. *Atmos. Environ.*, 17:501–523, 1982.

- [96] A. Meszaros. On the size distribution of atmospheric aerosol particles of different composition. *Atmos. Environ.*, 11:1075–1081, 1977.
- [97] G. Mie. Beitrag zur optik trüber medien. *Ann. Phys.*, 25:377–445, 1908.
- [98] J.B. Milford, A.G. Russell, and G.J. McRae. A new approach to photochemical pollution control: implications of spatial patterns in pollutant responses to reductions in nitrogen oxides and reactive organic gases. *Environ. Sci. and Tech.*, 23:1290–1301, 1989.
- [99] F. Moleni and T.N. Palmer. Predictability and finite-time instability of the northern winter circulation. *Q.J.R. Met. Soc.*, 119:269–298, 1992.
- [100] J.L. Monteith. Evaporation and environment. *Symp. Soc. Ecp. Biol.*, 19:205–234, 1964.
- [101] M.G. Morgan, M. Henrion, and M.J. Small. *Uncertainty, A Guide to Dealing with Uncertainty in Quantitative Risk and Policy Analysis*. Cambridge University Press, New York, 1992.
- [102] N. Newiger and K. Bahnke. Influence of cloud composition and cloud geometry on the absorption of solar radiation. *Contrib. Atmos. Physics.*, 54:370–382, 1981.
- [103] S. Nicholls. The dynamics of stratocumulus: aircraft observations and comparisons with a mixed layer model. *Q.J.R. Met. Soc.*, 110:783–820, 1984.
- [104] H. Niederreiter. *Random Number Generation and Quasi-Monte Carlo Methods*. SIAM, Philadelphia, 1992.
- [105] J. Nord. Long range transport of air pollutants in Europe and acid precipitation in Norway. *Water, Air, and Soil Pollution*, 6:199–217, 1976.
- [106] L. Peng, M.-D. Chou, and A. Arking. Climate warming due to increasing atmospheric CO_2 : Simulations with a multilayer coupled atmospheric-ocean seasonal energy balance model. *J. Geophys. Res.*, 92:5505–5521, 1987.
- [107] J.E. Penner, R.J. Charlson, J.M. Hales, N.S. Laulainen, R. Leifer, T. Novakov, J. Ogren, L.F. Radke, S.E. Schwartz, and L. Travis. Quantifying and minimizing uncertainty of climate forcing by anthropogenic aerosols. *Bull. Am. Met. Soc.*, 75:375–400, 1994.
- [108] J.E. Penner, S.J. Ghan, and J.J. Walton. The role of biomass burning in the budget and cycle of carbonaceous soot aerosols and their climate impact. In J. Levine, editor, *Global Biomass Burning*, pages 387–393. The MIT Press, 1991.
- [109] R.J. Perry, A.J. Hunt, and D.R. Huffman. Experimental determinations of Mueller scattering matrices for nonspherical particles. *Appl. Opt.*, 17:2700–2710, 1978.
- [110] J. Podzimek. Physical properties of aerosol in rural and forested areas. In P.V. Hobbs and M.P. McCormick, editors, *Aerosols and Climate*, pages 153–164. A. Deepak Publishing, Hampton, Virginia, 1987.

- [111] J.B. Pollack and J.N. Cuzzi. Scattering by nonspherical particles of size comparable to a wavelength: A new semi-empirical theory and its application to tropospheric aerosols. *J. Atmos. Sci.*, 37:868–881, 1979.
- [112] H.R. Pruppacher and J.D. Klett. *Microphysics of Clouds and Precipitation*. D. Reidel Publishing Company, Boston, 1980.
- [113] R.F. Pueschel, C.C. van Valin, R.C. Castillo, J.A. Kadlecek, and E. Ganor. Aerosols in polluted versus nonpolluted air masses: long-range transport and effects on clouds. *J. Clim. Appl. Met.*, 25:1908–1917, 1986.
- [114] L.F. Radke, J.A. Coakley, and M.D. King. Direct and remote sensing observations of the effects of ships on clouds. *Science*, 246:1146–1149, 1989.
- [115] V. Ramanathan. The role of ocean-atmosphere interactions in the CO_2 climate problem. *J. Atmos. Sci.*, 38:918–930, 1981.
- [116] V. Ramanathan, L. Callis, R. Cess, J. Hansen, I. Isaksen, W. Kuhn, A. Lacis, F. Luther, J. Mahlman, R. Reck, and M. Schlesinger. Climate-chemical interactions and effects of changing atmospheric trace gases. *Rev. of Geophysics*, 25:1441–1482, 1987.
- [117] S.I. Rasool and S.H. Schneider. Atmospheric carbon dioxide and aerosols: effects of large increases on global climate. *Science*, 173:138–141, 1971.
- [118] R.A. Reck. Thermal and radiative effects of atmospheric aerosols in the northern hemisphere calculated using a radiative convective model. *Atmos. Environ.*, 10:611–617, 1976.
- [119] N.O. Renno. *Cumulus convection parameterization and numerical modeling of moist atmosphere*. PhD thesis, Massachusetts Institute of Technology, Cambridge, Massachusetts, 1992.
- [120] T.J. Resch. *A Framework for the Modeling of Suspended Multicomponent Particulate Systems with Applications to Atmospheric Aerosols*. PhD thesis, Massachusetts Institute of Technology, Cambridge, Massachusetts, 1995.
- [121] W.T. Roach and A. Slingo. A high resolution infrared radiative transfer scheme to study the interaction of radiation with cloud. *Q.J.R. Met. Soc.*, 105:603–614, 1979.
- [122] A. Robock. The seasonal cycle of snow cover, sea ice and surface albedo. *Mon. Wea. Rev.*, 108:267–285, 1980.
- [123] A.G. Russell, K.F. McCue, and G.R. Cass. Mathematical modeling of the formation of nitrogen-containing air pollutants. 1. evaluation of an Eulerian photochemical model. *Environ. Sci. Technol.*, 22:263–271, 1988a.
- [124] A.G. Russell, K.F. McCue, and G.R. Cass. Prediction of formaldehyde concentrations in the south coast air basin. In *Presentation of the APRAC/CRC Methanol Workshop*, Anaheim, California, 1988b.
- [125] A.G. Russell, S.T. Pierre, and J.B. Milford. Ozone control and methanol fuel use. *Science*, 247:201–205, 1990.

- [126] A.G. Russell, D.A. Winner, K.F. McCue, and G.R. Cass. Mathematical modeling and control of the dry deposition flux of nitrogen-containing air pollutants. Report to the California Air Resources Board under Contract A6-188-32 EQL Report 29, Environmental Quality Laboratory, California Institute of Technology, Pasadena, California, 1992.
- [127] L. Schütz. Long-range transport of desert dust with special emphasis on the Sahara. *Ann. N.Y. Acad. Sci.*, 338:515–532, 1980.
- [128] S.E. Serrano. Using the C language to approximate non-linear stochastic systems. *Adv. Eng. Software*, 12(2):59–68, 1990.
- [129] S.E. Serrano and T.E. Unny. Random evolution equations in hydrology. *Applied Mathematics and Computation*, 39:97s–122s, 1990.
- [130] G.E. Shaw. Considerations on the origin and properties of the Antarctic aerosol. *Rev. Geophys. Space Phys.*, 8:1983–1998, 1979.
- [131] E.P. Shettle and R.W. Fenn. Models of atmospheric aerosols and their optical properties. In *AGARD Conference Proceedings No. 183: Optical Properties in the Atmosphere*, AGARD-CP-183, NTIS, ADA 028615, 1976.
- [132] E.P. Shettle and R.W. Fenn. Models for the aerosols of the lower atmosphere and the effects of humidity variations on their optical properties. Technical report, Air Force Geophysics Laboratory, Hanscom AFB, Massachusetts, 1979.
- [133] K.P. Shine, R.G. Derwent, D.J. Wuebbles, and J.-J. Morcrette. Radiative forcing of climate. In J.T. Houghton, G.T.J. Jenkins, and J.J. Ephraums, editors, *Intergovernmental Panel on Climate Change: The IPCC Scientific Assessment*, pages 41–68. Cambridge University Press, 1990.
- [134] J.E. Shore and R.W. Johnson. Properties of cross-entropy minimization. *IEEE Trans. Info. Theory*, IT-27(4):472–482, 1981.
- [135] W.G.N. Slinn. Some approximations for the wet and dry removal of particles and gases from the atmosphere. *Water, Air, and Soil Pollution*, 7:513–543, 1977.
- [136] F. Somieski. Mesoscale model parameterizations for radiation and turbulent fluxes at the lower boundary. *DFVLR-FB-88-48*, pages 13–22, 1988.
- [137] A. Staniforth and J. Cote. Semi-Lagrangian integration schemes for atmospheric models—a review. *Mon. Wea. Rev.*, 119:2206–2223, 1991.
- [138] W.E. Stewart, M. Caracotsios, and J.P. Sørensen. Parameter estimation from multiresponse data. *AIChE Journal*, 38(5):641–650, 1992.
- [139] R.S. Stolarski and A.R. Douglas. Sensitivity of an atmospheric photochemistry model to chlorine perturbations including consideration of uncertainty propagation. *J. Geophys. Res.*, 91:7853–7864, 1986.
- [140] G.E. Streit and F. Guzman. Mexico City air quality: progress of an international collaborative project to define air quality management options. *Atmos. Environ.*, 30:723–733, 1996.

- [141] P.R. Swan and I.Y. Lee. Meteorological and air pollution modeling for an urban airport. *J. Appl. Met.*, 19:534–544, 1979.
- [142] D. Tanre, J.F. Geleyn, and J. Slingo. First results of the introduction of an advanced aerosol radiation interaction in the ECMWF low resolution global model. In A. Deepak and H.E. Gerber, editors, *Aerosols and Their Climatic Effects*. A. Deepak Publishing, Hampton, Virginia, 1984.
- [143] M.C. Tapp and W.P. White. A non-hydrostatic mesoscale model. *Q.J.R. Met. Soc.*, 102:277–296, 1976.
- [144] M.A. Tatang. *Direct Incorporation of Uncertainty in Chemical and Environmental Engineering Systems*. PhD thesis, Massachusetts Institute of Technology, Cambridge, Massachusetts, 1994.
- [145] K.E. Taylor and J.E. Penner. Response of the climate system to atmospheric aerosols and greenhouse gases. *Nature*, 369:734–737, 1994.
- [146] O.B. Toon and Pollack J.B. A global average model of atmospheric aerosols for radiative transfer calculations. *J. Appl. Met.*, 15:225–246, 1976.
- [147] O.B. Toon, R.P. Turco, D. Westphal, R. Malone, and M.S. Liu. A multidimensional model for aerosols: Description of computational analogs. *J. Atmos. Sci.*, 45:2123–2143, 1988.
- [148] Z. Toth and E. Kalnay. Ensemble forecasting at NMC: The generation of perturbations. *Bull. Amer. Met. Soc.*, 74:2317–2330, 1993.
- [149] T. Trautmann, P.J. Elliott, and M.A. Box. Shortwave radiative effects of standard aerosol models: a perturbation approach. *Beitr. Phys. Atmosph.*, 65:59–78, 1992.
- [150] S. Twomey. The nuclei of natural cloud formation: The supersaturation in natural clouds and the variation of cloud droplet concentrations. *Geophys. Pura Appl.*, 43:243–249, 1959.
- [151] S. Twomey. *Atmospheric Aerosols*. Elsevier, Amsterdam, 1977.
- [152] S. Twomey. Aerosols, clouds and radiation. *Atmos. Environ.*, 25A:2435–2442, 1991.
- [153] H.C. Van der Hulst. *A new look at multiple scattering*. New York, 1963.
- [154] J. Villadsen and M.L. Michelsen. *Solution of Differential Equation Models by Polynomial Approximation*. Prentice-Hall Inc., Englewood Cliffs, 1978.
- [155] R. Viskanta, R.W. Bergstrom, and R.O. Johnson. Effects of air pollution on thermal structure and dispersion in an urban planetary boundary layer. *Contrib. Atmos. Phys.*, 50:419–440, 1977.
- [156] R. Viskanta and R.A. Daniel. Radiative effects of elevated pollutant layers on temperature structure and dispersion in an urban atmosphere. *J. Appl. Met.*, 19:53–70, 1980.

- [157] K.K. Wagner and P.D. Allen. SCAQS emissions inventory for August 27-29, 1987. Technical report, Technical Support Division, California Air Resources Board, Sacramento, California, 1990.
- [158] J.J. Walton, M.C. MacCracken, and S.J. Ghan. A global-scale Lagrangian trace species model of transport, transformation, and removal processes. *J. Geophys. Res.*, 93:8339–8354, 1988.
- [159] W.C. Wang and G.A. Domoto. The radiative effect of aerosols in the Earth's atmosphere. *J. Appl. Met.*, 13:521–534, 1974.
- [160] D.A. Warrilow, A.B. Sangster, and A. Slingo. Modeling of land surface processes and their influence on European climate. Dynamical Climatology Technical Note 38, United Kingdom Meteorological Office, 1986.
- [161] R.M. Welch, J. Paegle, and W.G. Zdunkowski. Two-dimensional numerical simulation of the effects of air pollution upon the urban-rural complex. *Tellus*, 30:136–150, 1978.
- [162] D.L. Westphal, T.N. Carlson, and O.B. Toon. The numerical simulation of the evolution of a Saharan dust outbreak using a general prognostic aerosol model. In A. Deepak and H.E. Gerber, editors, *Aerosols and Their Climatic Effects*. A. Deepak Publishing, Hampton, Virginia, 1984.
- [163] K.T. Whitby. The physical characteristics of sulfur aerosols. *Atmos. Environ.*, 12:135–159, 1978.
- [164] K.T. Whitby and G.M. Sverdrup. California aerosols: their physical and chemical characteristics. In G.M. G.M. Hidy, P.K. Mueller, D. Grosjean, B.R. Appel, and J.J. Wesolowski, editors, *The character and origins of smog aerosols: a digest of results from the California aerosol characterization experiment (ACHEX)*, pages 477–517. John Wiley & Sons, 1980.
- [165] D.L. Williamson and P.J. Rasch. Two-dimensional semi-Lagrangian transport with shape preserving interpolation. *Mon. Wea. Rev.*, 117:102–129, 1989.
- [166] W.J. Wiscombe and G.W. Grams. The backscattered fraction in two-stream approximations. *J. Atmos. Sci.*, 33:2440–2451, 1976.
- [167] World Meteorological Organization, Geneva. *A preliminary cloudless standard atmosphere for radiation computation*, WMO TD. No.24, 1986.
- [168] H. Wozniakowski. Average case complexity of multivariate integration. *Bull. Amer. Math. Soc.*, 24(1):185–194, 1991.
- [169] J. Wu. Wind stress coefficients over sea surface from breeze to hurricane. *J. Geophys. Res.*, 87:9704–9706, 1982.
- [170] T. Yamada and G.L. Mellor. A numerical simulation of BOMEX data using a turbulence closure model coupled with ensemble cloud relations. *Q.J.R. Met. Soc.*, 105:915–944, 1979.
- [171] G. Yamamoto and Tanaka M. Increase of global albedo due to air pollution. *J. Atmos. Sci.*, 29:1405–1412, 1974.

- [172] E.E. Yotter and D.L. Wade. Development of a gridded motor vehicle emission inventory for the southern california air quality study. In *Presentation of the 82nd annual meeting of the Air & Waste Management Association: Paper 89-137.2*, Anaheim, California, 1989.
- [173] W.G. Zdunkowski, R.M. Welch, and J. Paegle. One-dimensional numerical simulation of the effects of air pollution on the planetary boundary layer. *J. Atm. Sci*, 33:2399–2414, 1976.